SISSA
Scuola
Internazionale
Superiore di
Studi Avanzati

Physics Area — Ph.D. course in
Theory and Numerical Simulation of Condensed Matter

Topology and Nonlinearity in Driven-Dissipative Photonic Lattices: Semiclassical and Quantum Approaches

Candidate:
Matteo Seclì

Supervisor:
Massimo Capone, SISSA

Co-supervisors:
Iacopo Carusotto, INO–CNR BEC Center, Trento
Marco Schirò, Collège de France, Paris

Academic Year 2020–2021

Abstract

This Thesis aims to advance the understanding of photonic systems along two parallel but complementary tracks: the semiclassical analysis of lattices involving a macroscopic number of photons and the quantum analysis of strongly-correlated photonic lattices.

The semiclassical analysis is particularly suited to investigate systems, among others, that emerge in the context of topological photonics. In particular, this Thesis focuses on the analysis of so-called *topological lasers*, devices that aim to improve on traditional lasers by operating in special lasing modes, i.e. topological modes, that are more resilient against disruptions. Via a semiclassical description of the laser physics, we are able to determine the most efficient gain configurations, uncover new effects and new instability regimes, investigate the resilience to disorder, and design subtle mechanisms that allow the laser to select the desired topological mode even under unfavorable conditions.

The quantum analysis of strongly-correlated photonic lattices is instead complicated by the sheer size of the Hilbert space and by the inherent many-body correlations, which do not allow for an effective single-particle scenario. In absence of a coherent pump, though, small enough systems can still be studied via exact diagonalization by exploiting their phase rotation symmetry; we do so in the analysis of a *driven-dissipative Bose-Hubbard dimer*, where two nonlinear cavities are coupled. In this system, we reveal signatures of a localization-delocalization transition in steady-state observables and in steady-state response functions, as well as in the time dynamics of the observables. For the more ambitious goal of studying a full lattice of highly nonlinear cavities, though, this is no longer enough. Therefore, we employ a technique called *dynamical mean-field theory*, borrowed from the treatment of strongly-correlated electron systems, to reduce the size of the effective Hilbert space by replacing the interaction generated by the lattice on any one of its sites with an effective time-dependent field. As a case study for the effectiveness of our specific implementation of this technique in the context of driven-dissipative photonic lattices, we demonstrate the ability to reproduce the so-called quantum Zeno effect in a Bose-Hubbard lattice with strong two-particle dissipation.

Acknowledgments

This Thesis work would have not been possible without the support and contributions from many people.

First of all, my heartfelt thanks go to my supervisor, Massimo Capone, who supported me and encouraged me to pursue my scientific interests during these years at SISSA. I could always count on him and on his precious bits of advice, whenever I needed it. A big thank-you also goes to Iacopo Carusotto, for his never-ending patience and support during all these years, and for his unfaltering optimism and scientific enthusiasm. I've learned a lot from him, not only as a scientist, but also as a person. My thanks also go to Marco Schirò, for his irreplaceable guidance on the second part of this Thesis, and for stimulating my curiosity on new and exciting research subjects. I would also like to thank Aashish A. Clerk and Davide Rossini, who kindly accepted to review this Thesis, and Tomoki Ozawa and Boubacar Kanté, for our enlightening discussions over these years.

This Thesis is also the result, however, of the warm and welcoming environment I experienced every day at SISSA, surrounded by fantastic people who are not only colleagues, but also dearest friends. I want to thank all of them: Andrea, Claudio, Giulia, Lorenzo C., Matteo F., Matteo W., Yusuf, Adu, Claudia, Cristiano, Davide, Federica, Lucas, Mattia, Alberto S., Fabio, Martino, Vittorio, Francesca, Gabriele, Lorenzo P., Caterina, Alberto P., Federico, Adriano, Francesco, Uriel, Martina, Anna, Pierfrancesco, Sara, Bruno, all the members of the SISSA Choir, all the past, temporary, and present members of our band, "Cipolle Verdi", and all the others I might have forgotten here. A special thank-you goes to Luca, who, despite the geographical distance, has always been there for me, even in the darkest moments, and to Marlen. Thanks to all of you, for the true friendship and joy you bring to my life.

The years of doctoral studies often prove to be a demanding and stressful life period. The uncertainty of the future, the hurdles along the path, the toxicity of some highly competitive environments, tend to take a heavy mental and physical health toll. This last year and a half was further hardened by the outbreak of the COVID-19 pandemic, which left an indelible mark in our lives. I wouldn't have been able to go through all these hurdles without the constant support of the people that love me the most. I could always count on the loving presence of my family, despite the geographical distance, which unfortunately becomes no

easier to endure as time goes by. I send a warm hug to all of them: Valter, Irene, Chiara, Alberto, and my grandma "Peppa". At the same time, I will never forget the constant support of my late grandparents: Giovanni, "Uccio", and "Gina". I hope I would have made them proud, if they were still here. Last but not least, my thoughts go to the person who above all, day by day, has filled my life and my heart. Thank you, Angela: thank you for being there every day, thank you for putting up with me, thank you for being both my closest confidant and the person I love the most. You've made me the most fortunate person in the world, and your love has given me the strength to go on.

Matteo Seclì

Trieste, September 29, 2021

List of publications

1. Matteo Seclì, Massimo Capone, and Iacopo Carusotto. "Theory of chiral edge state lasing in a two-dimensional topological system". In: *Physical Review Research* 1.3 (Dec. 2019), p. 033148. ISSN: 2643-1564. DOI: 10.1103/PhysRevResearch.1.033148

2. Matteo Seclì and Iacopo Carusotto. "Harper-Hofstadter Topological Laser with Frequency-Dependent Gain". In: *2019 Conference on Lasers and Electro-Optics Europe & European Quantum Electronics Conference*. IEEE, June 2019, pp. 1–1. ISBN: 978-1-7281-0469-0. DOI: 10.1109/CLEOE-EQEC.2019.8872202

3. Matteo Seclì, Tomoki Ozawa, Massimo Capone, and Iacopo Carusotto. "Spatial and spectral mode-selection effects in topological lasers with frequency-dependent gain". In: *APL Photonics* 6.5 (May 2021), p. 050803. ISSN: 2378-0967. DOI: 10.1063/5.0041124

4. Matteo Seclì, Massimo Capone, and Marco Schirò. "Signatures of self-trapping in the driven-dissipative Bose–Hubbard dimer". In: *New Journal of Physics* 23.6 (June 2021), p. 063056. ISSN: 1367-2630. DOI: 10.1088/1367-2630/ac04c8

5. Aurelian Loirette-Pelous, Ivan Amelio, Matteo Seclì, and Iacopo Carusotto. "Linearized theory of the fluctuation dynamics in 2D topological lasers". In: *arXiv preprint* (Jan. 2021). arXiv: 2101.11737

6. Matteo Seclì et al. "Dynamical mean-field theory analysis of the quantum Zeno effect in a driven-dissipative Bose-Hubbard lattice". In preparation. 2021

Contents

Acronyms

AI Absolute Instability. 30–33

AIM Anderson Impurity Model. ix, 134, 138–140, 143, 144, 146, 147, 149, 151–154

AMEA Auxiliary Master Equation Approach. 139

AS Absolute Stability. 32, 33

BDMFT Bosonic Dynamical Mean Field Theory. 138

BHD Bose-Hubbard Dimer. 68, 103–106, 108, 112, 115, 117, 130, 131, 133, 142, 143, 159

CI Convective Instability. 30, 32, 33, 35, 36

DMFT Dynamical Mean Field Theory. 1, 2, 68, 88, 103, 132, 134–138, 140, 142, 145–147, 151, 152, 154, 155, 157, 158, 160, 161, 165

ED Exact Diagonalization. 2, 68, 147, 151

FWHM Full Width at Half Maximum. 42, 43, 47, 54

GPE Gross-Pitaevskii Equation. 14, 15

HWHM Half Width at Half Maximum. 157

NCA Non-Crossing Approximation. 158

NSS Noise-Sustained Structures. 30, 32

OBC Open Boundary Conditions. 20

OpenBDMFT Bosonic Dynamical Mean Field Theory for Open Systems. ix, 138, 139, 142, 146, 147, 149, 152, 157, 158, 160

PBC Periodic Boundary Conditions. 19, 20, 43

PDF Probability Density Function. 95

PEG Partial Edge Gain. vii, 22, 24, 27–33, 35, 39

PSD Power Spectral Density. 24, 26

QED Quantum Electrodynamics. 67

QRT Quantum Regression Theorem. 96, 97

RHS Right-Hand Side. 9, 14, 32, 35, 41, 72

RWA Rotating-Wave Approximation. 8, 9

SR Single Resonator. 23

TFR Time-Frequency Representation. 51, 52

TLA Two-Level Atom. 7, 8, 10, 15, 41, 61, 72

WEG Whole Edge Gain. vii, 22–30, 33, 36, 39

WSG Whole System Gain. vii, 23, 27, 36, 39, 44, 61, 62

WVD Wigner-Ville Distribution. 51–53

Introduction

The inception of my doctoral studies came at the beginning of a time of great excitement and renewed interest in a wide class of light-based open quantum systems, in fields ranging from optical lattices to photonics to quantum systems [1–23].

On one hand, I have been a curious witness of the explosion of the field of topological photonics, launched by the pioneering works [24–26], and in particular, I became interested in the efforts towards the realization of the first two-dimensional topological laser [27–29].

On the other hand, the recent advances in the development of new platforms for photonic quantum systems [2–8] started to stimulate a vivid demand for new techniques able to address the many-body problem in open bosonic systems. While semiclassical simulations at the mean-field level are inherently suitable to investigate systems with a large number of photons and weak nonlinearities, like the ones typically considered in topological photonics, the sheer size of the Hilbert space and the intrinsic strong correlations between the particles make the simulation of photonic systems with strong nonlinearities at the quantum level notoriously difficult, unless they are extremely small.

Motivated by the advances in these fields, this Thesis project started out by pursuing both the analysis of photonic systems at a semiclassical level, in particular in the context of topological photonics [30], and their analysis via full quantum simulations. We set out to reach, eventually, the ambitious goal of converging these two seemingly separate yet complementary paths in order to probe, at the quantum level, photonic systems whose Hilbert space is too large to be dealt with via standard quantum mechanical techniques.

In order to fill the gap between the simulation of photonic systems in a semiclassical context, where size is not an issue, and the simulation of photonic systems at the quantum level, which are extremely limited in size, we decided to employ a technique known as Dynamical Mean Field Theory (DMFT) [31], suitably generalized to deal with the open quantum systems at hand. While this Thesis does not report results combining the two research lines, namely the full quantum study of extended non-linear systems with non-trivial topology remains, it has brought on one hand important technical advances and on the other hand significant physical insight, paving the way for the successful convergence of the two research lines. I am indeed confident that, once a few remaining technical

roadblocks are solved, we'll soon be able to showcase the quantum analysis of larger classes of open quantum systems.

While working towards this convergence, the semiclassical investigation of the topological laser was nevertheless successful in uncovering new unexpected and exciting features [32], after having laid out the initial numerical foundations in my Master's Thesis. Furthermore, stimulated by the puzzling results in [29] that were calling for a theoretical explanation, I worked to advance the understanding of the promotion of topological edge modes to lasing modes [33].

At the same time, our work on the quantum analysis of photonic systems was instrumental in the investigation of the quantum dynamics and of the steady-state response functions of two coupled nonlinear cavities, which can be seen as a minimal non-trivial non-linear model which can be used to guide the study of larger systems as described by DMFT. Building upon this first step, our DMFT implementation was then successfully employed to investigate the physics of a full lattice model with strong nonlinear dissipation.

This Thesis will walk the reader through these two parallel paths in Part I and Part II; more detailed introductions for each of the two Parts can be found in Chapter 1 and in Chapter 6, respectively. In Chapter 2 we introduce the semiclassical theory of lasers, extensively used in Part I and referenced in Part II when discussing the presence of nonlinearities. In Chapters 3 and 4, instead, we present the results of our semiclassical investigation of two-dimensional topological lasers. Chapter 7 is devoted to a more systematic approach to the Lindblad equation, already employed in Part I; we discuss its solution via Exact Diagonalization (ED) in the superbosonic representation, and the consequential calculation of Green's functions in the Keldysh formalism. This technical toolkit is used to investigate a pair of nonlinear cavities in Chapter 8. Finally, in Chapter 9, we introduce the DMFT technique in the context of driven-dissipative bosonic systems. After providing a practical DMFT implementation built upon the technical skill set developed in Chapter 7, we showcase its excellent capabilities by investigating a lattice of highly nonlinear cavities.

The main results achieved in Part I and Part II are summarized, respectively, in Chapter 5 and Chapter 10; Chapter 11 is devoted to a summary of the Thesis at large.

Part I

Driven-dissipative semiclassical systems: investigating topological lasers

Chapter 1

Introduction

The birth of topological photonics can be traced back to 2005, when Haldane and Raghu [24, 25] proposed to replicate the electronic chiral edge states of the quantum Hall effect in photonic crystals, and use them as channels for unidirectional light propagation with robustness against bends and impurities. Their theoretical proposal was shortly after experimentally demonstrated in [26].

Since then, the vast breadth of possible technological applications has stimulated a vivid research activity towards the realization of band structures with non-trivial topological invariants. Such systems have testified the advantages of employing topological photonics in several contexts, from robust delay lines [16, 34] and slow-light waveguides [35, 36] to traveling-wave amplifiers [37], with promising applications that reach the realm of optical quantum computing and information processing [38–41]. For a more comprehensive overview, we refer the interested reader to [30, 42–44].

One of the most promising applications of topological photonics are the so-called *topological lasers* (in short, *topolasers*), where an active medium is inserted in the topological system. Topological lasers trace back to the first proposal of lasing into the zero-dimensional edge states of a one-dimensional Su-Schrieffer-Heeger (SSH) chain, put forward in [45, 46] and experimentally demonstrated with polariton micropillars [21], microring resonators [23, 47], and photonic crystals [48]. Extensions to nanolasers based on zero-dimensional corner states of two-dimensional lattices were reported in [49, 50]. Scaling up in dimension, the crucial advantages for optoelectronic applications offered by topological lasing into the one-dimensional edge modes of a two-dimensional lattice have been theoretically highlighted [27, 28, 51–53]: the topological protection of chirally prop-

agating one-dimensional edge modes appears as a promising strategy towards an efficient phase-locking of the laser oscillation at the different sites. In this way, the gain can be distributed over a large number of sites, while maintaining a globally stable single-mode coherent emission, which is very promising to realize high-power coherent sources [54]. Experiments along these lines were reported shortly afterwards using photonic crystals under a strong magnetic field [29] and arrays of coupled ring microcavities [55], followed by more recent valley-Hall quantum cascade [56] and telecom-wavelength [57] lasers.

Our analysis of topological lasers starts in Chapter 2, with a review of the foundations of the semiclassical theory of lasers. The broadband limit of this theory is commonly used for systems whose topological bandgap is much smaller than the gain linewidth, and it's the basis of our analysis in Chapter 3; in Chapter 4, instead, the full equations will be needed in order to include spectral selection effects that are essential in our analysis.

More specifically, in Chapter 3, we study the paradigmatic example of a Harper-Hofstadter topological laser with the purpose of building a generic theory of topological laser operation. Going beyond the pioneering works [51, 52, 58], we identify a number of peculiar effects that directly stem from the chirality of the lasing mode and thus differentiate topological lasers from standard lasers. Keeping the complexity of the model at a minimum level, our attention will be focused on those general effects that play a central role in different realizations of topological laser devices.

After this first analysis, in Chapter 4 we investigate the various mode-selection mechanisms that determine whether a topolaser device is going to lase in an edge or a bulk state. We go beyond previous works by including the additional spectral mode-selection mechanism coming from the frequency-dependence of gain, reviewed in Chapter 2. In its simplest formulation, spectral mode-selection allows suppressing competing cavity modes that are well separated in frequency by tuning a narrowband gain material in the spectral vicinity of the desired mode. In particular, we take motivation from the recent topolaser experiment in [29] to investigate how a subtle combination of spectral and spatial mode-selection mechanisms can conspire to stabilize laser oscillation into a chiral edge state. As an important outcome of our analysis, we point out a possible mechanism for the still unexplained experimental observation [29] of single-mode emission under a homogeneous pump with no need of concentrating pumping along the edge as it was instead done in other topolaser realizations, e.g., in [55].

Finally, in Chapter 5 we offer a summary of the main results presented in Part I.

Chapter 2

Semiclassical theory of lasers

In this Chapter we'll build up the basic theory that underlies the operation of a prototypical laser — not necessarily a topological one.

The basic idea behind a laser is to stimulate the emission of photons from the atoms of an active medium via a feedback loop, in such a way to obtain a macroscopically large number of photons. Given the macroscopic nature of laser emission, we can achieve an operating description via a semiclassical approach; this road was indeed taken by Willis E. Lamb, Jr., who developed a semiclassical theory of lasers by coupling the optical Bloch equations for the atoms of the active medium to an equation for the (classical) electric field derived from Maxwell's equations.

Lamb's approach is commonly found in laser textbooks (see e.g. [59, Chapters 7–8] and [60, Chapter 5]); here we present an alternative derivation that, in our opinion, has the virtue of providing a clearer connection between the macroscopic laser operation and its microscopic building blocks, and it's better suited to implement quantum Hamiltonians on top of active optical cavities.

Most of this Chapter is based on our publication "Spatial and spectral mode-selection effects in topological lasers with frequency-dependent gain" [33].

2.1 Model and equations

As mentioned in the opening of this Chapter, Lamb's semiclassical theory of lasing is usually derived by including, in the classical Maxwell's equations for the electromagnetic field, the dipole polarization of two-level atoms (TLAs) as predicted by a full quantum theory. Here instead, under a mean-field treatment

of the photon field, we show how to obtain the same theory by starting from a fully quantum Hamiltonian, e.g. the Jaynes-Cummings Hamiltonian.

The starting point is a Hamiltonian description of N identical TLAs inside a cavity with the dipole approximation and the rotating wave approximation (RWA); the choice of working with TLAs comes from the fact that they're the simplest — yet effective — model of an emitter. The multi-atom version of the Jaynes-Cummings Hamiltonian, also called Tavis-Cummings or Dicke model, reads as: [61]

Jaynes-Cummings Hamiltonian

$$\begin{aligned} H &= \hbar\omega_{\text{cav}} a^\dagger a + \sum_{n=1}^{N} \left\{ \frac{1}{2}\hbar\omega_{eg}\sigma_n^z + \hbar g\Big(\sigma_n^+ a + a^\dagger \sigma_n^-\Big) \right\} \\ &\doteq H^{(r)} + \sum_{n=1}^{N} H_n^{(ar)}, \end{aligned} \tag{2.1}$$

where (r) stands for "radiation" and (ar) for "atom-radiation" interaction. Here ω_{cav} is the natural frequency of the cavity, $\omega_{eg} = \omega_e - \omega_g$ is the energy difference between the atomic levels, $g = g_{eg} = g_{ge} = -\frac{d_{eg}E_0}{\hbar}$ is the light-atom coupling, $d_{eg} = |\mathbf{d}_{eg}| = ez_{eg} = d_{eg}^*$, $\mathbf{d}_{eg} = \mathbf{d}_{ge}^*$ is the matrix element $\langle e \,|\, e\mathbf{r} \,|\, g\rangle$ of the dipole moment — usually called the *transition dipole moment*, $E_0 = \sqrt{\frac{\hbar\omega_{\text{cav}}}{2\varepsilon_0 V}}$ and V is the volume of the cavity. In the Hamiltonian, $a^\dagger$ is an operator that creates a cavity photon and, for every atom n, $\sigma^+ = |e\rangle\langle g|$ and $\sigma^- = (\sigma^+)^\dagger = |g\rangle\langle e|$ are operators that describe transitions between the atomic levels, and $\sigma^z = |e\rangle\langle e| - |g\rangle\langle g|$. Additionally $|e\rangle\langle e| + |g\rangle\langle g| = I$, with I the identity operator.

The central assumption we now make is for the total density matrix ρ to be factorizable as a tensor product between a density matrix for the atoms and a density matrix for the photons, i.e. $\rho = \rho_{N-\text{at}} \otimes \rho_{\text{ph}}$, where the atomic part can be obtained by tracing out the photonic part: $\rho_{N-\text{at}} = \text{Tr}_{\text{ph}}\rho$. With this consideration, one can similarly obtain a time-evolution equation for the atomic density matrix $\rho_{N-\text{at}}$ by starting from the evolution of the full density matrix, $\frac{d\rho}{dt} = -\frac{i}{\hbar}[H, \rho]$, and tracing out the photonic part. The result is an equation very similar to the one for the full density matrix, but in which H is replaced by a mean-field Hamiltonian:

$$\begin{aligned} \frac{d\rho_{N-\text{at}}}{dt} &= -\frac{i}{\hbar}\left[H^{\text{MF}}, \rho_{N-\text{at}}\right] \\ &= -\frac{i}{\hbar}\sum_{n=1}^{N}\left[H_n^{\text{MF},\,(ar)}, \rho_{N-\text{at}}\right], \end{aligned} \tag{2.2}$$

where in H^{MF} all the photon operators have been replaced by their expectation values:

$$H^{\text{MF}} = \hbar\omega_{\text{cav}}\left\langle a^\dagger a\right\rangle + \sum_{n=1}^{N}\left\{\frac{1}{2}\hbar\omega_{eg}\sigma_n^z + \hbar g\Big(\sigma_n^+\left\langle a\right\rangle + \left\langle a^\dagger\right\rangle\sigma_n^-\Big)\right\} \tag{2.3}$$

The mean-field Hamiltonian we've just obtained is already reminiscent of the semiclassical light-atom interaction Hamiltonian under the dipole and RWA approximations, in which essentially the expectation value of the photon field $\langle a \rangle$ is replaced by the macroscopic electric field (see [62, Chapter 4–5]). We'll comment again briefly on this connection once we obtain the full set of equations.

If we further assume that the atomic density matrix can be factorized as a tensor product of the density matrices of all the atoms, i.e.

$$\rho_{N-\mathrm{at}} = \rho_{\mathrm{at}}^{(1)} \otimes \ldots \otimes \rho_{\mathrm{at}}^{(N)} \tag{2.4}$$

where $\rho_{\mathrm{at}}^{(n)} = \sum_{\{\alpha,\,\beta\}=\{e,\,g\}} \rho_{\alpha\beta}^{(n)} \left|\alpha\right\rangle \left\langle\beta\right|$ is the density matrix of the n-th atom, then the commutator above simplifies as

$$\left[H_n^{\mathrm{MF},(ar)}, \rho_{N-\mathrm{at}}\right] = \left[H_n^{\mathrm{MF},(ar)}, \rho_{\mathrm{at}}^{(n)}\right]. \tag{2.5}$$

If we trace away all the other atoms except for the n-th one, we get

$$\frac{d\rho_{\mathrm{at}}^{(n)}}{dt} = -\frac{i}{\hbar}\left[H_n^{\mathrm{MF},(ar)}, \rho_{\mathrm{at}}^{(n)}\right] \tag{2.6}$$

which is exactly the same time-evolution equation one would get from a single-atom Jaynes-Cummings Hamiltonian. This means that all the atoms are equivalent and have exactly the same evolution, so we can drop the (n) superscript.

Finally, we can provide every atom with decay and pumping mechanisms at the master equation level, by adding Lindblad terms of the following form:

$$\frac{d\rho_{\mathrm{at}}}{dt} = \ldots + \sum_{s=e,g} \gamma_s \left(L_s \rho_{\mathrm{at}} L_s^\dagger - \frac{1}{2}\left\{L_s^\dagger L_s, \rho_{\mathrm{at}}\right\}\right), \tag{2.7}$$

where the dots $\ldots$ indicate the RHS of (2.6), $L_e^\dagger = \left|e\right\rangle \left\langle g\right| = \sigma^+$ (the population of $\left|e\right\rangle$ is increased) and $L_e = \left|g\right\rangle \left\langle e\right| = \sigma^-$ (the population of $\left|e\right\rangle$ is decreased), and conversely $L_g^\dagger = \left|g\right\rangle \left\langle e\right| = \sigma^-$ and $L_g = \left|e\right\rangle \left\langle g\right| = \sigma^+$. A pictorial representation of the full Hamiltonian + Lindblad dynamics is given in Figure 2.1.

With these ingredients we can write down the equations for the matrix elements of the atomic density matrix of a generic atom in the cavity:

$$\begin{cases} \dot\rho_{ee} = \gamma_g \rho_{gg} - \gamma_e \rho_{ee} + i\dfrac{d_{eg}E_0}{\hbar}\Big(\langle a\rangle \rho_{ge} - \langle a\rangle^* \rho_{eg}\Big) \\ \dot\rho_{gg} = \gamma_e \rho_{ee} - \gamma_g \rho_{gg} - i\dfrac{d_{eg}E_0}{\hbar}\Big(\langle a\rangle \rho_{ge} - \langle a\rangle^* \rho_{eg}\Big) \\ \dot\rho_{eg} = -i(\omega_{eg} - i\gamma)\rho_{eg} - i\dfrac{d_{eg}E_0}{\hbar} \langle a\rangle \Big(\rho_{ee} - \rho_{gg}\Big) \end{cases} \tag{2.8}$$

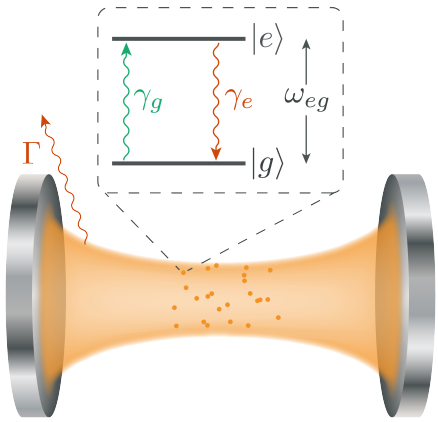

Figure 2.1: Scheme of a photonic cavity embedding two-level atoms (TLAs). The energy difference between the two atomic levels is ω_{eg}; pumping of the atoms from $|g\rangle$ to $|e\rangle$ occurs at a rate γ_g, while their spontaneous decay from $|e\rangle$ to $|g\rangle$ occurs at a rate γ_e. Additionally, the cavity decays at an intrinsic rate Γ.

where $\gamma = \gamma_{eg} + \gamma_{\text{ph}}$, $\gamma_{eg} = \frac{\gamma_e + \gamma_g}{2}$ and γ_{ph}, in the more general treatment (see [60, Chapter 5]), comes from dephasing processes[1]; for the sake of our discussion, though, $\gamma_{\text{ph}} = 0$. The fact that the evolution of the population of one of the levels is the negative of the evolution of the other one is due to the fact that the Lindblad losses preserve the trace of the density matrix (which is 1), and indeed from $\rho_{gg} + \rho_{ee} = 1$ we get $\dot{\rho}_{gg} = -\dot{\rho}_{ee}$.

We still miss an equation for the cavity field a, or better, for its expectation value. The Heisenberg equation for the field operator is

$$\frac{da}{dt} = \frac{i}{\hbar}[H, a] = -i\omega_{\text{cav}} a - ig \sum_{n=1}^{N} \sigma_n^- . \tag{2.9}$$

[1] Dephasing processes are due to e.g. elastic collisions of atoms in a gas. This kind of processes cause a frequency shift $\delta\omega(t)$ that enters the equation for the coherence ρ_{eg}; if we assume, though, that $\langle \delta\omega(t) \rangle = 0$ and that the process is Markovian, i.e.

$$\left\langle \delta\omega(t)\delta\omega(t') \right\rangle = 2\gamma_{\text{ph}}\delta(t - t'),$$

then we can just replace ρ_{eg} with its average over the ensemble of random variations in $\delta\omega(t)$. The resulting ensemble-averaged coherence, that we call again ρ_{eg} in order to simplify the notation, differs from the one without dephasing processes by an additional loss rate in its equation of motion. The equations for the populations are instead left unchanged.

The presence of these dephasing processes increases the linewidth of the gain, as well as the carrier lifetime. When the latter becomes larger than the photon lifetime and is combined with a strong photon-carrier coupling, it results in a strong effective photon-carrier repulsion that can give rise to dynamical instabilities [58, 63].

By noticing that σ^- is an atom-only operator, so that

$$\langle \sigma^- \rangle = \langle \sigma^- \rangle_{\text{at}} = \text{Tr}_{\text{at}}\Big(\rho_{\text{at}}\sigma^-\Big) = \rho_{eg}, \tag{2.10}$$

we can then take the expectation value of (2.9) and use the fact that the atoms are all equivalent to write

$$\begin{aligned}\frac{d\langle a\rangle}{dt} &= -i\omega_{\text{cav}}\langle a\rangle - ig\sum_{n=1}^{N}\rho_{eg}^{(n)} \\ &= -i\omega_{\text{cav}}\langle a\rangle - igN\rho_{eg}.\end{aligned} \tag{2.11}$$

Finally, by redefining $\langle a\rangle \to a$ for simplicity and by adding a phenomenological cavity loss coefficient Γ, we have a set of coupled semi-classical equations for the elements of the atomic density matrix and the expectation value of the photon field:

$$\begin{cases}\dot\rho_{ee} = \gamma_g\rho_{gg} - \gamma_e\rho_{ee} + i\dfrac{d_{eg}E_0}{\hbar}\Big(a\rho_{ge} - a^*\rho_{eg}\Big) \\ \dot\rho_{gg} = \gamma_e\rho_{ee} - \gamma_g\rho_{gg} - i\dfrac{d_{eg}E_0}{\hbar}\Big(a\rho_{ge} - a^*\rho_{eg}\Big) \\ \dot\rho_{eg} = -i(\omega_{eg} - i\gamma)\rho_{eg} - i\dfrac{d_{eg}E_0}{\hbar}a\Big(\rho_{ee} - \rho_{gg}\Big) \\ \dot a = -i\omega_{\text{cav}}a - \Gamma a + i\dfrac{d_{eg}E_0}{\hbar}N\rho_{eg}\end{cases} \tag{2.12}$$

Semiclassical laser equations

Interestingly the number of atoms in the cavity, N, appears only in the equation for the average photon field, in front of the off-diagonal atomic matrix element. Indeed, if you compare with the semiclassical theory by Lamb, [59, 60] you find that the time-evolution for the macroscopic electric field is

Connection to Lamb's theory

$$\dot E^+ = -i\omega_{\text{cav}}E^+ + i\frac{\omega_{\text{cav}}}{2\varepsilon_0}P^+, \tag{2.13}$$

where E^+ is the positive-frequency component of the electric field and P^+ is the positive-frequency component of the (macroscopic) polarization. Each atom here has a tiny dipole moment that can be shown to be $\langle e\mathbf{r}\rangle = d_{eg}(\rho_{eg} + \rho_{ge}) = d_{eg}(\rho_{eg} + \rho_{eg}^*)$, so one can assume that the macroscopic polarization vector is just the sum of these tiny dipole moments:

$$P = N\langle e\mathbf{r}\rangle = Nd_{eg}\Big(\rho_{eg} + \text{c.c.}\Big). \tag{2.14}$$

When you then identify $P^+ \equiv Nd_{eg}\rho_{eg}$, you get

$$\dot E^+ = -i\omega_{\text{cav}}E^+ - ig'N\rho_{eg} \tag{2.15}$$

where $g' = -\frac{\omega_{\text{cav}}d_{eg}}{2\varepsilon_0}$, which has the same form of (2.11).

At a first sight, it might seem odd that a semiclassical theory requiring Maxwell's equations can also be obtained from a mean-field treatment of a fully

quantum Hamiltonian, without any reference to Maxwell's equations. However, Maxwell's equations are definitely here, hidden behind the Jaynes-Cummings model; the model itself was, in fact, derived [64] by making full use of Maxwell's equations, followed by a field quantization, in a true semiclassical fashion.

2.2 Stationary state and gain profile

We can get additional insights and build up some intuition by solving the equations (2.12) for the *stationary state*.

In order to do that, let us first perform a change of variable. We define the overall oscillation frequency of the field as ω_L — which is not *a priori* guaranteed to be equal to ω_{cav}, so that it is convenient to define a new variable $\tilde{a}$ as

$$a(t) \doteq \tilde{a}(t) e^{-i\omega_L t}, \tag{2.16}$$

where now $\tilde{a}(t)$ is a *slowly-varying* quantity, i.e. $|\dot{\tilde{a}}/\tilde{a}| \ll \omega_L$. We also define $\tilde{\rho}_{eg} = \rho_{eg} e^{+i\omega_L t}$ and $\tilde{\rho}_{\alpha\alpha} \equiv \rho_{\alpha\alpha}$ $(\alpha = e, g)$, and we use the fact that $1 = \text{Tr}\rho = \rho_{gg} + \rho_{ee}$. Then the equations assume the following form:

$$\begin{cases} \dot{\rho}_{ee} = \gamma_g - 2\gamma_{eg}\rho_{ee} - ig\Big(\tilde{a}\tilde{\rho}_{ge} - \tilde{a}^*\tilde{\rho}_{eg}\Big) \\ \dot{\rho}_{gg} = \gamma_e - 2\gamma_{eg}\rho_{gg} + ig\Big(\tilde{a}\tilde{\rho}_{ge} - \tilde{a}^*\tilde{\rho}_{eg}\Big) \\ \dot{\tilde{\rho}}_{eg} = -i(\omega_{eg} - i\gamma)\tilde{\rho}_{eg} + ig\tilde{a}\Big(\rho_{ee} - \rho_{gg}\Big) \\ \dot{\tilde{a}} = -i\left(\omega_{\text{cav}} - \omega_L\right)\tilde{a} - \Gamma\tilde{a} - igN\rho_{eg} \end{cases} \tag{2.17}$$

The steady-state coherence in (2.12) can then be expressed as

$$\tilde{\rho}_{eg} = g\tilde{a}\frac{\Big[(\omega_{eg} - \omega_L) + i\gamma\Big]}{\Big[(\omega_{eg} - \omega_L)^2 + \gamma^2\Big]}\Big(\tilde{\rho}_{ee} - \tilde{\rho}_{gg}\Big), \tag{2.18}$$

while the steady-state population difference takes the form

$$\Big(\tilde{\rho}_{ee} - \tilde{\rho}_{gg}\Big) = \frac{\Big(\tilde{\rho}_{ee}^{(0)} - \tilde{\rho}_{gg}^{(0)}\Big)}{1 + R/\gamma_{eg}}, \qquad R = 2g^2|\tilde{a}|^2\frac{\gamma}{(\omega_{eg} - \omega_L)^2 + \gamma^2}, \tag{2.19}$$

where $\tilde{\rho}_{ee}^{(0)} = \frac{\gamma_g}{\gamma_g + \gamma_e}$ and $\tilde{\rho}_{gg}^{(0)} = \frac{\gamma_e}{\gamma_g + \gamma_e}$ are the steady-state populations at zero field.

By combining (2.18) and (2.19), the equation for the field can be written in the following form:

$$\dot{\tilde{a}} = i\Omega\tilde{a} - \Gamma\tilde{a} + \frac{P}{1 + \beta|\tilde{a}|^2}\tilde{a} \tag{2.20}$$

where

$$\Omega = \Omega(\{\omega\},\{\gamma\},|\tilde{a}|^2) = (\omega_L - \omega_{\rm cav}) - g^2 N \frac{(\omega_{eg}-\omega_L)}{\left[(\omega_{eg}-\omega_L)^2+\gamma^2\right]} \frac{\left(\tilde{\rho}_{ee}^{(0)} - \tilde{\rho}_{gg}^{(0)}\right)}{1+\beta|\tilde{a}|^2}, \tag{2.21}$$

$$P = P(\omega_{eg}-\omega_L,\{\gamma\}) = g^2 N \frac{\gamma}{\left[(\omega_{eg}-\omega_L)^2+\gamma^2\right]} \left(\tilde{\rho}_{ee}^{(0)} - \tilde{\rho}_{gg}^{(0)}\right) \tag{2.22}$$

and

$$\beta = \beta(\omega_{eg}-\omega_L,\gamma) = 2g^2 \frac{\gamma/\gamma_{eg}}{(\omega_{eg}-\omega_L)^2+\gamma^2}. \tag{2.23}$$

Here $\{\omega\}$ indicates the dependence on the frequencies ($\omega_{\rm cav}$, ω_{eg} and ω_L) and $\{\gamma\}$ indicates the dependence on the microscopic loss coefficients ($\gamma_e, \gamma_g, \gamma_{\rm ph}$).

As a key point, the P coefficient which, for a positive zero-field population difference $\left(\tilde{\rho}_{ee}^{(0)} - \tilde{\rho}_{gg}^{(0)}\right) = (\gamma_g - \gamma_e)/(\gamma_g + \gamma_e) > 0$, acts as a *gain*, is here *frequency-dependent*; you get most out of your cavity system when the lasing frequency ω_L is in resonance with the transition frequency between the two atomic levels ω_{eg}. If instead your lasing frequency gets farther apart from the transition frequency, then the gain decays by following a Lorentzian behavior — with the linewidth of the Lorentzian controlled by γ. Additionally, the lasing frequency experiences an intensity-dependent frequency shift that decays as the square of the detuning for large detunings but is exactly zero at resonance; this shift is responsible for the so-called *mode pulling*.

Frequency dependence of gain

A common limit considered in the literature is the so-called *broadband gain* limit, in which the gain linewidth controlled by γ is much larger than all the other energy scales. In this limit, the gain profile is essentially flat in frequency space and it's sufficient to solve just the equation for the photon field. The latter, in fact, takes the same form as in (2.20):

Broadband gain

$$\dot{\tilde{a}} = i\,(\omega_L - \omega_{\rm cav})\,\tilde{a} - \Gamma\tilde{a} + \frac{P}{1+\beta|\tilde{a}|^2}\tilde{a} \tag{2.24}$$

with the key difference that now the lasing frequency is set by the cavity frequency and that the parameters P and β are frequency-independent and can be treated as phenomenological quantities.

In this limit, it's immediate to see that the minimum amount of power $P_{\rm th}$ that's required for the operation of the laser is $P_{\rm th} = \Gamma$. Below this threshold, called *lasing threshold*, the emitted light intensity is in fact $I = |a|^2 = 0$; above the lasing threshold, the only dynamically stable solution of (2.24) is instead given by $I = \frac{1}{\beta}\left(\frac{P}{\Gamma} - 1\right)$, i.e. the emitted intensity grows linearly with P.

Lasing threshold

2.3 Connection to the generalized Gross-Pitaevskii equation

The semiclassical laser equations (2.12) can be also mapped into the generalized Gross-Pitaevskii equation (GPE) introduced in [65], with the difference that the parameters become frequency-dependent. Although we won't make use of it in this work, it's still an interesting point of view from which to look at the laser equations.

Let's start again from (2.17) and (2.18), with the difference that now we don't solve for the steady-state of the populations. As a convenient shortcut, we express the coherence as

$$\tilde{\rho}_{eg} = g\tilde{a}\mathcal{L}\Big(\tilde{\rho}_{ee} - \tilde{\rho}_{gg}\Big), \tag{2.25}$$

where $\mathcal{L} = \mathcal{L}_r + i\mathcal{L}_i$ is a Lorentzian factor with real part $\mathcal{L}_r = \frac{(\omega_{eg}-\omega_L)}{[(\omega_{eg}-\omega_L)^2+\gamma^2]}$ and imaginary part $\mathcal{L}_i = \frac{\gamma}{[(\omega_{eg}-\omega_L)^2+\gamma^2]}$.

We now define a new quantity $N_{\text{ex}} \doteq N\Big(\tilde{\rho}_{ee} - \tilde{\rho}_{gg}\Big)$ that we interpret as the excess of the atomic population in the excited state, i.e. as a number of excitations. The equation for the time-evolution of this new quantity and for the photon field can now be readily written in terms of each other from (2.17) and (2.18) as

Generalized GPE

$$\begin{cases} \dot{N}_{\text{ex}} = P - \Big[\gamma_R + 4R\,|\tilde{a}|^2\Big] N_{\text{ex}} \\ i\dot{\tilde{a}} = \Big[\,(\omega_{\text{cav}} - \omega_L) + g_R N_{\text{ex}} + i\,(RN_{\text{ex}} - \Gamma)\,\Big]\tilde{a} \end{cases} \tag{2.26}$$

with

$$P \doteq N\Big(\gamma_g - \gamma_e\Big), \qquad \gamma_R \doteq 2\gamma_{eg} = \gamma_g + \gamma_e, \qquad g_R \doteq g^2\mathcal{L}_r, \qquad R \doteq g^2\mathcal{L}_i. \tag{2.27}$$

Here the parameter P is a measure of the number of atoms pumped from the ground state to the excited state, and it's proportional to the pumping strength γ_g, so it acts as an amplification; the interaction $g^2\mathcal{L}$, that gives the frequency dependence, splits into a contribution g_R from the real part that describes the interaction between the field and a reservoir excitation, and into a contribution R from the real part that describes the efficiency of the stimulated emission; finally, the atomic Lindblad rates γ_g and γ_e describe the rate at which the reservoir is depleted.

In the event the gain material has an additional Kerr nonlinearity, beyond the gain saturation nonlinearity already present in eq. (2.26), we would also have an additional term of the form "$+\,g_U\,|\tilde{a}|^2\,a$" on the RHS of the second equation in (2.26) — where the "U" subscript reminds us that this is the same type of nonlinearity that characterizes the Hubbard Hamiltonian.

At this point, the equations (2.26) become a generalization of the GPE in [65] in which g_R and R have acquired a frequency-dependence. In particular, the sign

of the nonlinearity g_R self-consistently depends on the lasing frequency ω_L itself, as $g_R > 0$ ($g_R < 0$) for $\omega_L < \omega_{eg}$ ($\omega_L > \omega_{eg}$).

2.4 Conclusions

In this Chapter we've developed a semiclassical theory of laser operation from scratch, starting from a single-mode cavity embedding TLAs as a gain material.

The key ingredients that we've employed are the Jaynes-Cummings model — that provides perhaps the most simple description of light-matter interaction at the quantum level — and a mean-field treatment as a way to obtain semiclassical equations. The resulting coupled differential equations in (2.12) provide then a description of populations and coherence of the TLAs, and of the expectation value of the photonic field in the cavity.

The steady-state analysis that we've performed in Section 2.2 highlights how the presence of the TLAs accounts for the Lorentzian shape of the gain in the frequency domain; the frequency corresponding to the maximum gain matches the transition energy between the atomic levels. This means that a signal at a frequency close to the atomic transition will be amplified better than a signal detuned from that frequency, thereby effectively providing a *spectral* selection mechanism. In a situation in which the linewidth of the gain is much larger than the effective frequency range of the problem, the effects of the spectral selection become negligible; this limit is called the broadband limit, and can be described with a single equation for the photon field.

Finally, we've shown how the semiclassical laser equations (2.12) can be mapped into a generalized GPE (2.26), coupled to an equation that describes the evolution of reservoir excitations; several nonlinearities arise due to the coupling with the reservoir and due to the frequency-dependence of the coupling coefficients.

This theory is the cornerstone upon which we'll model topological lasers in the remainder of this journey; in particular, the frequency dependence of the gain will play a central role in Chapter 4, where we provide a possible explanation for the experimental observations in [29].

Chapter 3

Harper-Hofstadter broadband topological laser

In this Chapter we consider the broadband limit of the semiclassical theory of lasers developed in Chapter 2, in the context of a topological system.

As a key example of a topological lattice model, we focus here on the Harper-Hofstadter model, which was originally formulated to describe the lattice motion of an electron under a magnetic field perpendicular to the lattice itself. In the photonics community, this model has surged as an ideal playground to test, among others, robust transport of light signals [16, 34] and, more recently, the viability of topological lasers [32, 33, 51, 53, 55, 63].

The analysis of this Chapter starts in Section 3.1 with a review of the Harper-Hofstadter model and of the relevant topological concepts, while in Section 3.2 we write down the equations for a topological laser based on such model via the addition of an active medium. After a brief review of the chaotic behavior in the presence of a spatially uniform gain in Section 3.3, in Section 3.4 we discuss how restricting gain to the edge of the lattice allows obtaining a single-mode laser emission that is robust against disorder. The peculiar features that stem from the chiral nature of the lasing mode are highlighted, as well as the limitations they are expected to impose on the laser performance. In Section 3.5, we investigate the effect of restricting gain to a finite strip of sites along one edge. For this geometry, the finite group velocity of the chiral edge mode turns out to be responsible for a marked distinction between convective and absolute instabilities, which is characterized in terms of noise-sustained structures and traveling-wave amplification. A summary and a discussion of this Chapter's results is provided

in Section 3.6.

Most of this Chapter is based on our publication "Theory of chiral edge state lasing in a two-dimensional topological system" [32]; the Supplemental Videos referred in the text can be found at the following address: https://journals.aps.org/prresearch/supplemental/10.1103/PhysRevResearch.1.033148.

3.1 The Harper-Hofstadter model

The Harper-Hofstadter model [66, 67] was originally formulated to describe the motion of a charged particle on a lattice, under the influence of a normal, uniform magnetic field. It can be seen as a quantized description of the motion of a conduction electron in a two-dimensional metal plate subject to a magnetic field, and indeed it plays a key role in the analysis of the quantum Hall effect, the quantized counterpart of the Hall effect.

We do not go into these details, as they've been extensively discussed in the literature and as they'll drift us away from the original purpose of this work; we limit ourselves to the bare essentials, and the interested reader can refer to the pedagogical introductions in [68, 69]. We just mention that, although photons are not charged particles and therefore cannot be drifted by a magnetic field, it's still possible to create a synthetic field that acts on photons (or other uncharged objects like neutral atoms) like a real magnetic field would act on electrons; such a field is called a *synthetic gauge field*. In the context of silicon photonics and with specific reference to the Harper-Hofstadter model this has been achieved by connecting photonic cavities via asymmetric link waveguides, with lengths that were specifically tuned to reproduce the presence of a given magnetic field, both in the context of delay lines [16, 34] as well as in the topolaser experiment in [55].

Synthetic gauge field

We'll start by writing down the Hamiltonian of the model, that is a simple tight-binding Hamiltonian on a square lattice with a key twist: the hopping along one of the directions has an additional complex phase[1] that depends on the lattice location in the other direction and on the flux of a corresponding magnetic field:

$$H_{\text{bare}} = \sum_{m,n} \left\{ \hbar\omega_{\text{cav}} a^\dagger_{m,n} a_{m,n} - J\left(a^\dagger_{m,n} a_{m+1,n} + e^{-i2\pi\vartheta m} a^\dagger_{m,n} a_{m,n+1} + \text{h.c.} \right) \right\} \tag{3.1}$$

Harper-Hofstadter Hamiltonian

where $a^\dagger_{m,n}$ ($a_{m,n}$) is the operator that creates (annihilates) a photon at the (m,n) site. All sites are assumed to have a bare photon frequency ω_{cav}, the real and positive parameter J quantifies the hopping strength, and ϑ is the flux per plaquette of the synthetic gauge field that is responsible for the topological

[1] The fact that the hopping has a complex phase only in one of the two directions results from having chosen a Landau gauge for the magnetic vector potential $\mathbf{A}$, of the form $\mathbf{A} = B(-y, 0, 0)$ (1st Landau gauge) or $\mathbf{A} = B(0, x, 0)$ (2nd Landau gauge); here we work in the 2nd Landau gauge [70]. However, a fully equivalent magnetic field $\mathbf{B} = (0, 0, B)$ can also be obtained in the so-called symmetric gauge, where $\mathbf{A} = \mathbf{B}(-y, x, 0)/2$; with this gauge choice, the resulting Hamiltonian has complex hoppings in both directions.

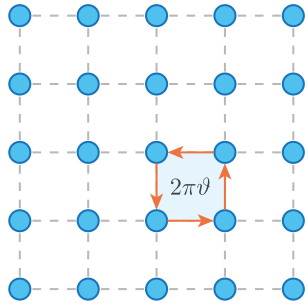

Figure 3.1: Sketch of a Harper-Hofstadter lattice. The lattice has a square unit cell and the lattice sites (blue dots) are coupled via a hopping coefficient with uniform absolute value (dashed gray lines). The presence of the synthetic magnetic field is included as an extra complex hopping phase, such that when a photon hops around a plaquette (orange arrows) picks up an extra phase $2\pi\vartheta$ due to the synthetic magnetic flux ϑ.

properties (unless otherwise, we'll always use $= \vartheta = 1/4$ for reasons that we are going to discuss shortly). We denote the Hamiltonian as "bare" as, in the context of an active photonic lattice, this Hamiltonian does not contain yet any pump or loss mechanism.

A photon that hops anti-clockwise around a plaquette acquires an additional complex phase controlled by ϑ (see Figure 3.1). For rational $\vartheta = p/q$ with p and q coprime integers, the Hamiltonian in (3.1) with periodic boundary conditions (PBC) in both directions can be written in $\mathbf{k}$-space as a $q \times q$ matrix, whose bulk eigenstates $u_\nu(\mathbf{k})$ ($\nu = 1, \dots, q$) distribute in q bands. The bulk bands, identified by the integers ν, can be characterized via the following topological quantities due to Berry [71]:

$$\boldsymbol{\mathcal{A}}_\nu(\mathbf{k}) \doteqdot \langle u_\nu(\mathbf{k}) \,|\, i\nabla_{\mathbf{k}} \,|\, u_\nu(\mathbf{k}) \rangle\,, \qquad \boldsymbol{\mathcal{B}}_\nu(\mathbf{k}) \doteqdot \nabla_{\mathbf{k}} \times \boldsymbol{\mathcal{A}}_\nu(\mathbf{k}),$$
$$\gamma_\nu = \int_{\mathcal{S}} \boldsymbol{\mathcal{B}}_\nu(\mathbf{k}) \cdot d\mathcal{S} = \oint_{\mathcal{C}} \boldsymbol{\mathcal{A}}_\nu(\mathbf{k}) \cdot d\mathbf{l} \tag{3.2}$$

where $\mathcal{C}$ is a closed path in the Brillouin zone and $\mathcal{S}$ is the $\mathbf{k}$-space surface enclosed by $\mathcal{C}$. Without going into details, the quantities $\boldsymbol{\mathcal{A}}_\nu(\mathbf{k})$ and $\boldsymbol{\mathcal{B}}_\nu(\mathbf{k})$, called respectively the *Berry connection* and the *Berry curvature*, act like a vector potential and a magnetic field in momentum space. The *Berry phase* γ_ν, that can be similarly interpreted as a magnetic flux in momentum space, is a gauge-invariant quantity that can be used to characterize the topological properties of the bands. Namely, when $\mathcal{S}$ corresponds to the whole Brillouin zone, the resulting Berry curvature is an integer multiple of 2π and we can define a new integer C_ν

Berry connection, curvature and phase

called the *Chern number*:

$$C_\nu = \frac{1}{2\pi}\int_{\mathrm{BZ}} \boldsymbol{\mathcal{B}}_\nu(\mathbf{k})\cdot\mathbf{k}_x dk_x dk_y, \qquad C_\nu \in \mathbb{Z}. \tag{3.3}$$

Up to now, we've taken advantage of the PBC to diagonalize the Hamiltonian and to define bulk quantities like the Chern number. What's then the role of these quantities when we have instead open boundary conditions (OBC), as in the case of an actual experimental device? The answer is given by the *bulk-edge correspondence* theorem, which tells us that when PBC are replaced by OBC, it's possible to have additional states spatially localized at the edge of the system and spectrally localized in a bandgap between two bands. If a bandgap possesses such *edge states*, it's called a *topological bandgap*. The number of edge states $N_{\mathrm{edge},\nu}$ ($\nu = 1,\dots,q-1$) in the bandgap between the ν-th band and the $\nu+1$-th band can be calculated by summing up all the Chern numbers of the bands below the bandgap itself:

Edge states and topological bandgap

$$N_{\mathrm{edge},\nu} = \left|\sum_{\mu\leq\nu} C_\mu\right|. \tag{3.4}$$

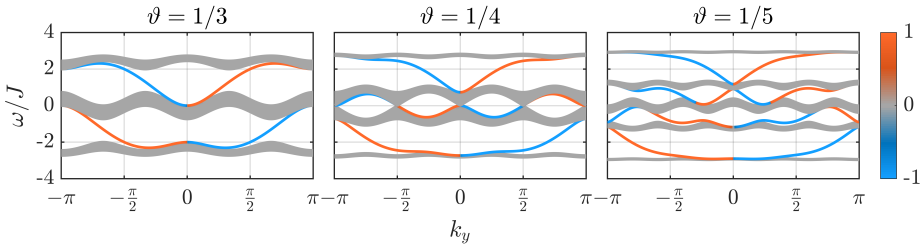

Figure 3.2: Energy dispersion of the Harper-Hofstadter Hamiltonian (3.1) in a cylindrical geometry for $\vartheta = 1/3, 1/4, 1/5$ (left to right), with PBC along y and $N_x = 299, 399, 499$ sites with OBC along x; the energies ω/J are measured with respect to ω_{cav}/J, and Hofstadter found them bounded as $-4 \leq \omega/J \leq +4$. The topologically protected edge states are indicated here with colorful lines, red (blue) color indicating localization on the right (left) edge, while the gray bands correspond to delocalized bulk states.

As an example, we can take a look at the bands and the Chern numbers of the Harper-Hofstadter Hamiltonian for $\vartheta = 1/3, 1/4, 1/5$ (see Figure 3.2); the Chern numbers and their cumulants are summarized in Table 3.1. For $\vartheta = 1/3$ we have two bandgaps, each hosting a single edge mode[2]. The sign in the cumulant

[2]In Figure 3.2, there are OBC only in one direction; therefore the system is equivalent to a cylinder and has two distinct edges, one on the left and one on the right, presented with different colors. Each edge has N_{edge} edge states. In the text, we discuss the case in which OBC are placed in both directions; the system becomes equivalent to a rectangle and it has therefore a single edge with N_{edge} edge states.

ϑ	$(C_\nu)_\nu$	$\left(\sum_{\mu\leq\nu} C_\nu\right)_\nu$
1/3	$-1,+2,-1$	$-1,+1$
1/4	$-1,+2,-1$	$-1,+1$
1/5	$-1,-1,+4,-1,-1$	$-1,-2,+2,+1$

Table 3.1: Sequence of Chern numbers C_ν and their cumulants $\sum_{\mu\leq\nu} C_\nu$ of the bulk bands of the Harper-Hofstadter Hamiltonian (3.1) with $\vartheta = 1/3,\ 1/4,\ 1/5$. For $\vartheta = 1/4$, the two central bands touch in degenerate Dirac points and are therefore considered as a single band in the calculation of the Chern number.

of the Chern numbers provides information about the *chirality* of these modes: a -1 sign indicates modes that travel around the edge with an anti-clockwise chirality, while a $+1$ sign indicates a clockwise chirality. The situation is similar for $\vartheta = 1/4$, despite having 4 bands; the reason is that the two central bands touch at degenerate Dirac points, thus there is no true bandgap between those bands and they have to be considered as if they were a single band when calculating the Chern number. The result is that we still have two topological bandgaps, one at negative energies and one at positive energies, hosting each one a single edge mode with opposite chiralities. Finally, for $\vartheta = 1/5$, there are 4 bandgaps; the two central ones host two edge modes each, again with anti-clockwise chirality for edge modes at negative energies and with clockwise chirality for edge modes at positive energies.

Chirality

In the remainder of this work, we'll always consider the case $\vartheta = 1/4$; like the case $\vartheta = 1/3$ it has only two topological bandgaps, each hosting a single chiral edge mode; however, for $\vartheta = 1/4$ the two bandgaps enjoy a wider spectral separation due to the presence of the two central bands touching in degenerate Dirac points.

3.2 Active Harper-Hofstadter lattice of cavities

We now write down the equations for an active version of a $\vartheta = 1/4$ Harper-Hofstadter lattice of optical cavities (see Figure 3.3); with the addition of a pumping mechanism, we will be able to turn our optical lattice into a lasing device.

The starting point is the semiclassical theory of lasers review in Chapter 2, in the form of equation (2.24) since we are considering the broadband limit. If we don't perform the transformation (2.16), that is useful only for theoretical calculations since we don't *a priori* know the lasing frequency, the equation has the following form:

$$\dot{a} = -i\omega_{\text{cav}} a - \Gamma a + \frac{P}{1+\beta|a|^2} a \tag{3.5}$$

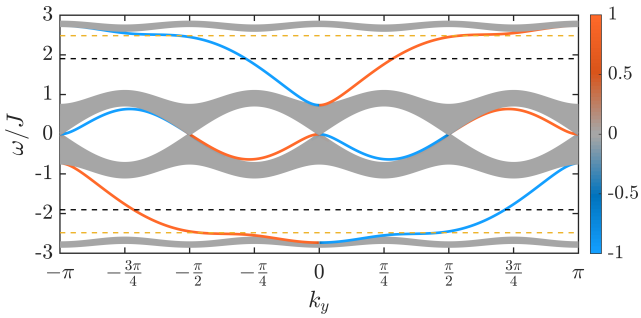

Figure 3.3: Energy bands of the conservative Harper-Hofstadter Hamiltonian (3.1) with flux $\vartheta = 1/4$ in a lattice of $N_x = 399$ sites along x and periodic boundary conditions along y. Blue vs. red color scale quantifies localization on the left or right edges. The horizontal black and orange lines indicate the WEG and PEG lasing frequencies shown in Figure 3.5(c).

where, we recall that a is the expectation value of the original field operator. The first term on the right-hand site is actually coming from the commutator in the Heisenberg equation for a single cavity, i.e. $-i\omega_{\text{cav}} a = -i\left[a, \omega_{\text{cav}} a^\dagger a\right]_{\langle a\rangle \to a}$, in which naturally a has to be considered as a field operator in order to compute the commutator, and subsequently replaced by its expectation value. Since we now have a lattice of cavities, we have a cavity field for each cavity and the commutator has to be computed with respect to the full lattice Hamiltonian H_{bare} specified in (3.1); this holds true for any lattice model, not just for the Harper-Hofstadter lattice we're considering here. Additionally, while we consider cavities with the same intrinsic loss coefficient Γ, we want to have the possibility to selectively pump only a given set of cavities; therefore we replace P with a site-dependent coefficient $P_{m,n}$.

To summarize, the semiclassical equations for an active Harper-Hofstadter lattice are:

Active lattice equations

$$\dot{a}_{m,n}(t) = -i\left[a_{m,n}, H_{\text{bare}}\right] + \left(\frac{P_{m,n}}{1+\beta|a_{m,n}|^2} - \Gamma\right) a_{m,n}. \tag{3.6}$$

For a $N_x \times N_y$ lattice, we have therefore a set of $N_x \times N_y$ coupled[3] differential equations; these equations can be solved via numerical integration, until a steady-state or a maximum integration time has been reached.

In our calculations, we've set the gain saturation parameter $\beta = 1$ and we've used a 4-th order Runge-Kutta numerical integration scheme, that provides direct access to time-dependent quantities. In order to reach a non-trivial solution, we numerically initialize the fields to a small Gaussian noise.

[3]The coupling is due to the Hamiltonian H_{bare}, which couples neighboring cavities.

3.3 Whole system gain (WSG)

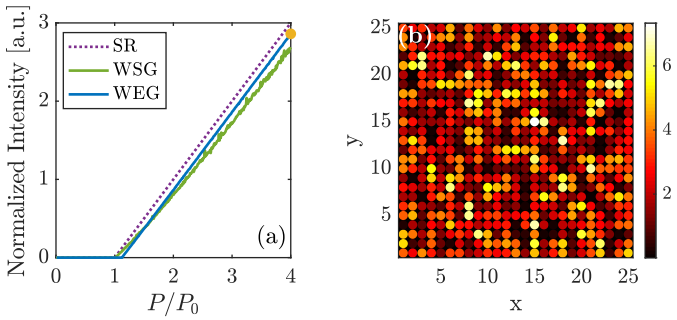

Figure 3.4: Topological lasing in a 25×25 Harper-Hofstadter lattice with a flux $\vartheta = 1/4$ per plaquette. Left panel: total intensity $I_T = \sum_{m,n} |a_{m,n}|^2$ normalized to the number of amplifying sites vs. gain strength for different configurations: single resonator (SR), whole system gain (WSG) and whole edge gain (WEG). Right panel: snapshot of the typical intensity distribution at an arbitrarily chosen time $t = 1000\Gamma^{-1}$ in a WSG configuration. If not differently specified, we have taken $\beta = 1$.

We start our discussion by reviewing the case of a spatially uniform $P_{m,n} = P$ gain. Figure 3.4(a) shows how the lasing threshold remains very close to the single-resonator (SR) value $P_0 \doteq \Gamma$ analytically extracted from (3.6), the slope efficiency dI_T/dP is only slightly lower than the single-resonator value, and the laser emission is spread throughout the whole system. However, due to complex mode-competition effects, the intensity distribution is very inhomogeneous in space [Figure 3.4(b)] and no monochromatically oscillating steady-state is ever reached. This strong spatio-temporal modulation persists indefinitely (see Supplemental Video 1) and is due to the simultaneous lasing into many modes that interfere and interact with each other via the intrinsic nonlinearity of the model. Such chaotic behaviors are very common in laser arrays unless some specific stabilization scheme is introduced [54, 72–74]. As one can see in the Supplemental Video 1, while the chaotic dynamics of the bulk does not appear to display any specific signature of the non-trivial topology, the intensity distribution on the edge keeps circulating around the system.

Slope efficiency

3.4 Whole edge gain (WEG)

A natural strategy to favor laser emission in the topological edge states is to restrict the gain to the sites on the geometrical border of the system,[4] as exper-

[4] Note that topological lasing in [29] was operated under a WSG; we will propose a physical reason why bulk mode lasing was suppressed in this experiment in Chapter 4.

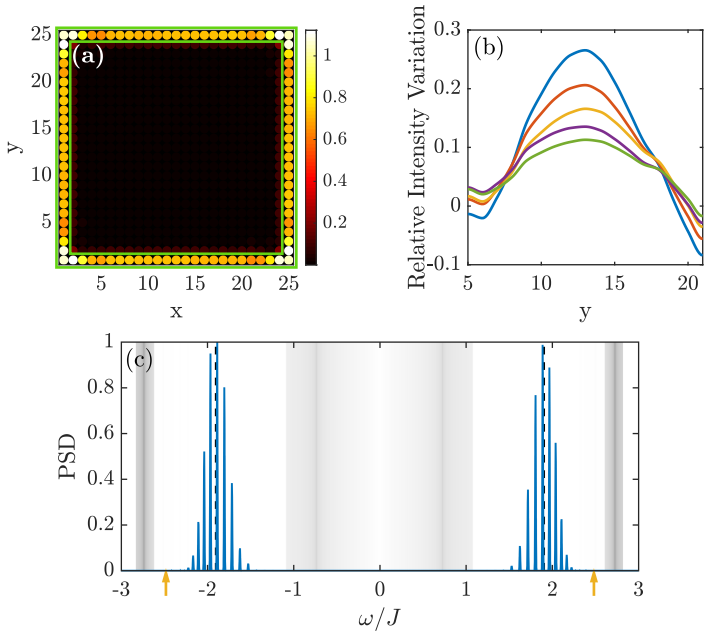

Figure 3.5: Topological lasing in a 25×25 HH lattice with $\vartheta = 1/4$ in a one-site-thick WEG configuration. Panel (a): snapshot of the steady-state intensity distribution. The green rectangle indicates the amplifying sites. Panel (b): cuts of the intensity distribution along the $x = 1$ line at times (from top to bottom) $\Gamma t = 43.85, 51.65, 59.45, 67.20, 75.00$. Panel (c): normalized realization-averaged power spectral density (PSD). The dashed lines indicate the center of mass of the distribution. For comparison, the orange arrows indicate the lasing frequency for a 1×15 PEG. The gray shading indicates the density of states of the bands in Figure 3.3(a).

imentally implemented in [55]. Figure 3.5(a) recovers the predictions of earlier theoretical work [51] and displays a stable monochromatic single-mode oscillation in a topological edge mode of the system.[5] The slope efficiency (i.e. the slope of the blue curve in Figure 3.4(a) right above the threshold) is very close to the single-site one and the slightly increased threshold $\tilde{P}_0 \gtrsim P_0$ is due to the weak but finite penetration of the edge mode into the non-amplifying bulk sites. Given the broadband gain used in the calculations, the oscillation frequency occurs with the same probability in either gap of the band structure [Figure 3.5(c)]: as expected from the band structure shown in Figure 3.3, the lasing mode will have opposite

[5]Note that the dynamical instabilities anticipated in [58] were due to specific features of semiconductor lasers, in particular to the presence of a slow carrier reservoir that induces site-dependent nonlinear frequency shifts. They are absent in our simple model of lasing. A theoretical study of the stability of edge state lasing has been subsequently carried out in [63].

chirality depending on which edge mode is selected.

3.4.1 Consequences of the chirality of the lasing mode

This general picture of topological lasing [51, 54] is the starting point to investigate the subtle physical consequences of the chirality of the lasing modes that are the core subject of this Chapter.

Selection of lasing frequency

As a first result, Figure 3.5(c) shows that the lasing frequency is randomly chosen among a number of available modes located around the gap centers. Since the penetration of the edge mode in the bulk is minimum at the center of the energy gap, lasing will preferentially occur in this frequency region that maximizes the overlap with the amplifying sites and thus the effective gain. As it happens in ring lasers, edge modes are discretized according to a round-trip quantization condition around the perimeter of the system. This gives a frequency spacing $\Delta\omega \simeq 2\pi\, v_g/L$ where v_g is the edge mode group velocity and L is the perimeter. The approximately equal spacing of the modes is due to the weak curvature of the edge mode band that is visible in Figure 3.3. Even though the mode spacing can be very small in large lattices, once a lasing mode has been selected, the single-mode emission remains stable for indefinite times in the absence of noise. The overall width of the distribution is determined by the k-dependent spatial overlap of edge modes with the gain region, which introduces an effective frequency dependence of the gain.

Ultra-slow relaxation rate

As an even more remarkable feature, Figure 3.5(b) displays a series of longitudinal cuts of the intensity profile along the $x = 1$ left edge for different times separated by an (approximate) round-trip time $T_{\rm rt} = L/v_g$. The intensity modulation due to the initially noisy state relaxes away on a much slower timescale than all other microscopic scales, including $T_{\rm rt}$. As an illustrative example, Supplemental Video 2 shows an intensity bump traveling in the clockwise direction around the system and slowly fading away. This ultra-slow relaxation rate is a consequence of the Goldstone theorem which imposes (at least) a k^2 behavior for the imaginary part of the complex frequency of the long-wavelength collective modes corresponding to spatially slow fluctuations of the laser emission [63, 65].

3.4.2 Robustness to disorder

To complete the picture, it is important to briefly investigate the robustness of these features against static disorder. Some first remarks on the effect of disorder were reported in [51].

The most straightforward way of including disorder in our model is to introduce a random frequency shift of the natural frequencies of the cavities. In Figure 3.6 we take the on-site disorder U to have a Gaussian distribution with standard deviation $\sigma(U)$. A specific realization of disorder is displayed in panel (g) for the $\sigma(U)/J = 0.1$ case. The disorder used in the cases $\sigma(U)/J = 0.4,\ 1.2$ is

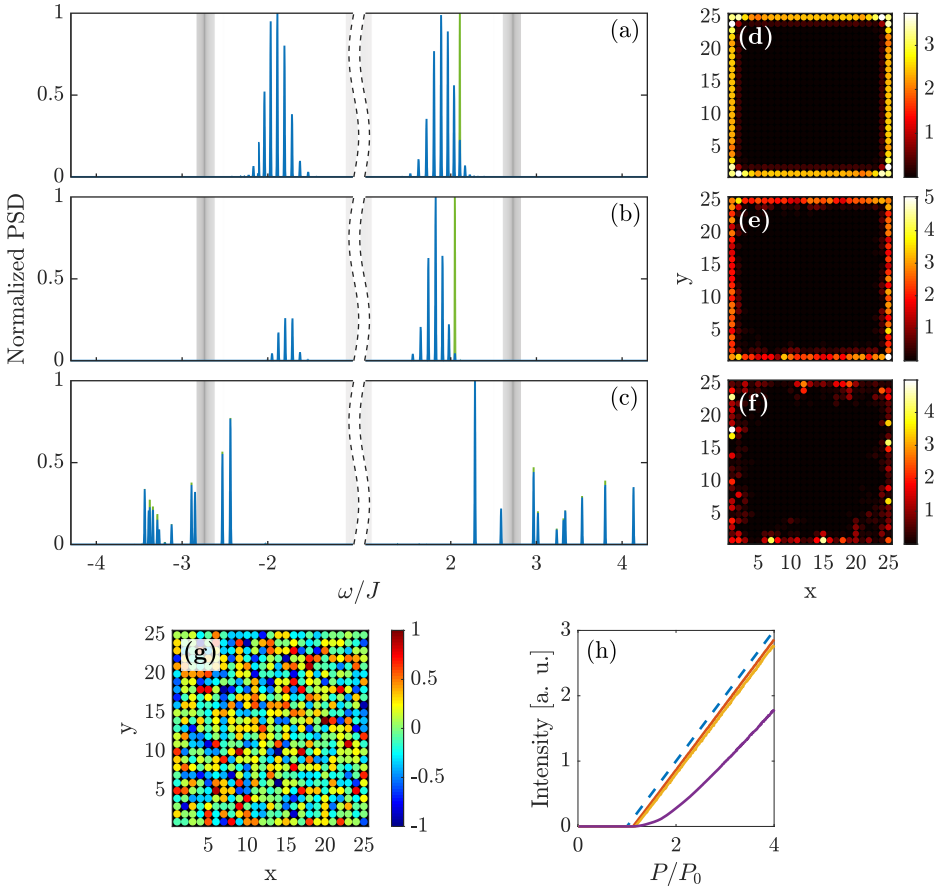

Figure 3.6: Panels (a)–(c): normalized spatially integrated power spectral density (PSD) in the WEG configuration without disorder (panel (a)) and with a disorder strength equal to $\sigma(U)/J = 0.4$ (panel (b)) and to $\sigma(U)/J = 1.2$ (panel (c)). The PSD for a single random realization of lasing is displayed in green, while the average over multiple realizations [5000 in panel (a), 2500 in panels (b)–(c)] is shown in blue. The shaded areas indicate the density of states of the bands in the absence of disorder, and the central band region has been cut out for visualization convenience. Panels (d)–(f): snapshots of the typical intensity distribution at an arbitrarily chosen late time $t = 500\Gamma^{-1}$ for the same values of disorder as in (a)–(c). Panel (g): realization of the disorder used (upon rescaling) for all other simulations in the figure. Colors indicate the frequency shift of the different sites for a disorder strength $\sigma(U)/J = 0.1$. Panel (h): normalized emitted intensity as a function of gain strength for a single resonator (blue dashed line), for the non-disordered case (solid red line), and for a few disordered cases with $\sigma(U)/J = 0.4$ (solid yellow line) and $\sigma(U)/J = 0.4$ (violet line).

obtained by simply rescaling this distribution. In addition to this "non-magnetic" disorder that is common to all systems, note that microrings-based implementations like the one in [55] can also host another source of disorder, called "magnetic" disorder since it couples the two pseudo-spin states [34, 51]. A study of this latter disorder goes beyond the scope of our work.

Topological protection (static disorder)

Thanks to the topological protection of the edge mode and its ability to circumnavigate impurities and defects, the intensity distribution for a WEG configuration remains spatially localized on the edge up to large values of the disorder strength comparable to the bandgap [panels (d)–(f)]. As one can see by comparing the different curves in panel (h), moderate values of disorder only slightly increase the lasing threshold, while the slope efficiency is almost unaffected. The unidirectional chiral motion of the lasing edge mode guarantees an efficient phase locking of the emission at different points along the edge, and the laser operation remains firmly single-mode [green lines in panels (a)–(b)].

Only when the disorder gets comparable to the energy band gap, the laser emission breaks into several independently lasing regions and the emission acquires a multi-mode and multi-frequency character, as shown in the intensity distribution in panel (f) and in the spectrum in panel (c). Correspondingly, one can see in panel (h) that the sharp threshold transforms into a smooth, progressive switch-on. As compared to the WSG case, the spatial separation of the different lasing modes makes the temporal fluctuations of the intensity profile less apparent than in Figure 3.4 and Supplemental Video 1.

The blue lines in panels (a)–(c) show a statistical analysis of the emission frequency over many realizations of laser operation with the same realization of the Gaussian disorder.[6] As long as the disorder is moderate and the lasing mode keeps extending around the whole system, the discretization of the modes is preserved [blue lines in panels (a)–(b)]. For stronger disorder, when many modes are simultaneously and independently lasing, the emission spectrum for a single realization matches the averaged one, so the distinction between the green and the blue curve is no longer visible in panel (c).

3.5 Partial edge gain (PEG)

Since the ultra-slow relaxation of long-wavelength fluctuations discussed in the previous Section is likely to compromise the coherence of the emission against quantum noise [53], it is interesting to explore a configuration where gain is restricted to a $1 \times N$ finite strip of sites along an edge. A related geometry was experimentally considered in [55].

In this case, a dramatically faster relaxation can be anticipated since any perturbation is rapidly expelled by the chiral motion into the surrounding non-

[6] The study of a single disordered realization is physically more meaningful, in this case, than averaging over multiple disorder realizations; it models a specific sample that has a single and immutable disordered configuration.

amplified edge region. Furthermore, while in the WEG configuration the round-trip quantization around the system perimeter gives a topologically protected winding number [75] characterizing the lasing mode as in standard ring lasers, in the present PEG configuration the lasing region is an open segment, for which no topologically protected winding number exists; as a result, the spatial profile of the lasing mode is able to continuously relax towards its optimal shape.

3.5.1 Spatial structure of the lasing mode

This expected behavior is confirmed in Figure 3.7. A steady-state with a stable monochromatic oscillation is indeed quickly reached on a microscopic timescale. For moderate values of N [panels (c) and (d)], all the emission is efficiently funneled into one of the two modes with opposite chiralities, randomly chosen at each realization. Given their relatively large frequency-separation of order J, one can anticipate that in practice one of them will be privileged by the small frequency-dependence of the gain[7].

The selected chirality reflects in the spatial asymmetry of the intensity profile within the amplifying region. This asymmetry is clearly visible on the dotted light-blue lines in panels (c) and (d) as a growing intensity along the positive-y chiral propagation direction. This asymmetry is still visible but less marked on the solid blue lines calculated for a higher gain far above the threshold, for which the light intensity displays within the amplifying region a faster growth towards the saturated value. Irrespectively of the gain strength, the chirality of the lasing edge mode is also apparent in the significant amount of light emission from the non-amplifying edge sites located just downstream of the amplifying region, while the ones located in the upstream direction remain dark. In Figure 3.7(c)–(d), this corresponds to a much more pronounced tail of the intensity distribution on the right-hand side of the amplifying region marked in yellow.

The situation is very different for large values of N. In this case, mode competition is not able to isolate a single mode, and lasing simultaneously occurs in modes of both chiralities, [panel (e)]. Nonetheless, local gain saturation effects are still able to keep the two chiralities almost spatially separated with a net outward flow (red arrows). The fringes that are visible in the central region arise from interference of the two lasing modes and oscillate at their frequency separation of the order of J.

3.5.2 Convective vs. absolute instability

Additional intriguing features of the PEG case are found in the dependence of the lasing threshold on the strip length N plotted in Figure 3.7(b). As expected, the threshold decreases for growing N, but a numerical fit of the form $aN^{-b} + c$

[7] Note that the pseudo-spin degree of freedom in [55] allows for more complex field configurations where modes of both chiralities are excited even in a monochromatic steady-state. As discussed there, more complex ring-resonators are then required to select a specific chirality.

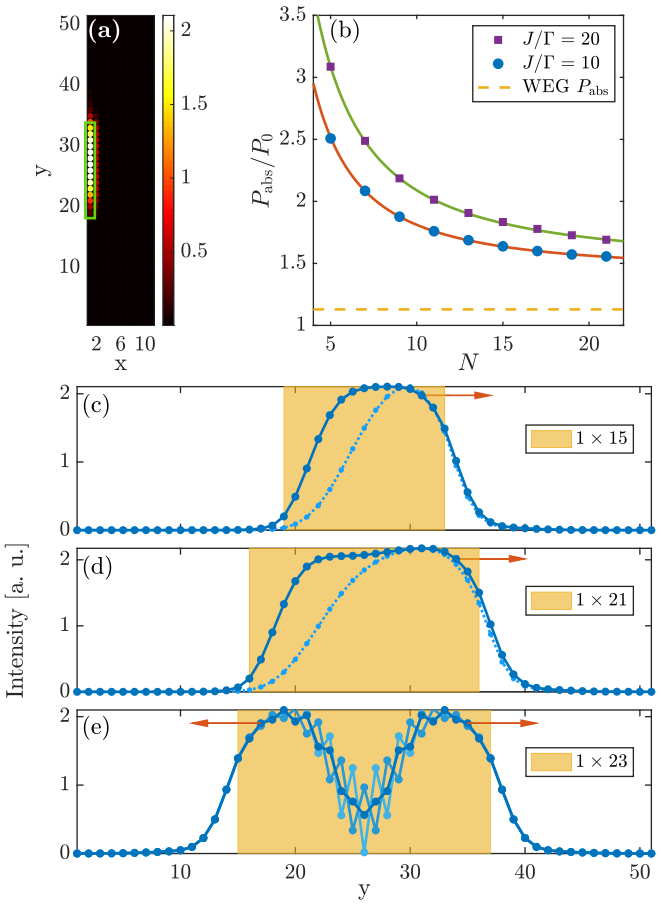

Figure 3.7: Panel (a): steady-state intensity distribution for a 1×15 PEG in a large 11×51 lattice. The green rectangle indicates the amplifying sites. Panel (b): lasing threshold for $1 \times N$ PEG with different $J/\Gamma = 20, 10$ (solid lines). Lasing threshold for a one-site-thick WEG case (dashed line). Panels (c)–(e): cuts of the intensity distribution along the $x = 1$ line for different PEG geometries (see legends). The shaded area indicates the amplifying sites. The different curves in (c)–(d) refer to the steady-state for different gain strengths $P/P_0 = 4$ (solid blue), $P/P_0 = 2$ (dotted, light blue; to facilitate reading, these curves have been rescaled to have the same maximum as the solid blue ones); the different curves in (e) refer to different times separated by $0.05\Gamma^{-1}$.

(solid lines) clearly shows that the large-N limit remains significantly higher than the WEG threshold (dashed line).

An explanation for this remarkable finding is offered by the distinction between convective and absolute instabilities, a well-known phenomenon in the theory of nonlinear dynamical systems and in hydrodynamics [76, 77]. The *absolute instability* (AI) corresponds to the standard dynamical instability of the zero-field state above a threshold P_{abs}. The *convective instability* (CI) is instead a weaker form of instability that is found whenever the exponential growth of a perturbation for $P > \tilde{P}_0$ is overcompensated by its quick motion at v_g: in this CI regime, even though the *peak* amplitude of the moving perturbation grows in time, its *local* value at any given spatial location quickly decreases back to zero. When the amplifying region is spatially finite, as in our PEG case, any perturbation immediately disappears upon entering the external lossy region. This distinction between CI and AI explains why the laser instability is only observed above the higher AI threshold $P_{\text{abs}} > \tilde{P}_0 \gtrsim P_0$. This phenomenon cannot occur in the WEG case where the closed shape of the amplifying region does not allow the perturbation to escape from it.[8]

Convective instability

Further evidence of the role of the convective instability in the PEG configuration is offered by the dependence of the lasing operation on the group velocity v_g. As we have seen in the previous Section, a lasing frequency next to the gap centers [Figure 3.5(c)] is chosen in the WEG case so to maximize the spatial overlap with gain. In the PEG case, instead, the location of the absolute threshold P_{abs} is dominantly controlled by v_g, so the AI is first reached by edge modes located next to the outer edge of the gaps (orange arrows) for which v_g is lower. A more subtle feature is visible in Figure 3.7(b). On one hand, the WEG threshold (dashed line) stays constant at $\tilde{P}_0 \gtrsim P_0$ when J/Γ (and thus v_g) is increased. On the other hand, the PEG threshold at P_{abs} monotonically grows when J and consequently v_g are increased (squares vs. circles).

3.5.3 Noise-sustained structures

A typical way to characterize the convective vs. absolute nature of a dynamical instability in generic nonlinear dynamical systems is to study the intensity distribution in the presence of some external noise and look for the so-called noise-sustained structures (NSS) [76–79].

Generic quantum optical systems are unavoidably subject to quantum noise due to the discreteness of the light quanta. An easy way to include the effects of the quantum noise is to switch to the Wigner representation [80–83] and write stochastic differential equations for the classical complex variables $a_{m,n}$ corresponding to the quantum field amplitudes $\hat{a}_{m,n}$. In the absence of extra noise sources, noise can be approximated by its expression in the linear gain regime,

[8] The transition between WEG to PEG occurs when the length of the non-pumped interval largely exceeds the absorption length along a (non-pumped) edge.

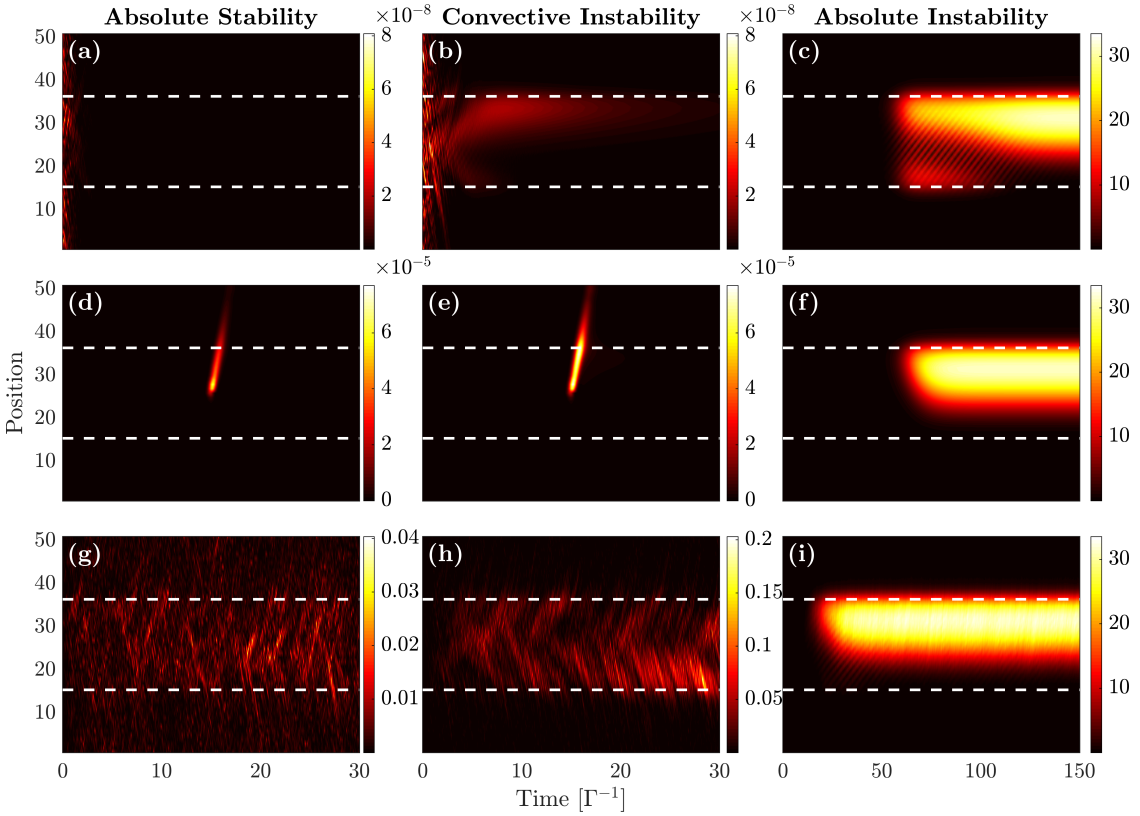

Figure 3.8: Spatio-temporal intensity patterns on the left border of a 11×51 lattice with a 1×21 amplified strip located at the center of the left side and indicated in all panels by the dashed white lines. In the first row there is a noisy seed only at $t = 0$, while on the third one there is noise at all times. In the second row there is no noise, but there is a Gaussian pulse at frequency $\omega/J = 1.9$ localized on the central site and centered in time at $t = 15$, with standard deviation $\sigma_t = 0.3$. All the times are measured in units of Γ^{-1}. For homogeneity, in the AI case we restricted to a realization of lasing into the clockwise propagating topological mode localized on the left edge. In this figure, $\beta = 0.01$ was taken.

where it amounts to an additional stochastic term in (3.6):

$$\dot{a}_{m,n}(t) = \ldots - \sqrt{\Gamma\left(1 + \frac{P_{m,n}}{P}\right)}\,\xi_{m,n}(t). \tag{3.7}$$

Here the dots ... summarize the RHS of (3.6) and $\xi_{m,n}(t)$ are independent, zero-mean normally-distributed complex white noises of variance 1.

Examples of simulations of noise-sustained structures in the topological laser PEG configuration are shown in Figure 3.8. We go through the different instability regimes by varying the pump power P, namely $P/P_0 = 0.9$ for the absolutely stable (AS) regime, $P/P_0 = 1.5$ for the CI regime, and $P/P_0 = 1.8$ for the AI regime. As shown in Figure 3.7(b) for the considered $J/\Gamma = 10$ and $N = 21$ case, the thresholds are at $P/P_0 = 1.13$ for the AS to CI transition and at $P/P_0 = 1.56$ for the CI to AI transition.

The spatio-temporal patterns in Figure 3.8 are calculated in three different cases, namely with a weak initial noisy seed (top row); with a coherent pulse incident on the system at a given time (central row); with a continuous white noise active during the whole evolution according to Equation (3.7) (bottom row).

Noise-sustained structures

In the CI regime without noise [panel (b)], the initial noisy seed gets quickly amplified in the amplifying region but is simultaneously advected away with group velocity v_g. Locally, the system then quickly returns to the equilibrium zero-field state. In the presence of continuous noise [panel (h)], the spatio-temporal pattern clearly shows so-called *noise-sustained structures* (NSS) [76, 77]. These consist of high-intensity stripes that keep appearing at random times and get amplified while being advected away at $\pm v_g$ (depending on which topological gap they are spectrally located in). As a result, the intensity is continuously fluctuating at all points, but its average and variance are strongest on the edge of the amplifying region. Of course, the field shows no long-time phase coherence. A short coherent pump pulse whose spectrum overlaps one of the two topological edge modes (the upwards propagating one in the figure) injects a wavepacket that gets quickly amplified while it propagates along the edge at v_g with a minor spatial broadening [panel (e)]. Once the wavepacket reaches the edge of the amplified region, it starts decaying.

These are the typical features of systems located in a convective instability regime and accurately match the ones displayed by other optical systems in the same regime [78, 79]. For the sake of completeness, it is interesting to compare these behaviors to the ones in the absolute stability and in the absolute instability regimes.

In absence of noise [panels (a)–(c)] the initial perturbation gets quickly damped in the AS regime, while it is exponentially amplified into a self-supporting lasing mode in the AI regime. In this latter case, the chirality of the lasing mode is randomly selected depending on the initial condition. In the shown case, the system starts lasing in both chiralities, but eventually one of them (the upwards

propagating one in the figure) dominates and ends up completely suppressing the other one.

We now replace the initial noisy perturbation with a short Gaussian pulse spectrally overlapping with the upwards propagating chiral edge mode. In the AS regime, we observe that the pulse propagates at v_g but is quickly damped during propagation [panel (d)]. In the AI regime, instead, the injected pulse has the time to expand across the whole amplified region before being advected away, so that it can eventually transform into a self-supporting lasing mode [panel (f)]. In this case, the chirality of the lasing mode is fixed from the beginning by the one of the incident pulse.

In the presence of noise at all times, the stripe-shaped intensity fluctuations that are visible in the amplifying region have different properties in the AS regime [panel (g)] as compared to the one discussed above for the CI regime [panel (h)]. Since decay now dominates over amplification, the intensity is now roughly uniform across the whole amplified region and is no longer peaked on the edges. Still, both chiralities are randomly selected during the evolution.

In the AI regime, the behavior in the presence of a continuous noise [panel (i)] is very similar to the other two cases [panels (c) and (f)]. As in (c), the chirality of the lasing mode is randomly selected. The main difference with (c) and (f) is that the noise accelerates the onset of lasing; furthermore, weak intensity fluctuations are visible on top of the lasing mode at all times and propagate in the same direction.

3.5.4 Robustness to disorder

In order to assess the robustness of lasing to disorder, we now consider a PEG configuration with a 1×15 strip of amplifying sites on the left border of a 11×51 lattice and we add the typical Gaussian disorder configuration shown in Figure 3.9(g). Snapshots of the spatial intensity distribution of the emission at a late time $t = 500\Gamma^{-1}$ are shown in panels (d)–(f) for different values of the overall disorder strength. These plots suggest that the disorder strength which is needed to spoil the single-mode nature of the topological laser emission is roughly 1/3 of what was needed in the WEG configuration discussed above. This relative fragility is due to proximity (visible in Figure 3.3) of the lasing frequency to the bulk bands: a weaker disorder is sufficient to mix the edge mode with the bulk bands and thus break the edge state into independently lasing regions, as shown in panel (f).

Further light on this physics can be obtained from the power spectral densities shown in panels (a)–(c). In contrast to the WEG case, no visible difference is found between the spectra for single realizations of lasing and the averaged ones. As already mentioned for the disorder-free case, this is due to the open boundaries of the amplifying region, which allow for a smooth adjustment of the lasing mode to the optimal gain. As long as the disorder remains moderate, we have a monochromatic and single-mode emission. For the strong disorder strength case

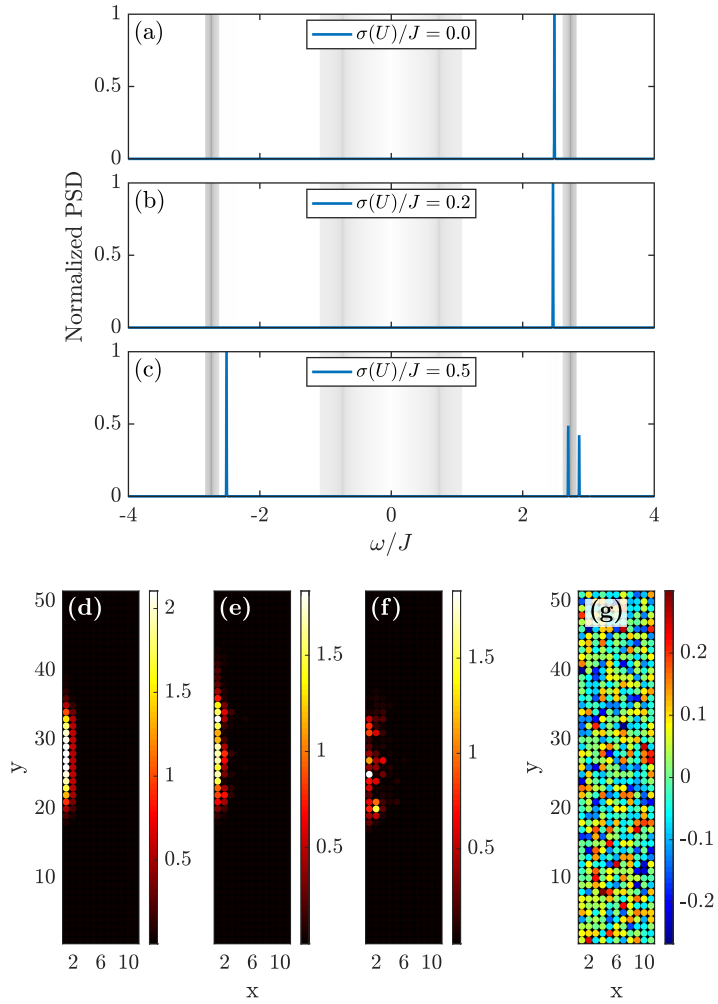

Figure 3.9: Panels (a)-(c): normalized spatially integrated power spectral densities for different values of the disorder strength $\sigma(U)/J = 0$ [panel (a)], 0.2 [panel (b)], 0.5 [panel (c)]; the shaded areas indicate the density of states of the bands in the absence of disorder. Panels (d)-(f): snapshots of the intensity distribution at a late time $t = 500\Gamma^{-1}$ for the same configurations of panels (a-c). Panel (g): frequency shift of the different sites for a disorder strength $\sigma(U)/J = 0.1$; upon a suitable rescaling, this realization of the disorder is used in all panels. Same geometry with a 1×15 amplifying strip in a 11×51 lattice as in Figure 3.7(a).

considered in panel (c), the spatial breaking into several independent lasing mode visible in panel (f) reflects in the multi-mode character of the emission, which also involves frequencies located within the bands.

3.5.5 Amplification of a propagating probe

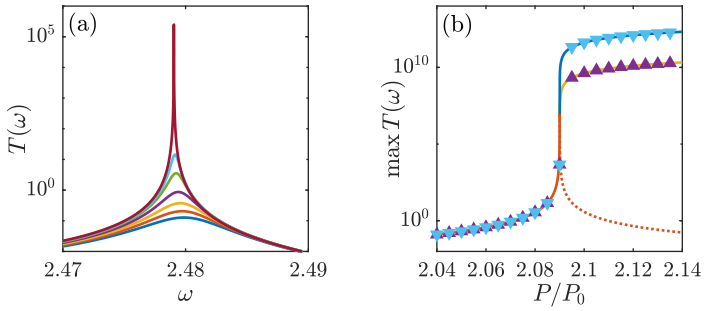

Figure 3.10: Left panel (a): Incident-frequency-dependent transmission spectrum for a 1×7 PEG and different gain strengths (from bottom to top) $P/P_0 = 2.04, 2.05, 2.06, 2.07, 2.08, 2.085, 2.09$ approaching the lasing threshold. Right panel (b): peak transmittivity as a function of gain strength for incident amplitude $E_0/\sqrt{J} = 10^{-7}$ (upwards triangles) or 10^{-8} (downwards triangles). Red lines indicate the result of the linearized calculation based on the input-output formalism of [34, 37].

As a final characterization of the CI regime, Figure 3.10 illustrates the possibility of an efficient traveling-wave amplification [37]. We consider a system of 11×25 sites with amplification restricted to a 1×7 vertical strip in the middle of the left border (sites 10 to 16). The chiral transmission of a coherent probe through the gain region is studied using a pair of input and output waveguides coupled to the neighboring sites 8 and 18 on the same border. The transmission is calculated by solving the temporal evolution until the steady-state is reached. As usual in input-output theory [84], new terms must be added to the time-evolution equations for the input and output sites,

$$\dot{a}_{\rm in}(t) = \ldots - \frac{\gamma_{\rm in}}{2} a_{\rm in} - \sqrt{\gamma_{\rm in}} E_0 e^{-i\omega t} \tag{3.8}$$

$$\dot{a}_{\rm out}(t) = \ldots - \frac{\gamma_{\rm out}}{2} a_{\rm out} \tag{3.9}$$

where the dots ... summarize the RHS of (3.6), the incident field has amplitude E_0 and frequency ω, and $\gamma_{\rm in,out}$ account for the extra radiative losses into the waveguides. The transmittivity (Figure 3.5) is obtained from the transmitted field $E_{\rm out} = \sqrt{\gamma_{\rm out}} a_{\rm out}$ as $T = |E_{\rm out}/E_0|^2$: below the lasing threshold $P_{\rm abs}$, the full numerical calculations (triangles) are perfectly recovered by a simpler

linearized calculation based on the Green's function approach for a weak probe (red lines) discussed in the supplementary material of [34] and extended to the quantum level in [37]. Above the threshold, nonlinear effects dominate and the linearized calculations are no longer reliable.

Transmittivity near threshold

Panel (a) shows the transmission spectrum for gain values in the CI region $\tilde{P}_0 < P < P_{\text{abs}}$. For $P < P_0$, the gain is not able to overcome losses: the net absorption of all sites combined with the impedance mismatch at the input and output waveguides conspire to give a very low transmission. As P grows above $\tilde{P}_0$, net amplification sets in, giving a broad transmission peak. As P further grows towards P_{abs}, the transmittivity grows far above 1 in a narrow frequency range and eventually diverges at the lasing frequency as the absolute threshold is approached ($P \to P_{\text{abs}}^-$). Panel (b) shows the peak transmittivity as a function of gain strength for two values of the probe intensity. Well below the laser threshold, the two curves coincide as the system behaves in a linear way. Around and above threshold, instead, nonlinear gain saturation sets in, limiting the effective amplification and thus distinguishing the two curves. Well above the laser threshold, the field intensity is fixed by the self-oscillation process independently of the probe, so the transmittivity is inversely proportional to $|E_0|^2$.

3.6 Conclusions

In this Chapter, we have theoretically studied a topological laser device based on a bosonic Harper-Hofstadter lattice model endowed with optical gain.

After a brief introduction on the Harper-Hofstadter model and on its topological properties, we have obtained the equations that describe a topolaser device by incorporating the lattice dynamics into the semiclassical theory of lasers, in the limit of a broadband gain. We have then numerically simulated the resulting set of equations in order to investigate the properties of the laser.

The numerical simulations have highlighted striking consequences of the chirality of the lasing mode: when the gain is distributed around the whole edge, lasing can occur in a number of closely-spaced modes, and relaxation towards the steady-state occurs on a very slow timescale; when the gain is restricted to a finite strip, relaxation is fast but the distinction between convective and absolute instabilities causes an increase of the threshold and introduces new amplification regimes. On this latter point, in analogy to other convectively unstable systems, we have illustrated the qualitative shape of the structures that appear in the presence of quantum noise. Finally, to complete the picture, we have quantitatively assessed the impact of disorder on topological lasing and highlighted the stronger robustness of the WEG configuration.

While the analysis developed in this Chapter offers new fundamental insights, especially on broadband topolasers like the one in [51, 55], it falls short of addressing the pioneering experimental observations in [29], in which a single-mode topolaser based on photonic crystals was obtained in a WSG configuration. Since

in this configuration a broadband analysis predicts, as discussed in Section 3.3 and as observed in [51, 55], a chaotic multi-mode emission even from topologically trivial modes, we felt the motivation to investigate on the interplay between spatial mode-selection mechanisms and spectral mode-selection mechanisms, which is the subject of Chapter 4.

Chapter 4

Harper-Hofstadter topological laser with spatial and spectral mode-selection

In the previous Chapter, we've analyzed a broadband topolaser based on the Harper-Hofstadter model, exploring the viability and the properties of different pumping schemes that we classified as WSG, WEG or PEG.

Under a WSG — i.e. spatially uniform pumping — configuration, such a system is not able to selectively promote an edge mode to a lasing mode, and when the pumping strength is above the absolute lasing threshold all the modes start to lase — even the bulk ones. This is the reason most topolaser realizations employ a WEG pumping scheme [21, 49, 55, 85] or a PEG pumping scheme [48, 50, 86], that are able to effectively increase the gain of the edge modes with respect to the bulk ones by exploiting the spatial overlap between the mode profile and the pumped region itself.

However, a notable exception in these experiments was reported in [29]; despite having an extremely narrow topological bandgap, the authors were able to get a clean single-mode emission from a topologically protected edge state by employing a WSG scheme — also used in later works [57, 87].

Motivated by these puzzling experimental results, we have decided to investigate the interplay between spatial and spectral mode-selection mechanisms, which requires treating the system beyond the broadband regime by incorporating the frequency-dependent contributions from the gain medium. In this Chapter we will explore the physics down this road, by suitably modifying the topological

laser equations and the system itself.

The Chapter is organized as follows. In Section 4.1 we introduce the underlying model and the equations used in the numerical simulations. In Section 4.2 we review the case of narrowband gain, and in Section 4.2.2 we discuss the interplay between mode pulling and the resonant frequency of the gain. In Section 4.3 we consider the case of a broadband gain, starting in Section 4.3.1 where we present a scheme that is able to qualitatively reproduce the observations of [29] and where we briefly discuss the main results at a more intuitive level, while leaving a more in-depth analysis to Sections 4.3.2 to 4.3.4. In Section 4.4 we discuss the connection between our model and the experimental observations in [29], and finally in Section 4.5 we draw the conclusions.

Most of this Chapter is based on our publication "Spatial and spectral mode-selection effects in topological lasers with frequency-dependent gain" [33].

4.1 The Bloch-Harper-Hofstadter model

As a starting model, we consider again the same Harper-Hofstadter lattice we have introduced in Chapter 3. Analogously to what we did in Section 3.2, we now want to write the corresponding semiclassical equations we have to solve; here, however, we don't restrict ourselves in the broadband limit anymore, so we need to use the full set of equations (2.12) that describe not only the evolution of the photon field, but also of the coherence and the populations of the atoms in the gain medium.

For clarity, let's write again the full semiclassical equations for a cavity with a gain medium:

$$\begin{cases} \dot{\rho}_{ee} = \gamma_g \rho_{gg} - \gamma_e \rho_{ee} + i\dfrac{d_{eg}E_0}{\hbar}\Big(a\rho_{ge} - a^*\rho_{eg}\Big) \\ \dot{\rho}_{gg} = \gamma_e \rho_{ee} - \gamma_g \rho_{gg} - i\dfrac{d_{eg}E_0}{\hbar}\Big(a\rho_{ge} - a^*\rho_{eg}\Big) \\ \dot{\rho}_{eg} = -i(\omega_{eg} - i\gamma)\rho_{eg} - i\dfrac{d_{eg}E_0}{\hbar}a\Big(\rho_{ee} - \rho_{gg}\Big) \\ \dot{a} = -\Gamma a + i\dfrac{d_{eg}E_0}{\hbar}N\rho_{eg} \end{cases} \tag{4.1}$$

Notice that, compared to (2.12), we have eliminated the cavity frequency ω_{cav} by using it as a reference frequency to measure all other frequencies, i.e. by performing the unitary transformation

$$a \to a e^{-i\omega_{\text{cav}}t} \qquad \text{and} \qquad \rho_{eg} \to \rho_{eg} e^{+i\omega_{\text{cav}}t}, \tag{4.2}$$

that does not affect the populations.

Just as before, we now have such a set of equations for each cavity in the lattice, so we have to add position indices; furthermore, the lattice cavities themselves are connected through the Harper-Hofstadter hopping term

$$H_{\text{hop}} = -J\sum_{m,n}\Big\{a^\dagger_{m,n}a_{m+1,n} + e^{-i2\pi\vartheta m}a^\dagger_{m,n}a_{m,n+1} + \text{h.c.}\Big\}, \tag{4.3}$$

so the equations for the photon field have to include it as $\dot{a}_{m,n} = \ldots + \frac{i}{\hbar}[H_{\text{hop}}, a_{m,n}]$, where the dots $\ldots$ indicate the existing terms in the RHS of (4.1).

As now J sets the lattice energy scale, it is also useful to perform a rescaling to dimensionless quantities for numerical purposes. This is done by performing the re-definitions $\frac{\hbar\gamma_{\{e,g,eg,\text{ph}\}}}{J} \to \gamma_{\{e,g,eg,\text{ph}\}}$, $\frac{\hbar\omega_{eg}}{J} \to \omega_{eg}$, $\frac{Jt}{\hbar} \to t$, $\frac{\hbar\Gamma}{J} \to \Gamma$, $-\frac{\hbar g}{J}a \to a$ (the extra "$-$" compensates the fact that g is negative), and by defining the new quantity

$$G \doteq \left(\frac{\hbar g}{J}\right)^2 N = \left(\frac{d_{eg}E_0}{J}\right)^2 N = \frac{d_{eg}^2 \hbar\omega_{\text{cav}}}{2J^2\varepsilon_0}\frac{N}{V}. \tag{4.4}$$

This parameter, which is proportional to the volumetric density $\frac{N}{V}$ of TLAs and to the natural frequency of the cavity, will act as a *gain parameter* in the following discussion — we comment more on this choice below.

With all these ingredients, the set of equations (4.1) for a single cavity turns into the following set of coupled equations (4.5) for our Harper-Hofstadter lattice, in dimensionless units, that we dub *Bloch-Harper-Hofstadter model*:

$$\begin{cases} \dot{\rho}_{ee}^{m,n} = \gamma_g - 2\gamma_{eg}\rho_{ee}^{m,n} + i\left(a_{m,n}\rho_{ge}^{m,n} - a_{m,n}^*\rho_{eg}^{m,n}\right) \\ \dot{\rho}_{gg}^{m,n} = \gamma_e - 2\gamma_{eg}\rho_{gg}^{m,n} - i\left(a_{m,n}\rho_{ge}^{m,n} - a_{m,n}^*\rho_{eg}^{m,n}\right) \\ \dot{\rho}_{eg}^{m,n} = -i\left(\omega_{eg} - i\gamma\right)\rho_{eg}^{m,n} - ia_{m,n}\left(\rho_{ee}^{m,n} - \rho_{gg}^{m,n}\right) \\ \dot{a}_{m,n} = -\Gamma a_{m,n} + iG\rho_{eg}^{m,n} + i\left(a_{m+1,n} + \alpha_{m-1,n}\right) \\ \qquad\quad + i\left(e^{-i2\pi\vartheta m}a_{m,n+1} + e^{+i2\pi\vartheta m}a_{m,n-1}\right) \end{cases} \tag{4.5}$$

Bloch-Harper-Hofstadter model

In all the simulations, we've set the on-site losses to a reasonable value $\Gamma = 0.1$.

We now seek the lasing condition of a single lattice cavity, bearing in mind that, as we have shown in Chapter 3, the lasing condition for a lattice of identical cavities has to be greater or equal than the threshold of a single cavity.

Choice of the amplification parameter

In actual devices, the amplification is controlled by γ_g, the rate at which the atoms are excited from their ground state $|g\rangle$ to a higher-energy state $|e\rangle$. However, this has also the additional side effect of possibly modifying both the height and the linewidth of the Lorentzian profile of the gain (see Section 2.2), depending on the relative value of γ_{ph}, as well as contributing to frequency-dependent shifts of the lasing frequency itself and of the saturation factor of the amplification term. In order to skim these side effects off the model and obtain a simpler, yet still meaningful description, we'll instead use G as the primary amplification parameter, and we'll write the lasing condition for G itself. Increasing G instead of ρ_{eg} (through γ_g) has the same effect on the amplification term in the equation for a, but helps avoid the effects described above and, if the range of probed G values is not too large, it still gives a faithful description.

The lasing condition in terms of G is easily obtained from the steady-state analysis done in Section 2.2, which shows we must have $\frac{P}{1+\beta|a|^2} > \Gamma$. By expand-

ing this expression, we have the threshold condition

Single-cavity lasing threshold

$$G > \frac{2\Gamma\gamma_{eg}/\gamma}{\gamma_g - \gamma_e}\left[\gamma^2 + \Delta_{\text{det}}^2\right], \tag{4.6}$$

where $\Delta_{\text{det}} = \omega_{eg} - \omega_L$ measures the detuning of the lasing frequency ω_L from the atomic transition frequency ω_{eg}. This relation shows that the threshold for a given mode has a quadratic dependence on its frequency, and that the mode that lases first — i.e. for which the threshold is as small as possible — is the one at resonance, $\omega_L = \omega_{eg}$. In this resonant case, the threshold condition becomes

Single-cavity resonant lasing threshold

$$G > \frac{2\gamma_{eg}\gamma\Gamma}{\gamma_g - \gamma_e} \doteq G_{\text{res},0}, \tag{4.7}$$

where we have defined $G_{\text{res},0}$ as the *single-cavity resonant lasing threshold*.

In the numerical simulations, for the atomic parameters we have set $\gamma_{\text{ph}} = 0$ and we have taken $\gamma_g = \frac{4}{3}\gamma$ and $\gamma_g = \frac{2}{3}\gamma$, with $2\gamma = \gamma_g + \gamma_e$ being the FWHM of the Lorentzian profile of the gain. With this choice of parameters, we then have $G_{\text{res},0} = 3\gamma\Gamma$. The remaining parameters are changed throughout the remainder of this Chapter.

4.2 Narrowband gain

In the previous Section 4.1, we have worked out the equations (4.5) for an active Harper-Hofstadter lattice, without any particular restriction on the linewidth of the gain. Together with the definition of the resonant lasing threshold $G_{\text{res},0}$ of a single lattice site, this provides us the conceptual building blocks to understand laser operation in a topological lattice. As a first step in this direction, in this Section we consider the simplest case where the narrowband gain spectrum is concentrated within a topological gap. In contrast to the chaotic multi-mode emission found in Section 3.3 for the extreme broadband gain, here we show that such narrowband gain can lead to a stable topological lasing even under a spatially uniform pumping. While such a narrowband gain might not be the technologically simplest option for practical devices, a detailed discussion of its features is an interesting first step to validate our Bloch-Harper-Hofstadter model and understand its behavior in the different regimes. In addition to that, because of mode-pulling effects, an interesting non-trivial relation is found between the lasing frequency and the bare frequencies of the discrete set of edge modes.

4.2.1 Single-mode topological laser emission

This narrowband gain configuration can be obtained by considering the Bloch-Harper-Hofstadter model introduced in Section 4.1 and tuning the atomic frequency ω_{eg} in the middle of the topological bandgap with a gain linewidth γ much smaller than the gap width, as sketched in Figure 4.1(c). In this way, the

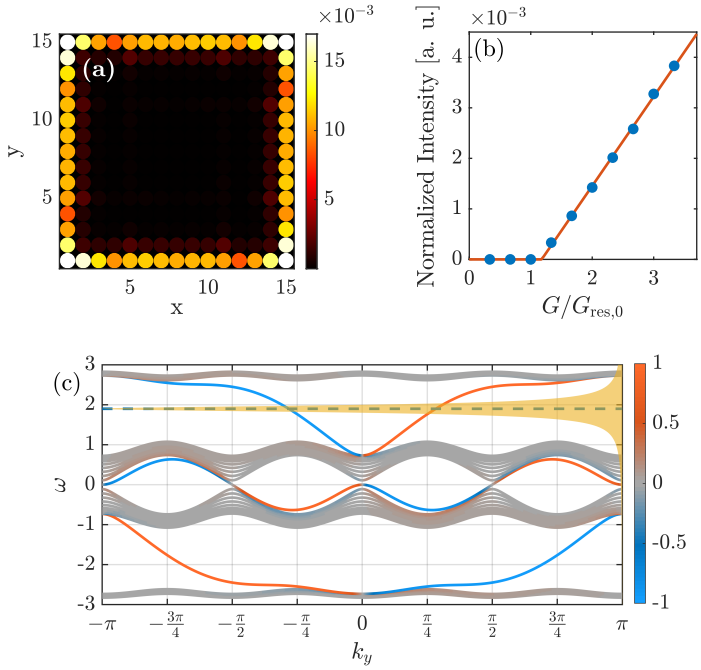

Figure 4.1: Panel (a): steady-state emission of a 15×15 lattice, uniformly pumped on all sites with a narrowband gain of strength $G/G_{\mathrm{res},0} = 3$. The atomic transition frequency is $\omega_{eg} = 1.9$. For these parameters, lasing is found to occur at $\omega = 1.87$. Panel (b): spatially averaged emitted intensity as a function of the gain strength G, showing the typical linear behavior after the lasing threshold. Panel (c): band structure of a Harper-Hofstadter lattice with PBC in the y-direction, but finite in the x-direction $N_x = 39$. The color scale from blue to red quantifies the localization of each mode from left to right in the x-direction, while the dashed line indicates the atomic resonance ω_{eg}. The narrowband gain used for the simulations in the panels above is represented as a Lorentzian in the frequency domain, centered at ω_{eg} and with a FWHM $2\gamma = 0.2$, i.e. roughly 13% of the topological bandgap.

frequency-dependence of gain strongly increases the effective threshold for laser operation in the off-resonant bulk band states while the one for edge state lasing remains almost unaffected.

Laser operation in this regime is illustrated in Figure 4.1(a)–(b). Emission into the edge state is stable and monochromatic and remains so up to high pump strengths well above the laser threshold [88]. Quite interestingly, such monochromatic single-mode emission is not restricted to small lattice sizes where a single eigenstate — classified by k_y for the strip geometry of Figure 4.1(c), or by

the winding number around the lattice for the geometry of Figure 4.1(a) — falls within the gain bandwidth: as it was pointed out in [32] for the extreme broadband gain case, the high spatial overlap of different edge states provides in fact a very efficient mode competition mechanism [59] eventually suppressing simultaneous laser operation in multiple modes. The dynamical stability of the single-mode emission was confirmed by the Bogoliubov analysis in [63]. A further illustration of the dynamics of this mode-competition process over time is provided in Section 4.3.2 where we display a time-frequency representation of the lasing process. As usual, the choice of the specific lasing mode is stochastically determined at each instance of lasing by the initial conditions and the noise. Still, for sufficiently narrowband gain, the resulting probability distribution for lasing in different modes will be very peaked on the most likely mode.

Of course, this monochromatic emission only holds up to moderate pump strengths, at which only the quasi-resonant edge modes experience an effective gain. At very high pump strength also the bulk modes go above threshold and the dynamics recovers the chaotic behavior found in Section 3.3 for a broadband gain distributed in the whole system (WSG).

4.2.2 Mode-pulling effects

It is a general feature of laser physics that a narrowband gain causes an additional *mode pulling* effect. For a single cavity this means that the lasing frequency *does not* correspond to the bare cavity frequency ω_{cav}, as it is pulled towards the center of the Lorentzian profile of the gain [60], i.e. towards ω_{eg}:

Mode-pulling (one cavity)

$$\omega_L = \frac{\omega_{\text{cav}} + \mathcal{S}\omega_{eg}}{1+\mathcal{S}}, \tag{4.8}$$

where $\mathcal{S} = \frac{\Gamma}{\gamma}$ is called the *stabilization factor*.

In the case of a lattice of cavities, we have to replace ω_{cav} with a frequency ω_0 that corresponds to the specific mode of the underlying lattice that the system is selecting for lasing:

Mode-pulling (lattice of cavities)

$$\omega_L = \frac{\omega_0 + \mathcal{S}\omega_{eg}}{1+\mathcal{S}}\,. \tag{4.9}$$

So, in contrast to the broadband gain case where the laser frequency ω_L is typically locked to the bare mode frequency ω_0, for a narrowband gain a possibly sizable mode-pulling effect has to be considered for a reliable calculation of frequency-dependent lasing thresholds and to correctly relate the lasing frequencies that we measure through a power spectral density analysis to the underlying lattice eigenmodes.

When $\mathcal{S} \ll 1$ mode pulling effects are negligible and $\omega_L = \omega_0$, where ω_0 is the frequency of the corresponding lattice mode selected by the lasing process. For equal $\Gamma = \gamma$, the stabilization factor is $\mathcal{S} = 1$ and the mode pulling effect becomes a simple average. Physically, this mode-pulling effect can be understood as the result of the refractive index change that is naturally associated to the

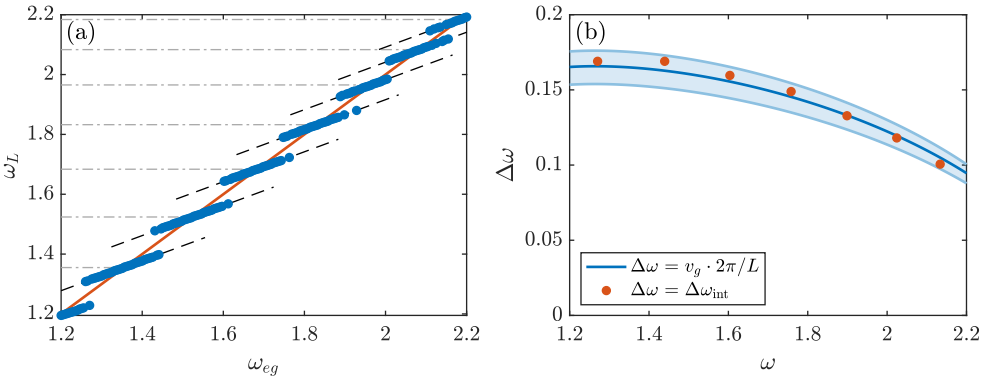

Figure 4.2: Numerical simulations of topological laser operation in a 15×15 Harper-Hofstadter lattice and $\Gamma = \gamma = 0.1$, up to a time $T = 500\,\Gamma^{-1}$. In panel (a), the blue dots represent the measured lasing frequencies obtained from a power spectral density analysis for different values of ω_{eg}. Each slant step is fitted with a black, dashed line with equation $\omega_L = \frac{1}{2}\omega_{eg} + b$. The light gray dash-dot lines mark the lasing frequency values for which $\omega_L = \omega_{eg} = \omega_0$ (see (4.9)), while the red line represents the approximated curve $\omega_L = \omega_{eg}$. In panel (b), we compare the mode spacing $\Delta\omega$ calculated from the difference between the intersections ω_{int} of adjacent steps in panel (a) (red dots) with the one obtained from the group velocity (blue line) as discussed in the text. All frequencies are measured in units of the hopping J, and the zero is at the bare cavity frequency ω_{cav}. The lasing frequency is extracted from the power spectral density of the emission that is obtained by a temporal Fourier transform of the light field amplitude in the latest $\Delta T = 150\,\Gamma^{-1}$ of the evolution.

gain via Kramers-Kronig causality relations: as usual, narrow resonances are responsible for quantitatively larger changes of the refractive index in their spectral neighborhood.

Let us explore the impact of this effect on topolaser operation for a narrowband gain centered inside the topological bandgap, thus perfectly overlapping with the edge state dispersion. In this case, one may naively expect that mode-pulling effects are irrelevant. The system is in fact expected to lase in the topological edge mode resonant with the gain for which the threshold is lowest. Since it is resonant, this mode does not experience any mode pulling — setting $\omega_0 = \omega_{eg}$ yields in fact $\omega_L = \frac{\omega_0 + \mathcal{S}\omega_{eg}}{1+\mathcal{S}} = \omega_{eg}$. In contrast to this expectation, the numerical experiment shown in Figure 4.2 shows that we actually have a richer physics due to the intrinsic discreteness of the modes.

In Figure 4.2(a) we have simulated a lattice with narrowband gain for multiple values of ω_{eg} and we have measured the steady-state frequency at which the system was emitting via a power spectral density analysis. While the measured

Frequency discretization & mode pulling

frequencies obey an *overall* approximate relation $\omega_L \sim \omega_{eg}$, that holds exactly only when ω_{eg} coincides with a lattice mode frequency ω_0 (light gray dash-dot lines), the reality is that ω_L is bound to assume only *discretized* values due to the periodic boundary conditions, as discussed in Section 3.4. In a broadband gain regime where mode-pulling effects are negligible ($\mathcal{S} \ll 1$), this would result in ω_L following a stair-like behavior as a function of ω_{eg}, with uniform spacing $\Delta\omega = v_g \cdot \frac{2\pi}{L}$ determined by the length L of the topological edge. Within each step, the emission frequency is locked to the one of the modes that is closest to resonance and for which gain is strongest. For a narrowband gain, the behavior is instead that of a *slant* stair and the slope of each of these slant steps is exactly $\frac{\mathcal{S}}{1+\mathcal{S}}$ (dashed lines). This results from the fact that ω_0 *cannot* continuously follow ω_{eg}, but it has to do so in steps, so it is actually *constant* in a certain frequency interval; then $\omega_L = \frac{\omega_0+\mathcal{S}\omega_{eg}}{1+\mathcal{S}}$ yields a behavior of type $y = a \cdot x + b$ with $a \equiv \frac{\mathcal{S}}{1+\mathcal{S}}$ and $b \equiv \frac{\omega_0}{1+\mathcal{S}}$. In the particular case $\mathcal{S} = 1$, we get $a = 1/2$ and $b = \omega_0/2$.

This also gives us the chance to quantitatively verify, in Figure 4.2(b), the relation between the spacing of the lasing frequencies and the group velocity of the topological edge mode in the presence of mode pulling. We can calculate the spacing between successive modes by just calculating the intersection frequencies ω_{int} between the fits of type $y = \frac{1}{2} \cdot x + b$ (dashed lines) and the line $y = x$ (red line) and then taking the difference $\Delta\omega_{\text{int}}$ between successive frequencies. We assign each value $\Delta\omega_{\text{int}}$ to the frequency at the center of its corresponding frequency interval; this first order approximation becomes exact for $L \to \infty$. From our periodic boundary condition argument, we should also have that the spacing between successive modes is $\Delta\omega \sim v_g \cdot \frac{2\pi}{L}$; as it's not clear how to treat the corner sites in the calculation of L, we show values ranging from $L = 4 \times 14$ to $L = 4 \times 16$ as a blue shaded area in the plot, with the solid blue line marking the value $L = 4 \times 15$.

The data shows a good agreement with respect to our predictions, highlighting the importance of including mode-pulling effects as well as the presence of mode discretization even in the narrowband case.

4.3 Broadband gain

In the previous Section, we have seen an efficient scheme to stabilize topolaser operation with a uniformly distributed gain, by spectrally concentrating the gain spectrum in the topological gap. While conceptually interesting, this scheme is hardly useful in practical semiconductor systems, where the gain linewidth is typically comparable if not larger than the width of the topological band gaps so that an efficient spectral selection of the edge mode from the neighboring bulk modes is hardly obtained.

In this Section we will explore a more sophisticated scheme that is able to stabilize topological lasing in a much wider range of parameters of potential technological relevance. The configuration we consider is inspired by the photonic

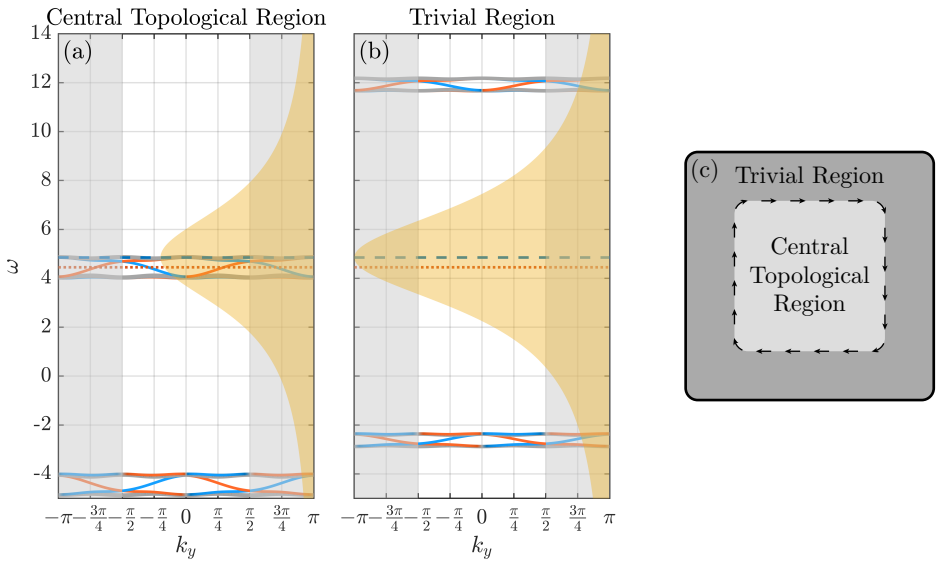

Figure 4.3: Panels (a)–(b): band structure for the proposed broadband scheme, with a geometry schematically depicted in panel (c). The central region (panel (a)) is a bipartite $\vartheta = 1/4$ Harper-Hofstadter lattice with checkerboard detuning $\Delta = 4.0$, while the surrounding region (panel (b)) has the same geometry with a larger checkerboard detuning $\Delta_{\text{trivial}} = 7.0$ and a global detuning $\omega_{\text{trivial}} = 4.65$ (red dotted line). The gain spectrum is centered at $\omega_{eg} = 4.85$ (blue dashed line) and has a FWHM linewidth $2\gamma = 5.2$ (yellow shading). The relative strength of gain on the two sides depends on $d = G_{\text{trivial}}/G$: for the specific case illustrated in the figure, the taller gain spectrum in panel (b) refers to a $d > 1$ case of stronger gain in the trivial region. The gray shaded areas indicate k_y-vectors outside the reduced Brillouin zone. For these parameters, the gain linewidth is around 8.2 larger than the width of the topological band gap of the central region and around 37% of the width of the trivial band gap in the surrounding region. It is around 63 times wider than the one considered in Figure 4.1.

crystal experiment in [29] where the topological band gap is orders of magnitude narrower than the gain linewidth. One of the aims of our work is to provide theoretical insight into the observed single-mode topolaser emission of this experiment.

4.3.1 Model and results

A sketch of the configuration under examination is shown in Figure 4.3(c). As in the experiment [29], we consider a central region, which has a narrow topological gap, surrounded by a region with a much wider and topologically trivial gap.

Chiral boundary modes are localized at the interface between the two regions. We also assume that the gain bandwidth is much larger than the narrow topological gap but comparable to the large trivial gap, as in the experiment, and that the gain is stronger in the trivial region than in the topological region. As a consequence, even though the gain material is pumped in a globally spatially uniform fashion we can expect clear topolaser operation in the edge states which partially penetrate into the trivial region with stronger gain, while lasing into the bulk states of the trivial region is suppressed by their detuning from the gain bandwidth. In this Section, we explain in detail how this idea works.

We first explain how we model a narrow and isolated topological gap in the central region. We start from the $\vartheta = 1/4$ Harper-Hofstadter lattice, which contains multiple topological band gaps with topological invariants adding up to zero. We want to isolate one topological band gap from these multiple gaps.

Checkerboard detuning

To this end, we add a checkerboard-shaped on-site frequency detuning $\pm\Delta$: the frequencies of the (m, n) sites are thus alternated and equal to $\omega_{\text{cav}} + \Delta \cdot (-1)^{m+n}$. The photonic bands of such a *bipartite* Harper-Hofstadter model are shown in panel (a) of Figure 4.3: because of the checkerboard detuning, the Brillouin zone is reduced to $k_y \in \left[-\frac{\pi}{2}, \frac{\pi}{2}\right]$ and the Dirac touching points between the middle two bands open into a trivial gap with size $\sim 2\Delta$. In agreement with the sequence $-1, +1, +1, -1$ of Chern numbers of the different bands, the two (small) gaps between the lower two bands and the upper two bands maintain their topological nature visible in the corresponding edge states. In what follows, we focus on the topological band gap of the two upper bands; the gain spectrum is centered around the frequency of the two upper bands. The two lower bands are, instead, off-resonant, and are not relevant in the laser operation and the discussion below.

Next, we explain how we prepare the surrounding region with a wide, trivial gap. We again start from the $\vartheta = 1/4$ Harper-Hofstadter model and add a checkerboard-shaped detuning Δ_{trivial}, which is larger than $\pm\Delta$ in the topological region. We add a global shift of all site frequencies by ω_{trivial} so that the large topologically trivial gap between the middle two bands is centered around the two upper bands of the topological region. The corresponding photonic bands are shown in panel (b). Although the two upper and two lower bands have narrow topological gaps, they are pushed away by the large Δ_{trivial}, and thus we can focus on the effect of the wide trivial gap between the middle two bands. We call this surrounding region a "trivial" region in this sense. The gain spectrum, which is indicated by the yellow shading in panels (a)–(b), is centered at the middle of the wide trivial gap and completely encompasses the topological gap in the central region.

Surrounding trivial region

The gain strength in the surrounding trivial region, G_{trivial}, can be reinforced either by locally increasing the pumping strength or, alternatively, by keeping a spatially uniform pumping but increasing the density of gain material with respect to the central region, as discussed in Chapter 2. Focusing on this latter case, which appears relevant for the experiment in [29], we can write $G_{\text{trivial}} = G \cdot d$, where d can be interpreted as the effective density of gain material in

Gain reinforcement in the trivial region

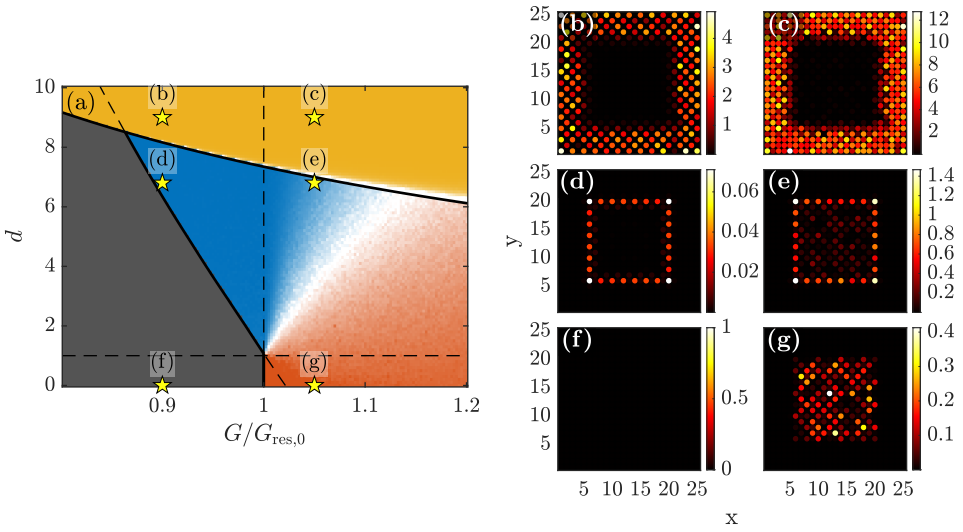

Figure 4.4: Result of simulations performed on a 25×25 lattice with a 5-sites thick surrounding region, configured as in Figure 4.3. Panel (a): phase diagram of the different lasing regimes as a function of the overall pumping strength $G/G_{\mathrm{res},0}$ and of the relative effective density of gain material of the surrounding region $d = G_{\mathrm{trivial}}/G$ for the same lattice parameters used in the dispersion plots shown in the top left panels. A gray color indicates no lasing; a blue color indicates lasing from the topological edge mode; a red color indicates lasing from the non-topological portion of the central region; a yellow color indicates lasing from the surrounding region. Fading to white indicates the coexistence of multiple phases. The thin dashed black lines indicate the $G/G_{\mathrm{res},0} = 1$ and $d = 1$ values. The solid and dot-dashed black transition lines between different phases are analytically predicted via the prescriptions in Section 4.3.4. The six yellow stars have a one-to-one correspondence with the six panels (b)–(g) presented on the right, showing sample snapshots of the real-space emitted intensity at the end of the integration time. The first, second, and third rows from the top are for decreasing values of $d = 9.0, 6.8, 0$ respectively. The left and right columns are for increasing $G/G_{\mathrm{res},0} = 0.90, 1.05$, respectively below and above the single-site resonant lasing threshold. All simulations have been performed by numerically integrating the Bloch-Harper-Hofstadter motion equations (4.5) up to a time $T = 10^4\,\Gamma^{-1}$.

the surrounding region relative to the central region, and treat $G/G_{\mathrm{res},0}$ as a global measure of the uniformly distributed pumping strength in units of the single-resonator resonant threshold.

The results of the numerical simulations are summarized in Figure 4.4, where

we show a phase diagram of the different regimes of laser operation as a function of the relative effective density of gain material in the surrounding region $d = G_{\text{trivial}}/G$ and of the pumping strength in the central topological region in units of the resonant, single-site threshold, $G/G_{\text{res},0}$.

Passive trivial region ($d = 0$)

When the surrounding trivial region is purely passive and does not display any gain ($d = 0$, Figure 4.4(f) and (g)), the system is almost equivalent to a bipartite 15×15 lattice without the surrounding region. We therefore expect the system to only lase above the resonant single-site lasing threshold, $G/G_{\text{res},0} = 1$, as shown by the red region at the bottom of the phase diagram. Since the gain is effectively broadband with respect to the upper pair of photonic bands in the central region, both bulk and boundary modes equally participate in the lasing process, forbidding a stable topological laser operation (panel (g)). Compared to the bulk states, boundary states are even slightly disfavored by the worse spectral overlap with the gain spectrum and by their evanescent tail that penetrates into the surrounding trivial region and reduces the spatial overlap with the gain region.

Monochromatic topological laser

We can induce lasing from the topological edge modes at the boundary by making the gain in the surrounding trivial region to be stronger than the one in the central topological region, that is $d > 1$. In this case, a region appears in the parameter space where the system displays a monochromatic topological laser behavior (panel (d)). Thanks to their evanescent tail overlapping with the stronger amplifying surrounding region, the effective threshold of the topological boundary modes is in fact pushed well below the one $G/G_{\text{res},0} = 1$ of the bulk modes (thick solid black line in the phase diagram), opening a window where only these modes can lase (blue region). In this $G/G_{\text{res},0} < 1$ regime, the monochromaticity of the topolaser emission is ensured by the same mode competition effects pointed out in [32] and reviewed in Section 4.2: since only topological edge modes experience a sufficient gain to lase and since these modes spatially share the same active medium, steady-state lasing ends up being concentrated in one of them only, thus making the emission monochromatic. A more detailed time-frequency analysis in support of this conclusion is reported in Section 4.3.2.

In order to better quantify the efficiency of our combined mode-selection scheme, we have investigated the constraints on the gain linewidth γ in order to have pure topolaser operation into the edge state. Quite interestingly, topolasing turns out to be robust as long as the effective gain experienced by the bulk bands in the trivial region remains below threshold. As it can be inferred from the discussion in Section 4.3.4, for sufficiently large Δ_{trivial} the upper bound on γ involves $\gamma/\Delta_{\text{trivial}}$ only. In particular, no restriction applies to the ratio of γ to the topological gap width. In the experiment of [29], the analog of Δ_{trivial} is way larger than the topological band-gap, which releases any constraint on the gain bandwidth compared to the topological gap and allows this latter to be arbitrarily small.

Note that this spectral structure is characteristic of the photonic crystal platform of [29] and is different from the typical one of the ring-resonator-based platforms considered in [55]. Here, additional copies of the band structure are in

fact present with a spacing set by the (relatively small) free spectral range of the single ring resonators and our mode-selection mechanism is not applicable in a straightforward way.

The situation is of course very different in the $G/G_{\mathrm{res},0} > 1$ case, when also the bulk modes of the topological region go above threshold. Since these modes have a reduced spatial overlap among them and with the edge mode, mode competition is no longer effective in ensuring a monochromatic emission and the latter acquires a complex multi-mode character (blue-to-white-to-red region). Still, thanks to the stronger gain of the surrounding trivial region, the intensity of boundary mode lasing can remain significantly stronger than the one of the central bulk modes even at values of G above the single-cavity lasing threshold (panel (e)).

For even higher values of the surrounding density d above the dash-dotted black line in the phase diagram, we reach a point where the spectral selection is no longer sufficient to suppress bulk lasing in the surrounding region and topological lasing is no longer possible. In this phase (yellow area in the phase diagram), the much stronger gain of the surrounding region makes the laser emission to be concentrated in this region (panels (b) and (c)).

A quantitative analytical discussion of the location of the transition lines in the phase diagram is given in Section 4.3.4. As expected, the area of the topological lasing region in parameter space can be increased by either increasing the trivial bandgap in the surrounding region or by using a narrower gain spectrum. This trend is confirmed by the additional numerical simulations with different values of the parameters that are shown in Section 4.3.3.

4.3.2 Time-frequency analysis of the lasing process

In this Section we discuss the spectral features of the lasing emission for the scheme presented in Section 4.3.1. As representatives for some of the different regimes identified in the phase diagram, we focus on three different parameter sets leading to the long-time snapshots of the emitted intensity shown in Figure 4.4(e),(d),(g). These parameters realize, respectively: a monochromatic topological laser, a multi-mode laser with a majority of the emission coming from a topological mode, and a non-topological multi-mode laser whose emission is due to the lasing of non-topological modes only.

The evolution of the system, numerically integrated up to $T = 500\Gamma^{-1}$ for the three different cases, is shown in Figure 4.5 as a time-frequency representation (TFR), where the color represents (in log scale) the spatially averaged amplitude of the smoothed pseudo Wigner-Ville distribution [89] (WVD) of field amplitude on individual lattice sites. In Figure 4.5(a)–(b) we focus around the relevant lasing frequencies for these cases; as a first observation, in the considered frequency interval the gain is effectively broadband (not shown). The band structure can also be used to classify the frequencies emerging from the TFR in panel (c), corresponding to a multi-mode laser in which, though, most of the emission is

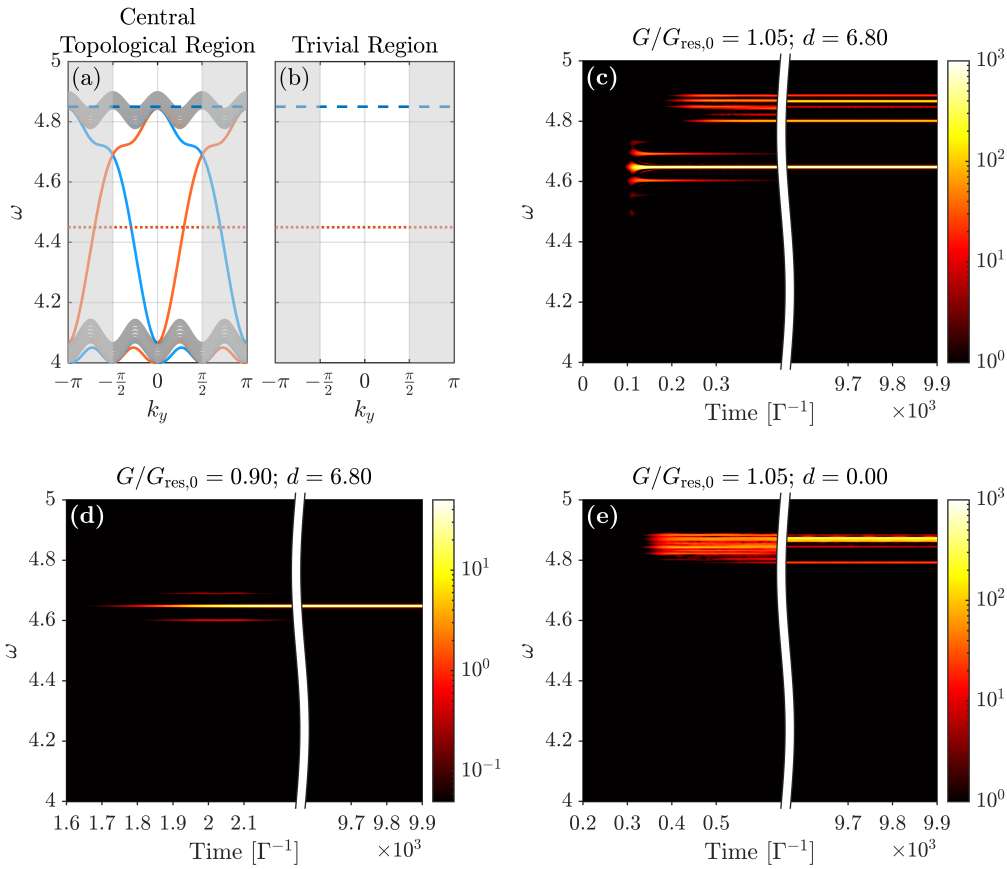

Figure 4.5: Time-frequency representation (TFR) of the lasing process, for the same parameters used in Figure 4.4(e),(d),(g). Panels (a)–(b): vertically zoomed-in view of the band structure shown in Figure 4.3(a)–(b). Panels (c)–(e): TFR for the same parameters as in Figure 4.4(e),(d),(g), respectively. The TFR is obtained by spatially averaging the smoothed pseudo Wigner-Ville distribution (WVD) of the field amplitude on individual lattice sites. The horizontal axis is broken so as to better focus on the initial and final moments of the time evolution; the WVD close to the limits of the temporal intervals of the transform is also removed, as it displays well-known unphysical artifacts due to border effects. The amplitude of the WVD is shown in log scale, color-coded according to the colorbar on the right of each panel; the colorbars span three orders of magnitude, and the ones in panels (c) and (e) are matched for reading convenience.

still coming from a topological edge mode. In this panel, the topological edge modes correspond to the well-separated horizontal features of the WVD falling inside the frequency range of the topological bandgap shown in panel (a). There are striking signatures of two distinct effects: the frequency discretization discussed in Section 4.2.2, and the well-known mode-competition. While due to the frequency discretization there are multiple topological modes that are able to ignite the lasing process, these modes spatially share the same active medium and therefore compete with each other until, at long enough times, only one of them is left.[59] The upper horizontal features, closer to each other, correspond instead to bulk modes located in the upper band of the central region; also in this case there are multiple modes that ignite the lasing process, but not all of them survive at long times.

If we turn off the surrounding trivial region (i.e. if we set $d = 0$, panel (e)), the modes in the topological bandgap are not able to ignite the lasing process and lasing occurs from the top band modes only. Note that the switch-on happens at a longer time, due to the fact that a surrounding trivial region with $d = 0$ creates an additional loss channel, especially for the modes that have a considerable overlap with the trivial region itself.

If instead we reduce $G/G_{\mathrm{res},0}$ below the lasing threshold of the bulk states (panel (d)) but we correspondingly increase d, we are able to prevent lasing from the bulk modes and only retain edge mode lasing at long times, thus obtaining a monochromatic topological laser. Due to the fact that the mechanism for providing the gain relies heavily, in this case, on the overlap of the edge mode tail with the trivial region (see Section 4.3.4), the switch-on is much slower than the previous cases.

4.3.3 Phase diagrams for different values of the gain linewidth

We show here additional simulations of the bipartite Harper-Hofstadter laser with the central topological region and the surrounding trivial region discussed in Section 4.3.1. In particular, we have pointed out in that Section that changing the gain linewidth reflects in a change of the area of the topological lasing region in the phase diagram. In Figure 4.6 we show simulations with an increased (top row) or reduced (bottom row) gain linewidth when compared to the value used in Figure 4.4.

For the increased (reduced) gain linewidth we take $2\gamma = 8.0$ ($2\gamma = 4.0$), to be compared with the value $2\gamma = 5.2$ used in Figure 4.4. With these settings, the gain linewidth is around $\times 12.5$ ($\times 6.3$) wider than the linewidth of the topological bandgap of the central region, so it is roughly 96 (48) times wider with respect to the topological bandgap than the gain linewidth shown in the narrowband case. The gain linewidth is also around 57% (29%) of the linewidth of the trivial bandgap in the surrounding region.

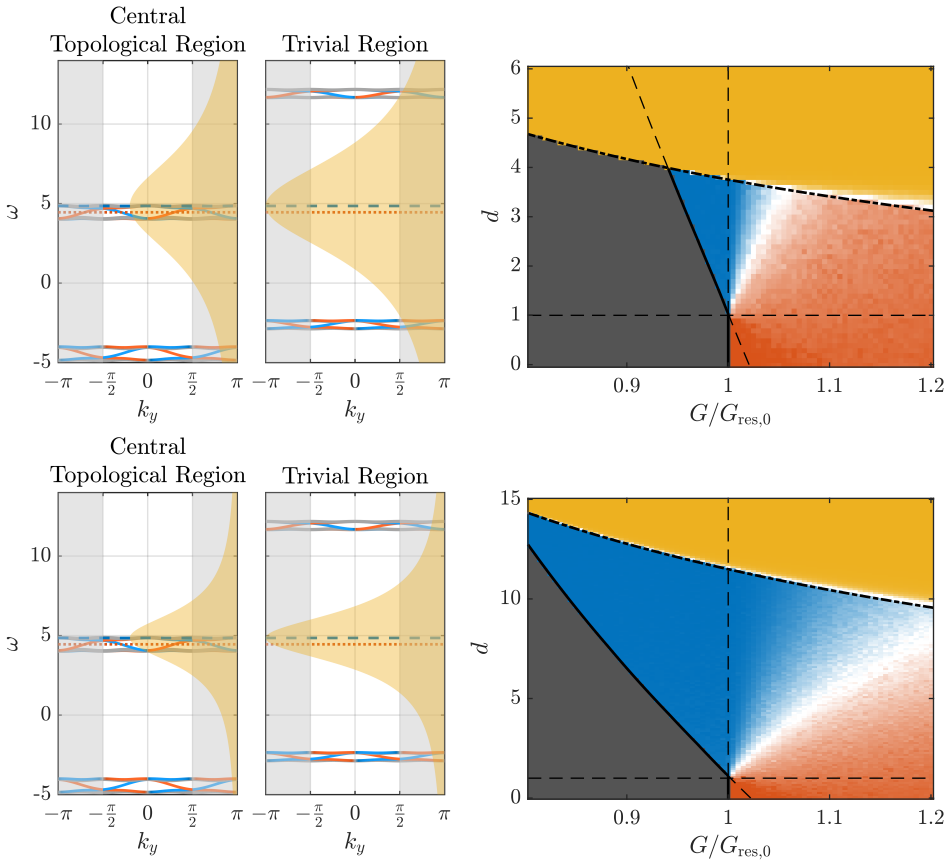

Figure 4.6: Simulations obtained on a 25×25 lattice with a 5-sites thick surrounding region with a trivial gap. (Left column) Band structure of the lattice. The central region has $\Delta = 4.0$, while the surrounding region has $\Delta_{\text{trivial}} = 7.0$ and $\omega_{\text{trivial}} = 4.65$ (red, dotted line). The gain is centered at $\omega_{eg} = 4.85$ (blue, dashed line). (Right column) Phase diagram of the different lasing regimes obtained from multiple simulations of equations (4.5) up to a long time $T = 10^4/\Gamma$ as a function of the density d of the surrounding region and the gain strength G. A gray color indicates no lasing; a blue color indicates topological lasing from the edge mode; a red color indicates lasing from the non-topological portion of the central region; a yellow color indicates lasing from the surrounding region. Fading to white indicates the coexistence of multiple phases. The panels on the two rows correspond to different values of the FWHM of the gain lineshape (yellow shading in the left panels), $2\gamma = 8.0$ (top), $2\gamma = 4.0$ (bottom). The solid and dot-dashed black lines in the phase diagrams indicate the analytical predictions in Section 4.3.4 for the transition between the different regions. The dashed black lines indicate $G/G_{\text{res},0} = 1$ and $d = 1$.

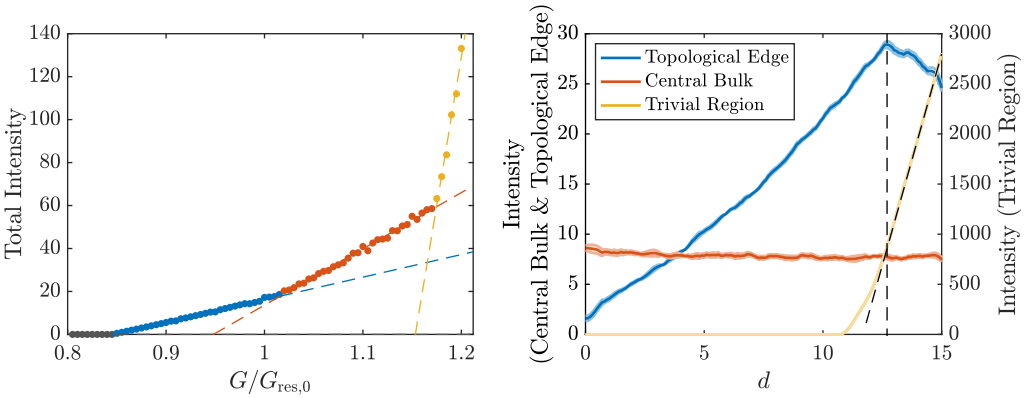

Figure 4.7: Emitted intensity along a horizontal (left panel) and a vertical (right panel) cut of the phase diagram shown in the bottom right panel of Figure 4.6. (Left panel) Total emitted intensity as a function of the gain strength $G/G_{\mathrm{res},0}$, at a fixed value of the density $d = 9.80$ of the surrounding region. The data has been classified into four color-coded groups, each fitted by a (accordingly colored) straight dashed line. Grey indicates no lasing, blue indicates lasing from the topological edge, red from the topological edge and the central bulk, and yellow from topological edge, central bulk, and the surrounding region. (Right panel) Emitted intensity by each spatial region as a function of the density d of the surrounding region, for a fixed value $G/G_{\mathrm{res},0} = 1.06$ of the gain strength. The intensity has been averaged in time for the last 1% of the simulation, with the shaded areas corresponding to one standard deviation from the mean. The vertical dashed line marks the peak of the topological edge emission, while the oblique straight dashed line is a fit of the right-most part of the emission from the surrounding region.

When using this increased/reduced gain linewidth, the area of the region of parameters that yields a topological laser shrinks/widens; in particular, the upper transition line (which describes the lasing threshold of the surrounding region) is extremely sensitive to the linewidth of the gain. It is possible to predict in advance the effects of such a reduced/increased gain linewidth on the phase diagram by a direct calculation of the transition lines — see Section 4.3.4.

It is also instructive to explore the phase diagram, with respect to the emitted intensity, along both a vertical and a horizontal cut; we do that in Figure 4.7 for the bottom right phase diagram of Figure 4.6.

If we fix the effective density of gain material d of the surrounding region at some value $d = 9.80$ and we plot the emitted intensity vs $G/G_{\mathrm{res},0}$ (left panel of Figure 4.7) we notice that the data can be grouped in four sets, each one fitting a distinct linear branch. The fitted linear branches highlight the presence of three thresholds: the first one for the topological edge, the second one for the central

bulk and the third one for the surrounding region.

We can also explore the emitted intensity along a vertical cut of the phase diagram, i.e. as a function of the density d of the surrounding region for a fixed value of the gain strength $G/G_{\text{res},0} = 1.06$; for the sake of clarity, it is best to separate the emission from the topological edge region (blue), from the central bulk (red), and from the surrounding region (yellow). First of all, we have to make a crucial observation: the scale of the emission from the surrounding region (right vertical axis) is two orders of magnitude bigger than the scale of the topological edge and the central bulk (left vertical axis). This means that if we look at real-space snapshots of the system when the surrounding region is lasing — e.g. Figure 4.4(b)–(c) — we get the wrong impression that the rest of the system (i.e. the central bulk and topological edge) is not lasing; the rest of the system *is* indeed lasing, but the value of the emitted intensity is negligibly small when compared to the one emitted from the surrounding region.

The other crucial observation is that the plot shows clear evidence that the topological edge is indeed lasing by exploiting the unused amplification in the surrounding region. First of all, after the surrounding region is above threshold, its emitted intensity has a non-linear ramp-up as a function of the density. This is due to the fact that, as one increases the density of the surrounding region, more and more modes from the surrounding region reach the lasing threshold. The first ones to lase are localized in the bulk of the surrounding region; however, at higher densities, the modes from the surrounding region localized on the border reach the lasing threshold as well. These modes, due to their sizable shared overlap, are in direct competition with the topological edge mode that is lasing in the central region; thus the emitted intensity of the latter starts decreasing (marked by a vertical dashed line in the plot).

4.3.4 Transition lines in the phase diagram

As pointed out in Section 4.3.1, the topological edge mode is able to lase thanks to an amplification leak from the surrounding region. This leak can be quantified and used to analytically determine the transition lines of the phase diagrams in Figure 4.6 and Figure 4.4(a) without having to resort at all to dynamical simulations.

The first ingredient is the knowledge of the energy spectrum and of the spatial structure of the eigenmodes of the lattice Hamiltonian, which we call H_{bare}:

$$H_{\text{bare}}\psi_i = E_i\psi_i, \tag{4.10}$$

where E_i is the energy corresponding to the mode with normalized wavefunction ψ_i, and ψ_i can be thought of as a matrix in position space, i.e. $\psi_i = (\psi_{i;m,n})$, with m and n respectively the x- and the y-index.

At this point we can define some spatial masks M_{topo}, M_{bulk} and M_{trivial}; these masks are matrices in position space and contain 1 in the entries representing points belonging to, respectively, the topological edge, the bulk of the central

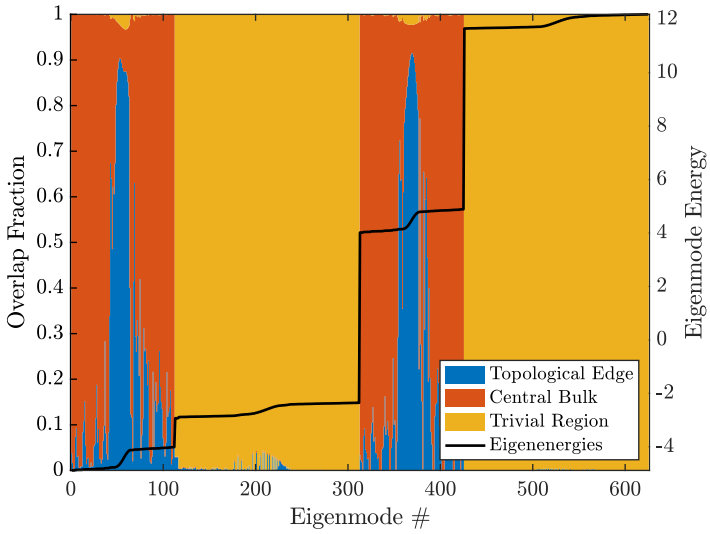

Figure 4.8: Overlaps S_{topo}, S_{bulk} and S_{trivial} of each eigenmode with the different regions (colored shading, left vertical axis) and energies E_i of the eigenmodes (solid black line). The calculations have been performed on the same 25×25 lattice geometry considered in Section 4.3.1.

region and the surrounding region, and zero elsewhere. These masks are the same ones used to calculate the emitted intensity overlaps in the phase diagram, and also allow us to calculate the overlap of a given wavefunction with these three spatial regions of the system, e.g. to calculate the overlap $S_{\text{topo},i}$ of the wavefunction ψ_i with the topological edge:

$$S_{\text{topo},i} = \sum_{m,n} |\psi_{i;m,n}|^2 \cdot M_{\text{topo};m,n}. \tag{4.11}$$

For a given wavefunction ψ_i the overlaps with the three regions sum to 1 since the wavefunction is normalized, i.e. $S_{\text{topo},i} + S_{\text{bulk},i} + S_{\text{trivial},i} = 1$. The overlaps of each mode can be visualized as in Figure 4.8.

The overlaps are useful to determine what is the *effective* amplification $G_{\text{eff},i}$ experienced by a given mode ψ_i as compared to the global parameter G characterizing the gain strength. For a completely flat gain profile, if all the system regions have the same density of the bulk, then $G_{\text{eff},i}/G = 1$ because the overlaps of any given wavefunction with the three regions of the system sum to 1. However, if we change the density d of the surrounding region, this ratio will be in general $G_{\text{eff},i}(d)/G = f_i(d) = S_{\text{topo},i} + S_{\text{bulk},i} + d \cdot S_{\text{trivial},i}$. If $d > 1$, then $f_i(d) > 1$ and it acts as an *enhancement factor* for the amplification of that mode.

If the gain is not flat but has e.g. a Lorentzian profile, as in our case, the expression of $f_i(d)$ in terms of wavefunction overlaps has to be modified. Namely, we have to add an extra Lorentzian factor

$$\mathcal{L}_i = \frac{1}{1 + \left(\frac{\tilde{E}_i - \omega_{eg}}{\gamma}\right)^2} \tag{4.12}$$

that is equal to 1 at zero energy detuning and falls to 0 at large energy differences. Analogously to Section 4.2.2, the energies $\tilde{E}_i$ are here corrected with respect to E_i in order to take into account the mode pulling, i.e.

$$\tilde{E}_i = \frac{E_i + \mathcal{S}\omega_{eg}}{1 + \mathcal{S}}, \qquad \mathcal{S} = \frac{\Gamma}{\gamma}. \tag{4.13}$$

Here, the mode pulling correction has the effect of increasing the value of $\mathcal{L}_i$ as compared to a Lorentzian factor calculated with the non-pulled energies E_i. So, the overall enhancement factor will be

$$f_i(d) = \frac{S_{\text{topo},i} + S_{\text{bulk},i} + d \cdot S_{\text{trivial},i}}{1 + \left(\frac{\tilde{E}_i - \omega_{eg}}{\gamma}\right)^2}. \tag{4.14}$$

With these ingredients, we are ready to calculate the transition line between the not-lasing region and the different lasing regions, starting with the one corresponding to a topological laser. The first mode to lase, i.e. the mode that determines the threshold, will be the mode with the largest effective amplification, i.e. with greater $f_i(d)$. That mode will have an enhancement factor equal to

$$\bar{f}_{\text{topo}}(d) = \max_{i\,:\,S_{\text{topo},i} > \varepsilon_{\text{topo}}} f_i(d). \tag{4.15}$$

Since we are looking for the lasing threshold among the topological edge modes, we take the max over the modes that have an overlap $S_{\text{topo},i}$ with the topological edge greater than a certain threshold $\varepsilon_{\text{topo}}$, e.g. $\varepsilon_{\text{topo}} = 0.80$. Similarly, to find the second transition line at which the surrounding region starts to lase, one defines

$$\bar{f}_{\text{trivial}}(d) = \max_{i\,:\,S_{\text{trivial},i} > \varepsilon_{\text{trivial}}} f_i(d). \tag{4.16}$$

Note that the mode that maximizes the enhancement factor depends on the specific d being considered. A more crude approximation not involving a maximization over the modes, but that still provides very good results, would be to define e.g. $\bar{f}_{\text{topo}}(d) = f_{i_{\text{topo}}}(d)$, where i_{topo} is the index of the topological edge mode that lases more frequently just above threshold in the time-domain simulations; i_{topo} is then independent on the choice of d. A similar consideration holds for $\bar{f}_{\text{trivial}}(d)$ as well.

In general, the threshold for lasing into a given mode is reduced by the same factor f_i characterizing the enhanced effective amplification as compared to the

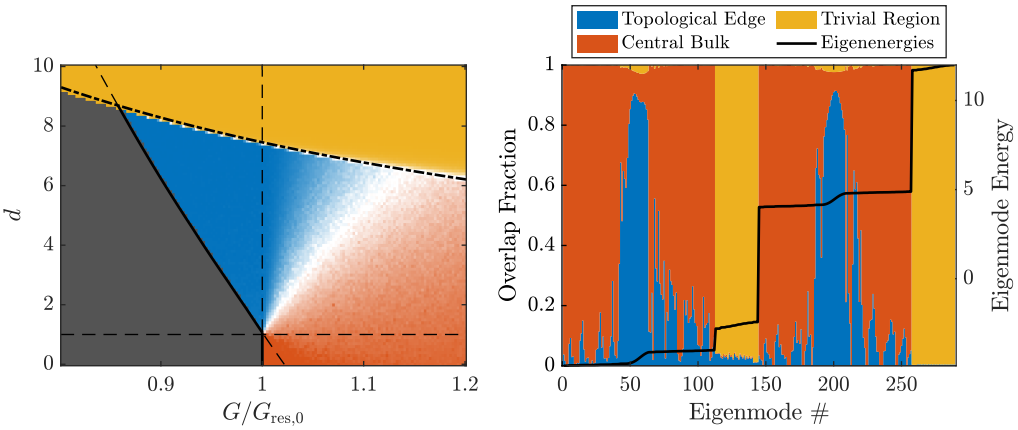

Figure 4.9: Calculations performed on a 17×17 lattice geometry obtained from a 15×15 lattice surrounded by a 1-site-thick trivial region. All the other parameters are equal to the ones used in Section 4.3.1. (Left) Transition lines of the considered 17×17 geometry with a 1-site-thick surrounding region on top of the phase diagram obtained with a 5-sites-thick surrounding region — identical to the one shown in Figure 4.4(a). (Right) Overlaps S_{topo}, S_{bulk} and S_{trivial} of each eigenmode with the different regions (colored shading, left vertical axis) and energies E_i of the eigenmodes (solid black line).

$d = 1$ case for which the threshold is at $G/G_{\mathrm{res},0} = 1$. As a result, the transition lines we are looking for are simply described by the equations

$$d = \frac{1}{\bar{f}_{\mathrm{topo}}(d)} \qquad \text{and} \qquad d = \frac{1}{\bar{f}_{\mathrm{trivial}}(d)}\,. \tag{4.17}$$

Both transition lines carry a dependency on γ, mediated by the Lorentzian factor in $f_i(d)$. However, the transition line between the not-lasing and the topo-lasing regimes has a much weaker dependence. The reason is that, by construction, the topological edge modes are much closer to the center of the Lorentzian than the bands in the surrounding region. Since this detuning contributes quadratically to the position of any transition line, the transition line involving modes farther from the gain center is therefore much more sensitive to γ itself.

As a final note, this calculation also allows us to easily determine the lasing thresholds when we vary the thickness of the surrounding region. The system considered in Section 4.3.1 has a 5-sites-thick surrounding region; in the left panel of Figure 4.9 we show again its phase diagram, but we calculate the transition lines of an otherwise identical system which differs by having a 1-site-thick surrounding region. There is a discrepancy between the two, albeit extremely small, which shows that a bare minimum 1-site-thick surrounding region is already enough to open a topological lasing region in the phase diagram. Already with a 2-

sites-thick surrounding region even this small discrepancy disappears, and the transition lines become virtually indistinguishable from the 5-sites-thick case.

The fact that a 1-site-thick surrounding region is already sufficient comes from the fact that the topological edge modes we want to enhance have an overlap with the surrounding region that is mainly concentrated in the surrounding sites closest to the edge itself, i.e. in the system region covered by a 1-site-thick surrounding region. As can be inferred by comparing the overlap fractions shown in Figure 4.8 and in the right panel of Figure 4.9, the positive-energy topological edge modes have an overlap with the surrounding region that's at best around 2.3% both when the surrounding region is 1-site-thick and when it's 5-sites-thick, thus contributing around the same enhancing factor in the calculation of the thresholds.

4.4 Discussion

In the previous Sections, we have concentrated our attention on a Harper-Hofstadter model which provides a relatively straightforward insight into the basic effects, but our conclusions extend to any combination of lattices with suitable spectral and topological properties. In particular, we expect that our physical conclusions extend even outside the tight-binding approximation that has been made in all theoretical studies of topological lasing so far.

As a most intriguing example, the results of our calculations are compatible with some key observations of the pioneering experiment in [29] that, to the best of our knowledge, remain so far unexplained. In particular, topological lasing was observed in this experiment without the need to concentrate gain along the edge separating the topological and trivial regions, as it was instead the case in other experiments [55, 56]. A key difference between the devices used in these works consists in that the topological system used in [55] is surrounded by empty space, while in [29] the central topological system is surrounded by a topologically trivial region where the field can penetrate with a significant evanescent tail. Most importantly for our purposes, the outer region displays a larger filling factor of the unit cell (compare Figs. 2A and 2B in [29]). For an equal level of optical pumping, we can thus reasonably expect the gain to be stronger in the outer region, which corresponds to $d > 1$ in our model. As a result, the overlap of the edge state with this stronger amplifying region favors topological lasing with respect to bulk lasing in the central region. At the same time, the much wider extension of the trivial photonic band gap of the outer region forbids laser operation in the outer region thanks to the natural frequency-dependence of gain in the used semiconductor quantum well material.

While these arguments provide a suggestive interpretation of experimental observations, they are of course not yet completely sufficient to rule out other possible explanations. For instance, in analogy to the arguments put forward in [57] for a different geometry, another potentially relevant mechanism for stabilizing the edge mode lasing could originate from the weaker losses of the edge mode compared to the ones of bulk modes [87]. In the specific system of [29],

reduced radiative losses may in fact originate from the evanescent tail in the outer trivial region, where bulk modes in the vicinity of the trivial gap are below the light cone. In our model theory, the reduced radiative losses of the trivial region could be explicitly included via a reduced Γ of the outer sites, but we expect their effect to be similar to the one of the increased gain G_{trivial} considered in our calculations. On this basis, we are confident that the qualitative conclusions of our theory directly apply to the experiment. However, a firm and definitive unraveling of these questions requires accurate experimental measurements and comprehensive microscopic calculations of the band structure and of the radiative and non-radiative decay rates of the different modes [87], which go beyond this work.

As a final point, it is worth briefly mentioning some straightforward experiments that may serve to shed light on the possible interpretations of the experimental observations even in the absence of a direct measurement of the Q factor of the different modes. In the IR spectral region of the experiment, magnetic effects are quite weak, as signaled by the smallness of the topological gap. This implies that the magnetic field is crucial to induce the topological edge state, but has a minor effect on the bulk regions. As a result, according to our theory, in the absence of any magnetic field no laser operation should be observed up to powers well above the topological laser threshold. Some evidence in this direction is found by comparing Figs. 3B and 3C of [29]. Further experimental insight could be obtained by keeping the magnetic field on and ramping up the pump intensity well above the topological laser threshold. According to our model, as discussed in Section 4.3, going up in gain strength G should move the system from the topological lasing region indicated in blue into the ones of multi-mode bulk lasing indicated in red/yellow. In particular, we expect that the threshold for bulk lasing at high gain strengths should be almost insensitive to the applied magnetic field.

4.5 Conclusions

In this Chapter we have investigated the effect of a frequency-dependent gain on a Harper-Hofstadter topological laser by simulating, at each cavity, the full frequency-dependent semiclassical laser theory developed in Chapter 2.

While in the case of broadband gain a spatially uniform pumping scheme (WSG) is not able to select a single lasing mode (see Section 3.3), in the case of a narrowband gain it's possible to select a topological edge mode by using TLAs with a transition energy tuned in the topological bandgap, as shown in Section 4.2.

In Section 4.3 we have then shown that, by combining this standard spectral selection mechanism with a suitable design of a topological cavity that takes into account the natural spatial distribution of the boundary modes and their overlap with the gain medium, it's possible to promote a topological edge mode to a

lasing mode even in a WSG configuration with a gain linewidth several times larger than the topological bandgap.

Based on our theory, we have proposed an interpretation of the recent experiments in [29], where stable topolaser emission was observed in spite of the gain being distributed across the whole photonic crystal structure and not localized on the topological edge as in [55], and at the same time being much larger than the topological bandgap.

In addition to offering additional validation of the experimental results in [29], our work can be applied to simplify the design and operation of topological lasers by allowing for smaller cavity designs and by lifting the need to precisely control the spatial location of the pump spot, thus helping to bridge the gap to a commercial-grade generation of topological lasers.

Chapter 5

Conclusions

In Part I we investigated the laser operation and the mode-selection mechanisms of topological lasers via a semiclassical analysis.

Our primary investigation tool was the numerical simulation of coupled differential equations obtained from the semiclassical theory of lasers, derived in Chapter 2 via a mean-field treatment of actively pumped atoms embedded in a single-mode cavity, that we chose as a simple model of light-matter interaction. The equations provide the time evolution of the macroscopic electric field and the populations of the atomic levels, as well as of the atomic coherence, linked to the macroscopic polarization. Their steady-state analysis reveals that the gain has a Lorentzian profile in frequency space, which favors the amplification of modes at frequencies closer to the atomic transition energy.

In several circumstances, however, the gain linewidth is so large compared to the relevant system bandwidth that the gain itself can be considered uniformly distributed in frequency space. In this limit, called the broadband limit, the equations of the semiclassical theory of lasers reduce to a single equation describing the evolution of the macroscopic electric field.

The broadband limit was employed in Chapter 3 in order to characterize the topological laser operation. We performed a numerical analysis of a topological laser based on the Harper-Hofstadter model, after a brief introduction on the lattice model itself. We highlighted crucial consequences of the chirality of the lasing edge modes, such as a sharp dependence of the lasing threshold on the geometrical shape of the amplifying region and the possibility of ultraslow relaxation times and of convectively unstable regimes. The different unstable regimes were characterized in terms of spatio-temporal structures sustained by noise, and

we showcased the strong amplification of a propagating probe beam in between the convective and the absolute (lasing) thresholds. We pointed out that, when the gain is distributed along the whole edge, topological lasers still suffer from the mode discretization commonly found in ring lasers and due to the periodic boundary conditions. Along the Chapter, we also discussed the robustness of topological laser operation against static disorder.

In Chapter 4, instead, we investigated the mode-selection mechanisms that are beneficial in order to promote lasing from a topological edge mode. In order to do so, we simulated the full coupled equations of the semiclassical theory of lasers. We first reviewed the case of a narrowband gain, i.e. with a linewidth smaller than the topological bandgap; in this case, even when the gain is spatially uniform, lasing from a topological edge mode can be promoted by working between two effective atomic levels of the gain medium with an energy separation that lies in the topological bandgap. In this regime, we also pointed out how the mode discretization identified in the previous Chapter is affected by mode-pulling.

In experimental settings, however, the gain linewidth is typically several times larger than the topological bandgap, becoming effectively broadband; it may then naively seem that, without a spatially-selective pumping like the one used in Chapter 3, it's not possible to obtain a topological laser. Motivated by the puzzling experimental results of [29], we proposed a cavity design that, even without a spatially-selective pumping, can still perform a spatial mode selection in tandem with spectral selection effects. Namely, we surrounded the original topological lattice with a trivial lattice; the trivial lattice was designed so to have a wide trivial bandgap, whose center was approximately around the topological bandgap of the inner lattice. The bulk bands of the trivial lattice were then spectrally excluded by using a gain linewidth smaller than the trivial bandgap, though such linewidth could still be several times larger than the topological bandgap, as in typical experimental settings. The gain material density in the trivial region was also chosen to be larger than the one in the topological region. Finally, the system was pumped below the original lasing threshold of the bulk modes of the topological region; while those bulk modes could not lase, the topological edge modes could experience a gain enhancement thanks to their sizable evanescent tail overlap with the denser trivial region, thus becoming lasing modes and realizing a topological laser. The gain enhancement experienced by the topological edge modes could persist even at moderate pumping powers above the lasing threshold of the bulk modes, with sizable improvements compared to the same system without an external trivial region.

Despite the fact that we did not explicitly model a photonic crystal and that we used different lattice models, our results are in qualitative agreement with the pioneering experimental observations in [29], offering a viable explanation for the physics at play in the experiment. After having worked here on this underlying, general mechanism, the next natural step in our investigation will be the experimental verification of our findings, as well as to take advantage of this physics in order to improve the design of new topolaser devices.

Part II

Driven-dissipative quantum systems: exploring nonlinear photonic systems via out-of-equilibrium dynamical mean-fields

Chapter 6

Introduction

The study of the quantum many-body problem has gained, in the last decade, considerable traction. This push was motivated both by the desire to answer fundamental questions and by the possibilities of exploiting new quantum technologies, and went hand in hand with the tremendous experimental advances.

The circuit QED platform [90–99], in particular, has attracted remarkable interest as a platform for quantum many-body physics. Not only its constituent superconducting circuits, originally developed for quantum computing purposes, feature long coherence times, single-photon nonlinearities and considerable scalability, but the platform itself allows a broad degree of flexibility in the system geometry design and in the light-matter coupling [100]. In this platform, the photons experience an effective interaction due to the presence of Josephson junctions [93, 99, 101, 102]; nowadays, transmon qubits (capacitively shunted Josephson junctions) are typically used as nonlinear lattice sites, due to their exponentially increased dephasing times compared to standard charge qubits [103].

Employing photonic systems as platforms for the study of many-body problems has also advantages in terms of ease of introduction of driving and dissipation. In contrast to the general understanding, until recently, that photonic systems would preclude the realization of strongly-correlated many-body states due to the presence of large losses, the idea of dissipation engineering [104–107] has been harnessed as a convenient tool for the preparation of such states, employed in the first experimental demonstration of a dissipatively stabilized Mott insulator of photons [98].

Despite the recent efforts devoted to the study of non-equilibrium many-body phases and non-equilibrium phase transitions [4, 13, 108–116], the general pic-

ture on driven-dissipative many-body quantum systems is still incomplete. As an example, it is not clear yet to what extent the many-body states prepared via dissipative stabilization map to their equilibrium counterparts, and how the critical behavior is affected in the presence of drive and dissipation [100]. The resulting need for deepening our understanding of the driven-dissipative many-body quantum problem vehemently calls, therefore, for the development of new, powerful numerical methods. This is especially true in the context of bosonic systems, in which the Hilbert space can reach intractable dimensions even for very small systems, and in that of strongly-correlated systems, which cannot be properly treated with standard mean-field techniques and require more careful handling of correlations.

In this Part, as a consequence, we work to advance the understanding of driven-dissipative strongly-correlated quantum systems by employing a technique known as Dynamical Mean Field Theory (DMFT), originally developed for strongly-correlated electron systems but extended to other classes of systems over the past decade.

We start our discussion in Chapter 7, where we introduce the Lindblad equation as a primary tool for the investigation of driven-dissipative quantum systems. We review its diagonalization in the superparticle representation, as well as the Keldysh formalism for the calculation of response functions, for which we provide numerically relevant expressions in the superparticle representation.

In Chapter 8, we employ the Exact Diagonalization (ED) technique on the Lindblad equation in order to investigate the signatures of a putative localization-delocalization transition in a driven-dissipative BHD, which can be seen as a fundamental building block in the study of driven-dissipative quantum many-body systems. We harness the technical tools introduced in Chapter 7 in order to study both the quantum dynamics and the steady-state, as well as the spectral properties encoded into the single-particle response functions of the system, discussing the interplay between the coherent evolution and the dissipative setting.

In Chapter 9 we take a further leap in complexity, focusing instead on the analysis of a driven-dissipative lattice with strong correlations, in the thermodynamic limit. Before delving into the analysis of the system, we briefly review the main concepts at the heart of the DMFT technique and, employing the toolbox gathered in Chapter 7, we build the "engine" of our DMFT calculation for driven-dissipative quantum many-body problems, based on ED. The lattice system is then simulated in the presence of strong two-particle dissipation, which leads to the emergence of hard-core bosons and to a driven-dissipative analog of the quantum Zeno effect.

Finally, in Chapter 10, we present a summary of the main results obtained in Part II.

Chapter 7

Technical background

In this Chapter we review the basic concepts and techniques that we will use throughout Part II of the Thesis.

We start in Section 7.1 by reviewing the Lindblad equation and in Section 7.2 by introducing the formalism of the superboson representation used to vectorize the Lindblad equation [117], while in Section 7.3 we go over the Keldysh formalism used for the calculations of out-of-equilibrium response functions. Finally, in Section 7.4 we derive the Källén-Lehmann representation of the response functions used in the numerical calculations.

We will keep the treatment of these prerequisites to the level of a functional knowledge, pointing the interested reader to more in-depth resources, as a full treatment of these topics goes beyond the scope of this Thesis. Additionally, as a common thread throughout the whole Chapter, we will provide a practical application of these tools by analyzing the basic building block of a single cavity in thermal equilibrium, that will be of fundamental importance in the following Chapters.

This Chapter owes much to the treatment of the analogous fermionic case in [117], and it follows it closely. The reader familiar with the Lindblad equation and with the Keldysh formalism can safely skip this Chapter without fears of compromising the logic flow of the discussion, and refer back to it only when strictly necessary in the following ones.

7.1 Lindblad equation

7.1.1 Generalities and interpretation

The so-called Lindblad equation [118] is nowadays the basic tool used to investigate open Markovian quantum systems. We have indeed already used the equation in Part I, and in this Section 7.1 we review the basic ideas and we provide an intuitive grasp of the formalism, referring to previous works [62, 80, 117, 119–121] for a formal proof of the derivation.

The Lindblad equation originates from the problem of studying a system of interest (S) connected to a bath (B), that live in a total (T) Hilbert space [122]

$$\mathcal{H}_T = \mathcal{H}_S \otimes \mathcal{H}_B \tag{7.1}$$

The total dynamics in the system is described by the Schrödinger equation obtained from the total Hamiltonian H_T, or alternatively by the equivalent Liouville equation for the density matrix:[1]

$$\dot{\rho}_T(t) = -i\left[H_T, \rho_T(t)\right], \tag{7.2}$$

where we've used $\hbar = 1$ and the dot notation for the time derivative.

So far, no approximation has been made. However, since we are typically interested in the system (S) only, we would like to trace out the bath (B) so to gather info just on the traced-out density matrix for the system:

$$\rho \doteqdot \rho_S = \mathrm{Tr}_B\, \rho_T, \tag{7.3}$$

where the trace is performed over the bath degrees of freedom. Under the Markov approximation (plus some auxiliary ones), i.e. under the assumption that the bath responds instantaneously to changes in the system, the equation for the traced-out density matrix ρ can be written as

Lindblad equation

$$\dot{\rho}(t) = -i\left[H, \rho(t)\right] + \mathcal{L}_D\left[\rho\right] \doteqdot \mathcal{L}\rho, \tag{7.4}$$

where in general H commutes with the Hamiltonian of the system of interest (S) — can be H_S itself — and [119]

Lindblad dissipator

$$\mathcal{L}_D\rho = 2 \sum_{i=1}^{\dim(\mathcal{H}_S)^2-1} \gamma_i \left(L_i \rho L_i^\dagger - \frac{1}{2}\left\{ L_i^\dagger L_i, \rho \right\} \right) \tag{7.5}$$

is called the *Lindblad dissipator*, with γ_i are non-negative coefficients. The operators L_i are called *jump operators*, and describe exchange processes between the reduced system and the bath that has been traced out. Throughout this

[1] The density matrix is the operator counterpart of a quantum state, i.e. it provides us with complete information about the state of a system. If the system is a pure state $|\psi\rangle$, the density matrix is indeed $\rho = |\psi\rangle\langle\psi|$; in general, instead, the density matrix can be written as $\rho = \sum_{ij} \rho_{ij} |\psi_i\rangle\langle\psi_j|$, with the condition $\mathrm{Tr}\,\rho = \sum_i \rho_{ii} = 1$ coming from the normalization of probabilities.

work we will call the *superoperator* $\mathcal{L}$, i.e a functional over the space of operators that according to eq. (7.4) encompasses both the Hermitian evolution and the Lindblad dissipator itself, the *Lindbladian*.[2]

Lindbladian

After having introduced the Lindblad equation, let's comment on its physical meaning. We do so by focusing on the simplest yet ubiquitous and perhaps most important example, i.e. the harmonic oscillator — that, since we work in the context of optics and photonics, we simply call a *single-mode cavity*.

Example: lossy single-mode cavity

The Hamiltonian for a single-mode cavity is simply

$$H = \omega_{\text{cav}} a^\dagger a, \tag{7.6}$$

where a ($a^\dagger$) destroys (creates) a photon with energy ω_{cav}. The lossy version of the single-mode cavity can be naively seen as having the same Hamiltonian above, in which we just allow for an extra imaginary part in the bare cavity frequency:

$$H = (\omega_{\text{cav}} - i\Gamma)\, a^\dagger a, \qquad \Gamma \geq 0. \tag{7.7}$$

To see why this should give a dissipative system, we can try for example to write the equation for the total number of photons $N = a^\dagger a$ in the limit of large N; from the Heisenberg equation for a, we get

$$\dot{a} = (-i\omega_{\text{cav}} - \Gamma)\, a \qquad \Longrightarrow \qquad a = a_0 e^{-i\omega_{\text{cav}} t} e^{-\Gamma t}, \tag{7.8}$$

that gives $N = N_0 e^{-2\Gamma t} \underset{t\to\infty}{\longrightarrow} 0$.

We now have a situation in which the Hamiltonian is not Hermitian anymore, but has a Hermitian part — that we call $H_+ = \omega_{\text{cav}} a^\dagger a$ — and an anti-Hermitian part — that we call $H_- = -i\Gamma a^\dagger a$. As a general fact, from the Schrödinger equation one immediately obtains that the Liouville equation associated to an operator $H = H_+ + H_-$ containing both a Hermitian and an anti-Hermitian part is

$$\dot{\rho}(t) = -i\,[H_+, \rho(t)] - i\,\{H_-, \rho(t)\}\,. \tag{7.9}$$

By explicitly using the expression for our anti-Hermitian term in the example of the single-mode cavity, we get

$$\dot{\rho}(t) = -i\,[H_+, \rho(t)] - \Gamma\left\{a^\dagger a, \rho(t)\right\}, \tag{7.10}$$

that starts to look like equations (7.4) and (7.5) when one identifies $\gamma \equiv \Gamma$ and $L \equiv a$. Since we've said that this is a lossy system and a is a one-photon operator, $L = a$ is the kind of jump operator that describes *single-particle losses*.

Single-particle losses

[2] It's also common, in the literature, to see the name "Liouvillian" to indicate what we call here "Lindbladian". However, in our opinion, the name "Liouvillian" can be ambiguous, and we opted instead for a name — still present in the literature [123–127] — that immediately makes the presence of a Lindblad dissipator clear.

We've said before that the Hamiltonian we've written for the lossy single-mode cavity is naive — although very useful in practice — since it doesn't preserve the trace of the density matrix. Indeed, if we take the trace of (7.9), we get that

$$\frac{d}{dt}\operatorname{Tr}\rho(t) = -2i\operatorname{Tr}\left(\rho(t)H_{-}\right). \tag{7.11}$$

The solution to this problem is the addition of a further term on the RHS of (7.9) whose trace is exactly $\operatorname{Tr}\left(+2i\rho(t)H_{-}\right)$. By taking again our single-mode cavity example, the extra term has to have trace $\operatorname{Tr}\left(+2\Gamma\rho a^{\dagger}a\right)$; instead of adding "$+2\Gamma\rho a^{\dagger}a$", however, we add the term "$+2\Gamma\left(a\rho a^{\dagger}\right)$"; this term has the same trace as the previous one, because of the cyclic property of the trace, but this particular form comes from the formal derivation of the Lindblad equation. After this correction — which can be obtained rigorously — we obtain the equation for the density matrix of the lossy single-mode cavity:

$$\dot{\rho} = -i\left[H,\rho\right] + 2\Gamma\left(a\rho a^{\dagger} - \frac{1}{2}\left\{a^{\dagger}a,\rho\right\}\right) \tag{7.12}$$

where $H = \omega_{\text{cav}}a^{\dagger}a$ is the Hamiltonian of the non-lossy cavity.

We reiterate again that the discussion above is *not* a formal proof of the Lindblad equation; for that, we refer the interested reader to one of the many derivations in the literature — see e.g. [62, 80, 117, 119–121]. Instead of a proof, we've chosen to focus on the relevant example of the single-mode cavity in order to provide an intuitive understanding of the meaning of the different terms in the Lindblad equation. Namely, we can argue that:

- the commutator $-i\left[H,\rho\right]$ provides the Hermitian part of the evolution;
- the anti-commutator $-\Gamma\left\{a^{\dagger}a,\rho\right\}$ provides the dissipation in terms of a non-Hermitian addition in what's usually called the *effective* Hamiltonian;
- the term $+2\Gamma a\rho a^{\dagger}$ restores the trace of the density matrix.

7.1.2 Connection to the semiclassical theory of lasers

In Chapter 2 we've derived the semiclassical theory of lasers for a cavity embedding a gain medium modeled as a collection of TLAs, and in Section 2.2 we've written the broadband limit of the theory. Such a limit does not involve the atoms at all, as it's just a single equation for the cavity field; is it then possible to get the same broadband semiclassical theory of lasers by means of proper jump operators acting on a single cavity? The answer is yes, and here we will briefly show how, since this discussion is relevant for our following analyses.

In order to build a laser, we need of course a pumping mechanism. We've seen in the previous Section that a jump operator $L = a$ with a non-negative

Lindblad coefficient Γ corresponds to having single-particle losses at a rate Γ, since a destroys a single-particle. This suggests a natural way to describe a single-particle (incoherent) pumping by introducing a term analogous to the single-particle losses, where the destruction operator a is replaced by the creation operator $L = a^\dagger$ with its own pumping rate P. So, the Lindblad equation for a single-mode cavity with (incoherent) drive and dissipation is simply ($H = \omega_{\text{cav}} a^\dagger a$)

Single-particle pumping

Example: driven-dissipative single-mode cavity

$$\dot{\rho} = -i\left[H,\rho\right] + 2\Gamma_1\left(a\rho a^\dagger - \frac{1}{2}\left\{a^\dagger a,\rho\right\}\right) + 2P_1\left(a^\dagger\rho a - \frac{1}{2}\left\{aa^\dagger,\rho\right\}\right) \tag{7.13}$$

where we've added a subscript "$_1$" in order to mark 1-particle processes.

Unfortunately, such a system cannot work as a laser. To see why, we derive the equation of motion for the expectation value of the photon field. The motivation for doing this is that the laser theory obtained in Chapter 2 is a *semi-classical* theory derived at a mean-field level, for a macroscopically large number of photons. From the definitions we get:

$$\begin{aligned}\frac{d}{dt}\langle a\rangle &= \frac{d}{dt}\operatorname{Tr}\left(a\rho\right) = \operatorname{Tr}\left(a\frac{d\rho}{dt}\right) = \operatorname{Tr}\left(a\mathcal{L}\rho\right)\\ &= -i\operatorname{Tr}\left(a\left[H,\rho\right]\right) + 2\Gamma_1\operatorname{Tr}\left(aa\rho a^\dagger - \frac{1}{2}a\left\{a^\dagger a,\rho\right\}\right)\\ &\quad + 2\Gamma_2\operatorname{Tr}\left(aa^\dagger\rho a - \frac{1}{2}a\left\{aa^\dagger,\rho\right\}\right).\end{aligned} \tag{7.14}$$

We treat each term one-by-one:

$$\begin{aligned}-i\operatorname{Tr}\left(a\left[H,\rho\right]\right) &= -i\operatorname{Tr}\left(aH\rho\right) - i\operatorname{Tr}\left(a\rho H_0\right) = -i\operatorname{Tr}\left(aH\rho\right) - i\operatorname{Tr}\left(H_0 a\rho\right)\\ &= -i\operatorname{Tr}\left(\left[a,H\right]\rho\right) = \operatorname{Tr}\left(i\left[H,a\right]\rho\right) = \left\langle i\left[H,a\right]\right\rangle.\end{aligned} \tag{7.15}$$

$$\begin{aligned}&2\Gamma_1\operatorname{Tr}\left(aa\rho a^\dagger - \frac{1}{2}a\left\{a^\dagger a,\rho\right\}\right)\\ &= 2\Gamma_1\left\{\operatorname{Tr}\left(aa\rho a^\dagger\right) - \frac{1}{2}\operatorname{Tr}\left(aa^\dagger a\rho\right) - \frac{1}{2}\operatorname{Tr}\left(a\rho a^\dagger a\right)\right\}\\ &= 2\Gamma_1\left\{\operatorname{Tr}\left(a^\dagger aa\rho\right) - \frac{1}{2}\operatorname{Tr}\left(aa^\dagger a\rho\right) - \frac{1}{2}\operatorname{Tr}\left(a^\dagger aa\rho\right)\right\}\\ &= \Gamma_1\left\{\operatorname{Tr}\left(a^\dagger aa\rho\right) - \operatorname{Tr}\left(aa^\dagger a\rho\right)\right\}\\ &= \Gamma_1\left\{\operatorname{Tr}\left(\left[a^\dagger,a\right]a\rho\right)\right\}\\ &= \operatorname{Tr}\left(-\Gamma_1 a\rho\right)\\ &= \left\langle-\Gamma_1 a\right\rangle.\end{aligned} \tag{7.16}$$

$$
\begin{aligned}
&2P_1 \operatorname{Tr}\left(aa^\dagger \rho a - \frac{1}{2} a \left\{aa^\dagger, \rho\right\}\right) \\
&= 2P_1 \left\{\operatorname{Tr}\left(aa^\dagger \rho a\right) - \frac{1}{2}\operatorname{Tr}\left(aaa^\dagger \rho\right) - \frac{1}{2}\operatorname{Tr}\left(a\rho aa^\dagger\right)\right\} \\
&= 2P_1 \left\{\operatorname{Tr}\left(aaa^\dagger \rho\right) - \frac{1}{2}\operatorname{Tr}\left(aaa^\dagger \rho\right) - \frac{1}{2}\operatorname{Tr}\left(aa^\dagger a \rho\right)\right\} \\
&= 2P_1 \left\{\operatorname{Tr}\left(aaa^\dagger \rho\right) - \operatorname{Tr}\left(aa^\dagger a \rho\right)\right\} \\
&= P_1 \left\{\operatorname{Tr}\left(a\left[a, a^\dagger\right]\rho\right)\right\} \\
&= \operatorname{Tr}\left(P_1 a \rho\right) \\
&= \langle P_1 a \rangle \,. \qquad (7.17)
\end{aligned}
$$

So, in the end, if we re-define $\langle a \rangle \to a$ with the caveat of taking the proper commutators, as done in the calculations of Chapter 2, we get

$$\dot{a} = i\left[H, a\right]_{\langle a\rangle \to a} + \left(P_1 - \Gamma_1\right) a = i\left[H_{\text{eff}}, a\right]_{\langle a\rangle \to a} \qquad (7.18)$$

where

$$H_{\text{eff}} = H + i\left(P_1 - \Gamma_1\right) a^\dagger a. \qquad (7.19)$$

This basically means that a evolves under a non-Hermitian Hamiltonian H_{eff} at a *mean-field* level. If we compare the equation for the time-evolution of the expectation of the photon field with the semiclassical equation for the broadband cavity laser (2.24) in the *linear regime* — i.e. for $|\langle a \rangle|^2 \ll 1$ — we get indeed the same evolution (possibly modulo some unitary transformation to get rid of the oscillation frequency).

While the combination of single-particle pumping and single-particle losses correctly reproduces the broadband theory of lasers in the linear regime, i.e. *below* the lasing threshold, it doesn't work *above* the lasing threshold, when one thus has a macroscopically large number of photons. If indeed we get rid of the Hermitian part of the evolution in (7.18) — which can always be done via a unitary transformation — we get

$$\dot{a} = \left(P_1 - \Gamma_1\right) a \qquad \Longrightarrow \qquad a = a_0 e^{(P_1 - \Gamma_1)t} \qquad (7.20)$$

that gives, for the expectation value of the total number of photons $N = a^\dagger a$ — that in this context we just call I as intensity

$$I = |a|^2 = I_0 e^{2(P_1 - \Gamma_1)t}. \qquad (7.21)$$

First, we immediately realize that, in order to have a non-diverging intensity for $t \to \infty$, we have to work under the condition that $P_1 \leq \Gamma_1$, i.e. with a pumping strength that cannot overcome the losses. This condition, which will be relevant for the results presented in Chapter 8, comes naturally from the fact that eq. (7.18) is equivalent to the semiclassical laser equations only in the linear

regime $|\langle a\rangle|^2 \ll 1$, which according to eq. (2.24) occurs for $P_1 \leq \Gamma_1$. The fact that we cannot overcome the losses means, however, that we will never get a lasing stationary state: indeed, at long times, we just get $\lim_{t\to\infty} I = 0$.

The impossibility to describe the system above the lasing threshold, where we must have a saturable gain in order to obtain a stable lasing branch, can be cured by introducing nonlinearities. Since the nonlinearity in a saturable gain is present at the level of the driven-dissipative description, and not at the level of the coherent dynamics, more specifically we need a nonlinearity in the Lindblad dissipator.

Such dissipative nonlinearity can be obtained from suitable jump operators inspired by the most straightforward nonlinearity in the coherent dynamics, i.e. the Kerr nonlinearity. While the quadratic terms in the Hamiltonian have a form $a^\dagger a$, and the corresponding linear jump operators are either a or $a^\dagger$, the Kerr nonlinearity has a form $(a^\dagger)^2 a^2$; thus, the corresponding nonlinear jump operators are a^2 and $(a^\dagger)^2$. Since they are quadratic in the fields, these jump operators describe respectively two-particle losses and two-particle pumping.

Two-particle pumping and losses

As we will see shortly, the right choice to describe the regime above the lasing threshold is to add two-particle losses to the model. We indicate the corresponding coefficient as Γ_2, where again the subscript indicates the number of particles involved, and the corresponding Lindblad equation is

$$\begin{aligned}\dot\rho = -i\,[H,\rho] &+ \beta\Gamma_2\left(aa\rho a^\dagger a^\dagger - \frac{1}{2}\left\{a^\dagger a^\dagger aa,\rho\right\}\right)\\ &+ 2\,(P_1-\Gamma_2)\left(a^\dagger\rho a - \frac{1}{2}\left\{aa^\dagger,\rho\right\}\right).\end{aligned} \tag{7.22}$$

The particular choice of coefficients will be clear below; we did not include single-particle losses since, at the mean-field level, they are simply subtracted from the pump coefficient — although they have a key role in the quantum fluctuations.

In the equation for the evolution for a, we now have the following term:

$$\begin{aligned}&\beta\Gamma_2\,\mathrm{Tr}\left(aaa\rho a^\dagger a^\dagger - \frac{1}{2}a\left\{a^\dagger a^\dagger aa,\rho\right\}\right)\\ &= \beta\Gamma_2\left\{\mathrm{Tr}\left(aaa\rho a^\dagger a^\dagger\right) - \frac{1}{2}\mathrm{Tr}\left(aa^\dagger a^\dagger aa\rho\right) - \frac{1}{2}\mathrm{Tr}\left(a\rho a^\dagger a^\dagger aa\right)\right\}\\ &= \beta\Gamma_2\left\{\frac{1}{2}\mathrm{Tr}\left(a^\dagger a^\dagger aaa\rho\right) - \frac{1}{2}\mathrm{Tr}\left(aa^\dagger a^\dagger aa\rho\right)\right\}\\ &= \frac{\beta\Gamma_2}{2}\left\{\left\langle a^\dagger a^\dagger aaa\right\rangle - \left\langle aa^\dagger a^\dagger aa\right\rangle\right\}\\ &\overset{(\triangle)}{=} \frac{\beta\Gamma_2}{2}\left\{\cancel{\left\langle a^\dagger a^\dagger aaa\right\rangle} - 2\left\langle a^\dagger aa\right\rangle - \cancel{\left\langle a^\dagger a^\dagger aaa\right\rangle}\right\}\\ &= \left\langle -\beta\Gamma_2(a^\dagger a)a\right\rangle\end{aligned} \tag{7.23}$$

where in the second-last equality ($\triangle$) we've recursively used the commutation relation $\left[a, a^\dagger\right] = 1$ obtaining

$$aa^\dagger a^\dagger a = a^\dagger a + a^\dagger a a^\dagger a = a^\dagger a + a^\dagger a + a^\dagger a^\dagger a a = 2a^\dagger a + a^\dagger a^\dagger a a. \tag{7.24}$$

If we then eliminate the Hermitian part of the evolution with a unitary transformation and we approximate-then-substitute $\left\langle a^\dagger a a\right\rangle \approx \left\langle a^\dagger\right\rangle \langle a\rangle \langle a\rangle = \langle a\rangle^* \langle a\rangle \langle a\rangle = |\langle a\rangle|^2 \langle a\rangle \longrightarrow |a|^2 a$ we obtain the following semiclassical equation

$$\dot{a} = \Big(P_1 - \Gamma_2 \left(1 + \beta |a|^2\right)\Big) a\,, \tag{7.25}$$

where we see that compared to (7.20) the losses have been renormalized by an additional factor $\beta|a|^2$ proportional to the field intensity itself. The steady-state solution of the equation above is

$$I_{\text{ss}} = |a|^2 = \begin{cases} 0 & P_1 < \Gamma_2 \\ \frac{1}{\beta}\left(\frac{P_1}{\Gamma_2} - 1\right) & P_1 \geq \Gamma_2 \end{cases} \tag{7.26}$$

We notice that the solution $|a|^2 = 0$ exists for *all* values of parameters, but it's *unstable* above the lasing threshold ($P_1 > \Gamma_2$). Therefore, above this threshold, the system spontaneously jumps into the lasing solution, which is instead stable. This piecewise solution is exactly equal to the steady-state solution of (2.24), so we've successfully reproduced the semiclassical theory of lasers in the limit of broadband gain by using the proper jump operators: we need both a single-particle incoherent pumping and two-particle losses, where the latter provides a way to saturate the gain above the lasing threshold.

Finally, notice that we cannot include such non-linear effects in a non-Hermitian Hamiltonian description. Hamiltonians are linear operators, and although we can have Hermitian nonlinearities in the Hamiltonian, we cannot reabsorb nonlinear terms in the Lindblad dissipator as additional non-Hermitian terms. For this reason we have to either integrate a nonlinear master equation for the expectation values of the fields, obtained by integrating out some other degrees of freedom as we did in Chapter 2, or to integrate a master equation for the density matrix with proper jump operators; this latter case doesn't require a mean-field approximation, and it's thus suitable to explore the quantum dynamics beyond the mean-field description.

7.2 Superbosons and Lindbladian diagonalization

In Section 7.1 we have spent plenty of paragraphs discussing the Lindblad equation, its properties, and its interpretation. An important aspect to notice is that while the Hamiltonian H that enters the Schrödinger equation is a linear operator over the Hilbert space, the Lindbladian $\mathcal{L}$ that enters the Lindblad equation is *not*

a linear operator over the Hilbert space itself, but over the space of linear operators acting on the Hilbert space. While in fact, on the Hilbert space, the action of the Hamiltonian on a state can be expressed as a matrix-by-vector product, the density matrix itself is already a matrix on its own — and the Lindbladian acts as a linear operator on the space of such matrices.

This doesn't mean, of course, that it's not possible to simply integrate the Lindblad equation in time in order to find a solution; however, for reasons that will become clearer later, we would still like to write the Lindblad equation as a linear differential equation, i.e. in such a way that the term $\mathcal{L}\rho$ can be interpreted as a matrix-by-vector product. At that point, the Lindblad equation would involve an eigenvalue problem, just as it happens with the Schrödinger equation. This procedure is commonly called *vectorization* of the Lindblad equation.

Vectorization

A straightforward, even if not physics-driven, way to turn the Lindblad equation into a linear differential equation is to transform the matrix ρ into a vector $|\rho\rangle$, for example by concatenating its columns, and then figuring out the matrix form of $\mathcal{L}$ when it acts on $|\rho\rangle$. There is however a more systematic way to turn ρ into a vector $|\rho\rangle$, not necessarily as a concatenation of the original matrix columns, and thus to obtain a matrix form for $\mathcal{L}$; this framework is the one of the *superfermion/superboson representation*.

Superfermion/superboson representation

In the following we walk the reader through the formalism, for what it concerns the class of problems we're dealing with; for a more comprehensive treatment, and for an overview of the related but more general concept of thermo fields, we point the interested reader to [128–132].

7.2.1 Left vacuum and tilde rules

We start again with a system (S) living in a Hilbert space $\mathcal{H}_S$, whose identity operator is written as

$$I_S = \sum_n |n\rangle \langle n| \tag{7.27}$$

in a complete Fock basis. The idea of this formalism, connected with the idea of purification of density operators, is to enlarge the Hilbert space by considering a "ghost" copy of the original system, marked by an additional tilde "$\sim$" and thus also called "tilde system", such that the total Hilbert space becomes $\mathcal{H} = \mathcal{H}_S \otimes \tilde{\mathcal{H}}_S$; the tilde system has the same Hamiltonian of the original system, with the difference that every operator is marked by an additional tilde. The identity operator over the tilde system is then simply

$$\tilde{I}_S = \sum_n |\tilde{n}\rangle \langle \tilde{n}| \ . \tag{7.28}$$

We now define a new state $|I\rangle$, living in the combined Hilbert space $\mathcal{H}$, as

$$|I\rangle = \sum_n |n\rangle \otimes |\tilde{n}\rangle \ . \tag{7.29}$$

Left vacuum

This state, called the *left vacuum* for reasons that will become clearer later, is the pillar of this formalism.

Purification

The nature of the left vacuum can be understood by recalling the concept of *purification* [133]: the purification of a density operator ρ on a Hilbert space $\mathcal{H}_S$ is a pure state $|\psi\rangle$ on an enlarged Hilbert space $\mathcal{H}_S \otimes \mathcal{H}_A$ such that $\rho = \mathrm{Tr}_A |\psi\rangle\langle\psi|$, where Tr_A is taken over the auxiliary system $\mathcal{H}_A$. In other words, every density matrix ρ representing a mixed state in a system (S) can be obtained from a density matrix representing a pure state $|\psi\rangle$ in a larger system (S+A) by tracing out (A). In the light of this definition, the state $|I\rangle$ can be interpreted as the purification of the identity operator. In fact, if we take $|I\rangle\langle I|$ and we trace out the tilde system, we get

$$\begin{aligned}
\mathrm{Tr}_\sim |I\rangle\langle I| &= \mathrm{Tr}_\sim \sum_{nn'} (|n\rangle\langle n'|) \otimes (|\tilde{n}\rangle\langle\tilde{n}'|) \\
&= \sum_{nn'} |n\rangle\langle n'| \otimes \mathrm{Tr}_\sim (|\tilde{n}\rangle\langle\tilde{n}'|) \\
&= \sum_{nn'n''} |n\rangle\langle n'| \otimes \underbrace{\langle\tilde{n}''|\tilde{n}\rangle\langle\tilde{n}'|\tilde{n}''\rangle}_{\delta_{\tilde{n}'',\tilde{n}}\delta_{\tilde{n}',\tilde{n}''}} \\
&= \sum_{n} |n\rangle\langle n| \equiv I_S \,. \qquad (7.30)
\end{aligned}$$

Now that we have the first basic vector of our theory, we would like to apply operators to it. The rule that relates an operator A belonging to the original system to an operator $\widetilde{A}$ belonging to the tilde system when they are applied to $|I\rangle$ is called the *tilde-conjugation rule* [129, 134, 135] — see also Appendix A:

Tilde-conjugation rule

$$A|I\rangle = \sigma_A \widetilde{A}^\dagger |I\rangle \,, \qquad (7.31)$$

where

$$\sigma_A = \begin{cases} -i & \text{if } A \text{ is a fermionic operator} \\ 1 & \text{if } A \text{ is a bosonic operator} \end{cases} \qquad (7.32)$$

Tilde-conjugation

The tilde-conjugation rule can in turn be used to define a new operation "$\sim$", called "tilde-conjugation", that acts via the following practical rules:

1. The vacuum $|I\rangle$ is invariant under tilde-conjugation:

$$\widetilde{|I\rangle} = |I\rangle \,. \qquad (7.33)$$

2. The double-tilde conjugation is the identity:

$$\widetilde{\widetilde{A}} = A. \qquad (7.34)$$

3. The tilde-conjugation preserves the ordering of the operators:

$$\widetilde{(AB)} = \widetilde{A}\widetilde{B}. \qquad (7.35)$$

4. The tilde-conjugation is antilinear:

$$\widetilde{(c_1 A + c_2 B)} = c_1^* \widetilde{A} + c_2^* \widetilde{B}. \tag{7.36}$$

5. The tilde-conjugation and the adjoint operation commute:

$$\widetilde{(A^\dagger)} = \widetilde{A}^\dagger. \tag{7.37}$$

For a proof of the above rules, we point the interested reader to [129, 130, 136].

7.2.2 Vectorization of the Lindblad equation

Armed with the set of rules introduced in Section 7.2.1 we can now take a generic operator $\mathcal{O}$, written in complete generality as

$$\mathcal{O} = \sum_{nm} \mathcal{O}_{nm} |n\rangle \langle m| , \tag{7.38}$$

and define its vectorized version as:[3]

$$|\mathcal{O}\rangle \doteq \mathcal{O} |I\rangle = \sum_{nmn'} \mathcal{O}_{nm} |n\rangle \langle m|n'\rangle |\tilde{n}'\rangle = \sum_{nm} \mathcal{O}_{nm} |n\rangle \otimes |\tilde{m}\rangle . \tag{7.39}$$

We see that, with the definition of $|I\rangle$, transforming a generic operator $\mathcal{O}$ as written in (7.38) to a vector $|\mathcal{O}\rangle = \mathcal{O}|I\rangle$ takes no more than taking the bra state $\langle m|$ in (7.38) and flipping it into a ket state in the auxiliary space, $|\tilde{m}\rangle$. In particular, if $\mathcal{O}$ is Hermitian, i.e. if $\mathcal{O}_{nm} = \mathcal{O}^*_{mn}$, the tilde rules give

$$|\mathcal{O}\rangle = \left|\tilde{\mathcal{O}}\right\rangle , \tag{7.40}$$

i.e. if $\mathcal{O}$ is Hermitian then $|\mathcal{O}\rangle$ is invariant under the tilde-conjugation.

In a similar way, by combining eqs. (7.29) and (7.39), we see that the trace of a generic operator $\mathcal{O}$ can be expressed as the expectation value of $\mathcal{O}$ over $|I\rangle$:

$$\mathrm{Tr}\, \mathcal{O} = \langle I|\mathcal{O}|I\rangle = \langle I|O\rangle . \tag{7.41}$$

If instead of a generic operator $\mathcal{O}$ we consider a density matrix, we get the vector representation we were originally looking for in the context of the Lindblad equation:

$$\rho = \sum_{nm} \rho_{nm} |n\rangle \langle m| \qquad \Longrightarrow \qquad |\rho\rangle = \sum_{nm} \rho_{nm} |n\rangle \otimes |\tilde{m}\rangle \equiv \rho |I\rangle . \tag{7.42}$$

In particular, (7.40) holds here as well: $|\tilde{\rho}\rangle = |\rho\rangle$.

[3] It is understood that, since $\mathcal{O}$ lives in (S), $\mathcal{O}|I\rangle \equiv \left(\mathcal{O} \otimes \tilde{I}_S\right) |I\rangle$

Considering that the trace in the vectorized representation is calculated via (7.41) and that the density matrix is represented as (7.42), we can then express the expectation value of a generic operator $\mathcal{O}$ as:

$$\langle \mathcal{O} \rangle = \mathrm{Tr}\,(\mathcal{O}\rho) = \langle I \,|\, \mathcal{O}\rho \,|\, I \rangle = \langle I \,|\, \mathcal{O} \,|\, \rho \rangle \ . \tag{7.43}$$

In particular, since the expectation value of the identity operator must be 1, we get the fundamental normalization relation

$$\langle I \,|\, \rho \rangle = 1 \tag{7.44}$$

which is the vectorized equivalent of the requirement that the density matrix has a unity trace: $\mathrm{Tr}\,\rho = 1$.

In the context of the following calculations, the following relation is particularly useful:

$$\rho\mathcal{O}\,|I\rangle = \widetilde{(\rho\mathcal{O})}^{\dagger}\,|I\rangle = (\widetilde{\rho}\widetilde{\mathcal{O}})^{\dagger}\,|I\rangle = \widetilde{\mathcal{O}}^{\dagger}\widetilde{\rho}^{\dagger}\,|I\rangle = \widetilde{\mathcal{O}}^{\dagger}\,|\widetilde{\rho}^{\dagger}\rangle = \widetilde{\mathcal{O}}^{\dagger}\,|\rho\rangle\,, \tag{7.45}$$

Finally, we want to vectorize the Lindblad equation:

$$\frac{d}{dt}\rho = \mathcal{L}\rho = \mathcal{L}_H\rho + \mathcal{L}_D\rho \qquad \Longrightarrow \qquad \frac{d}{dt}\,|\rho\rangle = \mathcal{L}\,|\rho\rangle\,, \tag{7.46}$$

where $\mathcal{L}_H\rho = -i\,[H,\rho]$ is the Hermitian contribution to the evolution, $\mathcal{L}_D$ is the Lindblad dissipator (see (7.5)) and, in the vectorized form of the Lindblad equation, $\mathcal{L}$ is finally a linear operator over the Hilbert space.

First, notice that from (7.44) and from the vectorized Lindblad equation above, we get

$$0 = \frac{d}{dt}1 = \frac{d}{dt}\,\langle I \,|\, \rho \rangle = \langle I \,|\, \mathcal{L} \,|\, \rho \rangle \ . \tag{7.47}$$

Origin of the term "left vacuum"

Since this relation holds for every $|\rho\rangle$, we get

$$\langle I|\,\mathcal{L} = 0, \tag{7.48}$$

i.e. $\langle I|$ is the left eigenvector of $\mathcal{L}$ with eigenvalue zero, justifying the name of left vacuum. On the other hand, the right eigenvector of $\mathcal{L}$ is, by definition, the stationary-state density matrix $|\rho_{\mathrm{ss}}\rangle$:

$$\mathcal{L}\,|\rho_{\mathrm{ss}}\rangle = 0. \tag{7.49}$$

Vectorization of the Lindblad equation

Now we proceed with the actual vectorization. As explained so far, in order to obtain the vectorized representation we have to apply the whole Lindblad equation to the left vacuum $|I\rangle$; let's proceed piece by piece.

- $\mathcal{L}_H\rho\,|I\rangle$.
  By using (7.45) we get:

$$\begin{aligned}\mathcal{L}_H\rho\,|I\rangle &= -i\,[H,\rho]\,|I\rangle = -i\Big(H\rho\,|I\rangle - \rho H\,|I\rangle\Big) \\ &= -i\Big(H\,|\rho\rangle - \widetilde{H}^{\dagger}\,|\rho\rangle\Big) = -i\Big(H - \widetilde{H}\Big)\,|\rho\rangle\,,\end{aligned} \tag{7.50}$$

where we remind that $\widetilde{H}$ is built out of H by applying the tilde-conjugation — i.e. by taking the tilde-conjugate of all the fields.

- $\mathcal{L}_D\rho\,|I\rangle$.
  Since the dissipator is additive, we can perform the calculation with just a single jump operator L; in the case of multiple jump operators, we would just sum similar terms. Then the dissipator takes the form

$$\mathcal{L}_D\rho = 2\gamma\left(L\rho L^\dagger - \frac{1}{2}\left\{L^\dagger L,\rho\right\}\right). \tag{7.51}$$

  In order to perform the calculation, we apply the dissipator to $|I\rangle$ by splitting it in pieces:

$$\left(L\rho L^\dagger - \frac{1}{2}\left\{L^\dagger L,\rho\right\}\right)|I\rangle = \underbrace{\left(L\rho L^\dagger\right)|I\rangle}_{①} - \frac{1}{2}\underbrace{\left(L^\dagger L\rho\right)|I\rangle}_{②} - \frac{1}{2}\underbrace{\left(\rho L^\dagger L\right)|I\rangle}_{③} \tag{7.52}$$

  ① By using the tilde-conjugation rules, we get (remind that σ_L is $-i$ for a fermionic L and 1 for a bosonic L)

$$L\rho L^\dagger\,|I\rangle = L\rho\sigma_L(\tilde{L})\,|I\rangle = \sigma_L L\tilde{L}\rho\,|I\rangle = \sigma_L L\tilde{L}\,|\rho\rangle\,. \tag{7.53}$$

  ② This is immediate:

$$L^\dagger L\rho\,|I\rangle = L^\dagger L\,|\rho\rangle\,. \tag{7.54}$$

  ③ Notice that $L^\dagger L$ is a bosonic operator when considered as a whole, independently of the fact that L itself is fermionic or bosonic; so we can apply again (7.45):

$$\rho\left(L^\dagger L\right)|I\rangle = \widetilde{\left(L^\dagger L\right)}^\dagger|\rho\rangle = \tilde{L}^\dagger\tilde{L}\,|\rho\rangle\,. \tag{7.55}$$

  So, finally, the dissipator in the vectorized representation is [135]:

$$\begin{aligned}\mathcal{L}_D\,|\rho\rangle &= 2\gamma\left(L\rho L^\dagger - \frac{1}{2}\left\{L^\dagger L,\rho\right\}\right)|I\rangle \\ &= 2\gamma\left(\sigma_L L\tilde{L} - \frac{1}{2}L^\dagger L - \frac{1}{2}\tilde{L}^\dagger\tilde{L}\right)|\rho\rangle\,.\end{aligned} \tag{7.56}$$

In order to get some insight, we apply the vectorization procedure to the Lindblad equation for a single-mode cavity with single-particle incoherent pumping

Example: nonlinear single-mode cavity with incoherent pumping and losses

and losses in (7.13). Since in this case a and $a^\dagger$ are themselves bosonic jump operators, the procedure above gives:

$$\frac{d}{dt}|\rho\rangle = \mathcal{L}|\rho\rangle = -i\Big(H - \widetilde{H}\Big)|\rho\rangle + \Gamma_1\Big(2a\tilde{a} - a^\dagger a - \tilde{a}^\dagger\tilde{a}\Big)|\rho\rangle + P_1\Big(2a^\dagger\tilde{a}^\dagger - aa^\dagger - \tilde{a}\tilde{a}^\dagger\Big)|\rho\rangle \quad (7.57)$$

If the cavity has an additional Kerr nonlinearity of amplitude U, i.e. if its Hamiltonian is

$$H = \omega_{\text{cav}}N + UN^2 \quad (7.58)$$

where $N = a^\dagger a$ is the occupation operator, then the Lindbladian $\mathcal{L}$ can be written as

$$\begin{aligned}\mathcal{L} = &-i\Big[\omega_{\text{cav}}\Big(N - \tilde{N}\Big) + U\Big(N^2 - \tilde{N}^2\Big)\Big] \\ &-\Gamma_1\Big[\Big(N + \tilde{N}\Big) - 2a\tilde{a}\Big] \\ &-P_1\Big[\Big(N + \tilde{N}\Big) - 2a^\dagger\tilde{a}^\dagger + 2\Big]\end{aligned} \quad (7.59)$$

At this point, we finally have a Lindbladian $\mathcal{L}$ written as a linear operator over the Hilbert space. In order to study its properties, we typically want to write it in matrix form, i.e. we want to calculate the matrix elements $\langle n', \tilde{m}'|\mathcal{L}|n, \tilde{m}\rangle$. In order to do that, we work in a basis of orthonormal states $|n, \tilde{m}\rangle$, that are a natural extension of the system Fock states over the tilde space, such that (see Appendix A)

$$\begin{cases} a|n,\tilde{m}\rangle = \sqrt{n}\,|n-1,\tilde{m}\rangle \\ a^\dagger|n,\tilde{m}\rangle = \sqrt{n+1}\,|n+1,\tilde{m}\rangle \end{cases} \quad \text{and} \quad \begin{cases} \tilde{a}|n,\tilde{m}\rangle = \sqrt{m}\,|n,\widetilde{m-1}\rangle \\ \tilde{a}^\dagger|n,\tilde{m}\rangle = \sqrt{m+1}\,|n,\widetilde{m+1}\rangle \end{cases} \quad (7.60)$$

which verify, as we expect

$$a^\dagger a|n,\tilde{m}\rangle = n|n,\tilde{m}\rangle \quad \text{and} \quad \tilde{a}^\dagger\tilde{a}|n,\tilde{m}\rangle = m|n,\tilde{m}\rangle\,. \quad (7.61)$$

By applying the rules above, we get

$$2a\tilde{a}|n,\tilde{m}\rangle = 2\sqrt{nm}\,|n-1,\widetilde{m-1}\rangle \quad (7.62)$$

$$2a^\dagger\tilde{a}^\dagger|n,\tilde{m}\rangle = 2\sqrt{(n+1)(m+1)}\,|n+1,\widetilde{m+1}\rangle\,. \quad (7.63)$$

So, by eventually applying the Lindbladian in linear operator form to a state $|n, \tilde{m}\rangle$, we get

$$\begin{aligned}\mathcal{L}|n,\tilde{m}\rangle = &\left\{-i\Big[\omega_{\text{cav}}\Big(n-m\Big) + U\Big(n^2-m^2\Big)\Big] - (\Gamma_1+P_1)(n+m) - 2P_1\right\}|n,\tilde{m}\rangle \\ &+ 2\Gamma_1\sqrt{nm}\,|n-1,\widetilde{m-1}\rangle \\ &+ 2P_1\sqrt{(n+1)(m+1)}\,|n+1,\widetilde{m+1}\rangle\end{aligned} \quad (7.64)$$

and the generic matrix element becomes

$$\begin{aligned}\langle n', \tilde{m}' \,|\, \mathcal{L} \,|\, n, \tilde{m}\rangle = \Bigg\{ & - i\Big[\omega_{\text{cav}}\Big(n - m\Big) + U\Big(n^2 - m^2\Big)\Big] \\ & - (\Gamma_1 + P_1)(n + m) - 2P_1 \Bigg\}\delta_{n',n}\delta_{m',m} \\ & + 2\Gamma_1\sqrt{nm}\,\delta_{n',n-1}\delta_{m',m-1} \\ & + 2P_1\sqrt{(n+1)(m+1)}\,\delta_{n',n+1}\delta_{m',m+1} \end{aligned} \tag{7.65}$$

The first observation we have to make is that the terms including U appear only on the diagonal (i.e. when $n = n'$ and $m = m'$ at the same time). Even here, however, all the terms including contributions from the Hamiltonian vanish for $n = m$. This fact, as we will see, it's connected with the theorem in [105]; for the time being, this suggests that some simplifications are possible.

Gauge symmetry

The key observation is that the dissipator has not disrupted the $U(1)$ gauge symmetry possessed by the Hamiltonian, i.e. the invariance with respect to phase rotations. Indeed, if we perform the transformation (consistent with the tilde-rules)

$$\begin{cases} a \to a e^{i\vartheta} \\ \tilde{a} \to \tilde{a} e^{-i\vartheta} \end{cases} \qquad (\vartheta \in \mathbb{R}) \tag{7.66}$$

the Lindbladian remains unchanged.

Since the generator of a phase rotation is the occupation operator $N = a^\dagger a$, we have $[H, N] = 0$ but also $[\mathcal{L}, \mathcal{K}] = 0$, where $\mathcal{L}$ is in superoperator form and, inspired by the form of the Hermitian contribution in the Lindblad equation, we have defined a new superoperator

$$\mathcal{K}\bullet = -i\,[N, \bullet] \qquad \underset{(vectorization)}{\Longrightarrow} \qquad \mathcal{K} = i\Big(\tilde{N} - N\Big) = ik, \tag{7.67}$$

where, since we work in the number basis, the linear operator $\mathcal{K}$ has eigenvalues ik, $k = 0, +1, -1, +2, -2, \ldots$. Since the Lindbladian and $\mathcal{K}$ commute, they share a common set of eigenvectors; this means we can classify the eigenvectors of the Lindbladian by labeling them with the eigenvalues of $\mathcal{K}$, i.e. with k if we drop the imaginary unit for convenience. In other words, we have discovered that the Lindbladian is block-diagonal, with each block (also called "sector") labeled by an integer value k that is equal to the difference between the occupation in the tilde-system and the occupation in the original system. This symmetry is also clearly visible in (7.64): when the Lindbladian is applied to a state $|n, \tilde{m}\rangle$ living in the sector $k = m - n$, we can jump to other states with different occupations in the tilde-system and in the original one, but always in such a way that k is preserved.

Lindbladian block structure

Let's proceed again with a practical example, by explicitly writing down the matrix in (7.65). In contrast to the fermionic case, where the matrix is finite-size,

Cutoff of the Hilbert space

in the bosonic case the matrix has infinite size. So, in order to be able to make any numerical calculation, we have to choose a maximum occupation number for the bosons, that we call N_{cutoff}; with this choice, the number of possible states becomes $\left(N_{\text{cutoff}}+1\right)^2$ and therefore the dimension of the Lindbladian matrix is $\left(N_{\text{cutoff}}+1\right)^2 \times \left(N_{\text{cutoff}}+1\right)^2$. Let's choose $N_{\text{cutoff}} = 3$ for this example; the resulting $(3+1)^2 = 16$ basis elements, organized by their k-sector, are:

$$
\begin{array}{llllll}
(k=0) & |0,\tilde{0}\rangle\,, & |1,\tilde{1}\rangle\,, & |2,\tilde{2}\rangle\,, & |3,\tilde{3}\rangle\,, \\
(k=+1) & |0,\tilde{1}\rangle\,, & |1,\tilde{2}\rangle\,, & |2,\tilde{3}\rangle\,, & \\
(k=-1) & |1,\tilde{0}\rangle\,, & |2,\tilde{1}\rangle\,, & |3,\tilde{2}\rangle\,, & \\
(k=+2) & |0,\tilde{2}\rangle\,, & |1,\tilde{3}\rangle\,, & & \\
(k=-2) & |2,\tilde{0}\rangle\,, & |3,\tilde{1}\rangle\,, & & \\
(k=+3) & |0,\tilde{3}\rangle\,, & & & \\
(k=-3) & |3,\tilde{0}\rangle\,. & & &
\end{array}
$$

Then the Lindbladian will have the following form:

$$
\mathcal{L} = \begin{pmatrix}
\mathcal{B}_0 & 0 & 0 & 0 & 0 & 0 & 0 \\
0 & \mathcal{B}_{+1} & 0 & 0 & 0 & 0 & 0 \\
0 & 0 & \mathcal{B}_{-1} & 0 & 0 & 0 & 0 \\
0 & 0 & 0 & \mathcal{B}_{+2} & 0 & 0 & 0 \\
0 & 0 & 0 & 0 & \mathcal{B}_{-2} & 0 & 0 \\
0 & 0 & 0 & 0 & 0 & \mathcal{B}_{+3} & 0 \\
0 & 0 & 0 & 0 & 0 & 0 & \mathcal{B}_{-3}
\end{pmatrix} \tag{7.68}
$$

where $\mathcal{B}_h$ is the Lindbladian block with $k = h$. For $N_{\text{cutoff}} = 2$, instead, we will have only 5 diagonal blocks with the following expressions:

$$
\mathcal{B}_0 = \begin{pmatrix}
-2P_1 & +2\Gamma_1 & 0 \\
+2P_1 & -2\left(\Gamma_1+P_1\right) - 2P_1 & +2\sqrt{4}\Gamma_1 \\
0 & +2\sqrt{4}P_1 & -4\left(\Gamma_1+P_1\right) - 2P_1
\end{pmatrix} \tag{7.69}
$$

$$
\mathcal{B}_{\pm 1} = \begin{pmatrix}
\pm i\left(\omega_0+U\right) - \left(\Gamma_1+P_1\right) - 2P_1 & +2\sqrt{2}\Gamma_1 \\
+2\sqrt{2}P_1 & \pm i\left(\omega_0+3U\right) - 3\left(\Gamma_1+P_1\right) - 2P_1
\end{pmatrix} \tag{7.70}
$$

$$
\mathcal{B}_{\pm 2} = \begin{pmatrix} \pm i\left(2\omega_0+4U\right) - 2\left(\Gamma_1+P_1\right) - 2P_1 \end{pmatrix} \tag{7.71}
$$

$|\rho_{\text{ss}}\rangle$ lives in $\mathcal{B}_0$ and does not depend on H

Thus, already with $N_{\text{cutoff}} = 2$, we are able to verify that $\langle I|\,\mathcal{L} = -2P_1 + 2P_1 = 0$, i.e. $\langle I|$ is indeed the left eigenvector of $\mathcal{L}$. In particular, since $|I\rangle$ lives by definition in (the eigenspace of) $\mathcal{B}_0$, $|\rho_{\text{ss}}\rangle$ is an eigenvector of $\mathcal{L}$ so it must live in some block[4] $\mathcal{B}_h$, and the unitarity of the trace of the density matrix requires that

[4] This is not true for a *generic* density matrix, i.e. a density matrix at intermediate times, since it's not necessarily an eigenvector of $\mathcal{L}$.

$\langle I \,|\, \rho_{\rm ss}\rangle = 1$, we get that $|\rho_{\rm ss}\rangle$ lives in $\mathcal{B}_0$ as well. This is an important result, that holds for any Hamiltonian and dissipator for which the gauge symmetry is preserved. Since in this case the first diagonal block does not depend on the details of the Hamiltonian, this means that the steady-state density matrix is independent of the Hamiltonian as well; it only depends on the details of the dissipator, that acts as a thermalizer for the system.

Naturally, if the density matrix at the steady-state is independent of the Hamiltonian, the same will hold for any steady-state observable. As an example, we compute the occupation of our nonlinear cavity; we do so via the *equation of motion technique*, that exploits the property $\langle I|\,\mathcal{L} = 0$ to get, for an observable $\mathcal{O}$:

Equation of motion technique

$$\frac{d}{dt}\langle \mathcal{O}(t)\rangle = \frac{d}{dt}\langle I \,|\, \mathcal{O} \,|\, \rho(t)\rangle = \langle I \,|\, \mathcal{O}\mathcal{L} \,|\, \rho(t)\rangle = \langle I \,|\, [\mathcal{O},\mathcal{L}] \,|\, \rho(t)\rangle\,. \tag{7.72}$$

In our case we want to calculate the commutator $[N,\mathcal{L}]$, that gives

$$[N,\mathcal{L}] = 2\Gamma_1\,[N, a\tilde{a}] + 2P_1\left[N, a^\dagger \tilde{a}^\dagger\right]. \tag{7.73}$$

By using the following commutators computed over $\langle I|$

$$\langle I|\,[N, a\tilde{a}] = -\,\langle I|\,N \qquad \text{and} \qquad \langle I|\left[N, a^\dagger\tilde{a}^\dagger\right] = \langle I|\,(N+1) \tag{7.74}$$

as well as the definition $N(t) = \langle I|N|\rho\rangle$ and $\langle I|\rho\rangle = 1$, we immediately get the following equation for $N(t)$:

$$\frac{d}{dt}N(t) = -2(\Gamma_1 - P_1)\left\{N(t) - \frac{P_1}{\Gamma_1 - P_1}\right\}, \tag{7.75}$$

where $\Gamma_1 > P_1$ in order to have a stationary state. Note that this is the same condition we have found when discussing the connection with the semiclassical theory of lasers in Section 7.1.2! The equation for $N(t)$ has the following solution ($N_0 = N(0)$, $N_\infty = \lim_{t\to\infty} N(t)$):

$$N(t) = \Big(N_0 - N_\infty\Big)e^{-2(\Gamma_1 - P_1)t} + N_\infty, \qquad N_\infty = \frac{P_1}{\Gamma_1 - P_1}\,, \tag{7.76}$$

so the steady-state is indeed independent of the details of the Hamiltonian and has a thermal occupation given by the Lindblad coefficients. In particular, if we define as $\Gamma^{\rm eff} = \Gamma_1 - P_1 > 0$ as the semiclassical effective loss coefficient, a stationary occupation equal to N_∞ can be realized by choosing the following Lindblad coefficients:

$$\Gamma_1 \equiv \Gamma^{\rm eff}\Big(N_\infty + 1\Big) \qquad \text{and} \qquad P_1 \equiv \Gamma^{\rm eff} N_\infty. \tag{7.77}$$

Finally, note that the mean-field description correctly predicts decay rate but completely misses the presence of a baseline occupation N_∞ at the stationary state; this term results in fact from a proper description of the cavity at the quantum level, as we've done here.

7.2.3 Diagonalization of the Lindbladian

As a last step after the vectorization procedure, let's spend a few words on the diagonalization of the Lindbladian in matrix form.

The calculation of physical quantities often requires working in the basis of the eigenstates of the Lindbladian, for example in order to find a Källén-Lehmann representation for the Green's functions (see Section 7.4). Namely, the formal solution of the Lindblad equation in the vectorized representation is

$$|\rho(t)\rangle = e^{\mathcal{L}t}\,|\rho(0)\rangle \tag{7.78}$$

and the Lindbladian $\mathcal{L}$ eigenvalues and right and left eigenvectors

$$\langle l_\alpha|\,\mathcal{L} = \mathcal{L}_\alpha\,\langle l_\alpha| \qquad \text{and} \qquad \mathcal{L}\,|r_\alpha\rangle = \mathcal{L}_\alpha\,|r_\alpha\rangle \tag{7.79}$$

or, if we drop the bra-ket notation and consider the kets as column vectors,

$$\mathbf{l}_\alpha^H\mathcal{L} = \mathcal{L}_\alpha\mathbf{l}_\alpha^H \qquad \text{and} \qquad \mathcal{L}\mathbf{r}_\alpha = \mathcal{L}_\alpha\mathbf{r}_\alpha \tag{7.80}$$

where H indicates the hermitian conjugate (transpose + complex conjugate). These equations can be written in matrix form as

$$X_L^H\mathcal{L} = DX_L^H, \qquad \mathcal{L}X_R = X_RD, \tag{7.81}$$

where X_L (X_R) is the matrix of *all* the left (right) eigenvectors (both stored as *columns*) and D is the diagonal matrix with the corresponding eigenvalues on the diagonal.

Note that, from the equations above, we have (by multiplying the first one by X_R on the right and the second one by X_L^H on the left) that

$$X_L^HLX_R = D(X_L^HX_R) = (X_L^HX_R)D.$$

Since the matrix $X_L^HX_R$ commutes with a diagonal matrix, it's diagonal[5] (unless for some special cases with degenerate eigenvalues). This means that left and

[5] **Observation.** Let $D = (d_{ij}) = (d_{ij}\delta_{ij})$ be a $n \times n$ diagonal matrix with n *distinct* diagonal elements $d_{ii} \neq d_{jj} \Leftrightarrow i \neq j$ and let $A = (a_{ij})$ be a $n \times n$ matrix such that A commutes with D, i.e. $AD = DA$. Then A is a diagonal matrix.
Proof. We prove the statement by simply proving that $a_{ij} = 0$ for $i \neq j$. Indeed,

$$(AD)_{ij} = \sum_k a_{ik}d_{kj} = \sum_k a_{ik}d_{kj}\delta_{kj} = a_{ij}d_{jj}$$
$$(DA)_{ij} = \sum_k d_{ik}a_{kj} = \sum_k d_{ik}\delta_{ik}a_{kj} = d_{ii}a_{ij}$$

thus

$$a_{ij}d_{jj} = a_{ij}d_{ii} \qquad \Leftrightarrow \qquad a_{ij}(d_{ii} - d_{jj}) = 0.$$

Under the hypothesis that $d_{ii} \neq d_{jj}$ for $i \neq j$, then we have that $a_{ij} = 0$ for $i \neq j$, i.e. $A = (a_{ij})$ is a diagonal matrix.
Note. The above proof can be extended to the case in which the matrix D is block-diagonal with *distinct* diagonal blocks (which is the case e.g. for a diagonal matrix D with degenerate diagonal elements). In this case, the matrix A is block-diagonal with the same block-diagonal structure as the matrix D.

right eigenvectors are bi-orthogonal to each other, though not necessarily normalized to one. So, in principle, one can achieve a bi-orthonormalization to 1 by simply rescaling left and right eigenvectors by a proper c-number. However, if there are degenerate eigenvalues, $X_L^H X_R$ is at least *block* diagonal (in this case, written for each degenerate block, the equation above is just a tautology – D is proportional to the identity! – so we must assume the most general form for each degenerate block – i.e., a dense matrix). Then, for each degenerate block, we can perform a LU decomposition[6]

$$X_L^H X_R = LU \qquad \Longrightarrow \qquad (X_L L^{-H})^H (X_R U^{-1}) = I, \tag{7.82}$$

Bi-orthonormalization

i.e. we can obtain a set of bi-orthonormalized eigenvectors by taking $X_L L^{-H}$ and $X_R U^{-1}$ as a set of left and right eigenvectors, respectively. All in all, we see that we can find (bi)normalized left and right eigenvectors such that

$$\langle l_\alpha | r_\beta \rangle = \delta_{\alpha\beta}. \tag{7.83}$$

Since they form a complete set, we can express the identity as

$$I = \sum_\alpha |r_\alpha\rangle \langle l_\alpha| . \tag{7.84}$$

This completeness relation allows us to expand any state $|\rho(t)\rangle$ as written in (7.78) in this basis:

$$\begin{aligned} |\rho(t)\rangle &= e^{\mathcal{L}t} |\rho(0)\rangle = e^{\mathcal{L}t} I |\rho(0)\rangle \\ &= \sum_\alpha e^{\mathcal{L}_\alpha t} |r_\alpha\rangle \langle l_\alpha | \rho(0)\rangle = \sum_\alpha \rho_\alpha(t) |r_\alpha\rangle , \end{aligned} \tag{7.85}$$

where (by using the above expression for $|\rho(0)\rangle$ and the bi-orthonormalization property)

$$\rho_\alpha(t) \doteqdot e^{\mathcal{L}_\alpha t} \langle l_\alpha | \rho(0)\rangle = e^{\mathcal{L}_\alpha t} \rho_\alpha(0). \tag{7.86}$$

So we see that, in order to have a non-exploding solution, we must have $\mathrm{Re}\,\mathcal{L}_\alpha \leq 0\ \forall\alpha$, which is ensured by the form of the Lindblad equation. We also have to remember that $\langle I|$ is the left eigenvector[7] of $\mathcal{L}$ with zero eigenvalue, i.e. $\langle I|\,\mathcal{L} = 0$. So we assume that there is exactly one zero eigenvalue and we denote it with $\alpha = 0$, i.e.

$$\langle l_0| \equiv \langle I| \qquad \text{and} \qquad |r_0\rangle \equiv |\rho_{\mathrm{ss}}\rangle . \tag{7.87}$$

[6] From a numerical perspective, it's still better to perform a LU decomposition of the whole matrix, as it's difficult to numerically acknowledge the presence of degeneracies and as the LU decomposition is still relatively inexpensive with respect to the diagonalization procedure itself. In this way, we have greater confidence in the proper normalization of the eigenstates.

[7] With the caveat that, for a bosonic system, $\langle I|$ is a left eigenvector of $\mathcal{L}$ only in the case of an infinite basis; since in general we use a finite cutoff N_{cutoff}, the numerical left vacuum will differ from the analytical one.

7.3 Keldysh field theory and Green's functions

Single-particle Green's functions provide a wealth of precious information, and they are the main quantities to be computed within the Dynamical Mean Field Theory (DMFT) technique that we introduce in Chapter 9. These functions provide spatio-temporal information about the system; for example, in the case of an optical cavity, the elements of the single-particle Green's function are related to optical coefficients like reflection and transmission. In the context of non-equilibrium systems, much of the formalism developed at equilibrium can be straightforwardly generalized by performing the calculations on a suitably defined contour in the complex-time space; the resulting theory is called *Keldysh field theory*.

Keldysh field theory

A full introduction to the Keldysh formalism would be way beyond the scope of this Thesis. However, in order to provide a self-contained presentation of our results and methods, we give here a very brief overview of the formalism, relying on the physical intuition rather than on full-blown proofs. For the reader interested in more solid mathematical foundations, we refer to [137–143]; in particular, [140, 142] focus on the context of non-equilibrium bosonic systems described by a Lindblad equation.

7.3.1 Keldysh formalism

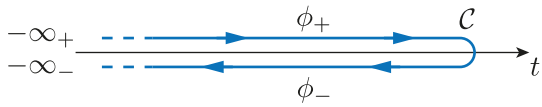

Figure 7.1: Schematic depiction of the Keldysh contour $\mathcal{C}$. The upper/lower branches, on which the $+/-$ fields are defined, are infinitesimally shifted respectively above and below the real-time axis in the complex plane and extend to $-\infty$; the arrows indicate the time ordering along the contour.

As a general idea, we want to calculate the Green's functions in the path integral formulation, in which, at the steady-state, the partition function is expressed as the integral of a certain action $S[\bar{\phi}, \phi]$ over all the possible paths:

$$Z = \int \mathcal{D}[\bar{\phi}, \phi] e^{iS[\bar{\phi},\phi]} = 1. \tag{7.88}$$

The $\mathcal{D}[\bar{\phi}, \phi]$ is a symbolic notation for products of differentials, normalized such that $Z = 1$. We will not delve into the details of the $\mathcal{D}$ as it's not important for our purposes; additionally, when we calculate expectation values, we integrate over the same degrees of freedom and we divide by Z, so any extra factor coming from the calculations that doesn't depend on the degrees of freedom in the integral can be safely discarded by reabsorbing it into $\mathcal{D}$ itself.

Ideally, we would like to write the action as a quadratic form

$$S[\bar{\phi}, \phi] = \int_{\mathcal{C}} dt\, \bar{\phi}(t) G^{-1} \phi(t) \tag{7.89}$$

from which we can directly read off $G^{-1}(t)$, i.e. the inverse of the local-in-time Green's function (propagator); here $\mathcal{C}$ is the Keldysh contour shown in Figure 7.1. The peculiarity of the Keldysh contour is that it has an upper branch traveling forward in time ($t > 0$), and a lower branch traveling backward in time ($t < 0$). We can thus split the field ϕ into two components: ϕ_+ on the upper branch (positive time flow), and ϕ_- on the lower branch (negative time flow). The action, therefore, becomes

$$S[\bar{\phi}, \phi] = \int_{\mathcal{C}} dt\, \bar{\phi}(t) G^{-1} \phi(t) = \int_t \left(\bar{\phi}_+(t) G^{-1} \phi_+(t) - \bar{\phi}_-(t) G^{-1} \phi_-(t) \right). \tag{7.90}$$

At this point, we perform the so-called *Keldysh rotation*:[8]

$$\phi_\pm = \frac{\phi_c \pm \phi_q}{\sqrt{2}}, \tag{7.91}$$

Keldysh rotation

where "c" stands for "classical" and "q" stands for "quantum". We collect these two components into a single vector $\psi = (\phi_c, \phi_q)^\intercal$, so that the action is written as the following quadratic form under a single integral:

$$S[\bar{\psi}, \psi] = \int_t \bar{\psi}(t) G^{-1}(t) \psi(t), \tag{7.92}$$

where now the advantage compared to (7.89) is that the integral is performed on the real axis and not along a contour in the complex plane. Finally, if we allow for a Green's function that is non-local in time,[9] a more generic quadratic form for the action is

$$S[\bar{\psi}, \psi] = \int_t \int_{t'} \bar{\psi}(t) G^{-1}(t, t') \psi(t'). \tag{7.93}$$

Notice that, at the steady-state, the Green's function only depends on time differences: $G^{-1}(t, t') = G^{-1}(t - t')$. By using the convolution theorem, one can

[8] Here we are dealing with bosonic systems, so the conjugated fields transform in the same way. For fermions, however, the conjugated fields transform with the opposite sign (see [137]); this produces a different causality structure and different signs when restoring the connection between the functional integral description and the operator formalism, thus resulting in an exchange between commutators and anti-commutators in the definitions of the retarded and of the Keldysh components.

[9] With this notation, if the generic $G^{-1}(t, t')$ is actually local in time then its connection with the local-in-time Green's function defined above is $G^{-1}(t, t') = \delta(t - t')^{-1} G(t')$.

therefore write the action as an integral in frequency space:[10,11]

$$S[\bar{\psi},\psi] = \int_{\omega} \bar{\psi}(\omega) G^{-1}(\omega) \psi(\omega). \tag{7.95}$$

From now on, unless otherwise specified, the Green's function with one time-argument will refer to the non-local-in-time steady-state Green's function $G^{-1}(t,t') = G^{-1}(t-t')$ in (7.93) evaluated at the time difference $t-t'$, and *not* to the local-in-time Green's function in (7.92).

At this point, we take the following definition of the Green's function (consistent with (7.93)) in terms of the original fields:

$$iG(t,t') \doteq \left\langle \phi(t)\bar{\phi}(t') \right\rangle = \int \mathcal{D}[\bar{\phi},\phi] e^{iS[\bar{\phi},\phi]} \phi(t)\bar{\phi}(t'). \tag{7.96}$$

Splitting into $+/-$ fields gives the following four combinations [137]:

$$iG^{<}(t,t') \doteq \left\langle \phi_+(t)\bar{\phi}_-(t') \right\rangle \tag{7.97}$$

$$iG^{>}(t,t') \doteq \left\langle \phi_-(t)\bar{\phi}_+(t') \right\rangle \tag{7.98}$$

$$iG^{T}(t,t') \doteq \left\langle \phi_+(t)\bar{\phi}_+(t') \right\rangle = \theta(t-t')iG^{>}(t,t') + \theta(t'-t)iG^{<}(t,t') \tag{7.99}$$

$$iG^{\tilde{T}}(t,t') \doteq \left\langle \phi_+(t)\bar{\phi}_-(t') \right\rangle = \theta(t'-t)iG^{>}(t,t') + \theta(t-'t)iG^{<}(t,t') \tag{7.100}$$

[10] We employ the following convention on Fourier transforms ($f(\omega) = \mathcal{FT}\{f(t)\}[\omega]$):

$$\begin{cases} f(\omega) = \int_t e^{i\omega t} f(t) & \int_t \equiv \int_{-\infty}^{\infty} dt \\ f(t) = \int_{\omega} e^{-i\omega t} f(\omega) & \int_{\omega} \equiv \int_{-\infty}^{\infty} \frac{d\omega}{2\pi} \end{cases} \tag{7.94}$$

[11] Typically, the propagator $G^{-1}(t)$ in (7.92) contains a free term $i\partial_t$; therefore, $G^{-1}(t,t') = G^{-1}(t-t')$ will contain a term $\delta(t-t')i\partial_{t'}$. The Fourier transform of this term with respect to the time difference is simply ω; therefore, when we encounter an action written locally in time as $S[\bar{\psi},\psi] = \int_t \bar{\psi}(t)\left(i\partial_t\right)\psi(t)$, we can simply rewrite the same action in the frequency representation as $S[\bar{\psi},\psi] = \int_t \bar{\psi}(\omega)\omega\psi(\omega)$. The Fourier transform above can be directly obtained from the convolution theorem. In fact, by defining $D(t-t') = \delta(t-t')i\partial_{t'}$ and $f(t')$ any test function,

$$\begin{aligned} D(\omega)f(\omega) &= \int_{\omega} e^{+i\omega t}\left\{D * f\right\}(t) = \int_{\omega} e^{+i\omega t} \int_{t'} D(t-t')f(t') \\ &= \int_{\omega} e^{+i\omega t} \int_{t'} D(t-t') \int_{\omega'} e^{-i\omega' t'} f(\omega') = \int_{\omega} e^{+i\omega t} \int_{t'} \delta(t-t') \int_{\omega'} \omega' e^{-i\omega' t'} f(\omega') \\ &= \int_{\omega} e^{+i\omega t} \int_{\omega'} \omega' e^{-i\omega' t} f(\omega') = \int_{\omega'} \int_{\omega} e^{-i(\omega'-\omega)t} \omega' f(\omega') \\ &= \int_{\omega'} \delta(\omega'-\omega)\omega' f(\omega') = \omega f(\omega)\,, \end{aligned}$$

from which we obtain the result $D(\omega) = \mathcal{FT}\{D(t)\}[\omega] = \omega$.

where $\theta(t)$ is the Heaviside step function and T and $\tilde{T}$ denote, respectively, the time-ordering and anti-time-ordering operators. For $t = t'$, we regularize the Heaviside step-function by taking $G^T(t,t) = G^{\tilde{T}}(t,t) = G^<(t,t)$, while for $t \neq t'$ one notices that $G^T + G^{\tilde{T}} = G^< + G^>$, i.e. the Green's functions are not independent of each other and since we have found one constraint, we can eliminate one degree of freedom and work with only three objects instead of four. This is precisely what is achieved by the Keldysh rotation (7.91); in this basis, indeed, one defines

$$iG^R(t,t') \doteq \left\langle \phi_c(t)\bar{\phi}_q(t')\right\rangle = \frac{i}{2}\left(G^T - G^{\tilde{T}} - G^< + G^>\right) = \theta(t-t')\left(G^> - G^<\right) \tag{7.101}$$

$$iG^A(t,t') \doteq \left\langle \phi_q(t)\bar{\phi}_c(t')\right\rangle = \frac{i}{2}\left(G^T - G^{\tilde{T}} + G^< - G^>\right) = \theta(t'-t)\left(G^< - G^>\right) \tag{7.102}$$

$$iG^K(t,t') \doteq \left\langle \phi_c(t)\bar{\phi}_c(t')\right\rangle = \frac{i}{2}\left(G^T + G^{\tilde{T}} + G^< + G^>\right) = G^< + G^> \tag{7.103}$$

$$\tag{7.104}$$

so the Green's function has the following structure, called *causality structure*:

$$\begin{aligned} G^{-1} &= \begin{pmatrix} G^K & G^R \\ G^A & 0 \end{pmatrix}^{-1} = \begin{pmatrix} 0 & (G^{-1})^A \\ (G^{-1})^R & (G^{-1})^K \end{pmatrix} \\ &= \begin{pmatrix} 0 & (G^A)^{-1} \\ (G^R)^{-1} & -(G^R)^{-1}G^K(G^A)^{-1} \end{pmatrix}, \end{aligned} \tag{7.105}$$

where G^R (G^A) is called the retarded (advanced) Green's function and G^K is called the Keldysh Green's function. The cancellation of the (q,q) component results from the constraint we've found and reflects the fact that for a classical field the action is zero, while the other three components have the following properties of Hermiticity and anti-Hermiticity:

$$G^A = \left(G^R\right)^\dagger, \qquad G^K = -\left(G^K\right)^\dagger. \tag{7.106}$$

Here, the first property is a manifestation of the causality of the response function; it also allows us to work with just two objects, the retarded and the Keldysh components. The second property is instead a manifestation of the non-equilibrium nature of the Keldysh Green's function.

Connection with operator formalism

Before dealing with a practical example, let's finally restore the connection between the functional integral description and the operator formalism. Take for example a system with a single bosonic field a, i.e. $\left[a, a^\dagger\right] = 1$. From the definition of the retarded Green's function in (7.101) we have:

$$\begin{aligned} iG^R(t,t') &= \left\langle a_c(t)a_q^*(t')\right\rangle = \theta(t-t')\left(G^> - G^<\right) \\ &= \theta(t-t')\left\langle a_-(t)a_+^*(t') - a_+(t)a_-^*(t')\right\rangle \\ &= \theta(t-t')\left\langle \left[a(t), a^\dagger(t')\right]\right\rangle \end{aligned} \tag{7.107}$$

and similarly, from the definition of the Keldysh Green's function in (7.103), we have:

$$\begin{aligned} iG^K(t,t') &= \langle a_c(t)a_c^*(t')\rangle = \big(G^> + G^<\big) \\ &= \big\langle a_-(t)a_+^*(t') + a_+(t)a_-^*(t')\big\rangle \\ &= \big\langle \big\{a(t), a^\dagger(t')\big\}\big\rangle \,. \end{aligned} \tag{7.108}$$

7.3.2 Keldysh action for the Lindblad equation

Example: single-mode cavity

As a first example, we apply the Keldysh formalism to a single-mode cavity in the absence of driving and dissipation. We know that the Hamiltonian of such a system is simply $H = \omega_{\rm cav} a^\dagger a$, so the local-in-time propagator is $i\partial_t - \omega_{\rm cav}$ and the action is:

$$\begin{aligned} S &= \int_{\mathcal{C}} \Big[a^*(t) i\partial_t a(t) - H(t)\Big] = \int_{\mathcal{C}} a^*(t)\Big(i\partial_t - \omega_{\rm cav}\Big)a(t) \\ &= \int_t \Big[a_+^*(t)\Big(i\partial_t - \omega_{\rm cav}\Big)a_+(t) - a_-^*(t)\Big(i\partial_t - \omega_{\rm cav}\Big)a_-(t)\Big] \\ &= \int_\omega \Big[a_+^*(\omega)\Big(\omega - \omega_{\rm cav}\Big)a_+(\omega) - a_-^*(\omega)\Big(\omega - \omega_{\rm cav}\Big)a_-(\omega)\Big] \,, \end{aligned} \tag{7.109}$$

where in the last step we've switched to the frequency representation as discussed before. Then one performs the Keldysh rotation by substituting the expressions in (7.91) for the $+/-$ fields and reads off the components of the Green's function; we will perform this stage below for the open cavity, as it's the system we are actually interested about.

In our open problems, the dynamics is governed by the Lindbladian rather than by the Hamiltonian. What's therefore the equivalent of the action $\int (a^* i\partial_t a - H)$ for a system evolving via a Lindblad equation? We refer the reader to [142] for a thorough discussion; here we will limit ourselves to the intuitive idea that the correct integrand for the action can be read off the proper time-evolution that governs the system.

For a closed system governed by a Hamiltonian, the proper time-evolution is given by the Schrödinger equation:

$$i\partial_t \psi = H\psi \qquad \Longrightarrow \qquad \Big(i\partial_t - H\Big)\psi = 0 \tag{7.110}$$

from which we can read off the action integrand as $(a^* i\partial_t a - H)$, where the fields are time-dependent. For a system whose dynamics is governed by a Lindblad equation, its evolution reads as:

$$i\partial_t \rho = i\mathcal{L}\rho \qquad \Longrightarrow \qquad \Big(i\partial_t - i\mathcal{L}\Big)\rho = 0 \tag{7.111}$$

from which we can read off the action integrand as $(a^* i\partial_t a - i\mathcal{L})$. Now, consider the fact that the density matrix provides time-evolved operators; therefore, we

argue here that, for a generic operator $\mathcal{O}$, $\mathcal{O}\rho$ and $\rho\mathcal{O}$ provide time-evolved operators that flow in opposite directions of time. Specifically, in the process of translating a Lindblad master equation into an action, we perform the following replacements:

$$\mathcal{O}\rho(t) \quad \longrightarrow \quad \mathcal{O}_+(t) \tag{7.112}$$

$$\rho(t)\mathcal{O} \quad \longrightarrow \quad \mathcal{O}_-(t) \tag{7.113}$$

As an example, take the Hermitian contribution to the evolution: $-i\,[H,\rho] = -i\,(H\rho - \rho H)$. The corresponding term in the action in terms of the $+/-$ fields is then $\int_t \left[a_+^* i\partial_t a_+ - a_-^* i\partial_t a_- - (H_+ - H_-)\right]$. Generalizing to a Lindblad dissipator in the form of (7.5) and to a field ϕ, the corresponding action has the form

$$S = \int_t \Bigg\{ \bar{\phi}_+ i\partial_t \phi_+ - \bar{\phi}_- i\partial_t \phi_- - \Big(H_+ - H_-\Big) - i\sum_\alpha \gamma_\alpha \left[2L_{\alpha+}L_{\alpha-}^* - \Big(L_{\alpha+}^* L_{\alpha+} + L_{\alpha-}^* L_{\alpha-}\Big)\right] \Bigg\} \tag{7.114}$$

where the first two terms come from the free propagator, the third one takes into account the Hermitian component, and the last one corresponds to the Lindblad dissipator. In other words, in contrast to the Schrödinger equation, the structure of the Lindblad equation lends itself naturally into a mapping over the $+/-$ fields on the Keldysh contour.

With this recipe, we can turn to the driven-dissipative system of eq. (7.13). For convenience, we rewrite here the Lindblad equation:

Example: driven-dissipative single-mode cavity

$$\dot{\rho} = -i\,[H,\rho] + 2\Gamma_1\left(a\rho a^\dagger - \frac{1}{2}\left\{a^\dagger a,\rho\right\}\right) + 2P_1\left(a^\dagger \rho a - \frac{1}{2}\left\{aa^\dagger,\rho\right\}\right) \tag{7.115}$$

where $H = \omega_{\rm cav} a^\dagger a$.

Via the recipe in (7.114), we can immediately write the corresponding Keldysh action:

$$S = \int_t \Bigg\{ a_+^*\Big(i\partial_t - \omega_{\rm cav}\Big)a_+ - a_-^*\Big(i\partial_t - \omega_{\rm cav}\Big)a_- - i\Gamma_1\left[2a_+a_-^* - \Big(a_+^*a_+ + a_-^*a_-\Big)\right] - iP_1\left[2a_+^*a_- - \Big(a_+a_+^* + a_-a_-^*\Big)\right] \Bigg\}. \tag{7.116}$$

If we perform the Keldysh rotation (7.91) and we go to frequency space (that just amounts to replacing every time argument and $i\partial_t$ with ω), we then get:

$$S = \int_\omega \begin{pmatrix} a_c^* & a_q^* \end{pmatrix} \begin{pmatrix} 0 & \omega - \omega_{\rm cav} - i(\Gamma_1 - P_1) \\ \omega - \omega_{\rm cav} + i(\Gamma_1 - P_1) & 2i(\Gamma_1 + P_1) \end{pmatrix} \begin{pmatrix} a_c \\ a_q \end{pmatrix} \tag{7.117}$$

which immediately allows reading out, as commented before, the following relations:

$$\begin{cases} (G^R)^{-1} = \omega - \omega_{\text{cav}} + i(\Gamma_1 - P_1) \\ (G^A)^{-1} = \omega - \omega_{\text{cav}} - i(\Gamma_1 - P_1) \\ -(G^R)^{-1} G^K (G^A)^{-1} = 2i(\Gamma_1 + P_1) \end{cases} . \tag{7.118}$$

If we finally solve for the Green's function components and we use the connection with the operator formalism outlined in (7.107) and (7.108), we get:

$$G^{R/A}(\omega) = \frac{1}{\omega - \omega_{\text{cav}} \pm i(\Gamma_1 - P_1)} \qquad \text{and} \qquad G^K(\omega) = \frac{-2i(\Gamma_1 + P_1)}{(\omega - \omega_{\text{cav}})^2 + (\Gamma_1 - P_1)^2} . \tag{7.119}$$

Notice in particular the fact that the loss/pumping rates appear in couple as $\Gamma_1 - P_1$, except for the Keldysh Green's function in which they also appear as $\Gamma_1 + P_1$. This is an important signature of the quantum nature of the system, encoded in the Keldysh Green's function, in the same way that it appears, for example, when adding quantum noise to a semiclassical treatment — see (3.7).

The connection with the operator formalism outlined in (7.107) and (7.108) results here in the following relations:

$$G^R(\omega) = \mathcal{FT}\left\{-i\theta(t)\left\langle\left[a(t), a^\dagger(0)\right]\right\rangle\right\} , \qquad G^K(\omega) = \mathcal{FT}\left\{-i\left\langle\left\{a(t), a^\dagger(0)\right\}\right\rangle\right\} . \tag{7.120}$$

This connection provides us with some important results; namely, since the commutator and the anti-commutator at equal times are respectively $\left[a, a^\dagger\right] = 1$ and $\left\{a, a^\dagger\right\} = 2N + 1$, with $a^\dagger a$ the occupation operator, we get that

$$\begin{aligned} \int d\omega\, \mathcal{A}(\omega) &= -2 \int_\omega \text{Im}\, G^R(\omega) = i \int_\omega e^{+i\omega 0} \left(G^R(\omega) - G^A(\omega)\right) \\ &= i\left(G^R(t=0) - G^A(t=0)\right) = \left\langle\left[a(t), a^\dagger(0)\right]\right\rangle = 1 \end{aligned} \tag{7.121}$$

and

$$\int d\omega\, \mathcal{C}(\omega) = i \int_\omega e^{+i\omega 0} G^K(\omega) = i G^K(t=0) = \left\langle\left\{a(t), a^\dagger(0)\right\}\right\rangle = 2n + 1 , \tag{7.122}$$

where we have defined the *spectral function* $\mathcal{A}(\omega)$ and the *cavity correlation function* $\mathcal{C}(\omega)$ to be respectively

Spectral function

$$\mathcal{A}(\omega) \doteq -\frac{1}{\pi} \text{Im} G^R(\omega) \tag{7.123}$$

Cavity correlation function

and

$$\mathcal{C}(\omega) \doteq -\frac{1}{2\pi i} G^K(\omega) , \tag{7.124}$$

and n is the steady-state occupation of the cavity.

We can indeed verify the so-called 0-*th sum rule* (7.121) by noting that the frequency integral corresponds to the integral of a Cauchy-Lorentz PDF:

$$\int d\omega\, \mathcal{A}(\omega) = \int d\omega\, \frac{(\Gamma_1 - P_1)}{(\omega - \omega_{\text{cav}})^2 + (\Gamma_1 - P_1)^2} = 1\,, \tag{7.125}$$

and by using this result in second sum rule (7.122):

$$\int d\omega\, \mathcal{C}(\omega) = \int d\omega\, \frac{\Gamma_1 + P_1}{\Gamma_1 - P_1}\mathcal{A}(\omega) = 2\frac{P_1}{\Gamma_1 - P_1} + 1\,, \tag{7.126}$$

from which we find that, at the stationary state,

$$n = \frac{P_1}{\Gamma_1 - P_1} \tag{7.127}$$

exactly as we've found in (7.76) directly from the Lindblad equation via the equation of motion technique.

7.4 Källén-Lehmann spectral representation of Green's functions

Analytical expressions for the Green's functions can be obtained only for non-interacting systems, i.e. in the absence of nonlinear terms. In general situations, we can exploit the vectorization procedure we've reviewed in Sections 7.2.2 and 7.2.3. The entire knowledge about the evolution of the system is encoded into the diagonalization result, i.e. into the eigenvalues and the right/left eigenvectors of the Lindbladian; we look therefore for a way to express the Green's function in terms of these objects. This representation is called Källén-Lehmann spectral representation, and has the huge advantage that, since eventually we want to perform a numerical diagonalization of the Lindbladian, we can numerically calculate the Green's function even when the system has strong nonlinearities.

We will now proceed to work out the spectral representation of the Green's function in the vectorized representation, closely following the treatment of the fermionic case in [117].

7.4.1 Green's functions and Lindblad equation

Let's first remind the fact that the expectation value of a system operator $\mathcal{O}(t)$ is, in the general,

$$\langle \mathcal{O}(t) \rangle = \text{Tr}(\mathcal{O}(t)\rho_T) = \text{Tr}_S\, \text{Tr}_B(\mathcal{O}\rho_T(t)) = \text{Tr}_S(\mathcal{O}\rho(t)), \tag{7.128}$$

with $\rho(t) = \text{Tr}_B\, \rho_T(t)$ the reduced density matrix of the system (S) obtained by tracing out the bath (B).

What we want to calculate in this case, however, are Green's functions of *two* generic system operators A and B, i.e.

$$iG_{AB}(t+\tau,t) \doteqdot \langle A(t+\tau)B(t)\rangle = \mathrm{Tr}(A(t+\tau)B(t)\rho_T) \tag{7.129}$$

where $\tau \in \mathbb{R}$. It's then useful to define a new system operator

$$B_S(\tau,t) \doteqdot \mathrm{Tr}_R\, e^{-iH\tau} B\rho_T(t) e^{iH\tau}, \tag{7.130}$$

with which the expression for the Green's function is

$$iG_{AB}(t+\tau,t) = \mathrm{Tr}_S(AB_S(\tau,t))\,, \tag{7.131}$$

i.e. it involves a trace over the system degrees of freedom only.

Unfortunately, in order to determine B_S, we still need the total density matrix ρ_T (S+B); there is in general no way to trace the bath away from the total density matrix in order to get an expression involving the system reduced density matrix ρ only. However, under the same Markovian conditions for which the system density matrix evolves via a Lindblad equation, we are able to get a Lindblad-type equation for the evolution of B_S thanks to the *quantum regression theorem* (QRT), which though holds only for $\tau > 0$:

Quantum regression theorem

$$\frac{d}{d\tau} B_S(\tau,t) = \mathcal{L}' B_S(\tau,t) \tag{7.132}$$

with the initial condition

$$B_S(0,t) = \mathrm{Tr}_B\, B\rho_T(t) = B\rho(t). \tag{7.133}$$

It's important to point out that the superoperator $\mathcal{L}'$ is generally different from $\mathcal{L}$ ($\mathcal{L}' = \mathcal{L}$ only in the case in which B is a bosonic operator, see Appendix B in [144]). However, in the vectorized representation, it can be shown that the associated matrices are equal ($\mathcal{L}' = \mathcal{L}$) for any kind of operator (see [117]); so, in particular, the vectorized $|B_S\rangle$ associated to B_S follows exactly the same Lindblad equation for $|\rho\rangle$ (for $\tau > 0$)

$$\frac{d}{d\tau} |B_S(\tau,t)\rangle = \mathcal{L}\, |B_S(\tau,t)\rangle\,, \qquad |B_S(0,t)\rangle = B\,|\rho(t)\rangle \tag{7.134}$$

with the formal solution

$$|B_S(\tau,t)\rangle = e^{\mathcal{L}\tau} B\,|\rho(t)\rangle \tag{7.135}$$

and the Green's function (7.131) can finally be written as, for $\tau > 0$,

$$\begin{aligned} iG_{AB}(t+\tau,t) &= \mathrm{Tr}_S(AB_S(\tau,t)) = \langle I\,|\,AB_S(\tau,t)\,|\,I\rangle \\ &= \langle I\,|\,A\,|\,B_S(\tau,t)\rangle = \left\langle I\,\middle|\,Ae^{\mathcal{L}\tau}B\,\middle|\,\rho(t)\right\rangle. \end{aligned} \tag{7.136}$$

The issue with the restriction that $\tau > 0$ can be dealt with by noticing that

$$iG_{AB}(t+\tau,t) = \Big(iG_{B^\dagger A^\dagger}(t,t+\tau)\Big)^* \tag{7.137}$$

which gives the right time ordering when $\tau < 0$.

At the steady-state, the Green's function can be written as $G(t,t') = G(t-t')$ — see also Section 7.3.1. So, in this case, we define

$$iG_{AB}(t+\tau,t), \quad \tau > 0 \quad \xrightarrow{\text{SS}} \quad iG_{AB}(\tau,+) \tag{7.138}$$

$$iG_{AB}(t+\tau,t), \quad \tau < 0 \quad \xrightarrow{\text{SS}} \quad iG_{AB}(\tau,-) \equiv \Big(iG_{B^\dagger A^\dagger}(-\tau,+)\Big)^* \tag{7.139}$$

where the second argument "+" or "−" reminds us that the first argument as a whole is either positive or negative. Then, from (7.136), we can directly write

$$iG_{AB}(\tau,+) = \theta(\tau)\left\langle I \,\middle|\, Ae^{\mathcal{L}\tau}B \,\middle|\, \rho_{\text{ss}}\right\rangle , \tag{7.140}$$

where we've added a $\theta(\tau)$ in order to make sure that $iG_{AB}(\tau,+) = 0$ for $\tau < 0$.

7.4.2 Spectral representation of Green's functions

We start by finding the spectral representations of $iG_{AB}(\pm t,\pm)$. From (7.140), by inserting two identities (7.84), we have:

$$\begin{aligned} iG_{AB}(t,+) &= \theta(t)\left\langle I \,\middle|\, Ae^{\mathcal{L}\tau}B \,\middle|\, \rho_{\text{ss}}\right\rangle = \theta(t)\left\langle I \,\middle|\, AIe^{\mathcal{L}\tau}IB \,\middle|\, \rho_{\text{ss}}\right\rangle \\ &= \theta(t)\sum_\alpha \langle I \,|\, A \,|\, r_\alpha\rangle \langle l_\alpha \,|\, B \,|\, \rho_{\text{ss}}\rangle e^{\mathcal{L}_\alpha t}. \end{aligned} \tag{7.141}$$

For the negative-time version, we use (7.139) to find (notice the swap of the operators in the subscript and the sign change in the time argument):

$$iG_{BA}(-t,-) = \left(\theta(-t)\sum_\alpha \left\langle I \,\middle|\, A^\dagger \,\middle|\, r_\alpha\right\rangle \left\langle l_\alpha \,\middle|\, B^\dagger \,\middle|\, \rho_{\text{ss}}\right\rangle e^{\mathcal{L}_\alpha t}\right)^* . \tag{7.142}$$

The frequency-domain versions of these expressions are found by performing a Fourier transform[12]

$$\begin{aligned} G_{AB}(\omega,+) &\doteqdot \int_{-\infty}^{+\infty} dt\, e^{i\omega t} G_{AB}(t,+) \\ &= \sum_\alpha \langle I \,|\, A \,|\, r_\alpha\rangle \langle l_\alpha \,|\, B \,|\, \rho_{\text{ss}}\rangle \frac{1}{\omega - i\mathcal{L}_\alpha} \end{aligned} \tag{7.143}$$

$$\begin{aligned} G_{BA}(\omega,-) &\doteqdot \int_{-\infty}^{+\infty} dt\, e^{i\omega t} G_{BA}(-t,-) \\ &= \left(\sum_\alpha \left\langle I \,\middle|\, A^\dagger \,\middle|\, r_\alpha\right\rangle \left\langle l_\alpha \,\middle|\, B^\dagger \,\middle|\, \rho_{\text{ss}}\right\rangle \frac{1}{\omega + i\mathcal{L}_\alpha}\right)^* \end{aligned} \tag{7.144}$$

[12] Notice that $G_{AB}(\pm t,\pm)$ both contain a $\theta(t)$ factor, so the integral is actually performed only for $t > 0$. This is a consequence of the fact that the QRT works only at positive times.

Greater and lesser Green's functions

At this point we generalize the definitions (7.97) and (7.98) by defining the bosonic *greater* and *lesser* Green's functions $G^{>}$ and $G^{<}$ as ($t > 0$)

$$\begin{cases} iG^{>}_{AB}(t) \doteq \langle A(t)B \rangle \\ iG^{<}_{AB}(t) \doteq \langle BA(t) \rangle \end{cases} \tag{7.145}$$

With these expressions, we find that, for $t > 0$,

$$\theta(t)G^{>}_{AB}(t) = -i\theta(t)\langle A(t)B \rangle \equiv G_{AB}(t,+) \tag{7.146}$$

and

$$\theta(t)G^{<}_{AB}(t) = -i\theta(t)\langle BA(t) \rangle = -i\theta(t)\langle B(-t)A \rangle \equiv G_{BA}(-t,-) \tag{7.147}$$

Steady-state retarded Green's function

The steady-state retarded Green's function is defined by generalizing (7.107) as

$$G^{R}_{AB}(t) \doteq -i\theta(t)\langle [A(t), B(0)] \rangle \, . \tag{7.148}$$

By expanding the commutator, we immediately see that

$$\begin{aligned} G^{R}_{AB}(t) &= -i\theta(t)\langle A(t)B \rangle + i\theta(t)\langle BA(t) \rangle \\ &= \theta(t)\Big(G^{>}_{AB}(t) - G^{<}_{AB}(t)\Big) \\ &= G_{AB}(t,+) - G_{BA}(-t,-) \end{aligned} \tag{7.149}$$

By using the last equality, the retarded Green's function in frequency space is then

$$G^{R}_{AB}(\omega) = G_{AB}(\omega,+) - G_{BA}(\omega,-). \tag{7.150}$$

Finally, by directly inserting the expressions (7.143) and (7.144), we get:

Retarded Green's function

$$\begin{aligned} G^{R}_{AB}(\omega) = &\sum_{\alpha} \langle I \,|\, A \,|\, r_\alpha \rangle \langle l_\alpha \,|\, B \,|\, \rho_{\mathrm{ss}} \rangle \frac{1}{\omega - i\mathcal{L}_\alpha} \\ &- \left(\sum_{\alpha} \langle I \,|\, A^\dagger \,|\, r_\alpha \rangle \langle l_\alpha \,|\, B^\dagger \,|\, \rho_{\mathrm{ss}} \rangle \frac{1}{\omega + i\mathcal{L}_\alpha} \right)^* \end{aligned} \tag{7.151}$$

Steady-state Keldysh Green's function

The steady-state Keldysh Green's function is defined by generalizing (7.108) as

$$G^{K}_{AB}(t) \doteq -i\langle \{A(t), B(0)\} \rangle \, . \tag{7.152}$$

By expanding the anticommutator, we immediately see that

$$\begin{aligned} G^{K}_{AB}(t) &= -i\langle A(t)B \rangle - i\langle BA(t) \rangle \\ &= G^{>}_{AB}(t) + G^{<}_{AB}(t) \\ &= \theta(t)G^{>}_{AB}(t) + \theta(-t)G^{<}_{AB}(t) + \theta(t)G^{<}_{AB}(t) + \theta(-t)G^{>}_{AB}(t). \end{aligned} \tag{7.153}$$

We go through the expression term by term, by using (7.146) and (7.147):

- $\theta(t)G^{>}_{AB}(t) \equiv G_{AB}(t,+)$
- $\theta(-t)G^{<}_{AB}(t) = -i\theta(-t)\langle BA(t)\rangle = -i\theta(-t)\langle B(-t)A\rangle \equiv G_{BA}(-t,+)$
- $\theta(t)G^{<}_{AB}(t) \equiv G_{BA}(-t,-)$
- $\theta(-t)G^{>}_{AB}(t) = -i\theta(-t)\langle A(t)B\rangle = -i\theta(-t)\langle AB(-t)\rangle \equiv G_{AB}(t,-)$

So:

$$\begin{aligned} G^{K}_{AB}(t) &= \theta(t)G^{>}_{AB}(t) + \theta(-t)G^{<}_{AB}(t) + \theta(t)G^{<}_{AB}(t) + \theta(-t)G^{>}_{AB}(t) \\ &= G_{AB}(t,+) + G_{BA}(-t,+) + G_{BA}(-t,-) + G_{AB}(t,-) \end{aligned} \tag{7.154}$$

By taking the Fourier transform of the last equality, we find

$$G^{K}_{AB}(\omega) = G_{AB}(\omega,+) + G_{BA}(-\omega,+) + G_{BA}(\omega,-) + G_{AB}(-\omega,-). \tag{7.155}$$

Finally, again by using (7.143) and (7.144), we get:

Keldysh Green's function

$$\begin{aligned} G^{K}_{AB}(\omega) = &\sum_{\alpha} \langle I \,|\, A \,|\, r_\alpha\rangle \langle l_\alpha \,|\, B \,|\, \rho_{\text{ss}}\rangle \frac{1}{\omega - i\mathcal{L}_\alpha} \\ &- \sum_{\alpha} \langle I \,|\, B \,|\, r_\alpha\rangle \langle l_\alpha \,|\, A \,|\, \rho_{\text{ss}}\rangle \frac{1}{\omega + i\mathcal{L}_\alpha} \\ &+ \left(\sum_{\alpha} \langle I \,|\, A^\dagger \,|\, r_\alpha\rangle \langle l_\alpha \,|\, B^\dagger \,|\, \rho_{\text{ss}}\rangle \frac{1}{\omega + i\mathcal{L}_\alpha}\right)^* \\ &- \left(\sum_{\alpha} \langle I \,|\, B^\dagger \,|\, r_\alpha\rangle \langle l_\alpha \,|\, A^\dagger \,|\, \rho_{\text{ss}}\rangle \frac{1}{\omega - i\mathcal{L}_\alpha}\right)^* \end{aligned} \tag{7.156}$$

Single-particle steady-state retarded and Keldysh Green's functions

The expressions (7.151) and (7.156) that we've derived above are for general operators A and B. We are actually interested in the *single-particle* Green's functions, where $A = a_i$ and $B = a^\dagger_j$:

$$G^{R}_{ij}(\omega) \doteq \mathcal{FT}\left\{ -i\theta(t)\left\langle \left[a_i(t), a^\dagger_j(0)\right]\right\rangle \right\}[\omega] \tag{7.157}$$

and

$$G^{K}_{ij}(\omega) \doteq \mathcal{FT}\left\{ -i\left\langle \left\{a_i(t), a^\dagger_j(0)\right\}\right\rangle \right\}[\omega]. \tag{7.158}$$

By direct insertion, we get:

$$G^R_{ij}(\omega) = \sum_\alpha \langle I \,|\, a_i \,|\, r_\alpha \rangle \left\langle l_\alpha \right| a_j^\dagger \left| \rho_{\rm ss} \right\rangle \frac{1}{\omega - i\mathcal{L}_\alpha} - \left(\sum_\alpha \left\langle I \right| a_i^\dagger \left| r_\alpha \right\rangle \langle l_\alpha \,|\, a_j \,|\, \rho_{\rm ss} \rangle \frac{1}{\omega + i\mathcal{L}_\alpha} \right)^* \tag{7.159}$$

$$\begin{aligned} G^K_{ij}(\omega) = &\sum_\alpha \langle I \,|\, a_i \,|\, r_\alpha \rangle \left\langle l_\alpha \right| a_j^\dagger \left| \rho_{\rm ss} \right\rangle \frac{1}{\omega - i\mathcal{L}_\alpha} \\ &- \sum_\alpha \left\langle I \right| a_j^\dagger \left| r_\alpha \right\rangle \langle l_\alpha \,|\, a_i \,|\, \rho_{\rm ss} \rangle \frac{1}{\omega + i\mathcal{L}_\alpha} \\ &+ \left(\sum_\alpha \left\langle I \right| a_i^\dagger \left| r_\alpha \right\rangle \langle l_\alpha \,|\, a_j \,|\, \rho_{\rm ss} \rangle \frac{1}{\omega + i\mathcal{L}_\alpha} \right)^* \\ &- \left(\sum_\alpha \langle I \,|\, a_j \,|\, r_\alpha \rangle \left\langle l_\alpha \right| a_i^\dagger \left| \rho_{\rm ss} \right\rangle \frac{1}{\omega - i\mathcal{L}_\alpha} \right)^* \end{aligned} \tag{7.160}$$

The single-particle Green's function connects $\mathcal{B}_0$ with $\mathcal{B}_{\pm 1}$

A key observation here is that the single-particle Green's function connects only the sector with $k = 0$ with the sectors $k = \pm 1$. Take for example the expression for the retarded Green's function in (7.159): the first piece of the sum lives in the block with $k = -1$, while the second piece lives in the block with $k = +1$. The reason is that both $\langle I|$ and $|\rho_{\rm ss}\rangle$ live in the block with $k = 0$, and the first piece has only terms that create a particle of the original system, either in the steady-state or in the left vacuum. Since k is the difference between the number of particles in the tilde system and the number of particles in the original system, going to a state with one more particle in the original system means decreasing k by one unit. A similar argument holds for the second piece of the sum as well, which instead has operators that increase k by one unit. Under these considerations, we can rewrite (7.159) as

$$G^R_{ij}(\omega) = \sum_{\alpha \in \mathcal{B}_{-1}} \left[\frac{\langle I \,|\, a_i \,|\, r_\alpha \rangle \left\langle l_\alpha \right| a_j^\dagger \left| \rho_{\rm ss} \right\rangle}{\omega - i\mathcal{L}_\alpha} \right] - \sum_{\alpha \in \mathcal{B}_{+1}} \left[\frac{\left(\left\langle I \right| a_i^\dagger \left| r_\alpha \right\rangle \langle l_\alpha \,|\, a_j \,|\, \rho_{\rm ss} \rangle \right)^*}{\omega - i\mathcal{L}^*_\alpha} \right] \tag{7.161}$$

where $\mathcal{B}_{\pm 1}$ indicate the blocks with $k = \pm 1$. The calculation can be simplified even more, at a computational level, if one realizes that the sums can be brought

inside the products:

$$G^R_{ij}(\omega) = \left\langle I \middle| a_i \left[\sum_{\alpha \in \mathcal{B}_{-1}} \frac{|r_\alpha\rangle \langle l_\alpha|}{\omega - i\mathcal{L}_\alpha} \right] a_j^\dagger \middle| \rho_{\text{ss}} \right\rangle - \left(\left\langle I \middle| a_i^\dagger \left[\sum_{\alpha \in \mathcal{B}_{+1}} \frac{|r_\alpha\rangle \langle l_\alpha|}{\omega + i\mathcal{L}_\alpha} \right] a_j \middle| \rho_{\text{ss}} \right\rangle \right)^* \tag{7.162}$$

Since the left and the right eigenvectors form a bi-orthonormal basis, the term $\left[\sum_{\alpha \in \mathcal{B}_{\pm 1}} \frac{|r_\alpha\rangle\langle l_\alpha|}{\omega \pm i\mathcal{L}_\alpha}\right]$ is nothing more than a diagonal matrix $\bar{D}^{\pm}(\omega)$ in this bi-orthogonal basis, with diagonal elements $\frac{1}{\omega \pm i\mathcal{L}_\alpha}$. Since we are working in the occupation number basis, we have to transform back into the diagonalizing basis; from the discussion in Section 7.2.3, it's easy to realize that the matrix $\bar{D}^{-}(\omega)$ expressed in the occupation number basis is

$$X_R \bar{D}^{-}(\omega) X_L^H, \tag{7.163}$$

where $\mathcal{L}_\alpha$, X_R, X_L belong to the block with $k = \pm 1$. All in all, the retarded Green's function can be expressed as the following sequence of matrix products:

$$G^R_{ij}(\omega) = \Big(\langle I| a_i X_{R,-1} \Big) \bar{D}^{-}_{-1}(\omega) \Big(X^H_{L,-1} a_j^\dagger |\rho_{\text{ss}}\rangle \Big) - \Big[\Big(\langle I| a_i^\dagger X_{R,+1} \Big) \bar{D}^{+}_{+1}(\omega) \Big(X^H_{L,+1} a_j |\rho_{\text{ss}}\rangle \Big) \Big]^* \tag{7.164}$$

where we added subscripts corresponding to the blocks' k's and we also grouped the quantities that, for a given (i, j), remain constant. In the same way, one can find an easy expression for the Keldysh component:

$$\begin{aligned} G^K_{ij}(\omega) = & \Big(\langle I| a_i X_{R,-1} \Big) \bar{D}^{-}_{-1}(\omega) \Big(X^H_{L,-1} a_j^\dagger |\rho_{\text{ss}}\rangle \Big) \\ & - \Big(\langle I| a_j^\dagger X_{R,+1} \Big) \bar{D}^{+}_{+1}(\omega) \Big(X^H_{L,+1} a_i |\rho_{\text{ss}}\rangle \Big) \\ & + \Big[\Big(\langle I| a_i^\dagger X_{R,+1} \Big) \bar{D}^{+}_{+1}(\omega) \Big(X^H_{L,+1} a_j |\rho_{\text{ss}}\rangle \Big) \Big]^* \\ & - \Big[\Big(\langle I| a_j X_{R,-1} \Big) \bar{D}^{-}_{-1}(\omega) \Big(X^H_{L,-1} a_i^\dagger |\rho_{\text{ss}}\rangle \Big) \Big]^* \end{aligned} \tag{7.165}$$

7.5 Conclusions

In this Chapter we reviewed the technical toolbox needed in the following ones, using the single-mode cavity as a common thread.

The driven-dissipative systems we are interested in are described via a Lindblad equation for the density matrix, commented in Section 7.1. In Section 7.2, we recast this equation in a matrix form within the superparticle representation;

not only this form is convenient in the light of numerical calculations, but it also proved to be a valuable asset in the derivation of analytical results.

In the following, we also need to be able to calculate response functions. In the non-equilibrium setting, these are calculated via the Keldysh field theory, reviewed in Section 7.3 in the context of systems described by a Lindblad equation. When the analytical calculation of the response functions is not analytically viable, we can obtain them numerically via the exact diagonalization of the Lindblad equation; this is discussed in Section 7.4, where we derived the Källén-Lehmann spectral representation of the response functions.

Chapter 8

Driven-dissipative Bose-Hubbard dimer

In the previous Chapter, we introduced the Lindblad description of a driven-dissipative system, and we established a framework in which the solution of the Lindblad equation can be recast into an eigenvalue problem. The solution of the eigenvalue problem allows us to reconstruct the whole dynamics of the system and, at the same time, to easily calculate its non-equilibrium response function in the Keldysh formalism.

Throughout the whole discussion, we considered the example of a single-mode cavity — possibly with a Kerr (Hubbard-like) nonlinearity — from multiple points of views, and we worked out analytical results in the linear limit. As a next relevant step, we focus here on the analysis of two such coupled nonlinear cavities, called the driven-dissipative Bose-Hubbard dimer (BHD); not only this problem is interesting *per se*, because of the presence of a self-trapping or localization-delocalization transition in the closed case, which has seen a surge of interest from the community in recent times, but also because it can be seen as a toy model of strongly correlated open Markovian quantum systems, since it encodes the basic competition between local dissipative processes, interactions, and non-local coherent hopping processes. Indeed, it will also be an important piece of our discussion in Chapter 9, in the context of the DMFT technique.

Besides its paradigmatic relevance, the driven-dissipative BHD has also been realized experimentally in a variety of quantum light-matter platforms, including superconducting circuits [9, 145], exciton-polaritons in semiconductor microcavities [146–148], and photonic crystals [149, 150].

In the closed isolated case, corresponding to a purely conservative Hamiltonian evolution, the BHD has been extensively studied in Bose-Einstein condensates, in particular its self-trapping, or localization-delocalization [151–157]. Here, an initial imbalance of particles between the two sites of the dimer is either rapidly redistributed by hopping processes leading to a homogeneous configuration or conserved indefinitely, leading to a self-trapped state below a critical ratio between hopping and interaction. This transition corresponds to a spontaneous breaking of the reflection symmetry between the two sites of the dimer. Open-Markovian extensions of the BHD have been mostly focused on the coherently driven case [145, 158–161] or, in the case of the related Jaynes-Cummings Dimer model [108], the purely dissipative case in absence of any external pumping.

The driven-dissipative BHD considered here employs single-particle losses and an incoherent single-particle drive. This case is somewhat peculiar, since it is known that for a perfectly symmetric model the stationary state of the problem is completely independent of Hamiltonian parameters and only set by the ratio between pump and losses [105], so it cannot contain any signature of a putative delocalization transition. In order to explore the competition between hopping and interactions in a dissipative setting, one has therefore to go beyond the analysis of steady-state observables and focus instead on response functions, or to introduce an asymmetry between the two sites of the dimer.

In particular, we prepare the system in different initial states and follow the exact quantum dynamics of the model, characterizing also the properties of the stationary state reached at long times. Furthermore, we focus on the spectral properties of the BHD as encoded in the Green's functions which for open Markovian quantum system, much like their closed system counterpart, contain rich insights on the structure of the single-particle excitations around the stationary state.

This Chapter is organized as follows. In Section 8.1 we introduce the BHD model, and we briefly review some of its properties, while in Section 8.2 we present details on its numerical solution. In Section 8.3 we review the known results about the semiclassical limit and the self-trapping transition in the isolated and dissipative cases. Our results for the quantum dynamics in the symmetric pumping regime are discussed in Section 8.4, while those for finite pump/loss asymmetry are presented in Section 8.5. In Section 8.6 we present our results for the Green's functions of the BHD, starting from closed analytical expressions in the linear case ($U = 0$) followed by an analysis of our numerical results at $U \neq 0$, both with and without a finite pump/loss asymmetry. In Section 8.7 we comment on our results, and we draw the conclusions.

This Chapter is largely based on our publication "Signatures of self-trapping in the driven-dissipative Bose–Hubbard dimer" [162].

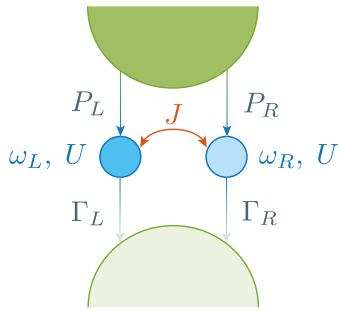

Figure 8.1: Sketch of a driven-dissipative BHD. The left (right) site has a natural frequency ω_L (ω_R); both have a Kerr nonlinearity U and are connected via a hopping of strength J. In most cases considered in the text, $\omega_L = \omega_R = \omega_0$. Both sites are connected to two Markovian environments, a completely full one (above) and a completely empty one (below). These two environments provide, respectively, an incoherent single-particle pumping to the left (right) cavity at a rate P_L (P_R), and single-particle losses to the left (right) cavity at a rate Γ_L (Γ_R).

8.1 The model

We start by considering the Hamiltonian of the Bose-Hubbard dimer (BHD) sketched in Figure 8.1. The model is a paradigmatic interacting lattice model which can be realized in a number of platforms. Our implementation including pumping and losses is naturally realized using optical cavities (see also Section 8.7). For this reason, in the following, we will refer to the two lattice sites as cavities and to the bosonic degrees of freedom involved in the physics as photons. The Hamiltonian reads

$$\hat{H} = \omega_0 \left(\hat{n}_L + \hat{n}_R\right) + U\left(\hat{n}_L\hat{n}_L + \hat{n}_R\hat{n}_R\right) + J\left(\hat{a}_L^\dagger \hat{a}_R + \hat{a}_R^\dagger \hat{a}_L\right), \tag{8.1}$$

Hamiltonian of the BHD

where $\hat{n}_L = \hat{a}_L^\dagger \hat{a}_L$ and $\hat{n}_R = \hat{a}_R^\dagger \hat{a}_R$ are the number operators of the left and the right cavities, respectively. The two cavities have the same resonant frequency ω_0 and Kerr nonlinearity U, and photons can hop between the cavities at a rate J.

We can add a simple mechanism for incoherent driving and dissipation at the master-equation level, by using single-particle pump and loss operators. In practice, we describe the driven-dissipative dimer by a reduced density matrix $\hat{\rho}$ that evolves according to the Lindblad master equation

$$\dot{\hat{\rho}} = \hat{\hat{\mathcal{L}}}\hat{\rho} = \hat{\hat{\mathcal{L}}}_H\hat{\rho} + \hat{\hat{\mathcal{L}}}_D\hat{\rho} \tag{8.2}$$

where

$$\hat{\mathcal{L}}_H\rho = -i\left[\hat{H}, \hat{\rho}\right] \tag{8.3}$$

Single-particle pump/loss mechanisms in the BHD

is the Hermitian part of the evolution, while the dissipative piece reads as

$$\hat{\hat{\mathcal{L}}}_D\hat{\rho} = 2\sum_{i=L,R}\left\{\Gamma_i\left(\hat{a}_i\hat{\rho}\hat{a}_i^\dagger - \frac{1}{2}\left\{\hat{a}_i^\dagger\hat{a}_i,\hat{\rho}\right\}\right) + P_i\left(\hat{a}_i^\dagger\hat{\rho}\hat{a}_i - \frac{1}{2}\left\{\hat{a}_i\hat{a}_i^\dagger,\hat{\rho}\right\}\right)\right\} \tag{8.4}$$

with the constraint that $P_i < \Gamma_i\ \forall i$, as if $\exists i : P_i > \Gamma_i$ single-particle jump operators alone may no longer be sufficient to provide a correct physical description of the system — see also the discussion in Section 7.1.2.

In this form, $\Gamma_{L/R}$ are interpreted as loss rates while $P_{L/R}$ as pumping rates. It is convenient to parametrize them as

$$\Gamma_i = \Gamma \pm \Delta\Gamma/2, \qquad \Delta\Gamma = \Gamma_L - \Gamma_R \tag{8.5}$$

$$P_i = P \pm \Delta P/2, \qquad \Delta P = P_L - P_R \tag{8.6}$$

to distinguish the case in which pump/loss rates are symmetric in the dimer, $\Delta\Gamma = \Delta P = 0$ or asymmetric due to an imbalance of pump and/or losses. In fact, it is known [105] that for a Bose-Hubbard lattice with uniform parameters and identical single-particle pump and loss rates, i.e. $\Delta\Gamma = \Delta P = 0$ the structure of the stationary-state density matrix is particularly simple and reads

$$\hat{\rho}_{\rm ss} = \sum_N \pi_N \left|N\right\rangle\left\langle N\right|$$

where $|N\rangle$ is a Fock state with N bosons and

Structureless stationary state for pump/loss symmetry

$$\pi_N = a\left(\frac{P}{\Gamma}\right)^N, \tag{8.7}$$

where a is a normalization constant. We note in the above expression that $\hat{\rho}_{\rm ss}$ is independent of any Hamiltonian parameter and only set by pump/loss ratio. This implies in particular that the stationary-state occupancy $n_\alpha = \mathrm{Tr}\left(\rho_{\rm ss}\hat{n}_\alpha\right)$ is equal in the two cavities and given by

$$n_L = n_R = \frac{P}{\Gamma - P} \tag{8.8}$$

which coincides with the value of an uncoupled Kerr resonator — see eq. (7.76). It should be clear, however, that this result holds only for stationary-state observables, while time-dependent quantities retain a non-trivial dependence on J/U, as we discuss in Sections 8.4 and 8.6.2. The above result is however no longer true in the presence of a finite asymmetry in the dissipative couplings, leading to $\Delta\Gamma,\ \Delta P \neq 0$, as we will see more in detail in Sections 8.5 and 8.6.3.

8.2 Methods

Diagonalization of the Lindbladian

The vectorized version of equation (8.2) is solved by exact diagonalization, as discussed in detail in Section 7.2, yielding a bi-normalized set of left and right eigenvectors ($\langle l_\alpha|$ and $|r_\alpha\rangle$, respectively) that satisfy

$$\langle l_\alpha | \hat{\mathcal{L}} = \mathcal{L}_\alpha \langle l_\alpha | \qquad \text{and} \qquad \hat{\mathcal{L}} | r_\alpha \rangle = \mathcal{L}_\alpha | r_\alpha \rangle \tag{8.9}$$

where $\hat{\mathcal{L}}$ is the matrix representation of the superoperator $\hat{\hat{\mathcal{L}}}$. The cokernel and the kernel[1] of $\hat{\mathcal{L}}$ are, respectively, the left vacuum $\langle I |$ and the steady-state density matrix $|\rho_{\text{ss}}\rangle$.

Global gauge symmetry

The diagonalization problem can actually be simplified by realizing that both the Hamiltonian and the dissipator posses a global gauge symmetry, expressed by an operator functional $\hat{\hat{\mathcal{K}}}$ that commutes with $\hat{\hat{\mathcal{L}}}$ and that acts as $\hat{\hat{\mathcal{K}}} \bullet = -i \left[\hat{N}, \bullet \right]$, with $\hat{N} = \hat{n}_L + \hat{n}_R$. By exploiting this symmetry, the matrix $\hat{\mathcal{L}}$ can then be written in a block-diagonal form, where each block is labeled by the eigenvalues of $\hat{\hat{\mathcal{K}}}$.

The matrix $\hat{\mathcal{L}}$ and its eigenvectors are written in a basis of Fock states, with a cutoff N_{cutoff} on each particle number. We've fixed $N_{\text{cutoff}} = 20$ throughout the work as a good compromise between accuracy and time and memory costs; this cutoff guarantees that the error on the displayed average steady-state occupations is equal or below 2%, while higher but more expensive cutoffs would not visibly change the results on the Green's functions.

8.2.1 Time dynamics

Having solved the eigenproblem, we can then expand [117]

$$|\rho(t)\rangle = e^{\mathcal{L}t} |\rho(0)\rangle = \sum_\alpha \rho_\alpha(t) |r_\alpha\rangle , \tag{8.10}$$

where

$$\rho_\alpha(t) \doteq e^{\mathcal{L}_\alpha t} \langle l_\alpha | \rho(0) \rangle = e^{\mathcal{L}_\alpha t} \rho_\alpha(0). \tag{8.11}$$

We note that the form of the Lindblad equation ensures $\operatorname{Re} \mathcal{L}_\alpha \leq 0 \; \forall \alpha$, which is a necessary condition to avoid an unbounded growth at long times. Again, if we can exploit the global gauge symmetry, and if the initial density matrix belongs to the null space of $\hat{\hat{\mathcal{K}}}$, then it is sufficient to diagonalize just the largest diagonal block of the Lindbladian. The knowledge of the time-evolution of the density matrix can then be used to calculate the time-evolution of other observables, for example, the occupations of the two cavities ($i = \{L, R\}$):

$$n_i(t) = \operatorname{Tr} \left(\hat{n}_i \rho(t) \right) = \sum_\alpha \langle I \, | \, \hat{n}_i \, | \, r_\alpha \rangle \, \rho_\alpha(t). \tag{8.12}$$

8.2.2 Steady-state Green's functions

As discussed in detail in Section 7.4.2, one can obtain frequency-domain expressions for the retarded and the Keldysh components of the steady-state Green's

[1] The left and right eigenvectors corresponding to the special eigenvalue $\mathcal{L}_0 = 0$.

function. From such expressions in eqs. (7.151) and (7.156), we see that the Green's functions of an open Markovian quantum system can be generically written as a sum of simple poles at complex frequencies given by the eigenvalues of the Lindbladian and with weights, in general complex, given by the transition matrix elements between the stationary state and some excited state of the system [117, 163].

From the practical point of view, if one focuses on the single-particle Green's functions, the calculation can be further simplified via the block-diagonal structure of the Lindbladian outlined above. In fact, as argued in Section 7.4.2, since the calculation of the single-particle Green's functions involves states that differ at most by one particle from the stationary state, it turns out that the full knowledge of the spectrum is not necessary; it is sufficient to diagonalize just the 3 largest blocks of the diagonal-block structure. Assuming that the diagonlization scales as the cube of the matrix linear dimension, this yielded a theoretical 10^4 speedup of the diagonalization with the 20-bosons cutoff we have used in both cavities, as well as a 99.7% reduction of the memory required to store the results — see also Appendix B.

8.3 Review of semiclassical dynamics and self-trapping transition

In order to have a reference point for the analysis of our results, we can start by recalling the predictions of a semiclassical treatment of the quantum dynamics for the BHD [151, 164]. This is obtained by writing the exact equations of motion for the cavity field operators $\hat{a}_{L/R}$ and by closing them by taking $\langle \hat{a}_{L/R} \rangle \to aL/R$, where $a_{L/R}$ are c-numbers. It is important to remark that this approach, which assumes a coherent state of bosons, works for large photon numbers, while in the quantum treatment we are typically interested in systems populated by only a few photons. The resulting equations of motion read

$$\dot{a}_L = -i\Big[(\omega_L - U) + 2U a_L^\dagger a_L\Big] a_L - iJ a_R - \Gamma_L^{\text{eff}} a_L$$
$$\dot{a}_R = -i\Big[(\omega_R - U) + 2U a_R^\dagger a_R\Big] a_R - iJ a_L - \Gamma_R^{\text{eff}} a_R$$

where $\Gamma_{L/R}^{\text{eff}} = \Gamma_{L/R} - P_{L/R}$ are the *effective* loss rates, which for single-particle losses must always be positive.

By applying the transformation

$$a_{L/R} \doteq \alpha_{L/R} e^{i\vartheta_{L/R}}, \qquad \alpha_i, \vartheta_i \in \mathbb{R} \tag{8.13}$$

one can then reduce the equations for the two complex numbers above into the following three equations for real quantities corresponding to the total number of photons $N = n_L + n_R$, to the occupation imbalance between the two cavities

$Z = n_L - n_R$, and to the phase difference $\phi = \vartheta_L - \vartheta_R$:

$$\begin{cases} \dot{N} = -\left(\Gamma_L^{\text{eff}} + \Gamma_R^{\text{eff}}\right) N - \left(\Gamma_L^{\text{eff}} - \Gamma_R^{\text{eff}}\right) Z \\ \dot{Z} = -\left(\Gamma_L^{\text{eff}} + \Gamma_R^{\text{eff}}\right) Z - \left(\Gamma_L^{\text{eff}} - \Gamma_R^{\text{eff}}\right) N \\ \qquad - 2J\sqrt{N^2 - Z^2}\sin(\phi) \\ \dot{\phi} = -\Delta\omega - 2UZ + 2J\dfrac{Z}{\sqrt{N^2 - Z^2}}\cos\phi \end{cases} \tag{8.14}$$

Semiclassical equations of motion

where $n_{L/R} = |\alpha_{L/R}|^2$ and $\Delta\omega = \omega_L - \omega_R$.

8.3.1 Closed system

The closed-system case, corresponding to $\Gamma_{L/R}^{\text{eff}} = 0$, has been studied extensively; experimental realizations [154, 165–167] and theoretical investigations [151, 157, 168–170] were reported in the context of double-well Bose-Einstein condensates, as well as an experimental implementation based on two internal atomic states of ^{87}Rb [171]. In this regime, the equations reduce to — we take $\Delta\omega = 0$ for simplicity:

$$\begin{cases} \dot{N} = 0 \qquad \Longrightarrow \qquad N = N_0 = \text{const.} \\ \dot{Z} = -2J\sqrt{N_0^2 - Z^2}\sin(\phi) \\ \dot{\phi} = -2UZ + 2J\dfrac{Z}{\sqrt{N_0^2 - Z^2}}\cos\phi \end{cases} \tag{8.15}$$

By using the fact that in a closed system the energy is conserved, the two remaining equations can be further reduced to a single equation for the macroscopic occupation imbalance:

$$\dot{Z} = -2\sqrt{p(Z)} \tag{8.16}$$

where $p(Z)$ is a polynomial that can be factorized as

$$p(Z) = -\frac{U^2}{4}\left(Z^2 - Z_0^2\right)\left(Z^2 - Z_1^2\right), \tag{8.17}$$

with Z_0 the initial imbalance and Z_1 equal to

$$Z_1 = \sqrt{Z_0^2 + 4\left(\frac{J}{U}\right)\sqrt{N_0^2 - Z_0^2} - 4\left(\frac{J}{U}\right)^2}. \tag{8.18}$$

The sign of the polynomial $p(Z)$ which appears under square root in the equation of motion (8.16) determines two different regimes. In turn, the sign of $p(Z)$ is completely determined by Z_1 being real or imaginary (since Z_0 is real). If Z_1 is real, then the polynomial is positive only in the region between Z_0 and Z_1 and in the region between $-Z_0$ and $-Z_1$, no matter whether Z_1 is greater or less than Z_0. If instead Z_1 is imaginary, then the polynomial is positive only in the region between $-Z_0$ and Z_0.

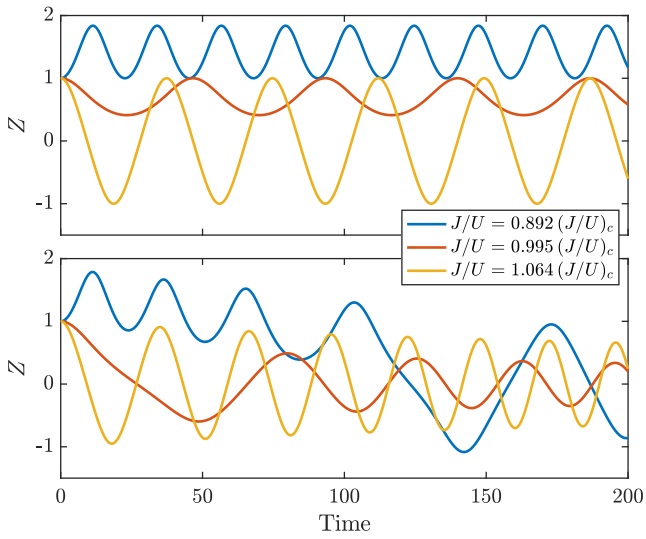

Figure 8.2: Evolution of the occupation imbalance for $N_0 = 3$, $Z_0 = 1$, $U = 0.1$ and $\Delta\omega = 0$. Different colors correspond to different values of J/U around the critical value, predicted via eq. (8.20). The lines in the top panel are for a closed system, while the ones of the same color in the bottom panel are for an open system with $\Gamma_L^{\text{eff}} = \Gamma_R^{\text{eff}} = 4 \times 10^{-4}$; they are obtained respectively by numerically solving the full system of equations discussed in Section 8.3 — see in particular eqs. (8.14) and (8.15).

The nature of Z_1 is in turn determined by the sign of the polynomial

$$\left(\frac{J}{U}\right)^2 - \sqrt{N_0^2 - Z_0^2}\left(\frac{J}{U}\right) - \frac{Z_0^2}{4}. \tag{8.19}$$

If we assume that J/U is positive, then the polynomial above provides a critical $\frac{J}{U}$

Semiclassical critical J/U

$$\left(\frac{J}{U}\right)_{\text{c}} = N_0 \left(\frac{\sqrt{1 - (Z_0/N_0)^2} + 1}{2}\right) \tag{8.20}$$

which depends on the initial total number of photons N_0 and imbalance Z_0. For $\frac{J}{U} < \left(\frac{J}{U}\right)_{\text{c}}$ Z_1 is real and therefore $Z(t)$ oscillates between Z_0 and Z_1; for $\frac{J}{U} > \left(\frac{J}{U}\right)_{\text{c}}$ Z_1 is imaginary and therefore $Z(t)$ oscillates between $-Z_0$ and Z_0 (see Figure 8.2). Then $\left(\frac{J}{U}\right)_{\text{c}}$, in this sense, can be interpreted as a critical value for a transition from a localized regime (low J) to a delocalized regime (high J).

This transition can also be seen as a sharp decay to zero of the time-averaged imbalance $\langle Z \rangle_T = \frac{1}{T}\int_{t_0}^{t_0+T} dt\, Z(t)$ (Figure 8.4, bottom panel), or through the divergence of the oscillation period at the critical point (Figure 8.3), which can

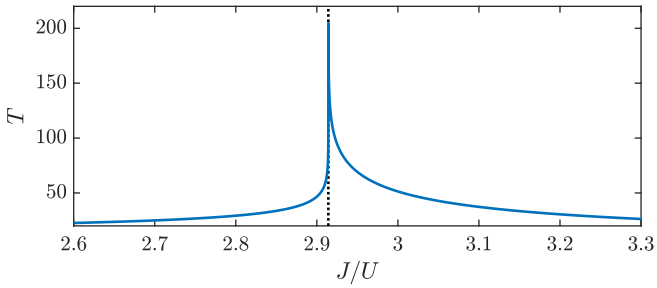

Figure 8.3: Oscillation period T obtained from (8.21) as a function of J/U; the settings are the same as in Figure 8.2.

be analytically expressed as

$$T = \begin{cases} \dfrac{4K\left(\left(\frac{Z_0}{Z_1}\right)^2\right)}{U\sqrt{-Z_1^2}} & \left(\frac{J}{U}\right) > \left(\frac{J}{U}\right)_c \\ \left| \dfrac{2\left[K\left(\left(\frac{Z_0}{Z_1}\right)^2\right) - F\left(\sin^{-1}\left(\frac{Z_1}{Z_0}\right), \left(\frac{Z_0}{Z_1}\right)^2\right)\right]}{U\sqrt{-Z_1^2}} \right| & \left(\frac{J}{U}\right) < \left(\frac{J}{U}\right)_c \end{cases} \tag{8.21}$$

where $F(\varphi, m) = \int_0^\varphi du \frac{1}{\sqrt{1-m^2\sin^2 u}}$ and $K(m) = F(\frac{\pi}{2}, m)$ are respectively the incomplete and the complete elliptic integral of the first kind.

The divergence is logarithmic, as one can infer by approximating the integral around the critical point ($Z_1 \to 0^+$). The fact that the period diverges, making the oscillations slower and slower, is a common signature of a phase transition called the *critical slowing down*.

8.3.2 Open system

The open system case is not analytically solvable, but the numerical solution of the equations for the total number of photons and for the cavity occupation imbalance shows that the closed-system picture is preserved for low enough values of the loss coefficients, with the difference that also in the regime where the oscillations at short times are centered around a non-zero value, the time evolution leads to a transition towards oscillations centered around zero (Figure 8.2, bottom panel). This behavior has been observed experimentally by using exciton-polaritons in two coupled semiconductor microcavities [148].

We can estimate the time at which this dynamical transition happens to be the time t_{cross} for which the imbalance $Z(t)$ crosses the value $Z = 0$ for the first time. If we plot this time as a function of J/U, see top panel of Figure 8.4, we expect that for the closed system this time is divergent for values of J/U below the critical value; for the open system, however, this time assumes finite values even below the critical point and the critical point itself is at a slightly lower value

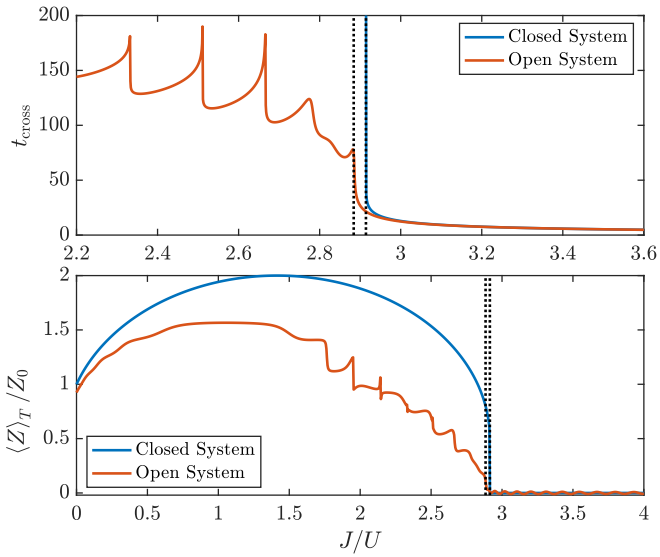

Figure 8.4: (Top) Time t_{cross} at which $Z(t)$ crosses the value $Z = 0$, as a function of J/U. (Bottom) Semiclassical time-averaged imbalance. While the closed system has an analytical expression, the open case requires solving the full dynamics (8.14) and choosing an upper time limit in the integration; in this plot, we integrate up to $t = 200$. In both panels, the critical value of J/U predicted via (8.20) (for the closed system) and as a numerical estimate (for the open system) is shown as a vertical dotted line.

than its closed-system counterpart ($(J/U)_c = 2.88$ vs. $(J/U)_c = 2.91$). The peak structure visible below $(J/U)_c$ for the open system is due to the commensurability between the period of the imbalance oscillations, which is a function of J/U itself, and t_{cross}.

Albeit holding in the limit of large photon number only, these semiclassical results provide a useful hint for the quantities to look at in the quantum case, as well as a point of comparison that highlights the intrinsic differences between the two types of analyses.

8.4 Dissipative quantum dynamics

In this Section we start the analysis of the full numerical solution of the dissipative dynamics of the BHD introduced in Section 8.1. We focus in particular on the occupation imbalance $Z(t) = n_L(t) - n_R(t)$ between the two cavities, which in the semiclassical limit shows a clear change of behavior as a function of the parameters.

In the following we set $\omega_0 = 1$, $U = 0.1$ and consider a situation of symmetric

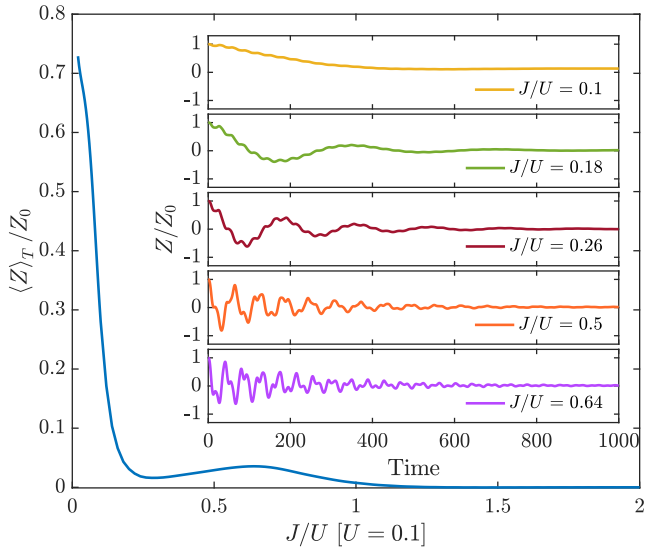

Figure 8.5: (Inset) Imbalance $Z(t) = n_L(t) - n_R(t)$ for different values of J/U $[U = 0.1]$, starting from a state $|3, 1\rangle$ at $t = 0$ ($Z_0 = 2$). The cavities have a base frequency $\omega_0 = 1.0$. The effective loss is $\Gamma_L^{\text{eff}} = \Gamma_R^{\text{eff}} = 1 \times 10^{-4}$ and the pumping rate realizes a steady-state occupation equal to 2 in both cavities, so that $Z_{\text{ss}} = 0$ by construction. The semiclassical, non-dissipative critical value of J/U for this particular configuration is $(J/U)_c \approx 3.73$. The time-averaged occupation imbalance computed over the time interval [0, 1000] is shown in the main panel.

pump and loss rates, $\Delta P = \Delta\Gamma = 0$, so that by construction the imbalance is zero at long times. We set the effective losses $\Gamma_{L/R}^{\text{eff}} = \Gamma_{L/R} - P_{L/R} = 1 \times 10^{-4}$ and the pump $P_{L/R} = 2 \times 10^{-4}$, such that the identical occupation in the two cavities is $n_L = n_R = 2$ (see eq. (8.8)), independently on J/U.

We start discussing the imbalance dynamics as a function from J/U, and we consider as an example an initial configuration with three bosons on the first site and one on the second site, described by the ket $|3, 1\rangle$, corresponding to an initial imbalance $Z_0 = 2$ and to an initial number of photons $N_0 = 4$. At the semiclassical level, see eq. (8.20), this would correspond to a critical coupling $(J/U)_c = 3.73$ for the self-trapping transition.

In the inset of Figure 8.5, we plot the time-dependent imbalance $Z(t)$ for different values of J/U. We find a clear crossover as the hopping is increased, from a pure exponential decay to zero at small $J/U = 0.1$, to an underdamped decay with fast oscillations superimposed at $J/U = 0.26$ which evolves further into strongly anharmonic oscillations at large values of the hopping, whose frequency grows with J/U. We can interpret this behavior as a signature of the self-trapping

transition in the dissipative quantum dynamics. In the small hopping regime each site of the dimer evolves almost independently and the imbalance goes to zero, while for larger values of the hopping there is a substantial transfer of photons across the dimer, resulting in coherent Rabi-like oscillations, before the imbalance reaches the stationary state.

Crossover of the time-averaged imbalance

The J/U dependence can also be studied from the point of view of the time-averaged occupation imbalance $\langle Z \rangle_T$. In contrast to the semiclassical case (Figure 8.4), where one expects a sharp transition[2] between $\langle Z \rangle_T \neq 0$ and $\langle Z \rangle_T = 0$, in the quantum case we have a smooth crossover between the two regimes. The average imbalance drops quickly with J/U due to the development of damped Rabi oscillations, reaching a minimum around $J/U \simeq 0.25$. Quite interestingly, though, we find the appearance of a region in which the imbalance actually *increases* as a function of J/U before completely dropping to 0 at higher values of J/U. We note that, with respect to the semiclassical case, the localized (self-trapped) phase with $\langle Z \rangle_T \neq 0$ is strongly suppressed and that already for $J/U \simeq 1.25$ the average imbalance is zero. This is consistent with the expectation that quantum fluctuations, included in the exact solution and not properly treated in the semiclassical approach, tend to reduce the broken symmetry phase.

We now discuss the dynamics on longer time scales, where we expect the small dissipative couplings to dominate over the Hamiltonian parameters. To this extent in Figure 8.6 we plot the time-dependent imbalance over a broad range of time scales and for different values of J/U. We see a clear separation of dynamical regimes, from a short-time one — strongly dependent on J/U, as we discussed above — to a longer-time one where the imbalance exponentially decays to zero. While naively one could have expected the decay rate to be set only by the dissipative couplings we see in the inset of Figure 8.6 that instead it shows a monotonic increase with J/U.

Finally, we consider the dependence of the time-dependent imbalance $Z(t)$ from the initial condition. To this extent, we fix as an initial density matrix a pure Fock state $\rho_0 = |n_{0L}, n_{0R}\rangle \langle n_{0L}, n_{0R}|$, corresponding to an initial imbalance $Z_0 = n_{0L} - n_{0R}$ and initial photon number $N_0 = n_{0L} + n_{0R}$, and change the values of n_{0L}, n_{0R}. At the semiclassical level, as we see in eq. (8.20), there is a critical value of J/U for any N_0, Z_0. In order to highlight the difference between the exact quantum dynamics and the semiclassical evolution, we fix the value of the hopping to interaction ratio J/U to be always below $(J/U)_c(N_0, Z_0)$, such that at the semiclassical level the system should be localized (self-trapped) at short times for all the chosen initial conditions (see eq. (8.20)) and delocalized at longer times (see Figure 8.2).

We plot in Figure 8.7 the quantum dynamics of the imbalance for different initial conditions. We see that, quite at the opposite of what we expected from the semiclassical analysis, for a fixed $(J/U)/(J/U)_c$ the evolution of $Z(t)$ has a strong dependence on the initial state in which the system is prepared. In particular,

[2] In the open case, the extent of the jump discontinuity in $\partial_{J/U} \langle Z \rangle_T$ depends on the upper limit of the integration time.

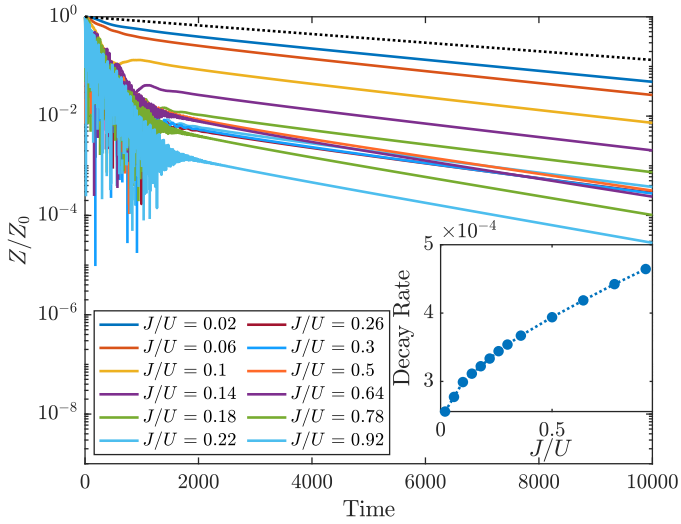

Figure 8.6: Evolution of the imbalance $Z(t)$ for the same settings of Figure 8.5, shown at longer times and at log scale. The black, dotted line is obtained analytically at $J/U = 0$; it corresponds to an exponential decay at a rate $2\Gamma^{\text{eff}}$ — see eq. (7.76). At long times, $\ln(Z(t)/Z_0)$ fits a straight line; the inset shows the corresponding decay rate as a function of J/U.

we find both regimes of slow decay to zero of the imbalance (see for example the initial conditions corresponding to $|3,1\rangle$ or $|4,1\rangle$), indicating localized/self-trapped behavior, as well as regimes of coherent Rabi-like oscillations of the imbalance (see for example the initial conditions corresponding to $|3,2\rangle$ or $|4,3\rangle$) that we can interpret as signatures of delocalization. This is consistent with the observation made earlier (see Figure 8.5) that quantum fluctuations renormalize the critical coupling and favor the delocalized regime. We conclude therefore that, as in the semiclassical case, the self-trapping crossover can be accessed by changing the initial condition; however, we could not identify a simple analytical trend in the dependence of $(J/U)_c$ on the initial values of N_0 and Z_0.

8.5 Quantum steady-state for finite pump/loss asymmetry

In the previous Section, we have considered the case of a BHD with symmetric pump and loss rates, resulting in a trivial stationary state with zero imbalance for any value of J/U, which is however reached after a rich and non-trivial non-equilibrium dynamics.

As we discussed in Section 8.1, in presence of a finite pump/loss asymmetry among the two cavities also the stationary state becomes more interesting. We

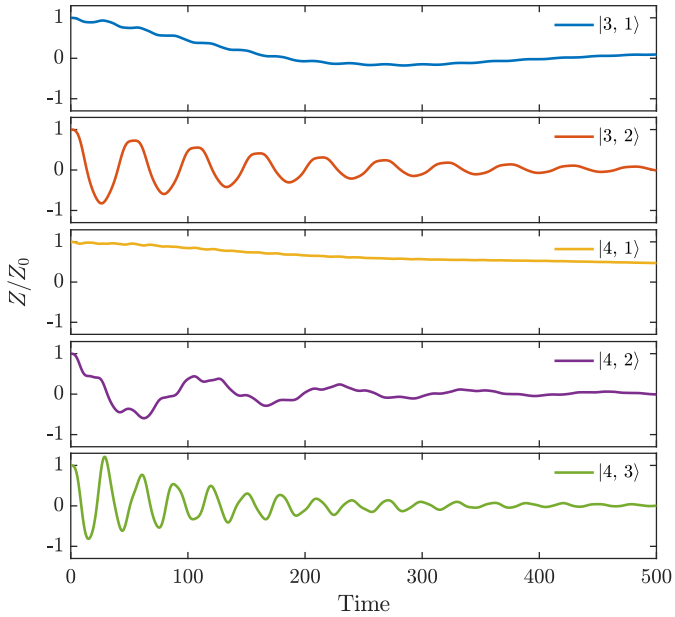

Figure 8.7: Imbalance $Z(t) = n_L(t) - n_R(t)$ for $(J/U) = 0.04(J/U)_c$ $[U = 0.1]$, starting from different $|n_{0L}, n_{0R}\rangle$ number states at $t = 0$. The cavities have a base frequency $\omega_0 = 1.0$. The effective loss is $\Gamma_L^{\text{eff}} = \Gamma_R^{\text{eff}} = 1 \times 10^{-4}$ and the pumping rate realizes a steady-state occupation equal to 2 in both cavities, so that $Z_{\text{ss}} = 0$ by construction. The quantity $(J/U)_c$ refers to the semiclassical non-dissipative value in (8.20).

can therefore look for signatures of a delocalization crossover, analogous to what we have shown in Figure 8.5, directly in observables such as the steady-state occupation or imbalance.

As an example, we consider two cavities with loss coefficients $(\Gamma_L, \Gamma_R) = (6 \times 10^{-2}, 2 \times 10^{-2})$ and pump coefficients $(P_L, P_R) = (4 \times 10^{-2}, 1 \times 10^{-2})$, that according to eq. (8.8) realize steady-state occupations $(n_{0L}, n_{0R}) = (2, 1)$ in the uncoupled limit $J = 0$. In Figure 8.8 we plot, respectively in the top and in the bottom panel, the dependence of the two cavities occupations and imbalance from the hopping to interaction ratio J/U, for different values of U and in units of $\omega_0 = 1$. We see in the top panel that as J/U is increased, the two occupations both converge towards a common value, which is essentially independent of U. The large-J/U limit of the occupations can be obtained analytically by considering the limit $U = 0$ and results in a weighted average of the two uncoupled occupations (see eq. (8.56)).

As a consequence of the two occupations becoming equal at large J/U, we see in the bottom panel that the steady-state imbalance between the two cavities

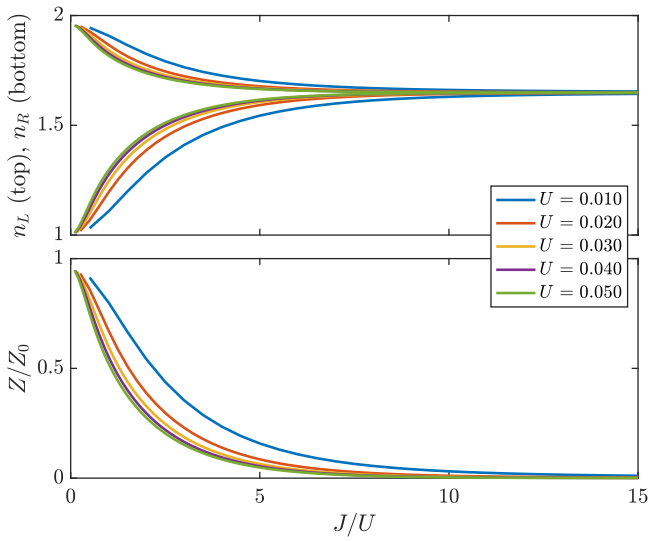

Figure 8.8: (Top) Steady-state cavity occupations as a function of J/U for a dimer with loss coefficients $(\Gamma_L, \Gamma_R) = (6\times10^{-2}, 2\times10^{-2})$ and pump coefficients $(P_L, P_R) = (4\times10^{-2}, 1\times10^{-2})$ described in the main text, at different values of U. The cavities have a base frequency $\omega_0 = 1.0$. The top curves are the occupations of the left cavity, while the bottom ones are the occupations of the right cavity. (Bottom) Steady-state imbalance $Z = n_L - n_R$ corresponding to the occupations in the top panel.

reduces and approaches zero for large enough J/U, a signature of delocalization. We also note that increasing U pushes the crossover J/U scale for delocalization to lower values.

8.6 Green's functions

A way to get some insights on the system even when the steady-state observables depend neither on J nor on U, as in the case of symmetric pump and losses, is to look instead at the single-particle Green's functions. Either by seeing them as the resolvent of the Lindbladian or as response functions that link different states and thus participate in the calculation of transport quantities like the optical transmission, the Green's functions are sensitive to the details of the Lindbladian spectrum, and not only to the zero mode (stationary state), as it appears clearly from the Källén-Lehmann representation derived in Section 7.4.

In this Section we present our results for the Green's function of the BHD, that we obtained from the exact diagonalization of the Lindbladian as discussed in Section 8.2. Specifically, we consider the single-particle Green's functions $G^R_{ij}(\omega)$

and $G^K_{ij}(\omega)$ with $i,j = L/R$, already defined in eqs. (7.157) and (7.158), and in particular the spectral function $\mathcal{A}_{ij}(\omega)$ and the cavity correlation function $\mathcal{C}_{ij}(\omega)$, defined as

$$\mathcal{A}_{ij}(\omega) \doteq -\frac{1}{\pi}\,\mathrm{Im}\,G^R_{ij}(\omega), \qquad \mathcal{C}_{ij}(\omega) \doteq -\frac{1}{2\pi i}G^K_{ij}(\omega) \tag{8.22}$$

with $i,j = L/R$. The diagonal components (for $i = j$) contain information on the local (on-site) spectrum and occupations of the bosonic mode and satisfy the sum rules

Diagonal sum rules

$$\int_{-\infty}^{+\infty} d\omega \mathcal{A}_i(\omega) = 1 \tag{8.23}$$

$$\int_{-\infty}^{+\infty} d\omega\, \mathcal{C}_i(\omega) = 2n_i + 1 \tag{8.24}$$

where n_i is the stationary state occupation. The off-diagonal components contain instead information on the delocalized modes across the dimer. In particular, the correlation function $C_{LR}(\omega)$ has real and imaginary parts which satisfy the sum-rules

Off-diagonal sum rules

$$J\int_{-\infty}^{+\infty} d\omega\ \mathrm{Re}\,\mathcal{C}_{LR}(\omega) = \langle\hat{T}\rangle \tag{8.25}$$

$$J\int_{-\infty}^{+\infty} d\omega\ \mathrm{Im}\,\mathcal{C}_{LR}(\omega) = \langle\hat{I}\rangle \tag{8.26}$$

where $\langle\hat{T}\rangle = J\,\langle\hat{a}^\dagger_L\hat{a}_R + \hat{a}^\dagger_R\hat{a}_L\rangle$ is the average kinetic energy in the stationary state while $\langle\hat{I}\rangle = -iJ\,\langle\hat{a}^\dagger_R\hat{a}_L - \hat{a}^\dagger_L\hat{a}_R\rangle$ is the average current flowing from L to R.

The diagonal sum-rules in (8.24) are the straightforward generalization of the ones we derived for a single cavity in eqs. (7.121) and (7.122). In order to derive eqs. (8.25) and (8.26) note that, by our definitions in eqs. (7.157), (7.158) and (8.22),

$$\int_{-\infty}^{+\infty} d\omega\, e^{-i\omega t}\mathcal{C}_{LR}(\omega) = \langle\hat{a}_L(t)\hat{a}^\dagger_R + \hat{a}^\dagger_R\hat{a}_L(t)\rangle \tag{8.27}$$

and that by taking the Hermitian conjugate we have

$$\int_{-\infty}^{+\infty} d\omega\, e^{i\omega t}\mathcal{C}^*_{LR}(\omega) = \langle\hat{a}_R\hat{a}^\dagger_L(t) + \hat{a}^\dagger_L(t)\hat{a}_R\rangle\,. \tag{8.28}$$

Taking the $t \to 0^+$ limit and the sum/difference of the above two equations we obtain

$$\int_{-\infty}^{+\infty} d\omega\ (\mathcal{C}_{LR}(\omega) + \mathcal{C}^*_{LR}(\omega)) = 2\,\langle\hat{a}^\dagger_L\hat{a}_R + \hat{a}^\dagger_R\hat{a}_L\rangle \tag{8.29}$$

as well as

$$\int_{-\infty}^{+\infty} d\omega\ (\mathcal{C}_{LR}(\omega) - \mathcal{C}^*_{LR}(\omega)) = 2\,\langle\hat{a}^\dagger_R\hat{a}_L - \hat{a}^\dagger_L\hat{a}_R\rangle\,, \tag{8.30}$$

from which eqs. (8.25) and (8.26) follow.

We now discuss some analytical results for these Green's functions in the linear case ($U = 0$), followed by our numerical analysis at $U \neq 0$ of the pump/loss symmetric case and of the role of a finite pump/loss asymmetry.

8.6.1 Analytical Green's functions at $U = 0$

We label the left and right cavities with a subscript L/R. The uncoupled Green's functions, denoted with a lowercase g, are the ones in (7.119) that we derived before for the single cavity, i.e.

$$g_i^{R/A}(\omega) = \frac{1}{\Delta_i \pm i\Gamma_{-i}}, \qquad g_i^K(\omega) = \frac{-2i\Gamma_{+i}}{\Delta_i^2 + \Gamma_{-i}^2} \tag{8.31}$$

where

$$\Delta_i \doteq \omega - \omega_i, \qquad i = L, R \tag{8.32}$$

$$\Gamma_{\pm i} \doteq \Gamma_i \pm P_i, \qquad i = L, R \tag{8.33}$$

In order to find analytical expressions for the L/R Green's functions of the coupled cavities, we have to go back to the Keldysh action and write it as a quadratic form — see the treatment for one cavity in Section 7.3.2. In particular, the action will have a contribution $s_L + s_R$ for the uncoupled L/R cavities, already written as a quadratic form, plus an interaction contribution that has the following form in terms of the $+/-$ fields on the Keldysh contour:

$$S = s_L + s_R + S_{\text{int}} = s_L + s_R - \int_\omega J \left[\left(a_{L+}^* a_{R+} - a_{L-}^* a_{R-}^* \right) + \text{h.c.} \right]. \tag{8.34}$$

After performing the Keldysh rotation, the total action takes the following form:

$$S = \int_\omega \left\{ \bar{\psi}_L g_L^{-1} \psi_L + \bar{\psi}_R g_R^{-1} \psi_R - \left[\left(J \bar{\psi}_L \sigma_x \right) \psi_R + \text{h.c.} \right] \right\} \tag{8.35}$$

where $\psi_i = (a_{i,c}, a_{i,q})^\intercal$ and $\sigma_x = \begin{pmatrix} 0 & 1 \\ 1 & 0 \end{pmatrix}$ is the first Pauli matrix.

The goal is now to write the *total* action S_L for the left cavity as a quadratic form:

$$S_L = \int_\omega \bar{\psi}_L G_L^{-1} \psi_L. \tag{8.36}$$

This is done by integrating out the degrees of freedom of the right cavity, i.e. by writing

$$Z = \int \mathcal{D}[\bar{\psi}_L, \psi_L] \mathcal{D}[\bar{\psi}_R, \psi_R] e^{iS[\bar{\psi}_L, \psi_L, \bar{\psi}_R, \psi_R]} = \int \mathcal{D}[\bar{\psi}_L, \psi_L] e^{iS_L[\bar{\psi}_L, \psi_L]} \tag{8.37}$$

where $S_L[\bar{\psi}_L, \psi_L]$ such that

$$e^{iS_L[\bar{\psi}_L,\psi_L]} = \int \mathcal{D}[\bar{\psi}_R, \psi_R] e^{iS[\bar{\psi}_L,\psi_L,\bar{\psi}_R,\psi_R]} \tag{8.38}$$

is the quadratic action for the left cavity we are looking for.

From (8.35) we can write:

$$\begin{aligned} &\int \mathcal{D}[\bar{\psi}_R, \psi_R] e^{iS[\bar{\psi}_L,\psi_L,\bar{\psi}_R,\psi_R]} \\ &= e^{i\int_\omega \bar{\psi}_L g_L^{-1} \psi_L} \int \mathcal{D}[\bar{\psi}_R, \psi_R] e^{i\int_\omega \left\{\bar{\psi}_R g_R^{-1} \psi_R - [\bar{\eta}_L \psi_R + \text{h.c.}]\right\}}, \end{aligned} \tag{8.39}$$

where $\bar{\eta}_L = \left(J\bar{\psi}_L \sigma_x\right)$ and we can then use the Gaussian integral (see [138])

$$\int \mathcal{D}[\bar{z}, z] e^{-\bar{z}Az + [\bar{w}z + \text{h.c.}]} = \frac{e^{\bar{w}A^{-1}w}}{\det A} \tag{8.40}$$

to get

$$\int \mathcal{D}[\bar{\psi}_R, \psi_R] e^{iS[\bar{\psi}_L,\psi_L,\bar{\psi}_R,\psi_R]} = e^{i\int_\omega \left[\bar{\psi}_L g_L^{-1} \psi_L - \bar{\eta}_L g_R \eta_L\right]}, \tag{8.41}$$

where the extra numerical factors have been reabsorbed into the definition of the path integral differential. From this form, we can immediately read out S_L:

Left cavity effective quadratic action

$$\begin{aligned} S_L &= \int_\omega \left[\bar{\psi}_L g_L^{-1} \psi_L - \bar{\eta}_L g_R \eta_L\right] \\ &= \int_\omega \left[\bar{\psi}_L g_L^{-1} \psi_L - \left(J\bar{\psi}_L \sigma_x\right) g_R \left(J\sigma_x \psi_L\right)\right] \\ &= \int_\omega \bar{\psi}_L \left[g_L^{-1} - J^2 \sigma_x g_R \sigma_x\right] \psi_L \\ &\doteq \int_\omega \bar{\psi}_L G_L^{-1} \psi_L. \end{aligned} \tag{8.42}$$

By using the fact that rotating through σ_x is equivalent to perform two successive reflections along the two main diagonals, i.e.

$$\sigma_x \begin{pmatrix} a & b \\ c & d \end{pmatrix} \sigma_x = \begin{pmatrix} d & c \\ b & a \end{pmatrix}, \tag{8.43}$$

we obtain the matrix equality

$$\begin{aligned} &\begin{pmatrix} 0 & (G_L^A)^{-1} \\ (G_L^R)^{-1} & -(G_L^R)^{-1} G_L^K (G_L^A)^{-1} \end{pmatrix} \\ &= \begin{pmatrix} 0 & (g_L^A)^{-1} \\ (g_L^R)^{-1} & -(g_L^R)^{-1} g_L^K (g_L^A)^{-1} \end{pmatrix} - J^2 \begin{pmatrix} 0 & g_R^A \\ g_R^R & g_R^K \end{pmatrix} \end{aligned} \tag{8.44}$$

i.e.

$$\begin{cases} (G_L^R)^{-1} = (g_L^R)^{-1} - J^2 g_R^R \\ (G_L^A)^{-1} = (g_L^A)^{-1} - J^2 g_R^A \\ (G_L^R)^{-1} G_L^K (G_L^A)^{-1} = (g_L^R)^{-1} g_L^K (g_L^A)^{-1} + J^2 g_R^K \end{cases} \tag{8.45}$$

which clearly shows that the other cavity's (real part of the) Green's function acts as a self-energy term for the cavity itself that shifts the spectral peaks, mediated by the hopping strength, while the imaginary part modifies the spectral linewidth.

Solving the system above eventually leads to the Green's function components for the left cavity:

$$G_L^R(\omega) = \frac{1}{\Delta_L + i\Gamma_{-L} - \frac{J^2}{\Delta_R + i\Gamma_{-R}}} \tag{8.46}$$

Left cavity Green's functions

$$G_L^A(\omega) = (G_L^R(\omega))^* \tag{8.47}$$

$$G_L^K(\omega) = -2i\left[\Gamma_{+L} + J^2 \frac{\Gamma_{+R}}{\Gamma_{+R}^2 + \Gamma_{-R}^2}\right] \left|G_L^R(\omega)\right|^2 \tag{8.48}$$

and the corresponding Green's functions for the right cavity are obtained by simply replacing $L \to R$.

The retarded Green's function of the left cavity can be also rewritten as

$$G_L^R(\omega) = \frac{\Delta_R + i\Gamma_{-R}}{\Delta_+\Delta_- + i\left(\Delta_L\Gamma_{-R} + \Delta_R\Gamma_{-L}\right)} \tag{8.49}$$

where $\Delta_\pm = \omega - \omega_\pm$ and

$$\omega_\pm = \frac{\omega_L + \omega_R}{2} \pm \sqrt{\left(\frac{\omega_L - \omega_R}{2}\right)^2 + J^2 + \Gamma_{-L}\Gamma_{-R}}. \tag{8.50}$$

Since the spectral function is proportional to the imaginary part of the retarded Green's function, this means that the frequency spectrum will be peaked around ω_+ and ω_-, and J will just have the effect of increasing or decreasing the separation between these two peaks.

With these shortcuts, it's possible to further write the spectral function and the cavity correlation function for the left cavity, defined in (8.22), as:

$$\mathcal{A}_L(\omega) = \frac{1}{\pi} \frac{\Gamma_{-L}\left(\Delta_R^2 + \Gamma_{-R}^2\right) + J^2\Gamma_{-R}}{\left[\Delta_+\Delta_-\right]^2 + \left[\left(\Delta_L\Gamma_{-R} + \Delta_R\Gamma_{-L}\right)\right]^2} \tag{8.51}$$

and

$$\mathcal{C}_L(\omega) = \frac{1}{\pi} \frac{\Gamma_{+L}\left(\Delta_R^2 + \Gamma_{-R}^2\right) + J^2\Gamma_{+R}}{\left[\Delta_+\Delta_-\right]^2 + \left[\left(\Delta_L\Gamma_{-R} + \Delta_R\Gamma_{-L}\right)\right]^2}. \tag{8.52}$$

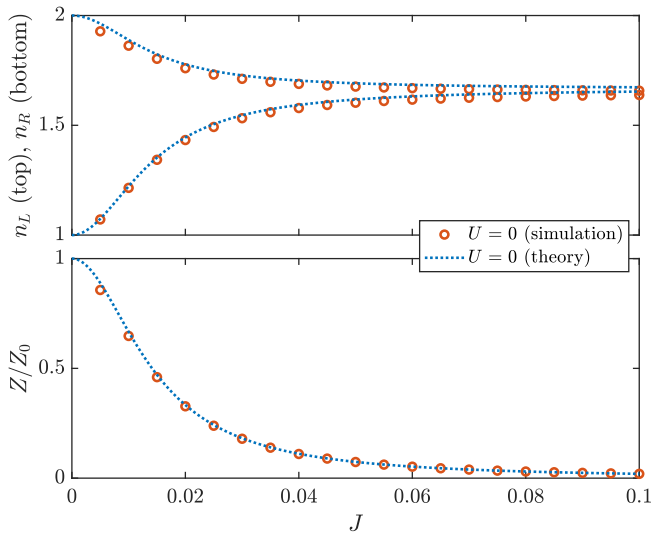

Figure 8.9: (Top) Steady-state cavity occupations as a function of J for the dimer with loss coefficients $(\Gamma_L, \Gamma_R) = (6\times10^{-2}, 2\times10^{-2})$ and pump coefficients $(P_L, P_R) = (4\times10^{-2}, 1\times10^{-2})$ described in Section 8.5, at $U = 0$. The dashed lines are the theoretical results calculated by combining the exact formula for the Keldysh Green's function (8.48) and (8.24). (Bottom) Steady-state imbalance $Z = n_L - n_R$ corresponding to the occupations in the top panel.

In particular, since the spectral function integrates to one, it's useful to factor it out in the expression for the cavity correlation function:

$$\mathcal{C}_L(\omega) = \mathcal{A}_L(\omega)\left[\frac{\Gamma_{+L}\left(\Delta_R^2+\Gamma_{-R}^2\right)+J^2\Gamma_{+R}}{\Gamma_{-L}\left(\Delta_R^2+\Gamma_{-R}^2\right)+J^2\Gamma_{-R}}\right]. \tag{8.53}$$

At this point, the occupations of the two cavities can be calculated via (8.24); analytical expressions can be easily obtained in some limiting cases.

For example, if $\Gamma_{\pm R} = \Gamma_{\pm L}$, you immediately obtain from (8.53) that

$$\int_{-\infty}^{+\infty} d\omega\, \mathcal{C}_L(\omega) = \frac{\Gamma_{+L}}{\Gamma_{-L}} \tag{8.54}$$

and therefore

$$n_L \equiv n_{0L} = \frac{P_L}{\Gamma_L - P_L} \tag{8.55}$$

(and similarly for the right cavity), i.e. the occupation of the cavities at the steady-state is equal to the occupation of the uncoupled cavities ($J = 0$) and it's completely fixed by the pump/loss rates, no matter what the value of J is. This is actually a special case of a result obtained in [105], showing that any number of

cavities with the same incoherent pump/loss rates have a trivial steady-state that does not depend on the details of their Hamiltonian, i.e. in this case neither on J nor on U. This means, in practice, that in order to have non-trivial physics at the steady-state we must have, if not a loss imbalance between the two cavities, at least a *pump imbalance*.

A more interesting case is the one at "large" J, where "large" means much bigger than at least all the loss coefficients. This time, we do not impose any prior condition on the pump/loss rates. If $\omega_L = \omega_R$ for simplicity, then the steady-state occupations become[3]

$$n_L \equiv n_R = \frac{\Gamma_{-L} n_{0L} + \Gamma_{-R} n_{0R}}{\Gamma_{-L} + \Gamma_{-R}}, \tag{8.56}$$

i.e., for large enough coupling the occupation of the left and of the right cavities are equal and equal to a weighted average of their bare occupations.[4]

In particular, if the effective losses are equal ($\Gamma_{-L} = \Gamma_{-R}$), then

$$n_L \equiv n_R = \frac{n_{0L} + n_{0R}}{2}, \tag{8.57}$$

[3]Note that the quantity $\Gamma_{-L/R}$ used in the quantum treatment has the same value of the semiclassical $\Gamma^{\text{eff}}_{L/R}$.

In addition, below the lasing threshold, we can always parameterize $\Gamma_{L/R}$ and $P_{L/R}$ as

$$\Gamma_{L/R} = \Gamma_{-L/R}\left(n_{0L/R} + 1\right)$$

and

$$P_{L/R} = \Gamma_{-L/R} n_{0L/R}\,.$$

[4]In order to prove eq. (8.56) use that in general, by doing a partial fraction decomposition, we have:

$$\frac{ax^2+b}{cx^4+dx^2+e} = \frac{1}{E}\left[\frac{-A+B}{\sqrt{C-D}}\frac{dy_-}{dx}\frac{1}{1+y_-^2} + \frac{A+B}{\sqrt{C+D}}\frac{dy_+}{dx}\frac{1}{1+y_+^2}\right]$$

where $y_\pm = \frac{\sqrt{2c}}{\sqrt{C\pm D}}x$, $A = ad - 2bc$, $B = aD = a\sqrt{d^2-4ce}$, $C = d$, $D = \sqrt{d^2-4ce}$, $E = \sqrt{2c}D = \sqrt{2c}\sqrt{d^2-4ce}$. So, the indefinite integral gives

$$\int dx\,\frac{ax^2+b}{cx^4+dx^2+e} = \frac{1}{E}\left[\frac{-A+B}{\sqrt{C-D}}\arctan\left(\frac{\sqrt{2c}}{\sqrt{C-D}}x\right) + \frac{A+B}{\sqrt{C+D}}\arctan\left(\frac{\sqrt{2c}}{\sqrt{C+D}}x\right)\right].$$

In our case, we first write $\mathcal{C}_L(\omega)$ as $\frac{1}{\pi}\frac{ax^2+b}{cx^4+dx^2+e}$ for some coefficients a, b, c, d, e. Then we replace them in the expressions for A, B, C, D, E while keeping only the leading order in J, obtaining

$$\frac{\pm A + B}{E\sqrt{C\pm D}} = \pm\frac{(\Gamma_{+L}+\Gamma_{+R})}{2(\Gamma_{-L}+\Gamma_{-R})} \qquad \text{and} \qquad \frac{\sqrt{2c}}{\sqrt{C\pm D}} = \frac{-i}{J}\,.$$

Finally, we calculate the definite integral by taking the limits $\omega \to \pm\infty$ and using $\lim_{x\to\infty}\arctan(\pm ix) = \pm\frac{\pi}{2}$, obtaining that

$$\int_{-\infty}^{+\infty} d\omega\,\mathcal{C}_L(\omega) = \frac{\Gamma_{+L}+\Gamma_{+R}}{\Gamma_{-L}+\Gamma_{-R}}\,.$$

i.e. the steady-state occupation of the two cavities is exactly the mean between the bare occupations.

The $J = 0$ and large J limits match our intuitive expectations, i.e. that the occupations of the cavities, as a function of J, start from their uncoupled values and get closer and closer to each other as J is increased, up to the point at which they match each other's value (Figure 8.9).

Another interesting limiting case is obtained if one of the cavities, say e.g. the right one, has $\Gamma_{\pm R} = 0$. Then, for any J, we get — again from (8.24)

$$n_L \equiv n_R \equiv n_{0L}. \tag{8.58}$$

In this case, the uncoupled occupation of the right cavity, n_{0R}, is formally ill-defined; however, it can be easily regularized by taking $P_R = 0$ and $\Gamma_R = \varepsilon$, with $\varepsilon > 0$ arbitrarily small, for which $n_{0R} = 0$.

From a physical point of view, in this case the steady-state occupations in the system are fixed by the only available Markovian environments, i.e. the ones attached to the left cavity, so the occupations become equal as soon as the two cavities are connected ($J > 0$). For this reason, we expect this result to be valid at $U \neq 0$ as well.

Having analytically discussed the $U = 0$ Green's functions, we now consider a non-zero Kerr nonlinearity ($U \neq 0$) in both cavities, and we present our numerical results.

8.6.2 Symmetric pump and losses at $U \neq 0$

We start considering the case of symmetric pump and loss rates, $\Delta\Gamma = \Delta P = 0$. As a result, the system is completely symmetric upon reflection ($L \leftrightarrow R$), and as such the diagonal spectral functions in eq. (8.22) do not depend on the index $i = L/R$. As an example, in Figure 8.10 we plot the spectral function of the left cavity for different values of J/U.

At low J/U the spectral function resembles much the one of a single driven-dissipative Kerr resonator, with a characteristic sequence of peaks located at frequencies given by the energy difference between states with $n+1$ and n photons, $\Delta_n = E_{n+1} - E_n = \omega_0 + U + 2Un$, where $E_n = \omega_0 n + Un^2$ is the energy of the Kerr resonator with n photons (see the Hamiltonian in eq. (8.1)). These peaks, which start at $\omega_0 + U$ and are equally spaced by $2U$, would be infinitely sharp in the closed system while are broadened by the dissipative processes by an amount roughly given by Γ_L^{eff} (it would perfectly match this value in the non-interacting, decoupled case $J = U = 0$, see Section 8.6.1).

As J/U is increased, we see that the first effect is the creation of sub-peaks within each resonance, particularly in the low-frequency ones, with the center of mass of each *band* remaining roughly located at the isolated Kerr excitation energies. Upon increasing further J/U we see how different bands start to merge in a continuum and for $J/U = 0.64$ a new feature arises, namely a finite spectral weight appears below the resonator frequency $\omega_0 = 1$, which becomes a sharp

Bonding/anti-bonding peaks

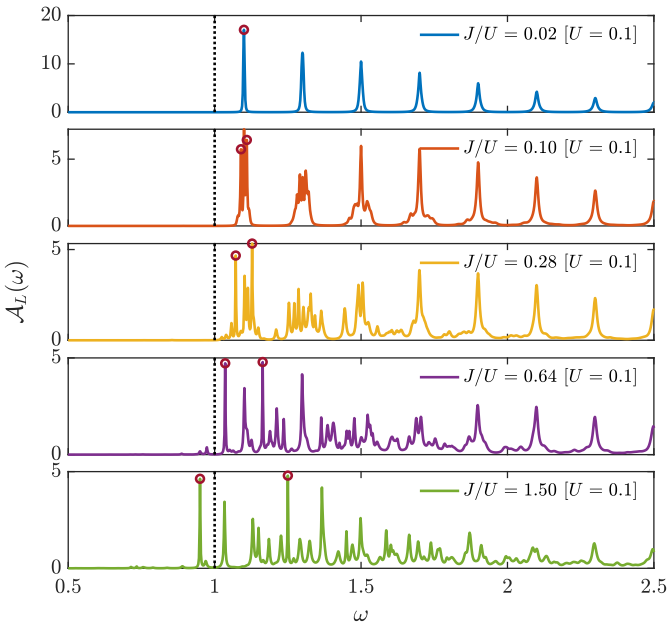

Figure 8.10: Spectral function $\mathcal{A}_L(\omega)$ for different values of J/U [$U = 0.1$]. The cavities have a base frequency $\omega_0 = 1.0$ (vertical dotted line), while the effective loss is $\Gamma_L^{\text{eff}} = \Gamma_R^{\text{eff}} = 1 \times 10^{-4}$ and the pumping rate realizes a steady-state occupation equal to 2 in both cavities. The circled peaks mark the bonding/anti-bonding states resulting from the splitting of the first excited state at $\omega_0 + U$ for decoupled cavities.

peak for large values of J/U (e.g. $J/U = 1.50$). This peak corresponds to a delocalized photonic excitation as one can realize by looking at the spectral function in the opposite limit of $U = 0$ (see Section 8.6.1), which has two poles at frequencies roughly $\omega_\pm \simeq \omega_0 \pm J$ since in this regime the dissipative couplings are very small.

It is interesting to connect these spectral features to the behavior of the time-dependent and of the time-averaged imbalance shown in Figure 8.5 for similar values of J/U. For small values of the hopping, the imbalance is different from zero at short and intermediate times, i.e. photons remain localized in one of the two cavities and the spectral function resembles the one of an isolated Kerr resonator. Upon increasing J/U, photons start to hop coherently within the dimer: the imbalance shows short-time Rabi oscillations with a period controlled by J/U and its time-average vanishes, while spectrally this translates into the emergence of two peaks above and below the bare resonator frequency.

In Figure 8.11 we plot the real part of the off-diagonal correlation function, for different values of J/U and $\Delta\Gamma = \Delta P = 0$. We note that quite interestingly

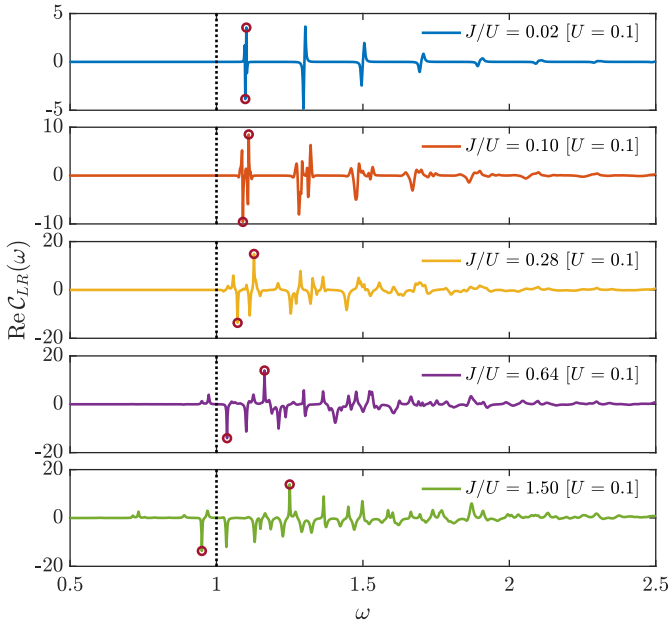

Figure 8.11: Real part of the off-diagonal cavity correlation function $\mathcal{C}_{LR}(\omega)$ for the same parameters considered in Figure 8.10. This function is negative (positive) for the bonding (anti-bonding) states marked by circles and discussed in Figure 8.10.

the imaginary part of this Green's function vanishes in this regime, a point we discuss also in the next Section. At small values of the hopping the real-part $\mathcal{C}_{LR}(\omega)$ is essentially zero, the cavities are almost decoupled, except at frequencies corresponding to the eigenmodes of the (interacting) single cavity (see Figure 8.10 at the same value of J/U), where an anti-resonance like contribution emerges. Upon increasing J/U, as we discussed for the spectral function, further peaks appear which start merging and shifting towards lower frequencies. We note that the structure of the peaks evolves as well: at small J/U they are almost perfectly asymmetric in frequency (leading to a vanishing integral, see eq. (8.25)) while upon increasing J/U, when the system becomes more delocalized, this asymmetry disappears. Furthermore, also the strength of the peaks increases with J/U (note the different scales in the panels) in a way that appears opposite to the peaks in the spectral function in Figure 8.10. This is again consistent with the idea that upon entering the delocalized regime, the weight is transferred from the localized (on-site) modes to the delocalized (off-diagonal ones).

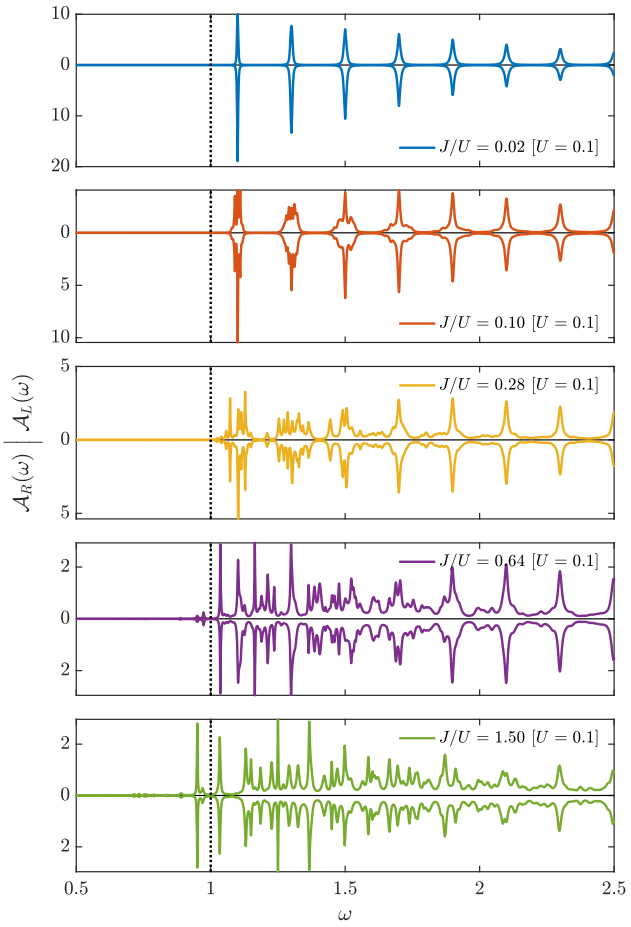

Figure 8.12: Spectral functions $\mathcal{A}_L(\omega)$ (top) and $\mathcal{A}_R(\omega)$ (bottom) for different values of J/U [$U = 0.1$]. The cavities have a base frequency $\omega_0 = 1.0$ (vertical dotted line), while the effective losses are $\Gamma_L^{\text{eff}} = 2.5 \times 10^{-4}$ and $\Gamma_R^{\text{eff}} = 1 \times 10^{-4}$ and the pumping rates realize uncoupled steady-state occupations equal to ~ 3.3 in the left cavity and 2 in the right cavity.

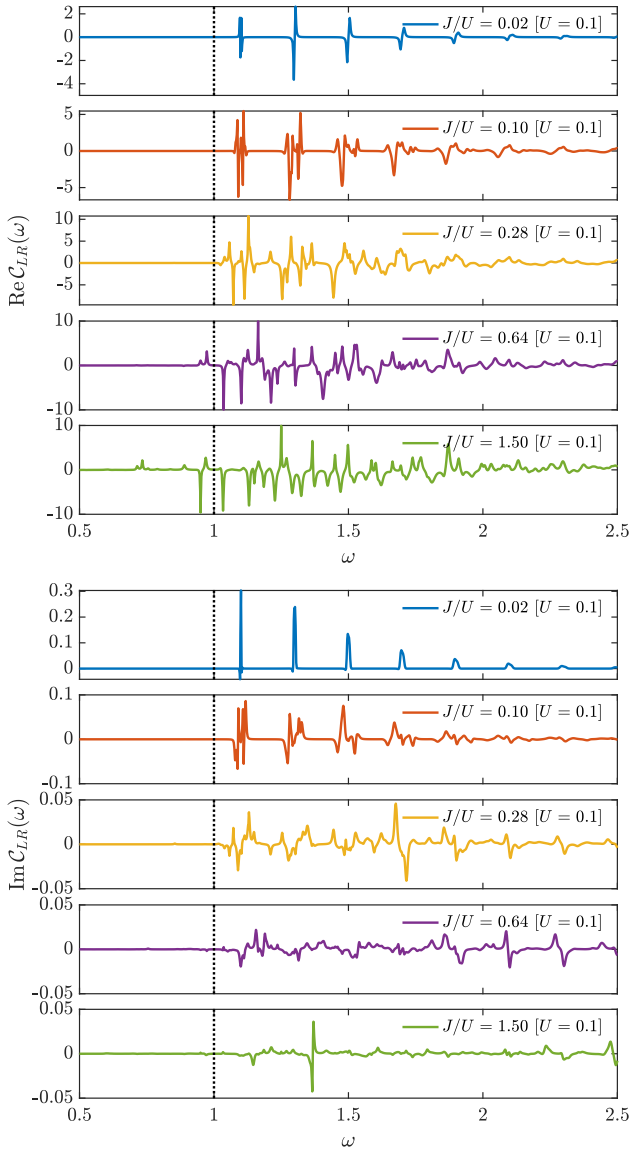

Figure 8.13: Cavity off-diagonal correlation function $C_{LR}(\omega)$ for different values of J/U $[U = 0.1]$. The cavities have a base frequency $\omega_0 = 1.0$ (vertical dotted line), while the effective losses are $\Gamma_L^{\mathrm{eff}} = 2.5 \times 10^{-4}$ and $\Gamma_R^{\mathrm{eff}} = 1 \times 10^{-4}$ and the pumping rates realize uncoupled steady-state occupations equal to ~ 3.3 in the left cavity and 2 in the right cavity.

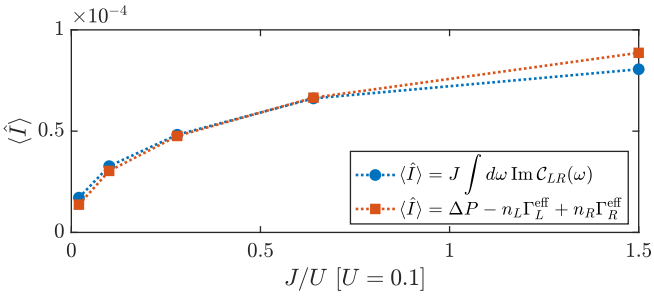

Figure 8.14: Current flowing in the dimer, as obtained from (8.26) and (8.63). The shown values of J/U are the same ones used for the panels of Figures 8.12 and 8.13.

8.6.3 Asymmetric pump and losses at $U \neq 0$

We now move to discuss the case of asymmetric pump and losses, $\Delta P, \Delta\Gamma \neq 0$, resulting as we know in a non-trivial stationary state density matrix (and finite imbalance, see Section 8.5). A natural question is whether this different nonequilibrium protocol results in a qualitatively different behavior of the Green's functions.

We start from the spectral functions, that we plot in Figure 8.12 for a fixed pump/loss asymmetry and different values of J/U. To highlight the comparison between the two cavities, we plot the left and right spectral functions on a common frequency scale. While we see a similar structure of peaks evolving with J/U, as compared to the symmetric case of Figure 8.10, we also note an interesting dependence from the pump/loss asymmetry and the hopping. In particular, for small J/U the right cavity spectral function (bottom panels) has slightly stronger peaks at low frequencies than the left cavity one, reflecting the asymmetry in the pump/loss rates. As the hopping is increased and the excitations are delocalized in the dimer, we see that this asymmetry in the left/right spectral functions decreases and for $J/U = 1.50$ the two spectra are essentially the same and very close in shape to the symmetric one for the same value of J/U (see Figure 8.10).

Then we consider the off-diagonal cavity correlation function, see Figure 8.13, that we study as a function of J/U. In the top panel we plot the real part, $\mathrm{Re}\, \mathcal{C}_{LR}(\omega)$, which shows a qualitative behavior very similar to the symmetric case shown in Figure 8.11, with anti-Lorentzian peaks which broaden and merge into a continuum at large J/U, indicating the increase in kinetic energy. On the other hand, an interesting difference appears in the imaginary part of the off-diagonal cavity correlation function, $\mathrm{Im}\, \mathcal{C}_{LR}(\omega)$, which is now different from zero and shows a non-trivial dependence from J/U, with narrow peaks which broaden and merge into a continuum as J/U is increased.

We can understand the origin of a finite imaginary part of the off-diagonal cavity correlation function by using the sum rule that relates the integral of

$\mathrm{Im}\,\mathcal{C}_{LR}(\omega)$ to the average current flowing from L to R (see eq. (8.26)), and by expressing the latter in terms of the pump/loss asymmetry.

The equations of motion for the BHD, $n_\alpha(t) = \mathrm{Tr}\Big(\hat{\rho}(t)\hat{n}_\alpha\Big)$, with $\alpha = L/R$, read

$$\frac{dn_L}{dt} = i\left\langle\left[\hat{T},\hat{n}_L\right]\right\rangle + 2\Big(P_L + n_L\left(P_L - \Gamma_L\right)\Big) \tag{8.59}$$

$$\frac{dn_R}{dt} = i\left\langle\left[\hat{T},\hat{n}_R\right]\right\rangle + 2\Big(P_R + n_R\left(P_R - \Gamma_R\right)\Big) \tag{8.60}$$

where $\hat{T} = J\Big(\hat{a}_L^\dagger\hat{a}_R + \hat{a}_R^\dagger\hat{a}_L\Big)$ is the kinetic energy operator. The commutator gives

$$\left[\hat{T},\hat{n}_L\right] = -\left[\hat{T},\hat{n}_R\right] = J\Big(\hat{a}_R^\dagger\hat{a}_L - \hat{a}_L^\dagger\hat{a}_R\Big) \equiv i\hat{I}\,. \tag{8.61}$$

If we take the difference between the two equations we obtain for the dynamics of the imbalance $Z = n_L - n_R$ the result

$$\frac{dZ}{dt} = -2\left\langle\hat{I}\right\rangle + 2\Big(\Delta P - n_L\Gamma_L^{\mathrm{eff}} + n_R\Gamma_R^{\mathrm{eff}}\Big)\,, \tag{8.62}$$

where ΔP is the pump asymmetry. In the stationary state, the right-hand side goes to zero, and we obtain

Connection between current and pump/loss imbalance

$$\left\langle\hat{I}\right\rangle = \Delta P - n_L\Gamma_L^{\mathrm{eff}} + n_R\Gamma_R^{\mathrm{eff}}\,. \tag{8.63}$$

We see that the right-hand side of this equation exactly vanishes in the symmetric case $\Delta P = 0$, $\Gamma_L^{\mathrm{eff}} = \Gamma_R^{\mathrm{eff}}$ since as we know the occupations of the two cavities become equal ($n_L = n_R$). On the other hand, for finite pump/loss asymmetry, there is a finite current flowing from L to R and therefore an intra-dimer dissipation. This is interesting since the two cavities are only coupled by a coherent hopping coupling. As a result of this finite current and dissipation, the imaginary part of the off-diagonal cavity correlation function has to be different from zero, both based on the sum-rule in eq. (8.26) and on physical intuition. In Figure 8.14 we plot the average current versus J/U and compare it with the integral over $\mathrm{Im}\,\mathcal{C}_{LR}(\omega)$ to confirm the quantitative agreement. We also see that the overall current, although very small, increases with J/U, an effect which does not appear clearly from the shape of $\mathrm{Im}\,\mathcal{C}_{LR}(\omega)$ in Figure 8.13 but that is consistent with the idea that delocalization leads to a more coherent exchange of excitations between the two cavities and therefore an increased current.

Finally, we have also considered the case of extreme pump/loss asymmetry, corresponding to the situation in which one of the two cavities is non-dissipative, i.e. $\Gamma_R^{\mathrm{eff}} = P_R = 0$. Quite interestingly we have found that also in this case, as for perfectly symmetric rates, the current and the dissipative part of the off-diagonal cavity correlation function $\mathrm{Im}\,\mathcal{C}_{LR}(\omega)$ are both zero, for any value of J/U. We can understand this result from a simple physical picture: in the absence of a Markovian environment coupled to the right cavity, the current flowing from left

to right cannot be dissipated and bounces back, resulting in a zero net current. This can be also understood more formally, by looking at eq. (8.63) and by noting that, for $\Gamma_R^{\text{eff}} = P_R = 0$, this reduces to $\langle \hat{I} \rangle = \Gamma_L^{\text{eff}} (n_{0L} - n_L)$. As we discussed in Section 8.6.1, in the limit $\Gamma_R^{\text{eff}} = P_R = 0$ the left cavity occupation reduces to the one of an isolated left site coupled to Markovian pump and losses, i.e. $n_L = n_{0L}$, resulting therefore in a vanishing current.

8.7 Conclusions

In this Chapter we have analyzed an open Bose-Hubbard dimer, and we have investigated the signatures of a dissipative localization-delocalization transition or crossover where, upon tuning the ratio of coherent hopping versus local interaction, an initial population imbalance is either trapped in one of the two cavities (self-trapping) or equally distributed across the dimer.

In general, such dissipative phase transitions emerge sharply in the limit of thermodynamically large systems [115, 172] — just like their conservative counterparts. In the open-systems context, this has been shown to usually arise when taking the large volume limit at fixed finite-density but also in the limit of large photon numbers, correspondingly to a well-defined classical limit. From this point of view, it is not surprising that for our BHD the localization-delocalization transition that exists at the semiclassical level, and that we reviewed for completeness in Section 8.3, turns in a crossover in the presence of quantum fluctuations. These are in fact particularly strong in the present case, where the system size is finite and therefore the spectrum of the Liouvillian is unavoidably gapped. This does not exclude of course the presence of sharp nonequilibrium phase transitions for arrays of driven-dissipative cavities with incoherent pumping, as it has been indeed recently discussed [13, 163].

In the context of experimental realization of the driven-dissipative BHD, the focus has been mostly on the case of coherently driven cavities, or of purely dissipative (lossy) dynamics; as an example, a driven-dissipative BHD can be obtained in a circuit QED platform by considering the large detuning limit of two coupled Jaynes-Cummings (JC) units, which can be realized by capacitively coupling two resonators, each containing a transmon qubit. However, an incoherent pump can be also engineered by weakly coupling each site of the dimer to a transmission line or to an incoherent noise [173], or to additional sites acting as a dissipative stabilizer [98]. This situation is particularly interesting in the full quantum regime, since it is known that in absence of any asymmetry in the system parameters the stationary state density matrix is independent of any Hamiltonian coupling and only set by the pump and loss coefficients. Therefore, in order to address possible signatures of a dissipative self-trapping crossover, it's necessary to go beyond simple steady-state observables or to explicitly break the symmetry between the two cavities. To this extent, in this Chapter we have exactly solved the problem by numerical diagonalization of the Lindbladian superoperator, and we have obtained the stationary state, the full dissipative quantum dynamics and

the properties of the excitations on top of the stationary state, as encoded in the single-particle Green's functions, see Section 8.2.

In Section 8.4 we have shown that the short-time dissipative dynamics shows clear signatures of a crossover between a localized behavior with finite residual imbalance and coherent oscillations leading to a vanishing imbalance, which can be accessed by either changing the ratio J/U or the initial condition. On the other hand, the long-times dynamics is largely controlled by the dissipative rates. In Section 8.5 we have shown that by breaking the symmetry of pump/loss rates between the two cavities one can induce a non-trivial stationary state and a finite imbalance which shows a smooth delocalization crossover upon increasing J/U.

In Section 8.6 we have presented our results for the single-particle Green's functions, in particular the spectral function and the cavity correlation function describing spectrum and occupation of the bosonic modes. These turn out to be sensitive probes of the Hamiltonian dynamics even in the fully symmetric case, where the delocalization crossover is signaled by the splitting of the lowest energy single-photon peak into bonding and anti-bonding modes as J/U is increased. In presence of a finite pump/loss asymmetry, we have shown that a finite current flows between the left and right cavities and this has direct consequences in the emergence of a non-vanishing imaginary part of the off-diagonal cavity correlation function.

Finally, we point out that, from an experimental point of view, our results for the quantum dynamics of the imbalance or its dependence on external parameters, as well as the Green's functions, can be directly measured experimentally. The former has been done in the context of a Jaynes-Cummings dimer through homodyne detection [9], while the latter can be naturally addressed in a transmission/reflection experiment. Furthermore, the methodology employed in this Chapter, based on the exact diagonalization of a few-sites Lindbladian and on the computation of Green's functions, can be applied to different problems. In particular, in Chapter 9 we will use this methodology to develop an exact-diagonalization Lindblad impurity solver for Dynamical Mean Field Theory (DMFT) [31, 124, 126, 174]; in this scheme, the DMFT self-consistent bath is approximated with a limited number of effective sites. In this respect, we note that a two-site model turns out to share many similarities [175] with a minimal, yet reasonably accurate, implementation of the DMFT using a single site in the bath [176]. The rationale is simply that, in the dimer, one of the two sites plays the role of the self-consistent bath for the other.

Chapter 9

Probing the quantum Zeno effect via dynamical mean-field theory

In the previous Chapters, we built up the necessary technical tools and fundamental building blocks for the treatment of driven-dissipative systems described by a Lindblad equation. In particular, in Chapter 7 we discussed a framework for the exact diagonalization of the Lindblad equation itself, and we briefly reviewed the Keldysh description of out-of-equilibrium Green's functions. We worked out some analytical results for a single nonlinear cavity, upon which we have built in Chapter 8 in order to describe a dimer of coupled nonlinear cavities, the so-called Bose-Hubbard Dimer (BHD). The exact numerical diagonalization allowed us to probe both observables and response functions at the steady-state, as well as to reconstruct the full time-dynamics of observables.

In this Chapter, we combine all the previous techniques with the goal of studying a translationally-invariant driven-dissipative lattice problem; as a paradigmatic example, we can think about a lattice of nonlinear optical cavities, each with some driving and dissipation mechanism. The nonlinear losses considered in the lattice we study here lead, in particular, to the onset of the so-called "Zeno regime", which displays a seemingly paradoxical behavior. This regime was experimentally observed in [18, 177, 178] by using ultracold gases in optical lattices, but the extremely non-local origin of this effect cannot be captured by a simple Gutzwiller mean-field theory. Additionally, the presence of nonlinearities, in general, makes the system not analytically solvable, so one needs to resort to numerical techniques; however, the brute-force diagonalization of a lattice big enough to correctly take into account the translational invariance is out of reach

even for today's most advanced machines.

In order to overcome these problems, we resort to a self-consistent description of the lattice provided by a technique known as Dynamical Mean Field Theory (DMFT), which has long proved its ability to provide a faithful description of strongly-correlated fermionic systems. The idea of DMFT, as we discuss in this Chapter, is to use the Green's function of the lattice as a proxy to calculate a mean interaction (i.e. "field") felt by each lattice site due to the presence of all the other lattice sites. This idea is of course a close relative of the standard mean-field; compared to the latter, however, the word "*dynamical*" indicates that the mean-field is not constant in time, and it's thus able to provide a description of dynamical correlations.

As a first step, in Section 9.1 we introduce the lattice problem we aim to solve and we walk the reader through the basic ideas behind the Dynamical Mean Field Theory (DMFT). Then, in Section 9.2 we present our parametrization of choice of the effective bath as a non-equilibrium Anderson Impurity Model (AIM) and in Section 9.3 we provide the details of the DMFT loop. Finally, in Section 9.4 we solve the lattice problem via the DMFT technique and we uncover the emergence of the Zeno regime. In Section 9.5 we draw the conclusions.

9.1 Model and general idea

9.1.1 Driven-dissipative Bose-Hubbard lattice

We want to study a translationally symmetric lattice of non-linear optical cavities in the normal phase, under single-photon driving and two-photon dissipation. The Hamiltonian of the system, also known as the Bose-Hubbard model, can be written as a local term in the occupation basis, plus a tunneling contribution:

Bose-Hubbard Hamiltonian

$$\hat{H}^{\mathrm{BH}} = \sum_{\mathbf{r}} \left(\omega_0 \hat{n}_{\mathbf{r}} + U \hat{n}_{\mathbf{r}}^2 \right) - \frac{J}{z} \sum_{\langle \mathbf{r}, \mathbf{r}' \rangle} \hat{a}_{\mathbf{r}}^\dagger \hat{a}_{\mathbf{r}'} \tag{9.1}$$

where ω_0 denotes the natural frequency of the cavities located at positions $\{\mathbf{r}\}$, $\hat{n}_{\mathbf{r}} = \hat{a}_{\mathbf{r}}^\dagger \hat{a}_{\mathbf{r}}$ is their occupation operator, U is the strength of the nonlinearity, z is the number of nearest-neighbors and J/z is the tunneling amplitude among any two of the nearest-neighbors indicated by $\langle \mathbf{r}, \mathbf{r}' \rangle$ in the sum.

Under driving and dissipation, the evolution is governed by a Lindblad master equation

$$\dot{\hat{\rho}}^{\mathrm{BH}} = \hat{\mathcal{L}}^{\mathrm{BH}} \hat{\rho}^{\mathrm{BH}} = \hat{\mathcal{L}}_H^{\mathrm{BH}} \hat{\rho}^{\mathrm{BH}} + \hat{\mathcal{L}}_D^{\mathrm{BH}} \hat{\rho}^{\mathrm{BH}} \tag{9.2}$$

where

$$\hat{\mathcal{L}}_H^{\mathrm{BH}} \rho^{\mathrm{BH}} = -i \left[\hat{H}^{\mathrm{BH}}, \hat{\rho}^{\mathrm{BH}} \right] \tag{9.3}$$

is the Hermitian contribution to the time-evolution, while the driven-dissipative contribution can be written as

$$\hat{\mathcal{L}}_D^{\rm BH}\hat{\rho}^{\rm BH} = 2\sum_{\mathbf{r}}\Bigg\{\Gamma_2\left(\hat{a}_{\mathbf{r}}\hat{a}_{\mathbf{r}}\hat{\rho}^{\rm BH}\hat{a}_{\mathbf{r}}^\dagger\hat{a}_{\mathbf{r}}^\dagger - \frac{1}{2}\left\{\hat{a}_{\mathbf{r}}^\dagger\hat{a}_{\mathbf{r}}^\dagger\hat{a}_{\mathbf{r}}\hat{a}_{\mathbf{r}},\hat{\rho}^{\rm BH}\right\}\right) + P_1\left(\hat{a}_{\mathbf{r}}^\dagger\hat{\rho}^{\rm BH}\hat{a}_{\mathbf{r}} - \frac{1}{2}\left\{\hat{a}_{\mathbf{r}}\hat{a}_{\mathbf{r}}^\dagger,\hat{\rho}^{\rm BH}\right\}\right)\Bigg\}. \tag{9.4}$$

Single-photon driving and two-photon losses

In the notation we employed for (9.4), "Γ" ("P") indicates a loss (pump) term, while the subscript "$_1$" or "$_2$" indicates the number of photons involved in the process. The term with amplitude Γ_2 is therefore describing a two-photon loss mechanism, that has to be interpreted as an additional nonlinearity providing a stabilizing gain saturation in the semiclassical limit, while the term with amplitude P_1 describes a single-photon incoherent pump — see the previous discussion in Section 7.1.2.

9.1.2 Sketch of dynamical mean-field theory

As simple as it might look, the system described by eqs. (9.2) and (9.4) is notoriously hard to solve. In this Chapter, in order to get to the solution, we employ a technique known as Dynamical Mean Field Theory (DMFT), originally formulated to study strongly correlated electron systems [31, 179] but extended over the past few years to handle bosonic and non-equilibrium systems as well [124, 126, 174, 180–183]. For more detailed information, we refer the interested reader to one of the recent reviews or walked-through introductions on the subject [31, 174, 179]; here, we limit ourselves to provide an intuitive overview of this technique, sketched in Figure 9.1.

DMFT is a powerful non-perturbative method to solve strongly correlated quantum lattice models, developed in the limit of large coordination z. In particular, the fermionic version becomes exact in the limit of large z, while the equilibrium bosonic version captures, non-perturbatively, the $1/z$ corrections to Gutzwiller mean-field theory through the solution of a quantum impurity model.

DMFT is essentially a mapping of the lattice model onto a quantum impurity model where only one lattice site features nonlinearities. The method can be derived following the scheme outlined below.

1. Assuming translational invariance, one can select one arbitrary lattice site (equivalent to any other) and construct an effective local theory which includes the effect of the rest of the lattice on the "selected" site. The effective local theory is in principle very complicated as it contains all the Green's functions of the rest of the lattice at any order (single-particle, two-particle, three-particle, ...) which make the problem intractable.

   Effective local theory

2. In the spirit of a mean-field theory, the effective theory can be truncated to the first non-trivial term, containing only the single-particle Green's

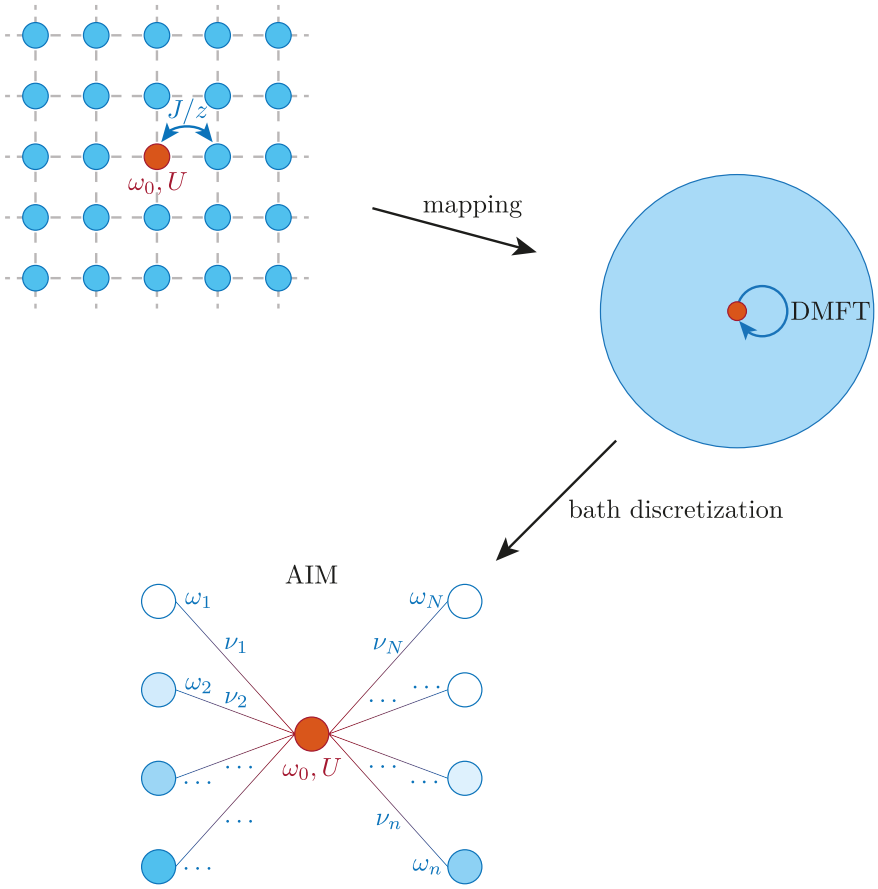

Figure 9.1: Sketch of the DMFT technique, inspired from [31]. We start from a translationally-invariant lattice problem, in which each site (i.e. "cavity") has a Kerr nonlinearity U — and possibly, in the case of driven-dissipative systems, a nonlinearity in the Lindblad dissipator. The lattice sketched here has a nearest-neighbor hopping strength J/z, where z is the lattice coordination number. Since the lattice is translationally invariant, we focus on a single site — marked here in red; at this point, the original lattice problem can be seen as the problem of a single site embedded in some effective bath generated by its interaction with all the other lattice sites. The DMFT technique provides an equation that mathematically connects such bath to the original lattice problem, by discarding spatial correlations in the lattice self-energy. In our case we use a discretized representation of the effective bath, i.e. we represent it as a collection of *linear* cavities (numbered from 1 to N) connected to the representative lattice site from the original lattice. As discussed in Section 9.2, in the case of driven-dissipative systems the bath sites have a (linear) Lindblad dissipator as well.

function of the rest of the lattice. This truncation can be derived rigorously in the limit of large coordination z.

3. The effective local theory, after this simplification, is the same of a quantum impurity model where the "selected" site plays the role of a nonlinear quantum impurity site embedded in a linear medium (or bath) which describes effectively the interaction of the site with the rest of the lattice. The key difference with standard mean-field is that this linear *effective bath* is time- (or frequency-) dependent. This quantity is often called the *dynamical Weiss field*. The impurity self-energy is the DMFT approximation of the lattice self-energy, which implies that the latter is approximated as momentum independent. This can be seen as the crucial approximation underlying the whole DMFT scheme.

Effective bath

DMFT approximation

4. The theory becomes a closed set of equations, since one can prove that the Green's function of the impurity model has to coincide with the local component of the Green's function of the original lattice model within the DMFT approximation. This condition can be written as a self-consistency condition relating the dynamical Weiss field with the impurity Green's function.

DMFT equations

5. This implies that the solution of a lattice model within DMFT requires a self-consistent solution of a quantum impurity model. The self-consistent scheme is implemented iteratively. We start from a guess for the bath or for the Weiss field, then we solve the impurity model computing the Green's function. Using the self-consistency, a new Weiss field is obtained, and the procedure is iterated until convergence.

DMFT loop

6. The engine of a DMFT calculation is a method to solve the impurity model, providing the Green's function or the self-energy. This is usually called the "impurity solver". In this work, we use the exact diagonalization algorithm described in the previous Chapters as an impurity solver. This naturally implies a discretization of the bath, which is described in detail in the following Section 9.2.

Impurity solver

9.2 Non-equilibrium Anderson impurity model

9.2.1 Parametrization of the effective bath

In order to solve the effective impurity model using an exact diagonalization solver, we have to represent the effective bath as a finite (and numerically affordable) matrix. This is usually done, for the fermionic Hamiltonian theory, by expanding the bath function in terms of a finite number of linear auxiliary levels (or sites) whose energies and couplings with the impurity site are chosen in order to represent the dynamical Weiss field. As an example, in Figure 9.1, these tunable parameters are respectively $\omega_1, \ldots, \omega_N$ and $\nu_1, \ldots, \nu_N$ for N bath sites, while

the impurity parameters ω_0 and U are fixed by the original lattice problem. This parametrization choice stems from the fact that, in principle, an infinite number of auxiliary sites would be able to perfectly reproduce any possible effective bath.

This idea can be straightforwardly applied to bosonic Hermitian DMFT as well; however, here we want to attack the non-Hermitian case. We can again take inspiration from what was developed for fermionic non-equilibrium DMFT; in particular, the authors of [124, 125] showed[1] that in order to extend to the non-equilibrium case, it's sufficient to provide the auxiliary sites with Markovian mechanisms of single-particle loss/pump that provide an effective thermalization, thus effectively employing a non-equilibrium AIM.

The ideas developed in [124, 125] can be applied to the bosonic DMFT theory for open systems (OpenBDMFT) as well, with the caveat that in this case also the impurity site has drive and dissipation. One can easily argue that the introduction of driving and dissipation on the bath sites is necessary to properly represent a driven-dissipative lattice system within the DMFT framework. Still, it is sufficient to provide the bath sites with single-particle loss/pump terms even when the lattice model features two-particle terms. This is of course a crucial point, because it means that, even in the presence of driving and dissipation, the lattice model can be mapped onto a single nonlinear site embedded in a linear bath.

So, compared to the Hermitian BDMFT, we can parametrize the auxiliary bath by using not only the energies of the auxiliary cavities and their coupling with the impurity, but also the Lindblad coefficients that describe single-particle pumping/loss processes in the bath. There is however one last additional degree of freedom that we can exploit for our bath parametrization: the choice of the Lindblad jump operators themselves. In fact, since the auxiliary cavities are a mere fitting tool, we can choose their jump operators as we like, provided that they are linear in the particle creation/annihilation operators. In order to see that, consider that the dissipator for the auxiliary bath sites has the typical form

Choice of jump operators

$$\sum_{n=1}^{N_B} \gamma_n \left(\hat{L}_n \hat{\rho} \hat{L}_n^\dagger - \frac{1}{2} \left\{ \hat{L}_n^\dagger \hat{L}_n, \hat{\rho} \right\} \right) \tag{9.5}$$

where N_B is the number of bath sites — again, the subscript "$_0$" is generally reserved for the impurity — and the most general form for the linear jump operators is

$$L_n = \sum_{m=1}^{N_B} U_{nm} l_m \tag{9.6}$$

with $l_m = a_m$ for single-particle losses and $l_m = a_m^\dagger$ for single-particle pumping. The linear combination coefficients U_{nm} form a unitary matrix, because

[1] Compared to [124, 125], which deal with a non-equilibrium though Hermitian problem, here we deal with a non-equilibrium non-Hermitian problem. The difference is that, in contrast to [124, 125], we also have driving and dissipation on the impurity site.

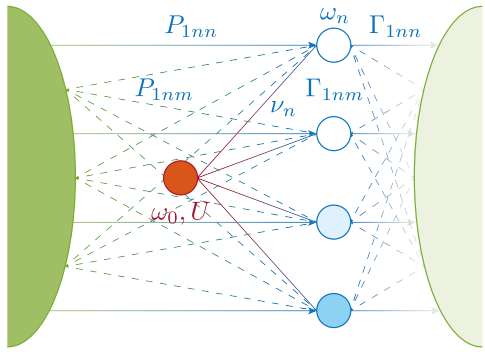

Figure 9.2: Sketch of a typical non-equilibrium AIM used to model a single lattice site plus effective bath in OpenBDMFT. The impurity (central red site) is the only site having nonlinearities, and it's connected to the auxiliary bath sites via some hopping amplitudes ν_n, where $n = 1, \ldots, N_N$ indexes the bath sites. The bath sites have energies ω_n and are connected to a completely full Markovian environment (dark green blob on the left), that provides single-particle pumping, and to a completely empty Markovian environment (light green blob on the right), that provides single-particle losses. The connection is visualized in terms of links corresponding to the Lindblad coefficients, with P_1 and Γ_1 representing the coefficients matrices of the single-particle loss and pump processes, respectively. The diagonal elements of the coefficient matrices correspond to solid lines, while the off-diagonal elements to dashed lines. This form of the effective impurity model was proposed in [124, 125] in the context of a technique called Auxiliary Master Equation Approach (AMEA) developed by the authors. While in the original proposal such an effective model was used to describe a non-equilibrium though still Hermitian lattice model, i.e. a lattice model fully described by a Schrödinger equation and not by a Lindblad equation, here it arises as a natural choice when even the lattice model itself is described by a Lindblad equation.

of the conditions on the Lindblad equation; we can therefore perform a unitary transformation and define a matrix Γ with elements

$$\Gamma_{nm} = U \Lambda U^\dagger, \tag{9.7}$$

where Λ is just a matrix with diagonal elements $\Lambda_{nn} = \gamma_n$ and the associated Lindblad dissipator takes the form

$$\sum_{n,m=1}^{N_B} \Gamma_{nm} \left(\hat{L}_n \hat{\rho} \hat{L}_m^\dagger - \frac{1}{2} \left\{ \hat{L}_m^\dagger \hat{L}_n, \hat{\rho} \right\} \right). \tag{9.8}$$

This shows that the freedom in choosing different jump operators for the auxiliary cavities translates into allowing for non-diagonal Lindblad couplings between

the auxiliary cavities with fixed, standard jump operators — see the sketch in Figure 9.2.

9.2.2 AIM equations

In the light of the discussion above, we can then finally write a non-equilibrium AIM corresponding within DMFT to the lattice model described by eqs. (9.1) to (9.4).

Specifically, we map the Bose-Hubbard lattice with the Hamiltonian H^{BH} in (9.1) into an AIM with the following Hamiltonian H:

AIM Hamiltonian

$$H = \omega_0 a_0^\dagger a_0 + U a_0^\dagger a_0 a_0^\dagger a_0 + \sum_{n=1}^{N_B} \left\{ \omega_n a_n^\dagger a_n + \nu_n a_n^\dagger a_0 + \nu_n^* a_0^\dagger a_n \right\}, \tag{9.9}$$

where we stress that ω_0 and U are the physical parameters of the lattice model used in (9.1), while ω_n and ν_n, $n = 1, \dots, N_B$, are discrete parameters used to represent the Weiss field that is in turn self-consistently determined. Then, the density matrix for the AIM evolves according to the Lindblad equation:

$$\dot{\rho} = \mathcal{L}\rho = \mathcal{L}_H \rho + \mathcal{L}_D \rho \tag{9.10}$$

where

$$\mathcal{L}_H \rho = -i \left[H, \rho \right] \tag{9.11}$$

and

AIM dissipator

$$\begin{aligned} \mathcal{L}_D \rho = 2 \sum_{n,m=0}^{N_B} \Bigg\{ & \Gamma_{1mn} \left(a_n \rho a_m^\dagger - \frac{1}{2} \left\{ a_m^\dagger a_n, \rho \right\} \right) \\ & + P_{1mn} \left(a_m^\dagger \rho a_n - \frac{1}{2} \left\{ a_n a_m^\dagger, \rho \right\} \right) \\ & + \Gamma_{2mn} \left(a_n a_n \rho a_m^\dagger a_m^\dagger - \frac{1}{2} \left\{ a_m^\dagger a_m^\dagger a_n a_n, \rho \right\} \right) \Bigg\}. \end{aligned} \tag{9.12}$$

Since the 0-th site is identical to every lattice site with dissipator (9.4) and the bath must not contain nonlinearities — i.e. neither the Kerr nonlinearity U neither the two-particle losses Γ_2, we make the choices $\Gamma_{10n} = \Gamma_{1n0} = \Gamma_{100}\delta_{n0} \equiv \Gamma_1 \delta_{n0}$, $P_{10n} = P_{1n0} = P_{100}\delta_{n0} \equiv P_1 \delta_{n0}$ and $\Gamma_{2mn} = \Gamma_{200}\delta_{m0}\delta_{n0} \equiv \Gamma_2 \delta_{m0}\delta_{n0}$, i.e. the central site is in contact with Markovian environments which do not provide connections to the other bath sites. Furthermore, we take $\nu_n = \nu_n^*$ in (9.9).

9.2.3 AIM diagonalization

At this point, the AIM in eqs. (9.9) to (9.12) can be numerically solved by diagonalizing the Lindbladian matrix obtained via the vectorization procedure discussed in Chapter 7.

To this end, we start to write the Hermitian and the dissipative contributions to the Lindblad equation (9.10) and (9.11), respectively, in the vectorized notation:

$$\mathcal{L}_H |\rho\rangle = -i\Bigg\{\omega_0(n_0 - \tilde{n}_0) + U(n_0^2 - \tilde{n}_0^2) + \sum_{i=1}^{N_B}\Big[\omega_i\left(n_i - \tilde{n}_i\right) + \nu_i\left(a_i^\dagger a_0 - \tilde{a}_i^\dagger \tilde{a}_0\right) + \nu_i^*\left(a_0^\dagger a_i - \tilde{a}_0^\dagger \tilde{a}_i\right)\Big]\Bigg\}|\rho\rangle \tag{9.13}$$

$$\mathcal{L}_D |\rho\rangle = \sum_{i,j=0}^{N_B}\Bigg\{\Gamma_{1ji}\left(2a_i\tilde{a}_j - a_j^\dagger a_i - \tilde{a}_i^\dagger \tilde{a}_j\right) + P_{1ji}\left(2a_j^\dagger \tilde{a}_i^\dagger - a_i^\dagger a_j - \tilde{a}_j^\dagger \tilde{a}_i\right) \Gamma_{2ji}\left(2a_i a_i \tilde{a}_j \tilde{a}_j - a_j^\dagger a_j^\dagger a_i a_i - \tilde{a}_i^\dagger \tilde{a}_i^\dagger \tilde{a}_j \tilde{a}_j\right)\Bigg\}|\rho\rangle \tag{9.14}$$

Finally, by evaluating $\mathcal{L}_H$ and $\mathcal{L}_D$ as written respectively in (9.13) and (9.14) between two generic elements in the number basis, and by using the fact that the two-particle losses are zero on the bath sites, we have — see Appendix A for more notational details:

$$\begin{aligned}\langle \mathbf{n}'; \tilde{\mathbf{m}}'| \mathcal{L}_H |\mathbf{n}; \tilde{\mathbf{m}}\rangle = -i\left[\sum_{i=0}^{N_B}\omega_i(n_i - m_i) + U(n_0^2 - m_0^2)\right]\delta_{\mathbf{n}',\mathbf{n}}\delta_{\tilde{\mathbf{m}}',\tilde{\mathbf{m}}} \\ - i\sum_{n=1}^{N_B}\Bigg\{\nu_i\Big[\sqrt{n_i' n_0}\,\delta_{n_0',n_0-1}\cdots\delta_{n_i',n_i+1}\cdots\delta_{\tilde{\mathbf{m}}',\tilde{\mathbf{m}}} \\ - \sqrt{m_i' m_0}\,\delta_{\mathbf{n}',\mathbf{n}}\delta_{m_0',m_0-1}\cdots\delta_{m_i',m_i+1}\cdots\Big] \\ + \nu_i^*\Big[\sqrt{n_0' n_i}\,\delta_{n_0',n_0+1}\cdots\delta_{n_i',n_i-1}\cdots\delta_{\tilde{\mathbf{m}}',\tilde{\mathbf{m}}} \\ - \sqrt{m_0' m_i}\,\delta_{\mathbf{n}',\mathbf{n}}\delta_{m_0',m_0+1}\cdots\delta_{m_i',m_i-1}\cdots\Big]\Bigg\}\end{aligned} \tag{9.15}$$

$$
\begin{aligned}
\langle \mathbf{n}'; \tilde{\mathbf{m}}' | \, \mathcal{L}_D \, | \mathbf{n}; \tilde{\mathbf{m}} \rangle = \sum_{i,j=0}^{N_B} \Bigg\{ & \delta_{ij} \Big[-(\Gamma_{1ji} + P_{1ji})(n_i + m_i) - 2P_{1ji} \Big] \delta_{\mathbf{n}',\mathbf{n}} \delta_{\tilde{\mathbf{m}}',\tilde{\mathbf{m}}} \\
& - (1-\delta_{ij})(\Gamma_{1ji} + P_{1ji}) \sqrt{n_i n'_j} \cdots \delta_{n'_i, n_i - 1} \cdots \delta_{n'_j, n_j + 1} \cdots \delta_{\tilde{\mathbf{m}}',\tilde{\mathbf{m}}} \\
& - (1-\delta_{ij})(\Gamma_{1ji} + P_{1ji}) \sqrt{m'_j m_i} \delta_{\mathbf{n}',\mathbf{n}} \delta_{m'_i, m_i + 1} \cdots \delta_{m'_j, m_j - 1} \cdots \\
& + 2\Gamma_{1ji} \sqrt{n_i m_j} \cdots \delta_{n'_i, n_i - 1} \cdots \delta_{m'_j, m_j - 1} \cdots \\
& + 2P_{1ji} \sqrt{n'_i m'_j} \cdots \delta_{n'_j, n_j + 1} \cdots \delta_{m'_i, m_i + 1} \cdots \Bigg\} \\
& + \Gamma_{200} \Bigg\{ - \Big[n_0(n_0 - 1) + m_0(m_0 - 1) \Big] \delta_{\mathbf{n}',\mathbf{n}} \delta_{\tilde{\mathbf{m}}',\tilde{\mathbf{m}}} \\
& + 2\sqrt{n_0(n_0 - 1) + m_0(m_0 - 1)} \cdots \delta_{n'_0, n_0 - 2} \cdots \delta_{m'_0, m_0 - 2} \cdots \Bigg\}
\end{aligned}
\tag{9.16}
$$

where the dots "$\cdots$" indicate Kronecker deltas of type $\delta_{n'_i,n_i}$ and $\delta_{m'_i,m_i}$, and we remind that the values ω_0, U, $\Gamma_{100} \equiv \Gamma_1$, $P_{100} \equiv P_1$ and $\Gamma_{200} \equiv \Gamma_2$ are provided by the original lattice model, while all the other parameters are meant to be found self-consistently via the DMFT equations.

Note that the presence of two-photon losses still preserves the global $U(1)$ gauge symmetry (i.e. phase rotation symmetry) possessed by the Lindbladian, so all the numerical simplifications discussed in Sections 7.2.2 and 7.4.2 and already exploited in the context of the BHD as discussed in Section 8.2, can be applied here as well. In this case, the superoperator $\hat{\hat{\mathcal{K}}}$ that commutes with $\hat{\hat{\mathcal{L}}}$ is simply the superoperator generated by the total number of particles, i.e. $\hat{\hat{\mathcal{K}}}\bullet = -i\left[\hat{N}, \bullet\right]$ where now $\hat{N} = \sum_{i=0}^{N_B} \hat{n}_i$, and the global gauge symmetry is then generated by the unitary operator $U = e^{i\hat{N}\vartheta}$. The eigenvalues of $\hat{\hat{\mathcal{K}}}$ are still good labels for the blocks in the resulting block-diagonal structure of the Lindbladian — see Figure 9.3; a calculation of the dimension of such blocks in provided in Appendix B.

Our C++ OpenBDMFT code can perform the numerical diagonalization via the standard `LAPACK` (or its high-speed replacements) libraries thanks to a user-friendly interface provided by the `Armadillo` library [184, 185], which we have extended to support the two-sided diagonalization of non-symmetric matrices. This extension, as well as another extension that enables a user-friendly shift-invert diagonalization of sparse matrices via `ARPACK`+`SuperLU`, was contributed upstream. However, due to the sheer size of the problem, the diagonalization times via CPU-based routines like `LAPACK`'s ones are particularly high. In order to further cut down on the diagonalization times, we eventually decided to customize `Armadillo`'s internal diagonalization routines so to accelerate the diagonalization

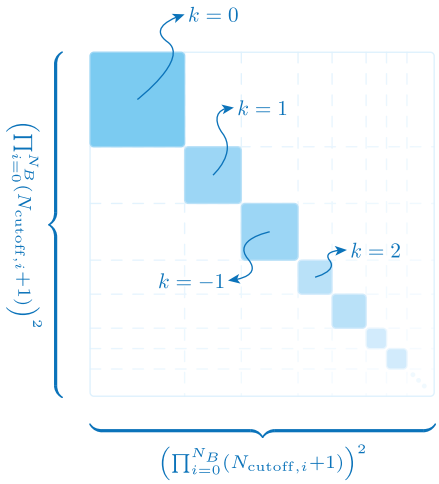

Figure 9.3: Block-diagonal structure for the gauge-symmetric Lindbladian of the AIM discussed in Section 9.2, with N_B bath sites plus the impurity. The full Lindbladian matrix has a size $\left(\prod_{i=0}^{N_B}(N_{\mathrm{cutoff},i}+1)\right)^2 \times \left(\prod_{i=0}^{N_B}(N_{\mathrm{cutoff},i}+1)\right)^2$, but it can be written as a block-diagonal matrix where each block is labeled by an integer k, with ik an eigenvalue of $\hat{\hat{\mathcal{K}}}\bullet = -i\left[\hat{N}, \bullet\right]$.

via GPUs, when they are available. The support for GPU acceleration is provided via the `MAGMA` library [186–188].

9.2.4 Keldysh Green's functions for the AIM

We now proceed to write the Green's function on the impurity site. In the following, we will only consider diagonal Lindblad couplings between the impurity site and the auxiliary bath sites. Before proceeding, we list in Table 9.1 the notation employed in the following. The impurity Green's functions are denoted by a subscript "$_\square$" in order not to mistake them with the noninteracting ($U, \Gamma_2 = 0$) Green's functions, denoted by a subscript "$_0$"; the lowercase Green's functions indicate instead the Green's functions of the uncoupled sites, i.e. for some $\nu_n = 0$, in the same way they did so in the context of the BHD in Section 8.6.1.

First, notice that we already know the uncoupled Green's functions of the bath sites, $g_n \equiv g_{0n}$: each of them is just the Green's function of a single cavity with single-particle pumping and single-particle losses, for whom we derived the retarded/Keldysh components in eq. (7.119). A similar statement holds for the uncoupled noninteracting Green's function of the impurity, $g_{0\square}$, with the difference that there is no single-particle pumping.

	Impurity	n-th bath site
Full	$G_\square$	G_n
$\mathbf{U, \Gamma_2 = 0,\ \nu_n \neq 0}$	$G_{0\square}$	G_{0n}
$\mathbf{U, \Gamma_2 = 0,\ \nu_n = 0}$	$g_{0\square}$	g_{0n}

Table 9.1: Notation used for the Green's functions. The impurity site is denoted by "□", while the bath sites are indexed with $n = 1, \dots, N_B$. Uppercase letters indicate $\nu_n \neq 0$, while lowercase letters indicate $\nu_n = 0$; noninteracting ($U, \Gamma_2 = 0$) Green's functions are instead indicated by an additional "0". Note that, since the bath sites are linear, $g_n \equiv g_{0n}$.

Impurity self-energy

We now take care of the full impurity Green's function, $G_\square$, that includes local nonlinearities as well as the interaction between the impurity and the bath sites. We first express it as a noninteracting contribution $G_{0\square}$ plus a *self-energy* term $\Sigma_\square$ that encodes the interactions:

$$G_\square = \left(G_{0\square}^{-1} - \Sigma_\square\right)^{-1} \tag{9.17}$$

While $\Sigma_\square$ is not known analytically, we can obtain $G_{0\square}^{-1}$ by using a reasoning fully akin to the one employed in Section 8.6.1. Namely, we write the Keldysh-rotated noninteracting action as

$$S_0 = \int_\omega \left\{ \bar{\psi}_\square g_{0\square}^{-1} \psi_\square + \sum_{n=1}^{N_B} \left[\bar{\psi}_n g_n^{-1} \psi_n - [\bar{\eta}_n \psi_n + \text{h.c.}] \right] \right\} \tag{9.18}$$

where $\psi_n = (a_{n,c}, a_{n,q})^\intercal$, $\bar{\eta}_n = (\nu_n \bar{\psi}_\square \sigma_x)$ and $\sigma_x = \begin{pmatrix} 0 & 1 \\ 1 & 0 \end{pmatrix}$ is the first Pauli matrix. The noninteracting effective action $S_{0\square}$ for the impurity is then obtained by integrating out all the other sites, i.e. by writing the partition function of the noninteracting AIM as

$$Z = \int \mathcal{D}[\bar{\psi}_\square, \psi_\square] \prod_{n=1}^{N_B} \mathcal{D}[\bar{\psi}_n, \psi_n] e^{iS_0[\bar{\psi}_\square, \psi_\square, \{\bar{\psi}_n, \psi_n\}]} = \int \mathcal{D}[\bar{\psi}_\square, \psi_\square] e^{iS_{0\square}[\bar{\psi}_\square, \psi_\square]} \tag{9.19}$$

where

$$e^{iS_{0\square}[\bar{\psi}_\square, \psi_\square]} = \int \prod_{n=1}^{N_B} \mathcal{D}[\bar{\psi}_n, \psi_n] e^{iS_0[\bar{\psi}_\square, \psi_\square, \{\bar{\psi}_n, \psi_n\}]}. \tag{9.20}$$

By writing

$$\int \prod_{n=1}^{N_B} \mathcal{D}[\bar{\psi}_n, \psi_n] e^{iS_0} = e^{i \int_\omega \bar{\psi}_\square g_{0\square}^{-1} \psi_\square} \prod_{n=1}^{N_B} \int \mathcal{D}[\bar{\psi}_n, \psi_n] e^{i \int_\omega \left[\bar{\psi}_n g_n^{-1} \psi_n - [\bar{\eta}_n \psi_n + \text{h.c.}] \right]} \tag{9.21}$$

and by applying the same Gaussian integral in eq. (8.40) to each factor in the product, taking also care to reabsorb any numerical factor into the definition of the differential, we can finally read out $S_{0\square}$ as

$$\begin{aligned} S_{0\square} &= \int_\omega \left[\bar{\psi}_\square g_{0\square}^{-1}\psi_\square - \sum_{n=1}^{N_B} \bar{\eta}_n g_n \eta_n\right] \\ &= \int_\omega \left[\bar{\psi}_\square g_{0\square}^{-1}\psi_\square - \sum_{n=1}^{N_B} \left(\nu_n \bar{\psi}_n \sigma_x\right) g_n \left(\nu_n \sigma_x \psi_n\right)\right] \\ &= \int_\omega \bar{\psi}_\square \left[g_{0\square}^{-1} - \sum_{n=1}^{N_B} \nu_n^2 \left(\sigma_x g_n \sigma_x\right)\right]\psi_\square \\ &\doteq \int_\omega \bar{\psi}_\square G_{0\square}^{-1}\psi_\square. \end{aligned} \tag{9.22}$$

Notice that the Green's functions above have the usual causality structure:

$$G_{0\square} = \begin{pmatrix} G_{0\square}^K & G_{0\square}^R \\ G_{0\square}^A & 0 \end{pmatrix}, \qquad g_n = \begin{pmatrix} g_n^K & g_n^R \\ g_n^A & 0 \end{pmatrix}, \tag{9.23}$$

so a σ_x rotation gives

$$\sigma_x g_n \sigma_x = \begin{pmatrix} 0 & g_n^A \\ g_n^R & g_n^K \end{pmatrix}. \tag{9.24}$$

In other words, the σ_x rotation provides a causality structure akin to the one of a self-energy. Indeed, by combining eqs. (9.17), (9.22) and (9.24), we get the following decomposed expression for the full impurity Green's function:

$$\begin{aligned} G_\square &= \left(G_{0\square}^{-1} - \Sigma_\square\right)^{-1} \\ &= \left(g_{0\square}^{-1} - \Delta - \Sigma_\square\right)^{-1} \end{aligned} \tag{9.25}$$

The term

$$G_{0\square} = \left(g_{0\square}^{-1} - \Delta\right)^{-1} \tag{9.26}$$

Weiss field

corresponds to the DMFT dynamical Weiss field. Its meaning is that of an effective field that describes the interaction between a generic lattice site and all the other ones in absence of nonlinearities; those latter ones, instead, are encoded in the lattice self-energy. The term

$$\Delta = \begin{pmatrix} 0 & \Delta^A \\ \Delta^R & \Delta^K \end{pmatrix} = \begin{pmatrix} 0 & \sum_{n=1}^{N_B} \nu_n^2 g_n^A \\ \sum_{n=1}^{N_B} \nu_n^2 g_n^R & \sum_{n=1}^{N_B} \nu_n^2 g_n^K \end{pmatrix}, \tag{9.27}$$

Bath hybridization function

instead, is known as the *bath hybridization function*.

In eq. (9.25), we marked the terms with different colors according to the following legend:

- ■ ⟶ We can obtain it via exact diagonalization
- ■ ⟶ Analytically known
- ■ ⟶ Unknown

So, given an AIM with any nonlinearity on the impurity site, but with fully linear bath sites, we can obtain the impurity self-energy $\Sigma_\square$ via a full diagonalization of the AIM itself; this is a key point in the DMFT procedure, for which we provide more details in Section 9.3.

9.3 The OpenBDMFT loop

The goal of DMFT is to describe a generic lattice site, embedded in the field generated by all the other lattice sites, as an equivalent AIM. At DMFT convergence, the impurity site in the AIM will then directly correspond to any lattice site; this equivalence is mathematically concretized by equating the lattice Green's function calculated on a generic lattice site, i.e. the local-in-space lattice Green's function $G_{\text{loc}} \equiv G_{i,i}$, and the impurity Green's function $G_\square$. The OpenBDMFT loop is obtained by enforcing this equality, which turns out to be a self-consistency equation.

We start by writing the local part of the original lattice Green's function, diagonal in the lattice sites indices, as the sum of its $\mathbf{k}$-space components:

$$G_{\text{loc}} = \sum_{\mathbf{k}} \left(G^{-1}_{0,\mathbf{k}} - \Sigma_{\mathbf{k}} \right)^{-1} . \tag{9.28}$$

G_{loc} is our final goal, since we want to solve the original lattice problem, $G^{-1}_{0,\mathbf{k}}$ is the non-interacting (bare) Green's function at a given $\mathbf{k}$ — so it can be found analytically, and it depends on the specific lattice problem at hand — and finally $\Sigma_{\mathbf{k}}$ is the lattice self-energy at a given $\mathbf{k}$. This is the unknown quantity that the DMFT technique replaces with the impurity self-energy of the equivalent AIM, see (9.25), which can in turn be obtained via the difference between the non-interacting impurity Green's function, known analytically, and the full one, obtained from the numerics. In other words, the DMFT cycle is imposed via the following two equalities:

Enforcing DMFT

$$G_{\text{loc}} = G_\square \qquad \text{and} \qquad \Sigma_{\mathbf{k}} = \Sigma_\square \tag{9.29}$$

In practice, the equalities (9.29) are self-consistently satisfied by performing the following *DMFT loop*:

DMFT loop

(1) Initial guess.
Start from a guess for the bath parameters ω_n, ν_n, Γ_{1nn}, and P_{1nn}, with $n = 1, \dots, N_B$, which corresponds to a guess for Δ given by eq. (9.27).

(2) From Δ to $G_\square$.
Given a bath hybridization function Δ, corresponding to a set of bath parameters for the AIM, obtain the impurity Green's function by diagonalizing the AIM via ED.

(3) From $G_\square$ to $\Delta^{(\text{new})}$.
Given $G_\square$, calculate a new bath hybridization function $\Delta^{(\text{new})}$. This is the step that involves the original lattice, i.e. the step in which we actually enforce the DMFT equalities (9.29).

(3.1) Obtain the impurity self-energy via (9.25) as: $\Sigma_\square = g_{0\square}^{-1} - \Delta - G_\square^{-1}$.

(3.2) Perform the DMFT approximation on the self-energy: $\Sigma_{\mathbf{k}} = \Sigma_\square$.

(3.3) Compute the local lattice Green's function G_{loc} via (9.28).

(3.4) Impose the DMFT condition to get a new impurity Green's function: $G_\square^{(\text{new})} = G_{\text{loc}}$.

(3.5) Numerically compute the new bath hybridization function via (9.25) as: $\Delta^{(\text{new})} = g_{0\square}^{-1} - \left(G_\square^{(\text{new})}\right)^{-1} - \Sigma_\square$.

(4) Fit of $\Delta^{(\text{new})}$.
Find new bath parameters such that the bath hybridization function computed via (9.27) is as close as possible to the given numerical $\Delta^{(\text{new})}$. This is done, as we will see, via a fitting procedure that minimizes a suitable distance between the two hybridization functions.

(5) Convergence test.
If the distance between the new bath hybridization function and the former one is less than the specified tolerance, i.e. if $\left|\left|\Delta^{(\text{new})} - \Delta\right|\right| < \delta_\Delta$, stop. Otherwise, set $\Delta = \Delta^{(\text{new})}$, go back to step (2) and iterate until convergence.

In some cases, the step (3) involving lattice quantities can be greatly simplified. As an example, on a Bethe lattice — see Figure 9.4, the self-consistency relation simply reads [31, 182]:

$$\Delta = c \cdot G_\square \tag{9.30}$$

Bethe lattice self-consistency

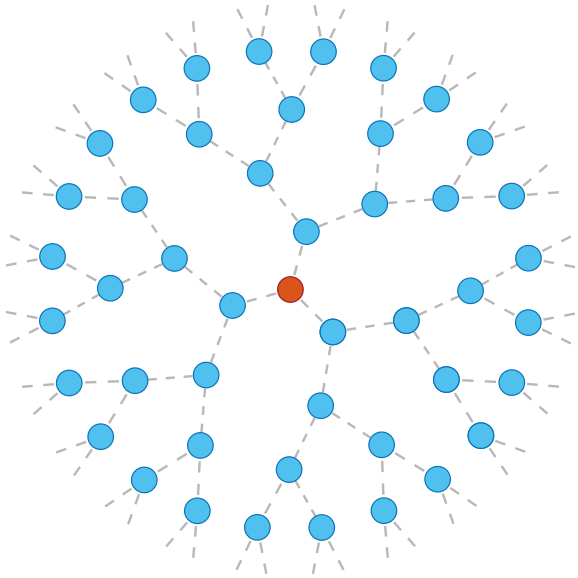

Figure 9.4: Illustration of a Bethe lattice with coordination number $z = 3$. A Bethe lattice [189] is an infinite, connected, cycle-free graph in which each node, connected to z neighboring nodes, is equivalent to all the others. If one of them is selected as a root node (red one in the illustration), the graph can be organized as an infinite number of shells centered around the root node, each containing $z(z-1)^{k-1}$ nodes, with $k \geq 1$. In the illustration above, we show the lattice only up to the shell $k = 4$.

where the proportionality constant c for a lattice like the one we are considering in (9.1) is [182]:

$$c = \frac{J^2}{z} \tag{9.31}$$

in contrast to the value $J^2/\sqrt{z}$ that c would take for an analogous fermionic lattice model [31].

The last point to address is how we can perform the fitting step in (4). First, we define a distance $\chi(\Delta_1, \Delta_2)$ between two generic hybridization functions Δ_1, Δ_2 as:

Distance between hybridization functions

$$\chi(\Delta_1, \Delta_2) = \sum_{\alpha=R,K} \int_{-\infty}^{+\infty} d\omega \, W^\alpha(\omega) \, |\Delta_1^\alpha(\omega) - \Delta_2^\alpha(\omega)|^n \,, \tag{9.32}$$

where $W^\alpha(\omega)$ is a weight function, $|\cdot|$ is the complex norm, and n can be typically fixed to 2. So, the basic idea is just to take the squared differences between

$\Delta_1^R(\omega)$ and $\Delta_2^R(\omega)$ at every frequency point, sum them up, and then add the corresponding contribution from the Keldysh component as well. $W^\alpha(\omega)$ can either be the identity function, a constant function serving as normalization, or some function of the frequency with the purpose of e.g. introducing a smooth high-frequency cutoff. As an example, when using the self-consistency condition on the Bethe lattice eq. (9.30), Δ is obtained from the Green's function by multiplying it by J^2/z (for bosons). This means that, when the lattice coupling constant J is small, χ itself becomes very small; in order to void this type of skewing, we've empirically found that using $W^\alpha(\omega) = (J^2/z)^{n-1}$ provides good results.

The fitting procedure is then achieved by performing a multidimensional numerical minimization of the function $\chi(\Delta_{\text{target}}, \Delta)$, where Δ_{target} is given *numerically* and it's the data we want to fit, while Δ is the *analytical* fitting function in eq. (9.27).

L-BFGS-B minimizer

Our code is able to use several minimizers provided by the libraries `ensmallen` [190], `LBFGS++` [191], and `CppOptimizationLibrary` [192], including some derivative-free minimizers; by default, we use the L-BFGS-B minimizer provided by `CppOptimizationLibrary`. The L-BFGS-B method [193] is a limited-memory (L-) version of the quasi-Netwon method known as BFGS, named after its author Broyden, Fletcher, Goldfarb, and Shanno, capable of handling simple box constraints (-B); it appears to be the same optimization method employed in [125] as well. In our case, the box constraints are used to ensure that the coefficient matrices in the Lindblad equation for the AIM are positive semi-definite. Since the BFGS family of methods performs the minimization by providing an estimate of the Hessian matrix of the function to minimize, providing the analytical derivatives of the cost function with respect to the parameters $\{\nu_n\}$, $\{\omega_n\}$, $\{\Gamma_{1nn}\}$, $\{P_{1nn}\}$ is essential in order to achieve a good numerical performance; all the relevant derivatives can be easily calculated from eqs. (7.119) and (9.27).

9.4 Quantum Zeno effect

Having established all the necessary technical components of our OpenBDMFT calculation, in this Section 9.4 we use it to probe the incoherently pumped Bose-Hubbard lattice with two-photon losses introduced in Section 9.1.1.

We focus in particular on the emergence of a so-called quantum Zeno regime [194]. In this regime, in analogy with Zeno's arrow paradox [195], an increase in the physical dissipation surprisingly leads to a *decrease* in the effective dissipation, up to a limit in which the effective dissipation is completely suppressed.

9.4.1 Mapping on hard-core bosons

In [1] it has been shown that, in the limit of large dissipation $\Gamma_2 \gg J$, the dissipative Bose-Hubbard model obtained from eqs. (9.1) to (9.4) by removing

the incoherent pump can be mapped onto the following effective Hamiltonian:

$$\hat{H}^{\text{eff}} = -\frac{J}{z}\sum_{\langle \mathbf{r},\,\mathbf{r}'\rangle}\hat{c}^{\dagger}_{\mathbf{r}}\hat{c}_{\mathbf{r}'} - J_2^{\text{eff}}\sum_{\mathbf{r}}\hat{C}^{\dagger}_{\mathbf{r}}\hat{C}_{\mathbf{r}}, \tag{9.33}$$

where $c_{\mathbf{r}}$, $c^{\dagger}_{\mathbf{r}}$ are *hard-core* bosonic operators, i.e. with a constraint enforcing a maximum occupation of one boson per site:

Hard-core bosons

$$c_{\mathbf{r}} = |0\rangle_{\mathbf{r}}\langle 1|_{\mathbf{r}}\,, \qquad c^{\dagger}_{\mathbf{r}} = |1\rangle_{\mathbf{r}}\langle 0|_{\mathbf{r}}\,. \tag{9.34}$$

The reason the system can be mapped, at the first order, into a lattice of hard-core bosons, is due to the fact that for $\Gamma_2 \gg J$ the two-photon losses are very large but there is no single-photon loss process, so all the states with 2 or more bosons per site are highly suppressed.

The second term in eq. (9.33) is instead written in terms of two-photon operators

$$\hat{C}_{\mathbf{r}} = \hat{c}_{\mathbf{r}}\sum_{\mathbf{r}':\langle \mathbf{r},\,\mathbf{r}'\rangle}\hat{c}_{\mathbf{r}'}\,, \tag{9.35}$$

where the sum over $\mathbf{r}'$ is carried over the first nearest-neighbors of $\mathbf{r}$, which destroy *pairs* of photons in neighboring sites. The quantity

$$J_2^{\text{eff}} = \left(\frac{J}{z}\right)^2\frac{U}{U^2+\Gamma_2^2} \tag{9.36}$$

is the effective energy associated with these pairs. Finally, the local two-photon dissipator in the Lindblad equation is replaced by an effective non-local two-photon dissipator

$$\hat{\mathcal{L}}_D^{\text{eff}}\hat{\rho}^{\text{BH}} = 2\sum_{\mathbf{r}}\Gamma_2^{\text{eff}}\left(\hat{C}_{\mathbf{r}}\hat{\rho}^{\text{BH}}\hat{C}^{\dagger}_{\mathbf{r}} - \frac{1}{2}\left\{\hat{C}^{\dagger}_{\mathbf{r}}\hat{C}_{\mathbf{r}}, \hat{\rho}^{\text{BH}}\right\}\right), \tag{9.37}$$

where

Effective dissipation rate

$$\Gamma_2^{\text{eff}} = \left(\frac{J}{z}\right)^2\frac{\Gamma_2}{U^2+\Gamma_2^2} \tag{9.38}$$

is the effective decay rate of pairs of photons on neighboring sites. The peculiarity of the effective dissipation is that it's mediated by the original tunneling amplitude J: as J increases, more and more photons on neighboring sites are discarded from the lattice. Even more interestingly, for $\Gamma_2 < U$ the effective dissipation increases with the physical dissipation Γ_2, but only up to a maximum at $\Gamma_2 = U$; for $\Gamma_2 > U$, instead, the effective dissipation *decreases* as the physical dissipation Γ_2 is increased. Eventually, at $\Gamma_2 \gg U$, the effective dissipation becomes

Quantum Zeno regime

$$\Gamma_2^{\text{eff}} \underset{\Gamma_2 \gg U}{\approx} \left(\frac{J}{z}\right)^2\frac{1}{\Gamma_2}\,, \tag{9.39}$$

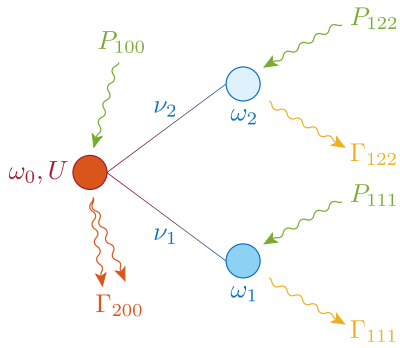

Figure 9.5: Effective AIM used for the numerical simulations in Section 9.4. The impurity site, representing a generic site of the original lattice, is depicted on the left and has a bare frequency ω_0 and a Kerr nonlinearity U; the bath sites, depicted on the right, do not have Kerr nonlinearities and have bare frequencies ω_1, ω_2 and couplings with the impurity ν_1, ν_2 that are treated as fitting parameters. Every site has single-particle pumping, with $P_{100} \equiv P_1$ and with P_{111}, P_{122} fitting parameters. The impurity site has two-particle losses $\Gamma_{200} \equiv \Gamma_2$, while the auxiliary bath sites have single-particle losses Γ_{111} and Γ_{122}, again treated as fitting parameters.

thus it decreases as Γ_2^{-1}. This regime where the effective dissipation shows a seemingly paradoxical behavior, experimentally observed with ultracold gases [18, 177, 178], has been called the *quantum Zeno regime* [19, 194, 196–198] for its analogy with Zeno's arrow paradox [195].

Because of their origin in terms of virtual processes, the hopping-induced dissipative processes described by eqs. (9.37) and (9.38) are completely neglected by simple approaches such as the Gutzwiller mean-field theory and, even in the context of DMFT, they cannot be handled using approximate solvers such as the Hubbard-I approximation [126]. On the other hand, our non-perturbative implementation of DMFT is not limited in this regard, and it is an ideal tool to explore this regime. We shall also see that our ED implementation provides an intriguing and insightful mapping on an effective two-site model.

9.4.2 Emergence of the Zeno regime

We can exploit the mapping to hard-core bosons to effectively reduce the size of the Hilbert space as the two-particle losses amplitude Γ_2 increases.

Such a reduced effective Hilbert space of the lattice allows us to reduce the Hilbert space of the auxiliary AIM as well. As a first point, in order not to have an empty stationary state, we introduce a small single-particle pumping $P_1 \ll \Gamma_2$ in the lattice; in the following, $P_1 = 0.1$. This is a key difference

compared to the effective model in eqs. (9.33) to (9.38), derived in [1] for a lattice without a pumping mechanism. In the deep Zeno regime ($\Gamma_2 \gg U > J$) we then expect that the Fock space on the impurity site is effectively reduced to $|0\rangle$ and $|1\rangle$, since states with 2 or more photons are strongly dissipated by the two-photon losses. As a consequence, the spectral function on the impurity site has a single peak around $\omega_0 + U$, corresponding to transitions between $|0\rangle$ and $|1\rangle$. This feature is particularly appealing, especially if we decide to work on the Bethe lattice, where the DMFT self-consistency condition (9.30) amounts to require that the spectral function of the impurity site must be proportional to the bath hybridization function.[2] The latter is in turn a weighted sum of Lorentzians, where each Lorentzian is contributed by a single auxiliary bath site; therefore, in order to be able to fit a single peak in the spectral function, a single auxiliary bath site is enough. If we also want to analyze the system at values of Γ_2 not necessarily in the deep Zeno regime, as in our case, we can add a second auxiliary bath site that takes into account the spectral peak around $\omega_0 + 3U$, that is suppressed in the deep Zeno regime only; the suppression experienced by peaks at even higher energy makes trying to reproduce them unworthy. A sketch of the resulting impurity model employed in the following is shown in Figure 9.5.

So, we work in a regime in which the local occupied states are mainly $|0\rangle$ and $|1\rangle$, while states $|n\rangle$ with $n \geq 2$ contribute at most an additional peak at higher energies in the spectral function and are highly suppressed. For this reason, we can choose quite a small Hilbert space cutoff $N_{\text{cutoff},0}$ on the impurity site in the numerical calculations; in the following, we fixed $N_{\text{cutoff},0} = 5$. As for the Hilbert space cutoff on the bath sites, instead, we have to take some extra care; these sites reproduce the presence of the original lattice, but while physical lattice sites may mainly occupy the states $|0\rangle$ and $|1\rangle$, this is not necessarily true for our auxiliary effective sites which are meant to represent the effect of the rest of the lattice on the impurity. In the following, we fixed $N_{\text{cutoff},1} = N_{\text{cutoff},2} = 7$; we validate this choice below.

Hilbert space cutoff

We start performing our OpenBDMFT simulations on a Bethe lattice with coordination number $z = 6$. We choose a large value of the Kerr nonlinearity, $U = 10$, so to have enough separation — equal to $2U$ for a single disconnected cavity — between the peaks in the spectral function. The lattice hopping strength is instead $J = 4$; since Γ_2^{eff} is proportional to J^2, decreasing/increasing J is expected to result in a less/more prominent Zeno effect. We then explore values of Γ_2 from 2.5 to 15.0, and we plot in Figure 9.6 the elements of the on-site reduced density matrix in all the three sites of the auxiliary AIM; these elements give the occupation probability in each on-site Fock state. We immediately notice that, on the impurity site (top panel), the contributions to the density matrix come mainly from the Fock states $|0\rangle$ and $|1\rangle$; together, these two states contribute (increasing from low to high Γ_2/U) 98.8%–99.8% of the total weight on the impurity site,

Occupation probabilities

[2] On a generic lattice, this relation does not hold. Yet, a variety of DMFT Hamiltonian studies have demonstrated a strong similarity between the results on the Bethe lattice and on other lattices. Therefore, we can expect a similar generality also for our results.

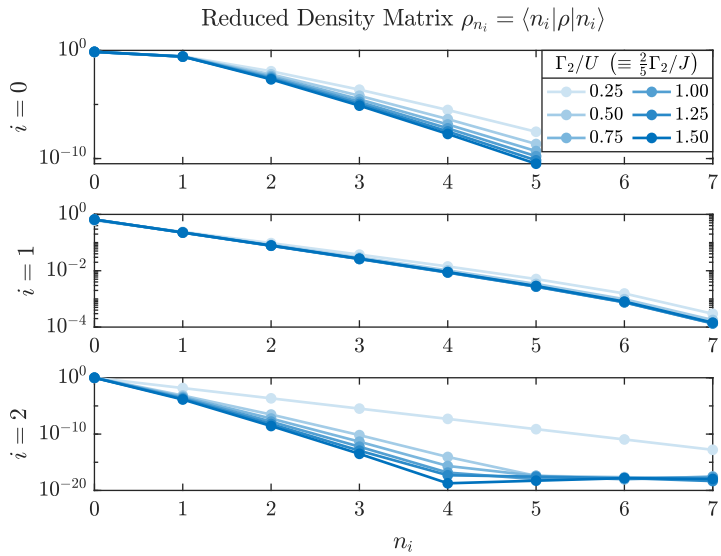

Figure 9.6: Elements of the AIM on-site reduced density matrix ρ_{n_i} in the Fock basis at site i with n_i bosons. The impurity site is indexed by $i = 0$, while the bath site indexed by $i = 1$ ($i = 2$) is the one at low (high) energies. Γ_2/U (or equivalently Γ_2/J) is increased from fading blue to strong blue. Parameters: $z = 6$ on the Bethe lattice, $\omega_0 = 1$, $U = 10$, $J = 4$, $P_1 = 0.1$, $\Gamma_2 = [2.5, 15.0]$. The cutoffs on the $i = 0, 1, 2$ sites are respectively $5, 7, 7$, as commented in the text.

thus validating our expectation on the extent of the reduced Hilbert space and our cutoff choice for $i = 0$. The situation is quite different in the auxiliary bath sites (central and bottom panels), that instead display a thermal-like occupation — although with a stark difference in the order of magnitude of the occupation probabilities. The fact that the Fock states $|n\rangle$ with $n \geq 2$ are still relevant even in the deep Zeno regime is the reason we are using a higher cutoff of 7 in the bath sites with respect to a cutoff of 5 that we use in the impurity site. However, as also made clear by the Bethe lattice self-consistency condition (9.30), the auxiliary bath in some sense mirrors the properties of the impurity site (and in turn, those of the lattice model). This means that, since the occupation on the impurity site is low due to the presence of two-particle losses that dissipate states with higher occupations, we can expect the occupation on the auxiliary bath sites to be low as well. Specifically, for the parameters discussed here, the occupation on the $i = 1$ bath site (central panel), having energy $\omega_1 \approx \omega_0 + U$, is roughly in the range 0.5–0.7, so based on the discussion on the choice of cutoffs made in Section 8.2, a cutoff of 7 is expected to provide results with a negligible error. This is especially clear for the $i = 2$ bath site (bottom panel), at energy

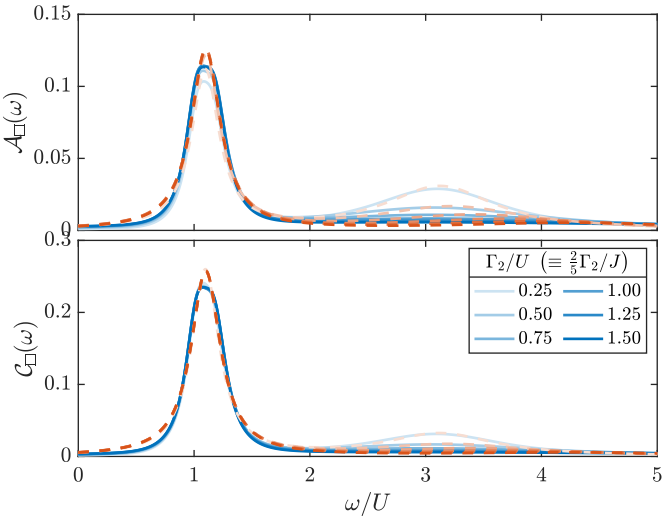

Figure 9.7: Spectral function $\mathcal{A}_\square$ (top panel) and cavity correlation function $\mathcal{C}_\square$ (bottom panel) of the impurity site, shown in solid lines for increasing values of Γ_2/U (fading blue to strong blue); the color scale is the same one used in Figure 9.6. The red dashed lines correspond to $-z\mathrm{Im}\{\Delta^R\}/(\pi J^2)$ (top panel) and $-z\Delta^K/(2\pi i J^2)$ (bottom panel), and are shaded in accordance with the respective solid blue lines. According to the self-consistency condition on the Bethe lattice eqs. (9.30) and (9.31), at a given value of Γ_2/U the solid blue line and its corresponding dashed red line should overlap for an ideal AIM.

$\omega_2 \approx \omega_0 + 3U$, whose occupation visibly decreases as Γ_2 is increased, due to the fact that in the deep Zeno regime we expect not to have any other spectral peaks except for the first one. At the higher values of Γ_2 shown here, the occupation probability of Fock states $|n\rangle$ with $n \gtrsim 4$ is already in the order of magnitude of the numerical noise. The sizable difference in the order of magnitude of the occupation probabilities of the two bath sites already points to the key result that the $i = 2$ bath site, at higher energies, becomes less and less relevant as the two-particle losses are increased. This effectively allows us to solve the problem, in the deep Zeno regime, via a DMFT with a single auxiliary bath site.

Response functions

We now take a look at the corresponding response functions on the impurity site ($i = 0$), shown in Figure 9.7 (solid blue lines) alongside their fitted bath hybridization functions (dashed red lines). At the lowest value of Γ_2/U shown in the plot, we still have two visible peaks in the spectral function (top panel), corresponding to the transitions between states discussed above. The bath sites contribute each one a Lorentzian in the bath hybridization function; the Lorentzian contributed by the site $i = 1$ fits the peak at low energies ($\omega_1 \approx \omega_0 + U$), while the

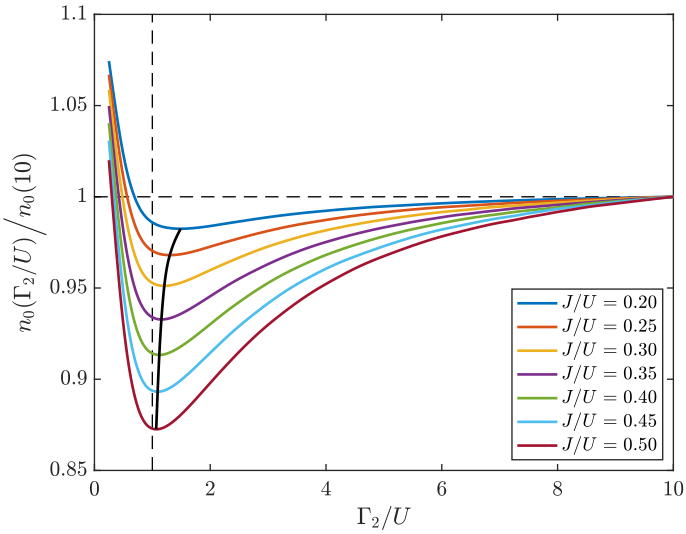

Figure 9.8: Mean occupation $n_0 = \langle \hat{n}_0 \rangle$ on the impurity site as a function of Γ_2/U, normalized to its value at $\Gamma_2/U = 10$; different colors correspond to different values of J/U. The horizontal and vertical dashed black lines mark the values $n_0(\Gamma_2/U)/n_0(10) = 1$ and $\Gamma_2/U = 1$, respectively; the solid black line marks the occupation minimum for different values of J/U. Parameters: as in Figure 9.6, except for $J = [2, 5]$ and $\Gamma_2 = [2.5, 100.0]$.

one contributed by the site $i = 2$ fits the peak at high energies ($\omega_2 \approx \omega_0 + 3U$). As Γ_2/U is increased, the peak at high energies quickly becomes less and less prominent until it becomes irrelevant in the spectral function; the deep Zeno regime could then be described via a linearized DMFT, i.e. a DMFT with a single bath site. Interestingly, a similar approach has been proposed as an approximate solution of DMFT in [176]. On the other hand, for increasing values of Γ_2/U, the first peak in the spectral function becomes more and more prominent; this is a signature of the effective narrowing of the Hilbert space to the two Fock states $|0\rangle$ and $|1\rangle$. While the disappearance of the secondary peak is also visible in the cavity correlation function (bottom panel), connected with the occupation, a corresponding increase or decrease in the first peak is not immediately apparent.

Steady-state occupations

The disappearance of the secondary peak in the cavity correlation function suggests that there are important signatures of the Zeno transition in the steady-state occupation, proportionally related to the integral of the cavity correlation function itself. Such occupation, calculated from the steady-state density matrix $\hat{\rho}_{\rm ss}$ as $\langle \hat{n}_0 \rangle = \mathrm{Tr}\,(\hat{n}_0 \hat{\rho}_{\rm ss})$ over a broad range of Γ_2/U and J/U, is shown in Figure 9.8, normalized to the latest available value in the deep Zeno regime; we show only a selection of J/U values due to data visualization constraints.

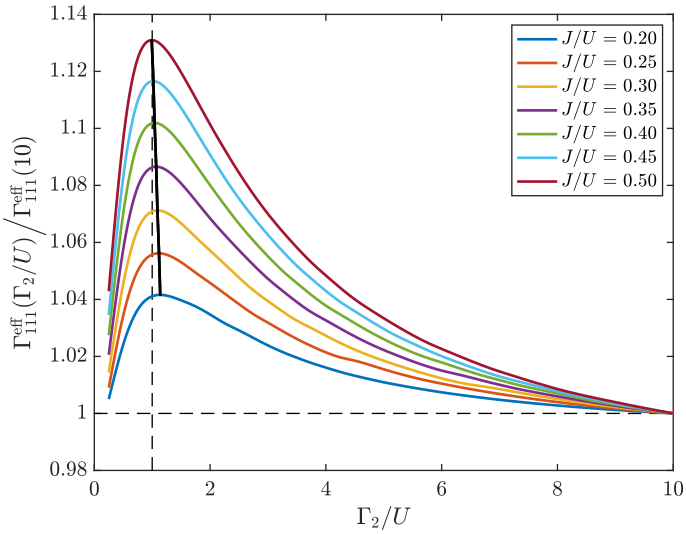

Figure 9.9: Effective loss rate $\Gamma^{\rm eff}_{111} = \Gamma_{111} - P_{111}$ on the first bath site $i = 1$ (see also Figures 9.6 and 9.7), normalized to its value at $\Gamma_2/U = 10$; different colors correspond to different values of J/U. The horizontal and vertical dashed black lines mark the values $\Gamma^{\rm eff}_{111}(\Gamma_2/U)/\Gamma^{\rm eff}_{111}(10) = 1$ and $\Gamma_2/U = 1$, respectively; the solid black line marks the maximum $\Gamma^{\rm eff}_{111}$ for different values of J/U. Parameters as in Figure 9.8.

The transition into the Zeno regime, marked at the stationary point $\Gamma_2/U = 1$ of the effective two-particle losses (9.38), results here in a stationary point of the steady-state occupation. Namely, at low values of Γ_2/U ($\lesssim 1$), the occupation decreases as a result of increased two-particle losses — that remain however smaller than the Kerr nonlinearity U. On the other hand, for larger values of Γ_2/U ($\gtrsim 1$) in which the system is fully into the hard-core bosons regime, the dissipation can only happen for *pairs* of particles on neighboring sites. Such dissipation, however, is less and less likely to happen as potential pairs of particles on the same site get dissipated by the local two-particle losses; the net result, as we also have a small, fixed pump, is an increase in the occupation.

The transition between a regime in which the steady-state occupation decreases and a regime in which it increases doesn't occur exactly at $\Gamma_2/U = 1$ for any value of J/U, as it happens instead for the effective two-particle losses (9.38). The reason, aside from the introduction of a small incoherent pump not present in the effective model eqs. (9.33) to (9.38) and that contributes to the steady-state occupation, is that we also have a first-order contribution in eq. (9.33), that scales with J/z, while the second-order contribution responsible for the Zeno effect scales as $(J/U)^2$. The first-order contribution is responsible for the shift of

the minimum of the steady-state occupation; however, when J is increased, the second-order contribution becomes progressively dominant, resulting in a convergence of the stationary point of the steady-state occupation towards $\Gamma_2/U = 1$ — see the solid black line in (9.8).

Zeno signatures in the auxiliary bath

Finally, it's interesting to look for signatures of such a transition in the properties of the auxiliary bath as well, since we already pointed out that the bath itself acts as a mirror image of the original lattice. Since the first bath site ($i = 1$) is the only relevant one in the deep Zeno regime, we can analyze its effective (in the semiclassical sense) dissipation rate, given by the difference $\Gamma^{\text{eff}}_{111} = \Gamma_{111} - P_{111}$ between the single-particle dissipation rate and the single-particle pump rate, as a function of Γ_2/U. This quantity corresponds to the HWHM of the Lorentzian contributed by this site to the bath hybridization function. We see in Figure 9.9 that this effective loss rate qualitatively reproduces the behavior of the two-particle effective loss rate Γ^{eff}_2, i.e. it first increases up to a maximum value at $\Gamma_2/U \approx 1$, after which it starts decreasing as Γ_2/U is increased. The behavior of the effective loss on the first auxiliary bath site provides a remarkably clear picture of the process in which DMFT successfully encodes the nonlinear effects characterizing the dynamics of a full lattice model into the parameters and the consequent properties of an effective linear system.

9.5 Conclusions

In this Chapter, we have showcased our implementation of a powerful technique for the analysis of strongly-correlated driven-dissipative photonic lattices, known as OpenBDMFT — an extension of the DMFT technique originally developed to study strongly correlated electronic systems. The core idea of this technique is to replace all the interconnected nonlinear lattice sites surrounding any given lattice site with an effective linear bath, which is in turn parameterized in terms of a finite number of linear auxiliary sites. The parameters of the auxiliary sites are then self-consistently fitted in order to correctly reproduce the frequency-dependent local physics of the lattice. This effective parametrization has, first of all, the benefit of dramatically reducing the size of the Hilbert space — a point that is especially important, as we saw, in the context of driven-dissipative quantum many-body problems. Furthermore, in contrast to the standard Gutzwiller mean-field technique, the dynamical mean-field obtained via the DMFT is able to reproduce even highly non-local effects.

As a paradigmatic example that can demonstrate the capabilities of this technique, we have analyzed a driven-dissipative Bose-Hubbard lattice in the thermodynamic limit, where the driving is achieved via a single-particle incoherent pump at a rate P_1 and the local dissipation removes pairs of particles from the system at a rate Γ_2. Such a driven-dissipative Bose-Hubbard lattice becomes especially interesting in the presence of strong — compared to the tunneling rate — local two-particle losses. In fact, in this limit, the lattice can be mapped into a lattice of hard-core bosons with non-local two-particle losses at a rate Γ^{eff}_2 induced by

the tunneling rate. Interestingly, when the local two-particle losses Γ_2 overcome the local Kerr nonlinearity U, the non-local two-particle losses Γ_2^{eff} actually start decreasing as Γ_2 is increased, with a behavior $\Gamma_2^{\text{eff}} \sim \Gamma_2^{-1}$ in the limit $\Gamma_2 \gg U$. This regime is known as the quantum Zeno regime.

Via our OpenBDMFT analysis, performed on a Bethe lattice under a weak incoherent pump, we have witnessed the emergence of hard-core bosons on the sites of the original lattice, signaled both by the negligible occupation probability of on-site Fock states $|n\rangle$ with $n \geq 2$ and by the progressive reduction of the response function to a single peak relative to the $|0\rangle \to |1\rangle$ transition.

The transition to the quantum Zeno regime is then testified by the behavior of the number of particles as a function of Γ_2/U on a given lattice site. While for $\Gamma_2/U \lesssim 1$ the occupation decreases as the local two-particle losses increase, for $\Gamma_2/U \gtrsim 1$ the quantum Zeno effect results in an increase of such occupation as Γ_2 is increased. This effect becomes stronger at higher values of J/U, and our observations are in qualitative agreement with OpenBDMFT results obtained with an NCA impurity solver [126].

An analogous behavior can also be found in the width of the spectral peak contributed by the auxiliary site at low energy. Here, the spectral peak has instead a maximum around $\Gamma_2/U = 1$, qualitatively reproducing the behavior of Γ_2^{eff} itself. This signature clearly shows how the OpenBDMFT procedure is able to encode the non-trivial nonlinear effects in the lattice into the parameters of a fully linear auxiliary bath, consisting in this case of just 2 auxiliary sites. In the deep Zeno regime, in particular, the effective reduction of the DMFT bath to a single auxiliary site shows that the OpenBDMFT method is able to map a translationally invariant, highly nonlinear lattice of cavities into a *dimer*, in which one of the cavities serves as a representative of any one of the lattice cavities, and the other one mimics the dynamical mean interaction with the rest of the lattice. This result stems directly from our choice for the impurity solver; in contrast to other solvers, the one we employ here inherently provides a more detailed insight on the structure of the DMFT auxiliary bath, and, as a consequence, it can directly point to a more simplified physical picture.

These initial exciting results open the way to further extensions of our numerical code, with the goal of being able to treat systems with a finite condensate fraction and with coherent pumping mechanisms, for which an exact diagonalization has to be ruled out due to the behemoth size of the Hilbert space[3] and one has to resort to Arnoldi-like diagonalization schemes. These technical advances would then allow us to explore systems with light-matter coupling at the quantum level [13, 98, 106, 199] and with non-trivial non-Markovian effects, making our OpenBDMFT implementation a promising platform for the investigation of novel many-body physics.

[3] A coherent pump would break the global gauge symmetry, thus it's not possible to use the numerical simplifications induced by the block structure of the Lindbladian matrix.

Chapter 10

Conclusions

In Part II we focused on the analysis of driven-dissipative strongly-correlated photonic systems described by a Lindblad equation for the density matrix.

The primary tools we employed in our analysis were the exact numerical diagonalization of the Lindblad equation, performed within the framework of the superparticle representation, and the Keldysh field theory for the calculation of non-equilibrium response functions; both are reviewed in Chapter 7. During our review of this technical toolbox, we focused in particular on the properties of the basic building block of any driven-dissipative photonic lattice system: a single driven-dissipative cavity. In absence of nonlinearities, such a cavity possesses a trivial Lorentzian-shaped spectral function, centered around the bare cavity frequency and with a width controlled by its single-particle loss/pump rates; yet, despite its simplicity, the analytical knowledge on the linear cavity is of the utmost importance in the design of more advanced numerical techniques. We also discussed how to dramatically reduce the computational resources required for the diagonalization by taking advantage of the global phase rotation symmetry possessed by the physical models we studied.

In Chapter 8 we then focused our attention on the study of two coupled driven-dissipative nonlinear cavities, the so-called driven-dissipative Bose-Hubbard Dimer (BHD). Such a system is both intriguing *per se*, due to the presence of a semi-classical localization-delocalization transition of which we looked for quantum signatures, but also as a basic building block for the analysis of full lattice systems. After a review of the semiclassical transition, we considered the quantum regime in the case of both uniform and non-uniform pumping. In the former case, the system is known to have a trivial steady-state density matrix that does not

depend on the Hamiltonian of the dimer; therefore, we looked for the signatures of the transition both in the time dynamics of the occupation imbalance and in the steady-state single-particle response functions, that are instead sensitive to the details of the Hamiltonian, finding a crossover between the localized and the delocalized phases. By using a non-uniform pumping, we were instead able to induce a non-trivial stationary state density matrix; therefore, we could obtain signatures of the transition in the steady-state occupation imbalance as well. In this case, we also derived a connection between the pump imbalance and the current flowing in the dimer via the Keldysh component of the single-particle response function.

We stepped up the complexity of the problem in Chapter 9, where we considered the problem of studying a driven-dissipative strongly-correlated photonic lattice in the thermodynamic limit. In order to be able to handle the massive size of the Hilbert space of the system and yet to retain crucial correlations, we resorted to a powerful technique known as Dynamical Mean Field Theory (DMFT) — also called OpenBDMFT in the specific context of driven-dissipative bosonic systems. In the DMFT picture, similar to a standard mean-field treatment, any lattice site experiences an effective interaction (or "bath") generated by all the other lattice sites; crucially for the treatment of strong correlations, though, the DMFT mean-field is not static, but is provided with temporal correlations. In our implementation of the DMFT technique, we modeled the effective bath as a collection of linear cavities connected to any one of the lattice sites; the parameters of the linear cavities modeling the bath were then self-consistently determined via a procedure involving the iterative diagonalization of the effective system composed by a generic lattice site connected to these linear cavities.

We showcased the capabilities of our DMFT implementation by studying a paradigmatic Bose-Hubbard lattice, provided with single-particle pumping and two-particle losses, which can be seen as the dissipative analogous of the Kerr nonlinearity. In presence of strong two-particle losses, the photons progressively acquire a hard-core behavior, i.e. the states with two or more photons per cavity are highly suppressed. The numerical results were able to recover the consequent narrowing of the Hilbert space in this regime, and we were able to reproduce the effective interaction resulting from a lattice of highly nonlinear cavities by employing instead, at most, two linear cavities in the bath. Even more impressively, we were able to reproduce the physics of the so-called Zeno regime with just one linear cavity in the bath, i.e. with a dimer of cavities. In this regime that, being due to non-local effects, is completely neglected by a Gutzwiller mean-field analysis, the effective dissipation decreases as the physical two-particle dissipation increases, in a seemingly paradoxical behavior. We showed striking signatures of this effect in the behavior of the average steady-state occupation obtained via DMFT; after a certain threshold, the occupation of the lattice cavities starts in fact to increase when we increase the two-particle dissipation. Thanks to our discretized representation of the effective bath, that in this regime reduced to just one linear cavity, we were able to establish that such effect was encoded by

the DMFT procedure into an analogous behavior of the effective lifetime of the bath cavity.

In the light of these very promising results obtained via our implementation of the DMFT technique for driven-dissipative photonic lattices, we plan to work on further extensions to enable the treatment of a wider class of photonic systems. These include, but are not limited to, the exploration of Krylov-space techniques to reduce the computational costs and to enable the treatment of much larger Hilbert spaces, the analysis of systems with a finite condensate fraction, the inclusion of a light-matter coupling at the quantum level, as well as the treatment of non-Markovian effects. We are confident that the development of the full potential of this technique will provide unprecedented possibilities to explore novel frontiers in the investigation of quantum many-body problems.

Chapter 11

Final remarks

This Thesis presented the investigation of driven-dissipative photonic lattices using two different routes: a semiclassical analysis, which is expected to be accurate for a large number of excited bosons (Part I), and a fully quantum analysis of the driven-dissipative strongly-correlated many-body problem (Part II).

The mechanisms of driving and dissipation considered here were described by a Lindblad equation, i.e. an equation for the time-evolution of the density matrix of the system of interest, where the surrounding environment — to which the open nature of the system is ascribed — is traced out. We went through a more thorough discussion on the Lindblad equation in Chapter 7, including its numerical diagonalization; however, already in Chapter 2, it was instrumental in deriving the semiclassical theory of lasers as a mean-field approximation of the Lindbladian dynamics in a cavity endowed with optical gain.

As a system of interest for the semiclassical investigation in Part I, we chose to focus on a topological laser (also dubbed *topolaser*), a device that lases in a topologically protected mode as a means to increase its robustness against static disorder, its flexibility in the design shape, and as a promising strategy to efficiently increase the power output upon increasing the active area of the device. In Chapter 3, we worked in a regime in which the optical medium responsible for the gain could be traced out from the mean-field equations of the semiclassical theory of lasers. Therefore, we explored different strategies for the spatial localization of the pump needed to sustain the lasing process, in such a way as to promote the emission from a topological mode. During our investigation, we uncovered the emergence of new instability regimes and of a potentially slow transient dynamics, and we pointed out key characteristics of the topological

robustness and of the lasing regime. In Chapter 3, instead, motivated by the goal of providing a theoretical explanation for the observations in the pioneering topolaser experiment in [29], we simulated the full equations that describe the frequency-dependent semiclassical theory of lasers. We then proposed a scheme in which the spectral selection mechanism, resulting from the explicit treatment of the gain medium in the theory, conspires with a suitably engineered spatial selection mechanism in order to promote lasing from a topological mode, even when the pump is uniformly distributed across the whole system.

Our quantum analysis in Part II, instead, focused on the treatment of lattices of driven-dissipative nonlinear cavities. The non-equilibrium nature of the problem was addressed by working in the framework of the Keldysh field theory, reviewed in Chapter 7 and instrumental in the calculation of response functions; at the numerical level, these latter were then obtained via a suitable spectral representation that involved the eigenvectors and the eigenvalues of the Lindbladian matrix representing the Lindblad equation.

As a first step towards our final goal, in Chapter 8 we performed an exact diagonalization analysis of a Bose-Hubbard dimer provided with incoherent single-particle pumping and single-particle losses; given the infinite size of the photonic Hilbert space, even this very small size requires some care. We were able to reduce the numerical diagonalization requirements by exploiting the global phase rotation symmetry of the Lindblad equation, managing therefore to reconstruct the full quantum dynamics of the observables and to probe the steady-state response functions. This allowed us to look for the quantum signatures of the localization-delocalization transition occurring in the semiclassical regime, in the case of both symmetric and asymmetric pumping and losses. The extension to a full lattice of cavities in the thermodynamic limit, however, required the development of a more sophisticated technique. In this context, we presented in Chapter 9 our implementation of a technique known as *dynamical mean-field theory*, originally developed for systems of strongly correlated electrons. The idea behind this technique consists in mapping a translationally invariant lattice model into a smaller, semi-analytical system of connected cavities that can be more easily numerically diagonalized. A consistent mapping between these two models is ensured by matching their local Green's functions, in such a way that, eventually, the complex non-linear action of a lattice on any one of its cavities is encoded into the properties of a finite set of linear cavities, to be determined self-consistently. In order to showcase the power of this idea, we analyzed a Bose-Hubbard lattice provided with incoherent pumping and two-particle losses. As a first application of the method, we focused on the regime of large two-particle losses which in turn induce a non-local effective loss process, that is responsible for the onset of the so-called quantum Zeno regime. In this regime, we face what may seem a paradox: the effective losses (the average occupation) decrease (increases) when the physical losses are increased. The Gutzwiller mean-field theory is not able to describe the onset of this quantum Zeno effect, because of the non-local origin of the latter; our dynamical mean-field theory implementation, instead, is able

to provide the correct physical picture, and to encode the complex non-linear features of the lattice model into the properties of a single, linear cavity.

The most natural, yet challenging and ambitious follow-up of this Thesis is a path to connect the two lines of research that we carried out during the Ph.D. work.

The methodology we have developed can indeed be generalized to different lattice models, and there is no conceptual obstacle preventing its application to systems in topological photonics. Though, for two-dimensional systems, DMFT becomes exact in the limit of infinite coordination, studies of strongly correlated fermionic topological insulators provided indeed very promising results and rich physics.

Possible extensions of DMFT can be envisaged to deal with the current limitations, and they will be guided by the physical insight derived from semiclassical methods and by a constant interaction with the experimental community.

Appendices

APPENDIX A

Superparticle states and tilde-rule

Let's take a system made of N sites. According to the vectorization procedure discussed in Section 7.2.1 we have to introduce a tilde-copy of the system, whose additional N sites are marked by a tilde "$\sim$". The particle creation/annihilation operators in the original system and the ones in the tilde system commute according to the following rules (adapted from [129]):

$$\left[a_i, a_j^\dagger\right]_\pm = \delta_{ij}, \qquad [a_i, a_j]_\pm = \left[a_i^\dagger, a_j^\dagger\right]_\pm = 0; \tag{A.1}$$

$$\left[\tilde{a}_i, \tilde{a}_j^\dagger\right]_\pm = \delta_{ij}, \qquad [\tilde{a}_i, \tilde{a}_j]_\pm = \left[\tilde{a}_i^\dagger, \tilde{a}_j^\dagger\right]_\pm = 0; \tag{A.2}$$

$$[a_i, \tilde{a}_j]_\pm = \left[a_i, \tilde{a}_j^\dagger\right]_\pm = \left[a_i^\dagger, \tilde{a}_j\right]_\pm = \left[a_i^\dagger, \tilde{a}_j^\dagger\right]_\pm = 0; \tag{A.3}$$

$$a_i \left|0\right\rangle \left|\tilde{0}\right\rangle = \tilde{a}_i \left|0\right\rangle \left|\tilde{0}\right\rangle = 0\,, \tag{A.4}$$

where $[A, B]_\pm = AB \pm BA$, and "+" holds for fermions while "−" holds for bosons.

You can then easily prove by induction that the following relation holds:

$$\left[a_j, \left(a_j^\dagger\right)^{n_j}\right]_\pm = n_j \left(a_j^\dagger\right)^{n_j - 1}, \tag{A.5}$$

with $n_j = 1$ for fermions and $n_j > 0$ for bosons.

At this point, if we define $\mathbf{n} = (n_1, \ldots, n_N)$ and $\tilde{\mathbf{m}} = (m_1, \ldots, m_N)$, we can define the following

$$|\mathbf{n}, \tilde{\mathbf{m}}\rangle \doteq \sqrt{\frac{(-i)^{\lambda \sum_i n_i}}{\prod_i n_i!}} \sqrt{\frac{(-i)^{\lambda \sum_i m_i}}{\prod_i m_i!}} \left(a_1^\dagger\right)^{n_1} \cdots \left(a_N^\dagger\right)^{n_N} \left(\tilde{a}_1^\dagger\right)^{m_1} \cdots \left(\tilde{a}_1^\dagger\right)^{m_N} |0\rangle\, |\tilde{0}\rangle \tag{A.6}$$

to be the N-particles state with n_1 particles in site 1 and m_1 particles in site $\tilde{1}$, n_2 particles in site 2 and m_2 particles in site $\tilde{2}$, and so on up to site N. Here, $\lambda = 1$ for fermions and $\lambda = 0$ for bosons. As an example, in the case of a single site, we get

$$|n, \tilde{m}\rangle \doteq \sqrt{\frac{(-i)^{\lambda n}}{n!}} \sqrt{\frac{(-i)^{\lambda m}}{m!}} \left(a^\dagger\right)^n \left(\tilde{a}^\dagger\right)^m |0\rangle\, |\tilde{0}\rangle\,. \tag{A.7}$$

We'll then show that:

1. That this definition is still consistent with the laddering rules, and in particular that the number operator acts as we expect;

2. That these states are normalized.

We will work out the bosonic case, as this is the case we treat in this work; the discussion for fermions is nonetheless very similar.

For the first point, by using the commutation relation (A.5) and the definition, we get:

$$\begin{aligned}
a_j\, |\mathbf{n}, \tilde{\mathbf{m}}\rangle &= \sqrt{\frac{1}{\cdots n_j! \cdots}} \sqrt{\frac{1}{\prod_i m_i!}} \cdots a_j \left(a_j^\dagger\right)^{n_j} \cdots |0\rangle\, |\tilde{0}\rangle \\
&= \sqrt{\frac{1}{\cdots n_j (n_j - 1)! \cdots}} \sqrt{\frac{1}{\prod_i m_i!}} \cdots n_j \left(a_j^\dagger\right)^{n_j - 1} \cdots |0\rangle\, |\tilde{0}\rangle \\
&= \sqrt{n_j} \sqrt{\frac{1}{\cdots (n_j - 1)! \cdots}} \sqrt{\frac{1}{\prod_i m_i!}} \cdots \left(a_j^\dagger\right)^{n_j - 1} \cdots |0\rangle\, |\tilde{0}\rangle \\
&= \sqrt{n_j}\, |\mathbf{n} : n_j - 1, \tilde{\mathbf{m}}\rangle
\end{aligned}$$

where the notation $|\mathbf{n} : n_j - 1, \tilde{\mathbf{m}}\rangle$ indicates a state obtained from $|\mathbf{n}, \tilde{\mathbf{m}}\rangle$ by replacing the j-th element of $\mathbf{n}$, n_j, with $n_j - 1$. Similarly, where now we don't

need the commutation relation (A.5), we get

$$\begin{aligned} a_j^\dagger \left|\mathbf{n}, \tilde{\mathbf{m}}\right\rangle &= \sqrt{\frac{1}{\cdots n_j! \cdots}} \sqrt{\frac{1}{\prod_i m_i!}} \cdots a_j^\dagger \left(a_j^\dagger\right)^{n_j} \cdots \left|0\right\rangle \left|\tilde{0}\right\rangle \\ &= \sqrt{\frac{1}{\cdots (n_j+1) n_j! \cdots}} \sqrt{\frac{1}{\prod_i m_i!}} \cdots \sqrt{n_j+1} \left(a_j^\dagger\right)^{n_j+1} \cdots \left|0\right\rangle \left|\tilde{0}\right\rangle \\ &= \sqrt{n_j+1} \sqrt{\frac{1}{\cdots (n_j+1)! \cdots}} \sqrt{\frac{1}{\prod_i m_i!}} \cdots \left(a_j^\dagger\right)^{n_j+1} \cdots \left|0\right\rangle \left|\tilde{0}\right\rangle \\ &= \sqrt{n_j+1} \left|\mathbf{n} : n_j+1, \tilde{\mathbf{m}}\right\rangle \end{aligned}$$

The proof goes in the same way for the tilde-equivalents; overall, we get the following laddering rules:

$$\begin{cases} a_j \left|\mathbf{n}, \tilde{\mathbf{m}}\right\rangle = \sqrt{n_j} \left|\mathbf{n} : n_j - 1, \tilde{\mathbf{m}}\right\rangle \\ a_j^\dagger \left|\mathbf{n}, \tilde{\mathbf{m}}\right\rangle = \sqrt{n_j+1} \left|\mathbf{n} : n_j + 1, \tilde{\mathbf{m}}\right\rangle \end{cases} \qquad \text{and} \qquad \begin{cases} \tilde{a}_j \left|\mathbf{n}, \tilde{\mathbf{m}}\right\rangle = \sqrt{m_j} \left|\mathbf{n}, \tilde{\mathbf{m}} : m_j - 1\right\rangle \\ \tilde{a}_j^\dagger \left|\mathbf{n}, \tilde{\mathbf{m}}\right\rangle = \sqrt{m_j+1} \left|\mathbf{n}, \tilde{\mathbf{m}} : m_j + 1\right\rangle \end{cases} \tag{A.8}$$

which verify, as we want,

$$a_j^\dagger a_j \left|\mathbf{n}, \tilde{\mathbf{m}}\right\rangle = n_j \left|\mathbf{n}, \tilde{\mathbf{m}}\right\rangle \qquad \text{and} \qquad \tilde{a}_j^\dagger \tilde{a}_j \left|\mathbf{n}, \tilde{\mathbf{m}}\right\rangle = m_j \left|\mathbf{n}, \tilde{\mathbf{m}}\right\rangle . \tag{A.9}$$

Now we check the normalization; we'll concentrate on the single-site case, since the extension to the multi-site case is immediate.

$$\langle n', \tilde{m}' | n, \tilde{m} \rangle = \sqrt{\frac{1}{n! m! n'! m'!}} \left\langle 0, \tilde{0} \middle| \left(\tilde{a}\right)^{m'} \underbrace{\left(a\right)^{n'} \left(a^\dagger\right)^{n}} \left(\tilde{a}^\dagger\right)^{n} \middle| 0, \tilde{0} \right\rangle$$

We focus on the terms grouped by the horizontal bracket. By applying recursively the commutator (A.5), we get

$$\left(a\right)^{n'} \left(a^\dagger\right)^{n} = \begin{cases} n! \left(a\right)^{n'-n} & \text{if } n' > n \\ n! & \text{if } n' = n \\ n'! \left(a^\dagger\right)^{n-n'} & \text{if } n > n' \end{cases} \tag{A.10}$$

and the same goes for the tilde-case. Overall, we have to distinguish the following cases for $\langle n', \tilde{m}' | n, \tilde{m} \rangle$:

- $\underline{n' > n \text{ or } m' > m}$
  Either $\left(a\right)^{n'-n}$ or $\left(\tilde{a}\right)^{m'-m}$ annihilates $\left|0, \tilde{0}\right\rangle \Longrightarrow \langle n', m' | n, m \rangle = 0$.

- $\underline{n > n' \text{ or } m > m'}$
  Either $\left(a^\dagger\right)^{n'-n}$ or $\left(\tilde{a}^\dagger\right)^{m'-m}$ annihilates $\langle 0, \tilde{0}| \implies \langle n', \tilde{m}'|n, \tilde{m}\rangle = 0$.
- $\underline{n = n' \text{ or } m = m'}$
  We are left with

$$\langle n', \tilde{m}'|n, \tilde{m}\rangle = \sqrt{\frac{1}{(n!)^2(m!)^2}} n!m! \cancelto{1}{\langle 0, \tilde{0}|0, \tilde{0}\rangle} = 1. \tag{A.11}$$

So, in general,

$$\langle \mathbf{n'}, \tilde{\mathbf{m}}'|\mathbf{n}, \tilde{\mathbf{m}}\rangle = \delta_{\mathbf{n},\mathbf{n}'}\delta_{\tilde{\mathbf{m}},\tilde{\mathbf{m}}'} \tag{A.12}$$

where $\delta_{\mathbf{n},\mathbf{n}'} = \delta_{n_1,n_1'}\delta_{n_2,n_2'}\cdots\delta_{n_N,n_N'}$ and similarly for the tilde counterpart.

Having defined (A.6), we now prove that it's consistent with the tilde-rule (7.32) — again for the bosonic case:

$$\begin{aligned}
a_j|I\rangle &= a_j \sum_{\mathbf{n}:n_j=0}^{\infty} |\mathbf{n}, \tilde{\mathbf{n}}\rangle = a_j \sum_{\mathbf{n}:n_j=0}^{\infty} \frac{1}{\cdots n_j! \cdots} \cdots (a_j^\dagger \tilde{a}_j^\dagger)^{n_j} \cdots |0\rangle\,|\tilde{0}\rangle \\
&= a_j \sum_{\mathbf{n}:n_j=1}^{\infty} \frac{1}{\cdots n_j! \cdots} \cdots (a_j^\dagger \tilde{a}_j^\dagger)^{n_j} \cdots |0\rangle\,|\tilde{0}\rangle \\
&= \sum_{\mathbf{n}:n_j=1}^{\infty} \frac{1}{\cdots n_j! \cdots} \cdots n_j \tilde{a}_j^\dagger (a_j^\dagger \tilde{a}_j^\dagger)^{n_j-1} \cdots |0\rangle\,|\tilde{0}\rangle \\
&= \tilde{a}_j^\dagger \sum_{\mathbf{n}:n_j=1}^{\infty} \frac{1}{\cdots (n_j-1)! \cdots} \cdots (a_j^\dagger \tilde{a}_j^\dagger)^{n_j-1} \cdots |0\rangle\,|\tilde{0}\rangle \\
&= \tilde{a}_j^\dagger \sum_{\mathbf{n}:n_j=0}^{\infty} \frac{1}{\cdots n_j! \cdots} \cdots (a_j^\dagger \tilde{a}_j^\dagger)^{n_j} \cdots |0\rangle\,|\tilde{0}\rangle \\
&= \tilde{a}_j^\dagger \sum_{\mathbf{n}:n_j=0}^{\infty} |\mathbf{n}, \tilde{\mathbf{n}}\rangle \\
&= \tilde{a}_j^\dagger |I\rangle
\end{aligned} \tag{A.13}$$

where we've applied the commutator (A.5) and we've used the fact that tilde and non-tilde operators always commute.

APPENDIX B

Size of the Lindbladian matrix and role of gauge symmetry

Let's take a system of N bosonic sites, each with a cutoff b_i, $i = 1, \ldots, N$ on the number of bosons. The number of possible Fock states is then $\prod_{i=1}^{N}(b_i+1)$. In the superbosonic representation (see Section 7.2) that we use to vectorize the Lindblad equation, tough, the Lindbladian matrix is written in the basis of the Fock states of an enlarged system, consisting of the original system plus an identical tilde-copy of it. The number of Fock states in such an enlarged system is then $\left(\prod_{i=1}^{N}(b_i+1)\right)^2$ (equal to the number of entries of the density matrix, that is now a vector), so the dimension of the Lindbladian matrix is $\left(\prod_{i=1}^{N}(b_i+1)\right)^2 \times \left(\prod_{i=1}^{N}(b_i+1)\right)^2$.

In the presence of a global gauge symmetry (i.e. phase rotation symmetry), though, we can write the Lindbladian matrix as a series of diagonal blocks of decreasing dimension, each labeled by an integer k equal to the difference between the total number of bosons in the tilde-system and the total number of bosons in the original system — see Figure 9.3. Given these constraints, k can take the values $k = 0, \pm 1, \pm 2, \ldots, \pm\sum_{i=1}^{N} b_i$, so we have a total of $1 + 2\sum_{i=1}^{N} b_i$ diagonal blocks.

In order to find the dimensions of these blocks, we first have to find the number of states we can form such that the total occupation of each state is equal to $M \in \mathbb{N}$. This number is equal to $c_M \doteq [x^M]F(x)$, where c_M is the M-th

degree coefficient of the generating polynomial

$$F(x) = \sum_{n=1}^{\sum_{i=1}^{N} b_i} c_n x^n = \prod_{i=1}^{N} \sum_{j=0}^{b_i} x^j. \tag{B.1}$$

By using the geometric series

$$\sum_{j=0}^{b_i} x^j = \frac{1 - x^{b_i+1}}{1 - x}, \tag{B.2}$$

we can write the generating polynomial as

$$F(x) = \prod_{i=1}^{N} \frac{1 - x^{b_i+1}}{1 - x} = \frac{\prod_{i=1}^{N} \left(1 - x^{b_i+1}\right)}{(1 - x)^N}. \tag{B.3}$$

The coefficient $[x^M]F(x)$ can be easily calculated via a symbolic math software, e.g. Mathematica® or MATLAB®'s Symbolic Math Toolbox™. We can obtain a closed expression is some limiting cases; as an example, if all the cutoffs b_i's have the same value, i.e. $b_i \equiv b \; \forall i$, then

$$F(x) = \left(1 + x + x^2 + \ldots + x^b\right)^N = \left(\sum_{j=0}^{b} x^j\right)^N = \left(\frac{1 - x^{b+1}}{1 - x}\right)^N. \tag{B.4}$$

We can apply the binomial formula twice to get

$$F(x) = \left(1 - x^{b+1}\right)^N (1 - x)^{-N} = \sum_{i=0}^{\infty} (-1)^i \binom{N}{i} x^{i(b+1)} \sum_{j=0}^{\infty} \binom{N + j - 1}{j} x^j \tag{B.5}$$

and we can group the terms as

$$F(x) = \sum_{i=0}^{\infty} \sum_{j=0}^{\infty} (-1)^i \binom{N}{i} \binom{N + j - 1}{j} x^{i(b+1)+j}. \tag{B.6}$$

The term of power x^M will satisfy $M = i(b + 1) + j$, so that $j = M - i(b + 1)$; substitution of j gives (note that $\binom{n}{k} = \binom{n}{n-k}$)

$$[x^M]F(x) = \sum_{i=0}^{\infty} (-1)^i \binom{N}{i} \binom{N - 1 + M - i(b + 1)}{M - i(b + 1)} \tag{B.7}$$

Now notice that the sum is not actually infinite; since $\binom{n}{k} = 0$ for $k > n$, we can restrict the sum up to $i = N$. We can simplify further by noting that we have non-zero entries only for $M - i(b + 1) \geq 0$, so since M and b are non-negative

and $M \leq bN$ we have the condition $i \leq \left\lfloor \frac{M}{b+1} \right\rfloor < N$. Eventually, the number of solutions c_M in this case is equal to

$$[x^M]F(x) = \sum_{i=0}^{\left\lfloor \frac{M}{b+1} \right\rfloor} (-1)^i \binom{N}{i} \binom{N-1+M-i(b+1)}{M-i(b+1)}. \tag{B.8}$$

Having found how many states we can form such that the total occupation of each state is equal to $M \in \mathbb{N}$, we can then ask what's the number $D(k)$ of *pairs* of states we can form such that the difference between the total occupations of the states is equal to $k \in \mathbb{Z}$, which is exactly the integer labeling the diagonal blocks of the Lindbladian with gauge symmetry. This number is given by

$$D(k) = D(|k|) = \sum_{n=1}^{\sum_{i=1}^{N} b_i - |k|} c_n \cdot c_{n+|k|}, \tag{B.9}$$

where c_n are the coefficients of the generating polynomial (B.3). So, each diagonal block has a dimension $D(k) \times D(k)$.

As an example of the advantage of having such a diagonal-block structure, we can take a look at the impurity model employed in Section 9.4, having 3 bosonic sites with cutoffs $\mathbf{b} = (5, 7, 7)^\intercal$. In Table B.1, we list the dimensions

k	$D(k)$
Whole Lindbladian	147456
0	11040
$+1$	10857
-1	10857
$+2$	10326
-2	10326
...	...

TABLE B.1: Linear dimension of the diagonal blocks of the Lindbladian for 3 bosonic sites with cutoffs $\mathbf{b} = (5, 7, 7)^\intercal$.

of the diagonal blocks in this case, plus the dimension of the full Lindbladian matrix. The first blocks are already one order of magnitude smaller than the full Lindbladian; this is important, since the storage requirements scale as the square of the linear dimension and the diagonalization times typically scale as the cube of the linear dimension. Assuming these scaling, exploiting the gauge symmetry allows us to solve this specific problem by diagonalizing the first three blocks only, which provide the steady-state density matrix and the steady-state single-particle response functions, thus by employing only the 1.64% of the memory required to diagonalize the full Lindbladian matrix and only the 0.12% of the time required to diagonalize the full Lindbladian.

Bibliography

[1] Juan José García-Ripoll et al. "Dissipation-induced hard-core boson gas in an optical lattice". In: *New Journal of Physics* 11.1 (Jan. 2009), p. 013053. ISSN: 1367-2630. DOI: 10.1088/1367-2630/11/1/013053 (cit. on pp. 1, 149, 152).

[2] Frank Verstraete, Michael M. Wolf, and Juan Ignacio Cirac. "Quantum computation and quantum-state engineering driven by dissipation". In: *Nature Physics* 5.9 (Sept. 2009), pp. 633–636. ISSN: 1745-2473. DOI: 10.1038/nphys1342 (cit. on p. 1).

[3] Sebastian Diehl et al. "Quantum states and phases in driven open quantum systems with cold atoms". In: *Nature Physics* 4.11 (Nov. 2008), pp. 878–883. ISSN: 1745-2473. DOI: 10.1038/nphys1073 (cit. on p. 1).

[4] Sebastian Diehl et al. "Dissipation-Induced d-Wave Pairing of Fermionic Atoms in an Optical Lattice". In: *Physical Review Letters* 105.22 (Nov. 2010), p. 227001. ISSN: 0031-9007. DOI: 10.1103/PhysRevLett.105.227001 (cit. on pp. 1, 67).

[5] Wei Yi et al. "Driven-dissipative many-body pairing states for cold fermionic atoms in an optical lattice". In: *New Journal of Physics* 14.5 (May 2012), p. 055002. ISSN: 1367-2630. DOI: 10.1088/1367-2630/14/5/055002 (cit. on p. 1).

[6] Julio T. Barreiro et al. "An open-system quantum simulator with trapped ions". In: *Nature* 470.7335 (Feb. 2011), pp. 486–491. ISSN: 0028-0836. DOI: 10.1038/nature09801 (cit. on p. 1).

[7] Hanna Krauter et al. "Entanglement Generated by Dissipation and Steady State Entanglement of Two Macroscopic Objects". In: *Physical Review Letters* 107.8 (Aug. 2011), p. 080503. ISSN: 0031-9007. DOI: 10.1103/PhysRevLett.107.080503 (cit. on p. 1).

[8] Yiheng Lin et al. "Dissipative production of a maximally entangled steady state of two quantum bits". In: *Nature* 504.7480 (Dec. 2013), pp. 415–418. ISSN: 0028-0836. DOI: 10.1038/nature12801 (cit. on p. 1).

[9] James Raftery et al. “Observation of a Dissipation-Induced Classical to Quantum Transition”. In: *Physical Review X* 4.3 (Sept. 2014), p. 031043. ISSN: 2160-3308. DOI: 10.1103/PhysRevX.4.031043 (cit. on pp. 1, 103, 132).

[10] Monika Aidelsburger et al. “Realization of the Hofstadter Hamiltonian with Ultracold Atoms in Optical Lattices”. In: *Physical Review Letters* 111.18 (Oct. 2013), p. 185301. ISSN: 0031-9007. DOI: 10.1103/PhysRevLett.111.185301 (cit. on p. 1).

[11] Hirokazu Miyake et al. “Realizing the Harper Hamiltonian with Laser-Assisted Tunneling in Optical Lattices”. In: *Physical Review Letters* 111.18 (Oct. 2013), p. 185302. ISSN: 0031-9007. DOI: 10.1103/PhysRevLett.111.185302 (cit. on p. 1).

[12] Marco Di Liberto, Andreas Hemmerich, and Cristiane Morais Smith. “Topological Varma Superfluid in Optical Lattices”. In: *Physical Review Letters* 117.16 (Oct. 2016), p. 163001. ISSN: 0031-9007. DOI: 10.1103/PhysRevLett.117.163001 (cit. on p. 1).

[13] Alberto Biella et al. “Phase diagram of incoherently driven strongly correlated photonic lattices”. In: *Physical Review A* 96.2 (Aug. 2017), p. 023839. ISSN: 2469-9926. DOI: 10.1103/PhysRevA.96.023839 (cit. on pp. 1, 67, 131, 158).

[14] Monika Aidelsburger et al. “Measuring the Chern number of Hofstadter bands with ultracold bosonic atoms”. In: *Nature Physics* 11.2 (Dec. 2014), pp. 162–166. ISSN: 1745-2473. DOI: 10.1038/nphys3171 (cit. on p. 1).

[15] Yaakov Lumer et al. “Self-Localized States in Photonic Topological Insulators”. In: *Physical Review Letters* 111.24 (Dec. 2013), p. 243905. ISSN: 0031-9007. DOI: 10.1103/PhysRevLett.111.243905 (cit. on p. 1).

[16] Mohammad Hafezi et al. “Imaging topological edge states in silicon photonics”. In: *Nature Photonics* 7.12 (Dec. 2013), pp. 1001–1005. ISSN: 1749-4885. DOI: 10.1038/nphoton.2013.274 (cit. on pp. 1, 5, 17, 18).

[17] Andrei C. Berceanu et al. “Momentum-space Landau levels in driven-dissipative cavity arrays”. In: *Physical Review A* 93.1 (2016), pp. 1–10. ISSN: 10941622. DOI: 10.1103/PhysRevA.93.013827 (cit. on p. 1).

[18] Niels Syassen et al. “Strong Dissipation Inhibits Losses and Induces Correlations in Cold Molecular Gases”. In: *Science* 320.5881 (June 2008), pp. 1329–1331. ISSN: 0036-8075. DOI: 10.1126/science.1155309 (cit. on pp. 1, 133, 151).

[19] Almut Beige et al. “Quantum Computing Using Dissipation to Remain in a Decoherence-Free Subspace”. In: (2000) (cit. on pp. 1, 151).

[20] Tomoki Ozawa and Iacopo Carusotto. "Anomalous and Quantum Hall Effects in Lossy Photonic Lattices". In: *Physical Review Letters* 112.13 (Apr. 2014), p. 133902. ISSN: 0031-9007. DOI: 10.1103/PhysRevLett.112.133902 (cit. on p. 1).

[21] Philippe St-Jean et al. "Lasing in topological edge states of a one-dimensional lattice". In: *Nature Photonics* 11.10 (Oct. 2017), pp. 651–656. ISSN: 1749-4885. DOI: 10.1038/s41566-017-0006-2 (cit. on pp. 1, 5, 39).

[22] Sebabrata Mukherjee et al. "Experimental observation of anomalous topological edge modes in a slowly driven photonic lattice". In: *Nature Communications* 8 (Jan. 2017), p. 13918. ISSN: 2041-1723. DOI: 10.1038/ncomms13918 (cit. on p. 1).

[23] Midya Parto et al. "Edge-Mode Lasing in 1D Topological Active Arrays". In: *Physical Review Letters* 120.11 (Mar. 2018), p. 113901. ISSN: 0031-9007. DOI: 10.1103/PhysRevLett.120.113901 (cit. on pp. 1, 5).

[24] Frederick Duncan Michael Haldane and Srinivas Raghu. "Possible Realization of Directional Optical Waveguides in Photonic Crystals with Broken Time-Reversal Symmetry". In: *Physical Review Letters* 100.1 (Jan. 2008), p. 013904. ISSN: 0031-9007. DOI: 10.1103/PhysRevLett.100.013904 (cit. on pp. 1, 5).

[25] Srinivas Raghu and Frederick Duncan Michael Haldane. "Analogs of quantum-Hall-effect edge states in photonic crystals". In: *Physical Review A* 78.3 (Sept. 2008), p. 033834. ISSN: 1050-2947. DOI: 10.1103/PhysRevA.78.033834 (cit. on pp. 1, 5).

[26] Zheng Wang et al. "Observation of unidirectional backscattering-immune topological electromagnetic states". In: *Nature* 461.7265 (Oct. 2009), pp. 772–775. ISSN: 0028-0836. DOI: 10.1038/nature08293 (cit. on pp. 1, 5).

[27] Gal Harari et al. "Topological Lasers". In: *Conference on Lasers and Electro-Optics*. Washington, D.C.: OSA, Dec. 2016, FM3A.3. ISBN: 978-1-943580-11-8. DOI: 10.1364/CLEO_QELS.2016.FM3A.3 (cit. on pp. 1, 5).

[28] Steffen Wittek et al. "Towards the Experimental Realization of the Topological Insulator Laser". In: *Conference on Lasers and Electro-Optics*. Washington, D.C.: Optical Society of America, 2017, FTh1D.3. ISBN: 978-1-943580-27-9. DOI: 10.1364/CLEO_QELS.2017.FTh1D.3 (cit. on pp. 1, 5).

[29] Babak Bahari et al. "Nonreciprocal lasing in topological cavities of arbitrary geometries". In: *Science* 358.6363 (Nov. 2017), pp. 636–640. ISSN: 0036-8075. DOI: 10.1126/science.aao4551 (cit. on pp. 1, 2, 6, 15, 23, 36, 39, 40, 47, 48, 50, 60–62, 64, 164).

[30] Tomoki Ozawa et al. "Topological photonics". In: *Reviews of Modern Physics* 91.1 (Mar. 2019), p. 015006. ISSN: 0034-6861. DOI: 10.1103/RevModPhys.91.015006 (cit. on pp. 1, 5).

[31] Antoine Georges et al. "Dynamical mean-field theory of strongly correlated fermion systems and the limit of infinite dimensions". In: *Reviews of Modern Physics* 68.1 (Jan. 1996), pp. 13–125. ISSN: 0034-6861. DOI: 10.1103/RevModPhys.68.13 (cit. on pp. 1, 132, 135, 136, 147, 148).

[32] Matteo Seclì, Massimo Capone, and Iacopo Carusotto. "Theory of chiral edge state lasing in a two-dimensional topological system". In: *Physical Review Research* 1.3 (Dec. 2019), p. 033148. ISSN: 2643-1564. DOI: 10.1103/PhysRevResearch.1.033148 (cit. on pp. 2, 17, 18, 44, 50).

[33] Matteo Seclì et al. "Spatial and spectral mode-selection effects in topological lasers with frequency-dependent gain". In: *APL Photonics* 6.5 (May 2021), p. 050803. ISSN: 2378-0967. DOI: 10.1063/5.0041124 (cit. on pp. 2, 7, 17, 40).

[34] Mohammad Hafezi et al. "Robust optical delay lines with topological protection". In: *Nature Physics* 7.11 (Nov. 2011), pp. 907–912. ISSN: 1745-2473. DOI: 10.1038/nphys2063 (cit. on pp. 5, 17, 18, 27, 35, 36).

[35] Yan Yang et al. "Experimental demonstration of one-way slow wave in waveguide involving gyromagnetic photonic crystals". In: *Applied Physics Letters* 102.23 (June 2013), p. 231113. ISSN: 0003-6951. DOI: 10.1063/1.4809956 (cit. on p. 5).

[36] Jonathan Guglielmon and Mikael C. Rechtsman. "Broadband Topological Slow Light through Higher Momentum-Space Winding". In: *Physical Review Letters* 122.15 (Apr. 2019), p. 153904. ISSN: 0031-9007. DOI: 10.1103/PhysRevLett.122.153904 (cit. on p. 5).

[37] Vittorio Peano et al. "Topological Quantum Fluctuations and Traveling Wave Amplifiers". In: *Physical Review X* 6.4 (Nov. 2016), p. 041026. ISSN: 2160-3308. DOI: 10.1103/PhysRevX.6.041026 (cit. on pp. 5, 35, 36).

[38] Mikael C. Rechtsman et al. "Topological protection of photonic path entanglement". In: *Optica* 3.9 (Sept. 2016), p. 925. ISSN: 2334-2536. DOI: 10.1364/OPTICA.3.000925 (cit. on p. 5).

[39] Sunil Mittal, Venkata Vikram Orre, and Mohammad Hafezi. "Topologically robust transport of entangled photons in a 2D photonic system". In: *Optics Express* 24.14 (July 2016), p. 15631. ISSN: 1094-4087. DOI: 10.1364/OE.24.015631 (cit. on p. 5).

[40] Yao Wang et al. "Topological protection of two-photon quantum correlation on a photonic chip". In: *Optica* 6.8 (Aug. 2019), p. 955. ISSN: 2334-2536. DOI: 10.1364/OPTICA.6.000955 (cit. on p. 5).

[41] Konrad Tschernig et al. "Topological protection versus degree of entanglement of two-photon light in photonic topological insulators". In: *Nature Communications 2021 12:1* 12.1 (Mar. 2021), pp. 1–8. ISSN: 2041-1723. DOI: 10.1038/s41467-021-22264-3 (cit. on p. 5).

[42] Ling Lu, John D. Joannopoulos, and Marin Soljačić. "Topological photonics". In: *Nature Photonics* 8.11 (Nov. 2014), pp. 821–829. ISSN: 1749-4885. DOI: 10.1038/nphoton.2014.248 (cit. on p. 5).

[43] You Wu et al. "Applications of Topological Photonics in Integrated Photonic Devices". In: *Advanced Optical Materials* 5.18 (Sept. 2017), p. 1700357. ISSN: 2195-1071. DOI: 10.1002/ADOM.201700357 (cit. on p. 5).

[44] Yasutomo Ota et al. "Active topological photonics". In: *Nanophotonics* 9.3 (Jan. 2020), pp. 547–567. ISSN: 2192-8614. DOI: 10.1515/nanoph-2019-0376 (cit. on p. 5).

[45] Laura Pilozzi and Claudio Conti. "Topological lasing in resonant photonic structures". In: *Physical Review B* 93.19 (May 2016), p. 195317. ISSN: 2469-9950. DOI: 10.1103/PhysRevB.93.195317 (cit. on p. 5).

[46] Dmitry D. Solnyshkov, Anton V. Nalitov, and Guillaume Malpuech. "Kibble-Zurek Mechanism in Topologically Nontrivial Zigzag Chains of Polariton Micropillars". In: *Physical Review Letters* 116.4 (Jan. 2016), p. 046402. ISSN: 0031-9007. DOI: 10.1103/PhysRevLett.116.046402 (cit. on p. 5).

[47] Han Zhao et al. "Topological hybrid silicon microlasers". In: *Nature Communications* 9.1 (Dec. 2018), p. 981. ISSN: 2041-1723. DOI: 10.1038/s41467-018-03434-2 (cit. on p. 5).

[48] Changhyun Han et al. "Lasing at topological edge states in a photonic crystal L3 nanocavity dimer array". In: *Light: Science & Applications* 8.1 (2019), p. 40. DOI: 10.1038/s41377-019-0149-7 (cit. on pp. 5, 39).

[49] Weixuan Zhang et al. "Low-threshold topological nanolasers based on the second-order corner state". In: *Light: Science & Applications* 9.1 (Dec. 2020), p. 109. ISSN: 2047-7538. DOI: 10.1038/s41377-020-00352-1 (cit. on pp. 5, 39).

[50] Ha-Reem Kim et al. "Multipolar lasing modes from topological corner states". In: *Nature Communications* 11.1 (Dec. 2020), p. 5758. ISSN: 2041-1723. DOI: 10.1038/s41467-020-19609-9 (cit. on pp. 5, 39).

[51] Gal Harari et al. "Topological insulator laser: Theory". In: *Science* 359.6381 (Mar. 2018), eaar4003. ISSN: 0036-8075. DOI: 10.1126/science.aar4003 (cit. on pp. 5, 6, 17, 24, 25, 27, 36, 37).

[52] Yaroslav V. Kartashov and Dmitry V. Skryabin. "Two-Dimensional Topological Polariton Laser". In: *Physical Review Letters* 122.8 (Feb. 2019), p. 083902. ISSN: 0031-9007. DOI: 10.1103/PhysRevLett.122.083902 (cit. on pp. 5, 6).

[53] Ivan Amelio and Iacopo Carusotto. "Theory of the Coherence of Topological Lasers". In: *Physical Review X* 10.4 (Dec. 2020), p. 041060. ISSN: 2160-3308. DOI: 10.1103/PhysRevX.10.041060 (cit. on pp. 5, 17, 27).

[54] Stefano Longhi and Liang Feng. "Invited Article: Mitigation of dynamical instabilities in laser arrays via non-Hermitian coupling". In: *APL Photonics* 3.6 (June 2018), p. 060802. ISSN: 2378-0967. DOI: 10.1063/1.5028453 (cit. on pp. 6, 23, 25).

[55] Miguel A. Bandres et al. "Topological insulator laser: Experiments". In: *Science* 359.6381 (Mar. 2018), eaar4005. ISSN: 0036-8075. DOI: 10.1126/science.aar4005 (cit. on pp. 6, 17, 18, 24, 27, 28, 36, 37, 39, 50, 60, 62).

[56] Yongquan Zeng et al. "Electrically pumped topological laser with valley edge modes". In: *Nature* 578.7794 (Feb. 2020), pp. 246–250. ISSN: 0028-0836. DOI: 10.1038/s41586-020-1981-x (cit. on pp. 6, 60).

[57] Wanwoo Noh et al. "Experimental demonstration of single-mode topological valley-Hall lasing at telecommunication wavelength controlled by the degree of asymmetry". In: *Optics Letters* 45.15 (Aug. 2020), p. 4108. ISSN: 0146-9592. DOI: 10.1364/OL.399053 (cit. on pp. 6, 39, 60).

[58] Stefano Longhi, Yannis Kominis, and Vassilios Kovanis. "Presence of temporal dynamical instabilities in topological insulator lasers". In: *Europhysics Letters* 122.1 (June 2018), p. 14004. ISSN: 0295-5075. DOI: 10.1209/0295-5075/122/14004 (cit. on pp. 6, 10, 24).

[59] Murray Sargent, Marlan Orvil Scully, and Willis Eugene Lamb. *Laser Physics*. 1st ed. Westview Press, 1974, pp. i–xxx, 1–432. ISBN: 9780201069037. URL: http://www.worldcat.org/oclc/918290542 (cit. on pp. 7, 11, 44, 53).

[60] Marlan Orvil Scully and Muhammad Suhail Zubairy. *Quantum Optics*. Cambridge University Press, 1997, pp. xvi, 630. ISBN: 9780521435956. DOI: 10.1017/CBO9780511813993 (cit. on pp. 7, 10, 11, 44).

[61] Josip Seke, Roman Schnabl, and Frank Rattay. "Collective Radiation Inhibition Effects in the Many-Atom Jaynes-Cummings Model". In: *Coherence and Quantum Optics VI*. Boston, MA: Springer US, 1990, pp. 1065–1069. DOI: 10.1007/978-1-4613-0847-8_193 (cit. on p. 8).

[62] Claude Cohen-Tannoudj, Jacques Dupont-Roc, and Gilbert Grynberg. *Atom-Photon Interactions. Basic Processes and Applications.* Wiley-VCH, 2004, pp. xxii, 656. ISBN: 9780471293361, 9783527617197. DOI: 10.1002/9783527617197 (cit. on pp. 9, 70, 72).

[63] Aurelian Loirette-Pelous et al. "Linearized theory of the fluctuation dynamics in 2D topological lasers". In: *arXiv preprint* (Jan. 2021). arXiv: 2101.11737 (cit. on pp. 10, 17, 24, 25, 44).

[64] Edwin Thompson Jaynes and Frederick Williams Cummings. "Comparison of quantum and semiclassical radiation theories with application to the beam maser". In: *Proceedings of the IEEE* 51.1 (1963), pp. 89–109. ISSN: 0018-9219. DOI: 10.1109/PROC.1963.1664 (cit. on p. 12).

[65] Michiel Wouters and Iacopo Carusotto. "Excitations in a Nonequilibrium Bose-Einstein Condensate of Exciton Polaritons". In: *Physical Review Letters* 99.14 (Oct. 2007), p. 140402. ISSN: 0031-9007. DOI: 10.1103/PhysRevLett.99.140402 (cit. on pp. 14, 25).

[66] Philip G. Harper. "Single Band Motion of Conduction Electrons in a Uniform Magnetic Field". In: *Proceedings of the Physical Society. Section A* 68.10 (Oct. 1955), pp. 874–878. ISSN: 0370-1298. DOI: 10.1088/0370-1298/68/10/304 (cit. on p. 18).

[67] Douglas R. Hofstadter. "Energy levels and wave functions of Bloch electrons in rational and irrational magnetic fields". In: *Physical Review B* 14.6 (Sept. 1976), pp. 2239–2249. ISSN: 0556-2805. DOI: 10.1103/PhysRevB.14.2239 (cit. on p. 18).

[68] David Tong. "Lectures on the Quantum Hall Effect". In: *arXiv preprint* (June 2016). arXiv: 1606.06687 (cit. on p. 18).

[69] Grazia Salerno. "Artificial gauge fields in photonics and mechanical systems". PhD thesis. University of Trento, 2016, p. 124. URL: http://eprints-phd.biblio.unitn.it/1722/ (cit. on p. 18).

[70] Masashi Wakamatsu, Yoshio Kitadono, and Pengming Zhang. "The issue of gauge choice in the Landau problem and the physics of canonical and mechanical orbital angular momenta". In: *Annals of Physics* 392 (Sept. 2017), pp. 287–322. ISSN: 1096035X. DOI: 10.1016/j.aop.2018.03.019 (cit. on p. 18).

[71] Michael Victor Berry. "Quantal Phase Factors Accompanying Adiabatic Changes". In: *Proceedings of the Royal Society A* 392.1802 (1984), pp. 45–57. ISSN: 1364-5021. DOI: 10.1098/rspa.1984.0023 (cit. on p. 19).

[72] Herbert Graves Winful and Shawe-Shiuan Wang. "Stability of phase locking in coupled semiconductor laser arrays". In: *Applied Physics Letters* 53.20 (Nov. 1988), pp. 1894–1896. ISSN: 0003-6951. DOI: 10.1063/1.100363 (cit. on p. 23).

[73] Angela Hohl et al. "Localized Synchronization in Two Coupled Nonidentical Semiconductor Lasers". In: *Physical Review Letters* 78.25 (June 1997), pp. 4745–4748. ISSN: 0031-9007. DOI: 10.1103/PhysRevLett.78.4745 (cit. on p. 23).

[74] Joseph Katz, Shlomo Margalit, and Amnon Yariv. "Diffraction coupled phase-locked semiconductor laser array". In: *Applied Physics Letters* 42.7 (Apr. 1983), pp. 554–556. ISSN: 0003-6951. DOI: 10.1063/1.94025 (cit. on p. 23).

[75] Nathaniel David Mermin. "The topological theory of defects in ordered media". In: *Reviews of Modern Physics* 51.3 (July 1979), pp. 591–648. ISSN: 0034-6861. DOI: 10.1103/RevModPhys.51.591 (cit. on p. 28).

[76] Michael C. Cross and Pierre C. Hohenberg. "Pattern formation outside of equilibrium". In: *Reviews of Modern Physics* 65.3 (July 1993), pp. 851–1112. ISSN: 0034-6861. DOI: 10.1103/RevModPhys.65.851 (cit. on pp. 30, 32).

[77] Robert J. Deissler. "Noise-sustained structure, intermittency, and the Ginzburg-Landau equation". In: *Journal of Statistical Physics* 40.3-4 (Aug. 1985), pp. 371–395. ISSN: 0022-4715. DOI: 10.1007/BF01017180 (cit. on pp. 30, 32).

[78] Marco Santagiustina et al. "Noise-Sustained Convective Structures in Nonlinear Optics". In: *Physical Review Letters* 79.19 (Nov. 1997), pp. 3633–3636. ISSN: 0031-9007. DOI: 10.1103/PhysRevLett.79.3633 (cit. on pp. 30, 32).

[79] Eric Louvergneaux et al. "Experimental Evidence of Absolute and Convective Instabilities in Optics". In: *Physical Review Letters* 92.4 (Jan. 2004), p. 043901. ISSN: 0031-9007. DOI: 10.1103/PhysRevLett.92.043901 (cit. on pp. 30, 32).

[80] Crispin W. Gardiner and Peter Zoller. *Quantum Noise: A Handbook of Markovian and Non-Markovian Quantum Stochastic Methods with Applications to Quantum optics*. 2nd ed. Springer Series in Synergetics. Springer-Verlag Berlin Heidelberg, 2000, pp. i–xxi, 1–438. ISBN: 9783540665717 (cit. on pp. 30, 70, 72).

[81] Michael J. Steel et al. "Dynamical quantum noise in trapped Bose-Einstein condensates". In: *Physical Review A* 58.6 (Dec. 1998), pp. 4824–4835. ISSN: 1050-2947. DOI: 10.1103/PhysRevA.58.4824 (cit. on p. 30).

[82] Alice Sinatra, Carlos Lobo, and Yvan Castin. "The truncated Wigner method for Bose-condensed gases: limits of validity and applications". In: *Journal of Physics B: Atomic, Molecular and Optical Physics* 35.17 (Sept. 2002), pp. 3599–3631. ISSN: 0953-4075. DOI: 10.1088/0953-4075/35/17/301 (cit. on p. 30).

[83] Iacopo Carusotto and Cristiano Ciuti. "Spontaneous microcavity-polariton coherence across the parametric threshold: Quantum Monte Carlo studies". In: *Physical Review B* 72.12 (Sept. 2005), p. 125335. ISSN: 1098-0121. DOI: 10.1103/PhysRevB.72.125335 (cit. on p. 30).

[84] Crispin W. Gardiner and Matthew J. Collett. "Input and output in damped quantum systems: Quantum stochastic differential equations and the master equation". In: *Physical Review A* 31.6 (June 1985), pp. 3761–3774. ISSN: 0556-2791. DOI: 10.1103/PhysRevA.31.3761 (cit. on p. 35).

[85] Yasutomo Ota et al. “Topological photonic crystal nanocavity laser”. In: *Communications Physics* 1.1 (2018), p. 86. ISSN: 23993650. DOI: 10.1038/s42005-018-0083-7 (cit. on p. 39).

[86] Sebastian Klembt et al. “Exciton-polariton topological insulator”. In: *Nature* 562.7728 (Oct. 2018), pp. 552–556. ISSN: 0028-0836. DOI: 10.1038/s41586-018-0601-5 (cit. on p. 39).

[87] Babak Bahari et al. “Photonic quantum Hall effect and multiplexed light sources of large orbital angular momenta”. In: *Nature Physics* (Feb. 2021), pp. 4–8. ISSN: 1745-2473. DOI: 10.1038/s41567-021-01165-8 (cit. on pp. 39, 60, 61).

[88] Matteo Seclì and Iacopo Carusotto. “Harper-Hofstadter Topological Laser with Frequency-Dependent Gain”. In: *2019 Conference on Lasers and Electro-Optics Europe & European Quantum Electronics Conference*. IEEE, June 2019, pp. 1–1. ISBN: 978-1-7281-0469-0. DOI: 10.1109/CLEOE-EQEC.2019.8872202 (cit. on p. 43).

[89] John M. O’Toole and Boualem Boashash. “Fast and memory-efficient algorithms for computing quadratic time–frequency distributions”. In: *Applied and Computational Harmonic Analysis* 35.2 (Sept. 2013), pp. 350–358. ISSN: 10635203. DOI: 10.1016/j.acha.2013.01.003 (cit. on p. 51).

[90] Alexandre Blais et al. “Cavity quantum electrodynamics for superconducting electrical circuits: An architecture for quantum computation”. In: *Physical Review A* 69.6 (June 2004), p. 062320. ISSN: 1050-2947. DOI: 10.1103/PhysRevA.69.062320 (cit. on p. 67).

[91] Andreas Wallraff et al. “Strong coupling of a single photon to a superconducting qubit using circuit quantum electrodynamics”. In: *Nature* 431.7005 (Sept. 2004), pp. 162–167. ISSN: 0028-0836. DOI: 10.1038/nature02851 (cit. on p. 67).

[92] Xiu Gu et al. “Microwave photonics with superconducting quantum circuits”. In: *Physics Reports* 718-719 (Nov. 2017), pp. 1–102. ISSN: 03701573. DOI: 10.1016/j.physrep.2017.10.002 (cit. on p. 67).

[93] Johannes M. Fink. *Quantum Nonlinearities in Strong Coupling Circuit QED: On-Chip Quantum Optics with Microwave Photons*. Lambert Academic Publishing, 2011. ISBN: 9783845419718 (cit. on p. 67).

[94] Andrew A. Houck, Hakan E. Türeci, and Jens Koch. “On-chip quantum simulation with superconducting circuits”. In: *Nature Physics* 8.4 (Apr. 2012), pp. 292–299. ISSN: 1745-2473. DOI: 10.1038/nphys2251 (cit. on p. 67).

[95] Karyn Le Hur et al. “Many-body quantum electrodynamics networks: Non-equilibrium condensed matter physics with light”. In: *Comptes Rendus Physique* 17.8 (Oct. 2016), pp. 808–835. ISSN: 16310705. DOI: 10.1016/j.crhy.2016.05.003 (cit. on p. 67).

[96] Mattias Fitzpatrick et al. "Observation of a Dissipative Phase Transition in a One-Dimensional Circuit QED Lattice". In: *Physical Review X* 7.1 (Feb. 2017), p. 011016. ISSN: 2160-3308. DOI: 10.1103/PhysRevX.7.011016 (cit. on p. 67).

[97] Johannes M. Fink et al. "Observation of the Photon-Blockade Breakdown Phase Transition". In: *Physical Review X* 7.1 (Jan. 2017), p. 011012. ISSN: 2160-3308. DOI: 10.1103/PhysRevX.7.011012 (cit. on p. 67).

[98] Ruichao Ma et al. "A dissipatively stabilized Mott insulator of photons". In: *Nature* 566.7742 (Feb. 2019), pp. 51–57. ISSN: 0028-0836. DOI: 10.1038/s41586-019-0897-9 (cit. on pp. 67, 131, 158).

[99] Alexandre Blais et al. "Circuit quantum electrodynamics". In: *Reviews of Modern Physics* 93.2 (May 2021), p. 025005. ISSN: 0034-6861. DOI: 10.1103/RevModPhys.93.025005 (cit. on p. 67).

[100] Iacopo Carusotto et al. "Photonic materials in circuit quantum electrodynamics". In: *Nature Physics* 16.3 (Mar. 2020), pp. 268–279. ISSN: 1745-2473. DOI: 10.1038/s41567-020-0815-y (cit. on pp. 67, 68).

[101] Michel H. Devoret, Andreas Wallraff, and John M. Martinis. "Superconducting Qubits: A Short Review". In: (Nov. 2004). arXiv: 0411174 [cond-mat] (cit. on p. 67).

[102] Anton Frisk Kockum and Franco Nori. "Quantum Bits with Josephson Junctions". In: *Fundamentals and Frontiers of the Josephson Effect*. Ed. by Francesco Tafuri. Cham: Springer International Publishing, 2019, pp. 703–741. ISBN: 978-3-030-20726-7. DOI: 10.1007/978-3-030-20726-7_17 (cit. on p. 67).

[103] Jens Koch et al. "Charge-insensitive qubit design derived from the Cooper pair box". In: *Physical Review A* 76.4 (Oct. 2007), p. 042319. ISSN: 1050-2947. DOI: 10.1103/PhysRevA.76.042319 (cit. on p. 67).

[104] Eliot Kapit, Mohammad Hafezi, and Steven H. Simon. "Induced Self-Stabilization in Fractional Quantum Hall States of Light". In: *Physical Review X* 4.3 (Sept. 2014), p. 031039. ISSN: 2160-3308. DOI: 10.1103/PhysRevX.4.031039 (cit. on p. 67).

[105] José Lebreuilly, Michiel Wouters, and Iacopo Carusotto. "Towards strongly correlated photons in arrays of dissipative nonlinear cavities under a frequency-dependent incoherent pumping". In: *Comptes Rendus Physique* 17.8 (2016), pp. 836–860. ISSN: 16310705. DOI: 10.1016/j.crhy.2016.07.001 (cit. on pp. 67, 83, 104, 106, 122).

[106] José Lebreuilly et al. "Stabilizing strongly correlated photon fluids with non-Markovian reservoirs". In: *Physical Review A* 96.3 (2017), pp. 1–15. ISSN: 24699934. DOI: 10.1103/PhysRevA.96.033828 (cit. on pp. 67, 158).

[107] Ruichao Ma et al. "Autonomous stabilizer for incompressible photon fluids and solids". In: *Physical Review A* 95.4 (Apr. 2017), p. 043811. ISSN: 2469-9926. DOI: 10.1103/PhysRevA.95.043811 (cit. on p. 67).

[108] Sebastian Schmidt et al. "Nonequilibrium delocalization-localization transition of photons in circuit quantum electrodynamics". In: *Physical Review B* 82.10 (Sept. 2010), p. 100507. ISSN: 1098-0121. DOI: 10.1103/PhysRevB.82.100507 (cit. on pp. 67, 104).

[109] José Lebreuilly, Camille Aron, and Christophe Mora. "Stabilizing Arrays of Photonic Cat States via Spontaneous Symmetry Breaking". In: *Physical Review Letters* 122.12 (Mar. 2019), p. 120402. ISSN: 0031-9007. DOI: 10.1103/PhysRevLett.122.120402 (cit. on p. 67).

[110] Filippo Vicentini et al. "Critical slowing down in driven-dissipative Bose-Hubbard lattices". In: *Physical Review A* 97.1 (Jan. 2018), p. 013853. ISSN: 2469-9926. DOI: 10.1103/PhysRevA.97.013853 (cit. on p. 67).

[111] Alexandre Le Boité, Giuliano Orso, and Cristiano Ciuti. "Steady-State Phases and Tunneling-Induced Instabilities in the Driven Dissipative Bose-Hubbard Model". In: *Physical Review Letters* 110.23 (June 2013), p. 233601. ISSN: 0031-9007. DOI: 10.1103/PhysRevLett.110.233601 (cit. on p. 67).

[112] Alexandre Le Boité, Giuliano Orso, and Cristiano Ciuti. "Bose-Hubbard model: Relation between driven-dissipative steady states and equilibrium quantum phases". In: *Physical Review A* 90.6 (Dec. 2014), p. 063821. ISSN: 1050-2947. DOI: 10.1103/PhysRevA.90.063821 (cit. on p. 67).

[113] Kristian Baumann et al. "Dicke quantum phase transition with a superfluid gas in an optical cavity". In: *Nature* 464.7293 (Apr. 2010), pp. 1301–1306. ISSN: 0028-0836. DOI: 10.1038/nature09009 (cit. on p. 67).

[114] Lukas M. Sieberer et al. "Dynamical Critical Phenomena in Driven-Dissipative Systems". In: *Physical Review Letters* 110.19 (May 2013), p. 195301. ISSN: 0031-9007. DOI: 10.1103/PhysRevLett.110.195301 (cit. on p. 67).

[115] Fabrizio Minganti et al. "Spectral theory of Liouvillians for dissipative phase transitions". In: *Physical Review A* 98.4 (Oct. 2018), p. 042118. ISSN: 2469-9926. DOI: 10.1103/PhysRevA.98.042118 (cit. on pp. 67, 131).

[116] Riccardo Rota et al. "Quantum Critical Regime in a Quadratically Driven Nonlinear Photonic Lattice". In: *Physical Review Letters* 122.11 (Mar. 2019), p. 110405. ISSN: 0031-9007. DOI: 10.1103/PhysRevLett.122.110405 (cit. on p. 67).

[117] Enrico Arrigoni and Antonius Dorda. "Master Equations Versus Keldysh Green's Functions for Correlated Quantum Systems Out of Equilibrium". In: *Out-of-Equilibrium Physics of Correlated Electron Systems*. Ed. by Roberta Citro and Ferdinando Mancini. Springer Series in Solid-State Sciences. Springer International Publishing, 2018. Chap. 4, pp. 121–188. ISBN: 9783319949567. DOI: 10.1007/978-3-319-94956-7_4 (cit. on pp. 69, 70, 72, 95, 96, 107, 108).

[118] Göran Lindblad. "On the generators of quantum dynamical semigroups". In: *Communications in Mathematical Physics* 48.2 (June 1976), pp. 119–130. ISSN: 0010-3616. DOI: 10.1007/BF01608499 (cit. on p. 70).

[119] Heinz-Peter Breuer and Francesco Petruccione. *The Theory of Open Quantum Systems*. Oxford University Press, Jan. 2007. ISBN: 9780199213900. DOI: 10.1093/acprof:oso/9780199213900.001.0001 (cit. on pp. 70, 72).

[120] Carlos Alexandre Brasil, Felipe Fernandes Fanchini, and Reginaldo de Jesus Napolitano. "A simple derivation of the Lindblad equation". In: *Revista Brasileira de Ensino de Física* 35.1 (Mar. 2013), pp. 01–09. ISSN: 1806-9126. DOI: 10.1590/S1806-11172013000100003 (cit. on pp. 70, 72).

[121] Daniel Manzano. "A short introduction to the Lindblad master equation". In: *AIP Advances* 10.2 (Feb. 2020), p. 025106. ISSN: 2158-3226. DOI: 10.1063/1.5115323 (cit. on pp. 70, 72).

[122] Konstantin G. Zloshchastiev and Alessandro Sergi. "Comparison and unification of non-Hermitian and Lindblad approaches with applications to open quantum optical systems". In: *Journal of Modern Optics* 61.16 (Sept. 2014), pp. 1298–1308. ISSN: 0950-0340. DOI: 10.1080/09500340.2014.930528 (cit. on p. 70).

[123] Ulrich Schollwöck. "The density-matrix renormalization group". In: *Reviews of Modern Physics* 77.1 (Apr. 2005), pp. 259–315. ISSN: 0034-6861. DOI: 10.1103/RevModPhys.77.259 (cit. on p. 71).

[124] Enrico Arrigoni, Michael Knap, and Wolfgang von der Linden. "Nonequilibrium Dynamical Mean-Field Theory: An Auxiliary Quantum Master Equation Approach". In: *Physical Review Letters* 110.8 (Feb. 2013), p. 086403. ISSN: 0031-9007. DOI: 10.1103/PhysRevLett.110.086403 (cit. on pp. 71, 132, 135, 138, 139).

[125] Antonius Dorda et al. "Auxiliary master equation approach to nonequilibrium correlated impurities". In: *Physical Review B* 89.16 (Apr. 2014), p. 165105. ISSN: 1098-0121. DOI: 10.1103/PhysRevB.89.165105 (cit. on pp. 71, 138, 139, 149).

[126] Orazio Scarlatella et al. "Dynamical Mean-Field Theory for Markovian Open Quantum Many-Body Systems". In: *Physical Review X* 11.3 (July 2021), p. 031018. ISSN: 2160-3308. DOI: 10.1103/PhysRevX.11.031018 (cit. on pp. 71, 132, 135, 151, 158).

[127] Emil J. Bergholtz, Jan Carl Budich, and Flore K. Kunst. "Exceptional topology of non-Hermitian systems". In: *Reviews of Modern Physics* 93.1 (Feb. 2021), p. 015005. ISSN: 0034-6861. DOI: 10.1103/RevModPhys.93.015005 (cit. on p. 71).

[128] Manfred Schmutz. "Real-time green's functions in many body problems". In: *Zeitschrift für Physik B Condensed Matter and Quanta* 30.1 (Mar. 1978), pp. 97–106. ISSN: 0340-224X. DOI: 10.1007/BF01323673 (cit. on p. 77).

[129] Izumi Ojima. "Gauge fields at finite temperatures — "Thermo field dynamics" and the KMS condition and their extension to gauge theories". In: *Annals of Physics* 137.1 (Nov. 1981), pp. 1–32. ISSN: 00034916. DOI: 10.1016/0003-4916(81)90058-0 (cit. on pp. 77–79, 169).

[130] Hiroomi Umezawa, Hideki Matsumoto, and Masashi Tachiki. *Thermo Field Dynamics and Condensed States*. North-Holland, 1982, pp. i–xvi, 1–591. ISBN: 9780444863614. URL: http://www.worldcat.org/oclc/803101452 (cit. on pp. 77, 79).

[131] Hiroomi Umezawa. *Advanced Field Theory: Micro, Macro, and Thermal Physics*. New York: American Institute of Physics, 1992, pp. i–xii, 1–238. ISBN: 9781563964565. URL: http://www.worldcat.org/oclc/907419727 (cit. on p. 77).

[132] Yasushi Takahashi and Hiroomi Umezawa. "Thermo Field Dynamics". In: *International Journal of Modern Physics B* 10.13-14 (June 1996), pp. 1755–1805. ISSN: 0217-9792. DOI: 10.1142/S0217979296000817 (cit. on p. 77).

[133] Thomas Barthel, Ulrich Schollwöck, and Steven R. White. "Spectral functions in one-dimensional quantum systems at finite temperature using the density matrix renormalization group". In: *Physical Review B* 79.24 (June 2009), p. 245101. ISSN: 1098-0121. DOI: 10.1103/PhysRevB.79.245101 (cit. on p. 78).

[134] Alan A. Dzhioev and Daniel S. Kosov. "Super-fermion representation of quantum kinetic equations for the electron transport problem". In: *The Journal of Chemical Physics* 134.4 (Jan. 2011), p. 044121. ISSN: 0021-9606. DOI: 10.1063/1.3548065 (cit. on p. 78).

[135] Daniel S. Kosov. "Distribution of waiting times between superoperator quantum jumps in Lindblad dynamics". In: (May 2016). arXiv: 1605.02170 (cit. on pp. 78, 81).

[136] Hiroomi Umezawa. "Equilibrium and Non-Equilibrium Thermal Physics". In: *Banff/CAP Workshop on Thermal Field Theory: Proceedings of the 3rd Workshop on Thermal Field Theories and Their Applications*. Ed. by Faqir C Khanna et al. World Scientific, 1994. Chap. 3, pp. 109–135. ISBN: 9789814534307. DOI: 10.1142/2364 (cit. on p. 79).

[137] Alex Kamenev. "Many-body theory of non-equilibrium systems". In: (Dec. 2004). arXiv: 0412296 [cond-mat] (cit. on pp. 88–90).

[138] Alex Kamenev. *Introduction to the Keldysh Formalism*. 2009. URL: http://www.capri-school.eu/capri09/ (cit. on pp. 88, 120).

[139] Takafumi Kita. "Introduction to Nonequilibrium Statistical Mechanics with Quantum Field Theory". In: *Progress of Theoretical Physics* 123.4 (Apr. 2010), pp. 581–658. ISSN: 0033-068X. DOI: 10.1143/PTP.123.581 (cit. on p. 88).

[140] Emanuele G. Dalla Torre et al. "Keldysh approach for nonequilibrium phase transitions in quantum optics: Beyond the Dicke model in optical cavities". In: *Physical Review A* 87.2 (Feb. 2013), p. 023831. ISSN: 1050-2947. DOI: 10.1103/PhysRevA.87.023831 (cit. on p. 88).

[141] Petr I. Arseev. "On the nonequilibrium diagram technique: derivation, some features, and applications". In: *Physics-Uspekhi* 58.12 (Dec. 2015), pp. 1159–1205. ISSN: 1063-7869. DOI: 10.3367/UFNe.0185.201512b.1271 (cit. on p. 88).

[142] Lukas M. Sieberer, Michael Buchhold, and Sebastian Diehl. "Keldysh field theory for driven open quantum systems". In: *Reports on Progress in Physics* 79.9 (Sept. 2016), p. 096001. ISSN: 0034-4885. DOI: 10.1088/0034-4885/79/9/096001 (cit. on pp. 88, 92).

[143] Mohammad F. Maghrebi and Alexey V. Gorshkov. "Nonequilibrium many-body steady states via Keldysh formalism". In: *Physical Review B* 93.1 (Jan. 2016), p. 014307. ISSN: 2469-9950. DOI: 10.1103/PhysRevB.93.014307 (cit. on p. 88).

[144] Frauke Schwarz et al. "Lindblad-driven discretized leads for nonequilibrium steady-state transport in quantum impurity models: Recovering the continuum limit". In: *Physical Review B* 94.15 (Oct. 2016), p. 155142. ISSN: 2469-9950. DOI: 10.1103/PhysRevB.94.155142 (cit. on p. 96).

[145] Christopher Eichler et al. "Quantum-Limited Amplification and Entanglement in Coupled Nonlinear Resonators". In: *Physical Review Letters* 113.11 (Sept. 2014), p. 110502. ISSN: 0031-9007. DOI: 10.1103/PhysRevLett.113.110502 (cit. on pp. 103, 104).

[146] Konstantinos G. Lagoudakis et al. "Coherent Oscillations in an Exciton-Polariton Josephson Junction". In: *Physical Review Letters* 105.12 (Sept. 2010), p. 120403. ISSN: 0031-9007. DOI: 10.1103/PhysRevLett.105.120403 (cit. on p. 103).

[147] Marta Galbiati et al. "Polariton Condensation in Photonic Molecules". In: *Physical Review Letters* 108.12 (Mar. 2012), p. 126403. ISSN: 0031-9007. DOI: 10.1103/PhysRevLett.108.126403 (cit. on p. 103).

[148] Marco Abbarchi et al. “Macroscopic quantum self-trapping and Josephson oscillations of exciton polaritons”. In: *Nature Physics* 9.5 (May 2013), pp. 275–279. ISSN: 1745-2473. DOI: 10.1038/nphys2609 (cit. on pp. 103, 111).

[149] Philippe Hamel et al. “Spontaneous mirror-symmetry breaking in coupled photonic-crystal nanolasers”. In: *Nature Photonics* 9.5 (May 2015), pp. 311–315. ISSN: 1749-4885. DOI: 10.1038/nphoton.2015.65 (cit. on p. 103).

[150] Mathias Marconi et al. “Mesoscopic Limit Cycles in Coupled Nanolasers”. In: *Physical Review Letters* 124.21 (May 2020), p. 213602. ISSN: 0031-9007. DOI: 10.1103/PhysRevLett.124.213602 (cit. on p. 103).

[151] Augusto Smerzi et al. “Quantum Coherent Atomic Tunneling between Two Trapped Bose-Einstein Condensates”. In: *Physical Review Letters* 79.25 (Dec. 1997), pp. 4950–4953. ISSN: 0031-9007. DOI: 10.1103/PhysRevLett.79.4950 (cit. on pp. 104, 108, 109).

[152] Lev Petrovič Pitaevskii and Sandro Stringari. “Thermal vs Quantum Decoherence in Double Well Trapped Bose-Einstein Condensates”. In: *Physical Review Letters* 87.18 (Oct. 2001), p. 180402. ISSN: 0031-9007. DOI: 10.1103/PhysRevLett.87.180402 (cit. on p. 104).

[153] Anatoli Polkovnikov, Subir Sachdev, and Steven M. Girvin. “Nonequilibrium Gross-Pitaevskii dynamics of boson lattice models”. In: *Physical Review A* 66.5 (Nov. 2002), p. 053607. ISSN: 1050-2947. DOI: 10.1103/PhysRevA.66.053607 (cit. on p. 104).

[154] Michael Albiez et al. “Direct Observation of Tunneling and Nonlinear Self-Trapping in a Single Bosonic Josephson Junction”. In: *Physical Review Letters* 95.1 (June 2005), p. 010402. ISSN: 0031-9007. DOI: 10.1103/PhysRevLett.95.010402 (cit. on pp. 104, 109).

[155] Mauricio Trujillo-Martinez, Anna Posazhennikova, and Johann Kroha. “Nonequilibrium Josephson Oscillations in Bose-Einstein Condensates without Dissipation”. In: *Physical Review Letters* 103.10 (Sept. 2009), p. 105302. ISSN: 0031-9007. DOI: 10.1103/PhysRevLett.103.105302 (cit. on p. 104).

[156] Tejaswi Venumadhav, Masudul Haque, and Roderich Moessner. “Finite-rate quenches of site bias in the Bose-Hubbard dimer”. In: *Physical Review B* 81.5 (Feb. 2010), p. 054305. ISSN: 1098-0121. DOI: 10.1103/PhysRevB.81.054305 (cit. on p. 104).

[157] Tadeusz Pudlik et al. “Dynamics of entanglement in a dissipative Bose-Hubbard dimer”. In: *Physical Review A* 88.6 (Dec. 2013), p. 063606. ISSN: 1050-2947. DOI: 10.1103/PhysRevA.88.063606 (cit. on pp. 104, 109).

[158] Timothy C. H. Liew and Vincenzo Savona. "Single Photons from Coupled Quantum Modes". In: *Physical Review Letters* 104.18 (May 2010), p. 183601. ISSN: 0031-9007. DOI: 10.1103/PhysRevLett.104.183601 (cit. on p. 104).

[159] Motoaki Bamba et al. "Origin of strong photon antibunching in weakly nonlinear photonic molecules". In: *Physical Review A* 83.2 (Feb. 2011), p. 021802. ISSN: 1050-2947. DOI: 10.1103/PhysRevA.83.021802 (cit. on p. 104).

[160] Wim Casteels and Cristiano Ciuti. "Quantum entanglement in the spatial-symmetry-breaking phase transition of a driven-dissipative Bose-Hubbard dimer". In: *Physical Review A* 95.1 (Jan. 2017), p. 013812. ISSN: 2469-9926. DOI: 10.1103/PhysRevA.95.013812 (cit. on p. 104).

[161] Kilian Seibold, Riccardo Rota, and Vincenzo Savona. "Dissipative time crystal in an asymmetric nonlinear photonic dimer". In: *Physical Review A* 101.3 (Mar. 2020), p. 033839. ISSN: 2469-9926. DOI: 10.1103/PhysRevA.101.033839 (cit. on p. 104).

[162] Matteo Seclì, Massimo Capone, and Marco Schirò. "Signatures of self-trapping in the driven-dissipative Bose–Hubbard dimer". In: *New Journal of Physics* 23.6 (June 2021), p. 063056. ISSN: 1367-2630. DOI: 10.1088/1367-2630/ac04c8 (cit. on p. 104).

[163] Orazio Scarlatella, Aashish A. Clerk, and Marco Schirò. "Spectral functions and negative density of states of a driven-dissipative nonlinear quantum resonator". In: *New Journal of Physics* 21.4 (Apr. 2019), p. 043040. ISSN: 1367-2630. DOI: 10.1088/1367-2630/ab0ce9 (cit. on pp. 108, 131).

[164] Davide Sarchi et al. "Coherent dynamics and parametric instabilities of microcavity polaritons in double-well systems". In: *Physical Review B* 77.12 (Mar. 2008), p. 125324. ISSN: 1098-0121. DOI: 10.1103/PhysRevB.77.125324 (cit. on p. 108).

[165] Rudolf Gati et al. "A primary noise thermometer for ultracold Bose gases". In: *New Journal of Physics* 8.9 (Sept. 2006), pp. 189–189. ISSN: 1367-2630. DOI: 10.1088/1367-2630/8/9/189 (cit. on p. 109).

[166] Rudolf Gati et al. "Noise Thermometry with Two Weakly Coupled Bose-Einstein Condensates". In: *Physical Review Letters* 96.13 (Apr. 2006), p. 130404. ISSN: 0031-9007. DOI: 10.1103/PhysRevLett.96.130404 (cit. on p. 109).

[167] Shahar Levy et al. "The a.c. and d.c. Josephson effects in a Bose–Einstein condensate". In: *Nature* 449.7162 (Oct. 2007), pp. 579–583. ISSN: 0028-0836. DOI: 10.1038/nature06186 (cit. on p. 109).

[168] Lindsay J. LeBlanc et al. "Dynamics of a Tunable Superfluid Junction". In: *Physical Review Letters* 106.2 (Jan. 2011), p. 025302. ISSN: 0031-9007. DOI: 10.1103/PhysRevLett.106.025302 (cit. on p. 109).

[169] Holger Hennig, Dirk Witthaut, and David K. Campbell. "Global phase space of coherence and entanglement in a double-well Bose-Einstein condensate". In: *Physical Review A* 86.5 (Nov. 2012), p. 051604. ISSN: 1050-2947. DOI: 10.1103/PhysRevA.86.051604 (cit. on p. 109).

[170] Tadeusz Pudlik et al. "Tunneling in the self-trapped regime of a two-well Bose-Einstein condensate". In: *Physical Review A* 90.5 (Nov. 2014), p. 053610. ISSN: 1050-2947. DOI: 10.1103/PhysRevA.90.053610 (cit. on p. 109).

[171] Tilman Zibold et al. "Classical Bifurcation at the Transition from Rabi to Josephson Dynamics". In: *Physical Review Letters* 105.20 (Nov. 2010), p. 204101. ISSN: 0031-9007. DOI: 10.1103/PhysRevLett.105.204101 (cit. on p. 109).

[172] Haggai Landa, Marco Schirò, and Grégoire Misguich. "Multistability of Driven-Dissipative Quantum Spins". In: *Physical Review Letters* 124.4 (Jan. 2020), p. 043601. ISSN: 0031-9007. DOI: 10.1103/PhysRevLett.124.043601 (cit. on p. 131).

[173] Anthony James Hoffman et al. "Dispersive Photon Blockade in a Superconducting Circuit". In: *Physical Review Letters* 107.5 (July 2011), p. 053602. ISSN: 0031-9007. DOI: 10.1103/PhysRevLett.107.053602 (cit. on p. 131).

[174] Hideo Aoki et al. "Nonequilibrium dynamical mean-field theory and its applications". In: *Reviews of Modern Physics* 86.2 (June 2014), pp. 779–837. ISSN: 0034-6861. DOI: 10.1103/RevModPhys.86.779 (cit. on pp. 132, 135).

[175] Massimo Capone and Sergio Ciuchi. "Interplay between spin and phonon fluctuations in the double-exchange model for the manganites". In: *Phys. Rev. B* 65.10 (Feb. 2002), p. 104409. DOI: 10.1103/PhysRevB.65.104409 (cit. on p. 132).

[176] Michael Potthoff. "Two-site dynamical mean-field theory". In: *Physical Review B* 64.16 (Oct. 2001), p. 165114. ISSN: 0163-1829. DOI: 10.1103/PhysRevB.64.165114 (cit. on pp. 132, 155).

[177] Bo Yan et al. "Observation of dipolar spin-exchange interactions with lattice-confined polar molecules". In: *Nature* 501.7468 (Sept. 2013), pp. 521–525. ISSN: 0028-0836. DOI: 10.1038/nature12483 (cit. on pp. 133, 151).

[178] Takafumi Tomita et al. "Observation of the Mott insulator to superfluid crossover of a driven-dissipative Bose-Hubbard system". In: *Science Advances* 3.12 (Dec. 2017), e1701513. ISSN: 2375-2548. DOI: 10.1126/sciadv.1701513 (cit. on pp. 133, 151).

[179] Dieter Vollhardt. "Dynamical Mean-Field Theory of Electronic Correlations in Models and Materials". In: *Lectures on the Physics of Strongly Correlated Systems XIV: Fourteenth Training Course in the Physics of Strongly Correlated Systems*. Ed. by Adolfo Avella and Ferdinando Mancini. Vol. 1297. Apr. 2010, pp. 339–403. DOI: 10.1063/1.3518901 (cit. on p. 135).

[180] Peter Anders et al. "Dynamical mean-field theory for bosons". In: *New Journal of Physics* 13.7 (July 2011), p. 075013. ISSN: 1367-2630. DOI: 10.1088/1367-2630/13/7/075013 (cit. on p. 135).

[181] Michiel Snoek and Walter Hofstetter. "Bosonic Dynamical Mean-Field Theory". In: *Quantum Gases: Finite Temperature and Non-Equilibrium Dynamics*. Ed. by Nick Proukakis et al. Apr. 2013, pp. 355–365. DOI: 10.1142/9781848168121_0023 (cit. on p. 135).

[182] Hugo U. R. Strand, Martin Eckstein, and Philipp Werner. "Nonequilibrium Dynamical Mean-Field Theory for Bosonic Lattice Models". In: *Physical Review X* 5.1 (Mar. 2015), p. 011038. ISSN: 2160-3308. DOI: 10.1103/PhysRevX.5.011038 (cit. on pp. 135, 147, 148).

[183] Hugo U. R. Strand, Martin Eckstein, and Philipp Werner. "Beyond the Hubbard bands in strongly correlated lattice bosons". In: *Physical Review A* 92.6 (Dec. 2015), p. 063602. ISSN: 1050-2947. DOI: 10.1103/PhysRevA.92.063602 (cit. on p. 135).

[184] Conrad Sanderson and Ryan Curtin. "Armadillo: a template-based C++ library for linear algebra". In: *The Journal of Open Source Software* 1.2 (June 2016), p. 26. ISSN: 2475-9066. DOI: 10.21105/joss.00026 (cit. on p. 142).

[185] Conrad Sanderson and Ryan Curtin. "A User-Friendly Hybrid Sparse Matrix Class in C++". In: *Lecture Notes in Computer Science (including subseries Lecture Notes in Artificial Intelligence and Lecture Notes in Bioinformatics)*. Vol. 10931 LNCS. Springer, Cham, July 2018, pp. 422–430. DOI: 10.1007/978-3-319-96418-8_50 (cit. on p. 142).

[186] Stanimire Tomov, Jack Dongarra, and Marc Baboulin. "Towards dense linear algebra for hybrid GPU accelerated manycore systems". In: *Parallel Computing* 36.5-6 (June 2010), pp. 232–240. ISSN: 0167-8191. DOI: 10.1016/J.PARCO.2009.12.005 (cit. on p. 143).

[187] Stanimire Tomov et al. "Dense linear algebra solvers for multicore with GPU accelerators". In: *Proceedings of the 2010 IEEE International Symposium on Parallel and Distributed Processing, Workshops and Phd Forum, IPDPSW 2010* (2010). DOI: 10.1109/IPDPSW.2010.5470941 (cit. on p. 143).

[188] Jack Dongarra et al. "Accelerating Numerical Dense Linear Algebra Calculations with GPUs". In: *Numerical Computations with GPUs* (Jan. 2014), pp. 3–28. DOI: 10.1007/978-3-319-06548-9_1 (cit. on p. 143).

[189] Hans Albrecht Bethe. "Statistical theory of superlattices". In: *Proceedings of the Royal Society of London. Series A - Mathematical and Physical Sciences* 150.871 (July 1935), pp. 552–575. ISSN: 0080-4630. DOI: 10.1098/rspa.1935.0122 (cit. on p. 148).

[190] Shikhar Bhardwaj et al. "ensmallen: a flexible C++ library for efficient function optimization". In: *CoRR* (Oct. 2018). DOI: 10.5281/zenodo.2008650 (cit. on p. 149).

[191] Yixuan Qiu. *LBFGS++: A Header-only C++ Library for L-BFGS and L-BFGS-B Algorithms*. 2016. URL: https://github.com/yixuan/LBFGSpp (cit. on p. 149).

[192] Patrick Wieschollek. *CppOptimizationLibrary*. 2016. URL: https://github.com/PatWie/CppNumericalSolvers (cit. on p. 149).

[193] Richard H. Byrd et al. "A Limited Memory Algorithm for Bound Constrained Optimization". In: *SIAM Journal on Scientific Computing* 16.5 (Sept. 1995), pp. 1190–1208. ISSN: 1064-8275. DOI: 10.1137/0916069 (cit. on p. 149).

[194] Baidyanath Misra and Ennackal Chandy George Sudarshan. "The Zeno's paradox in quantum theory". In: *Journal of Mathematical Physics* 18.4 (Apr. 1977), pp. 756–763. ISSN: 0022-2488. DOI: 10.1063/1.523304 (cit. on pp. 149, 151).

[195] Robert Purves Hardie and Russel Kerr Gaye. "Physics". In: *Complete Works of Aristotle, Volume 1*. Ed. by Jonathan Barnes. The Revised Oxford Translation. Princeton University Press, Aug. 1984, pp. 315–446. ISBN: 9780691016504. DOI: 10.1515/9781400835843-010 (cit. on pp. 149, 151).

[196] Asher Peres. "Zeno paradox in quantum theory". In: *American Journal of Physics* 48.11 (Nov. 1980), pp. 931–932. ISSN: 0002-9505. DOI: 10.1119/1.12204 (cit. on p. 151).

[197] Wayne M. Itano et al. "Quantum Zeno effect". In: *Physical Review A* 41.5 (Mar. 1990), pp. 2295–2300. ISSN: 1050-2947. DOI: 10.1103/PhysRevA.41.2295 (cit. on p. 151).

[198] Davide Rossini et al. "Strong correlations in lossy one-dimensional quantum gases: from the quantum Zeno effect to the generalized Gibbs ensemble". In: *arXiv preprint* (Nov. 2020). arXiv: 2011.04318 (cit. on p. 151).

[199] José Lebreuilly. "Strongly correlated quantum fluids and effective thermalization in non-Markovian driven-dissipative photonic systems". PhD Thesis. Trento: Università degli Studi di Trento, 2017, pp. i–xii, 1–134. ISBN: 1210824108. URL: http://eprints-phd.biblio.unitn.it/2708/ (cit. on p. 158).

Index